HEAT AND MASS TRANSFER DURING THE MELTING PROCESS OF A POROUS FROST LAYER ON A VERTICAL SURFACE

A DISSERTATION
SUBMITTED TO THE FACULTY OF THE GRADUATE SCHOOL
OF THE UNIVERSITY OF MINNESOTA
BY

WILLIAM FRANCIS MOHS

IN PARTIAL FULFILLMENT OF THE REQUIREMENTS
FOR THE DEGREE OF
DOCTOR OF
PHILOSOPHY

PROFESSOR FRANCIS A. KULACKI

MAY 2013

Acknowledgements

First I acknowledge the support, guidance, and counsel I received over the past several years from my advisor, Professor Frank Kulacki. I appreciate the patience you have shown me as we developed a rough idea into this document. I thoroughly enjoyed our discussion about all topics, including my research. I am also indebted to my fellow students in the Heat Transfer Laboratory, namely Charlie Beckie, Molly Lefebver, and Dan Janssen. Thank you for your help. I look forward to continuing my work with Prof. Kulacki and his students for the years to come.

This work would not have been completed without the generous financial support of Thermo King\Ingersoll Rand. In this day and age, where the loyalty of a company is in question, TK-IR has shown respect and courage to support me in my academic endeavors. I am eternally indebted to my manager, Jeff Berge, who not only was willing to let me join his group, but also had the courage and tenacity to support my research. I would also like to acknowledge my fellow R&D engineers, who through their own ways helped me over the past several years. I hope that I show the same loyalty and dedication to TK as I have received from the company and my colleagues.

I would like to close by acknowledging the support of my family. As the years have passed, my research has grown from a vague idea to this final thesis, so too have my children grown from small infants to precocious children. They have proven to be the best diversion in the world. Gabe and Paige, I have learned more from you than all the books and papers in the world. I love you dearly. Finally, I need to acknowledge my wife and partner, Mary. You have shown me so much patience and dedication over these past several years. You have been there when I needed an editor, sounding board, or just a bit of motivation. I appreciate everything you have done for me and I look forward to all of the future adventures we will share together. You bring out the best in me.

Dedication

To Gabe and Paige

The path to knowledge is a road that never ends. Take your time and enjoy the journey.

Abstract

An important problem in the refrigeration industry is the formation and removal of frost layers on sub-freezing air coolers. The frost layer, a porous structure of ice and air, directly diminishes the performance and efficiency of the entire cooling system by presenting resistances to air flow and heat transfer in the air cooler. To return the system to pre-frosted performance the layer must be removed through a defrost cycle. The most common defrost cycle uses heat applied at the heat exchanger surfaces to melt the frost. Current methods of defrosting are inherently inefficient, with the majority of the heat being lost to the surrounding environment. Most studies have concentrated on the formation of the frost layer, and not the melting phenomena during the defrost cycle.

In this study, direct measurements and a fundamental model to describe the melting process of a frost layer on a vertical heated surface are presented. The experimental facility provides the first direct measurements of heat and mass transfer during defrost. The measurements confirmed the multistage nature of defrost. The multistage model characterized the different thermal and mass transport processes that dominate each stage.

The first stage is dominated by sensible heating of the frost layer. Both the experiment and model showed that heat and mass transfer through sublimation during the initial stages are insignificant, accounting for less than 1% of the total energy transfer. The second stage of defrost is dominated by the melting of the frost layer. The melt rate model generally predicts the front velocity within 25% of the velocity determined using the digital image analysis technique. Higher heat transfer rates resulted in faster melt velocity, and thus shortened defrost times. Evaporation of the melt liquid from the surface dominates the final stage. The heat transfer model for this stage predicts the heat transfer coefficient within ±25% of the experiment. The overall defrost efficiency was found to be primarily dependent on the initial frost thickness, with thicker layer having less heat lost to the ambient space and a higher efficiency.

Contents

List of Tables

List of Figures

Nomenclature

A	area [m^2]
Bi	Biot Number, $\delta h/k$
c_p	specific heat [J/kg-K]
C	thermal capacitance [J/K], arbitrary constant
d	diameter [m]
D	diffusion coefficient [m^2/s]
E	energy [J]
f	wetted area fraction
g	gravity [9.81 m/s^2]
h	convective heat transfer coefficient [W/m^2K], enthalpy [kJ/kg],
h_m	mass transfer coefficient [kg/s]
H	height of fin [m]
k	thermal conductivity [W/m-K]
L	length of fin [m]
Le	Lewis Number, α/D
m	mass [kg], slope of water vapor density equation [kg/m^3-K]
m”	mass flux [kg/s-m^2]
$\dot{m}$	mass flow rate [kg/s]
M	dimensionless mass transfer
N	number of pixels
P	perimeter[m]
p	pressure [Pa]
q”	heat flux [W/m^2]
Q	heat flow [W]
R	Individual Gas Constant [J/kg-K]
R	Thermal resistance [K/W]
RH	relative humidity [%]
S	Water content ratio [m^3/m^3]
St	Stefan Number, $c_p \Delta T/ \lambda_{if}$
t	time [s]
T	temperature [°C]
u	velocity [m/s]
$\overline{u_w}$	average velocity [m/s]
U	dimensionless velocity
UA	overall heat transfer coefficient [W/K]
V	Volume [m^3]
$\dot{V}$	Volumetric flow [m^3/s]
w	half thickness of fin [m]
W	humidity ratio [kg/kg]
x	direction along surface perpendicular to gravity
y	direction perpendicular to surface
z	direction along surface parallel to gravity

Greek Symbols

α	thermal diffusivity [m^2/s]
Γ	sublimation coefficient [-]
δ	thickness [m]
Δ	difference
ε	porosity, void fraction [-]
η	efficiency [-], dimensionless thickness [-]
θ	dimensionless temperature [-]
κ	dimensionless conductivity [-]
λ_{if}	latent heat of fusion [334 kJ/kg]
λ_{fg}	latent heat of vaporization [2270 kJ/kg]
λ_{ig}	latent heat of sublimation [2604 kJ/kg]
π	dimensionless mass diffusion [-]
ρ	density [kg/m^3]
τ	tortuosity [-], dimensionless time [-]
φ	dimensionless vapor pressure [-]

Subscripts

a	air
c	cold sink, coil, critical
ch	chamber
cp	cold plate
d	defrost, droplet
e	extended surface, fin
eff	effective
f	frost
fs	frost surface
g	glycol
h	hot sink
hfs	heat flux sensor
hu	humidifier
i	ice, inlet
l	liquid
lt	latent
m	melt
o	outlet
p	permeation layer
r	refrigerant
s	surface, saturation
sp	spreader
sn	sensible
t	total
ts	test surface
TE	thermal electric
v	vapor
w	water
∞	ambient
0	initial
1	defrost stage I
2	defrost stage II
3	defrost stage III

1 Introduction

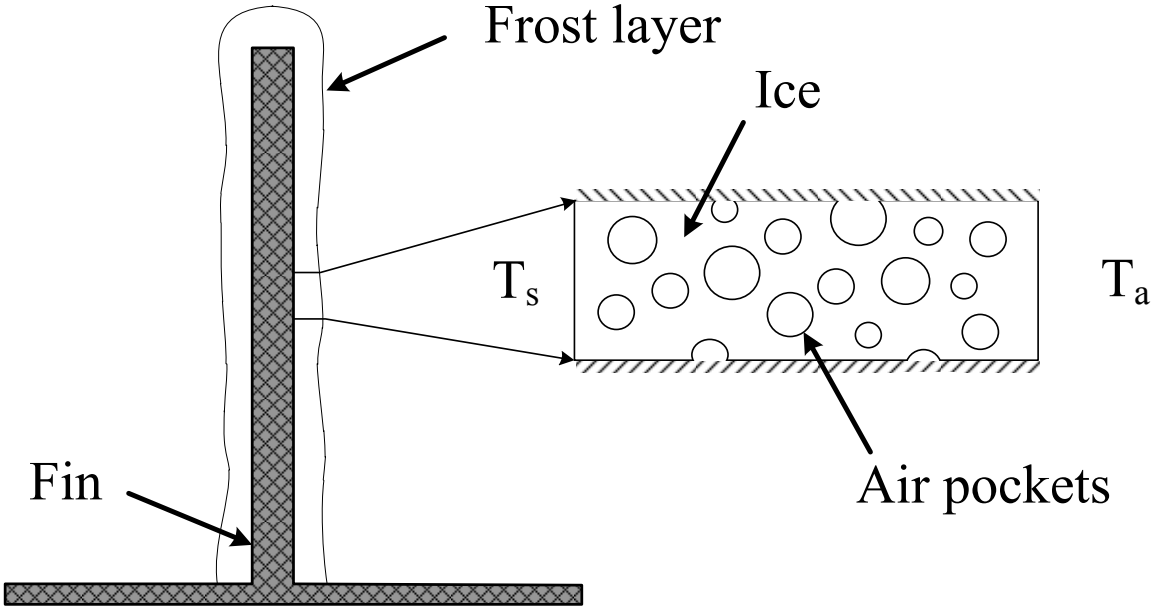

Figure 1-1. Frost on a fin anchored to the surface of a heat exchanger tube.

An important problem in the refrigeration industry is the formation and melting of frost layers on the surfaces of low temperature heat exchanger surfaces (commonly referred to as "coils" in the industry). Water vapor will condense on the surface of the heat exchanger when its surface temperature is below the local dew point of the air-water vapor mixture in contact with it. When the surface temperature is below the freezing point of water, frost will form either by freezing of the water condensate or via direct sublimation to the surface.

Figure 1-1 shows an idealized frost layer on an extended surface (a fin) anchored to a heat exchanger tube. The frost layer is a porous structure of water-ice and air pockets of various sizes and geometries. Experimental studies have found the growth process to occur in a predictable pattern: nucleation, tip-growth, densification, and ultimately re-nucleation and a repeat of this process. The frost growth process and properties have been well documented in the recent literature with correlations to calculate frost thickness, density, and conductivity as a function of growth time.

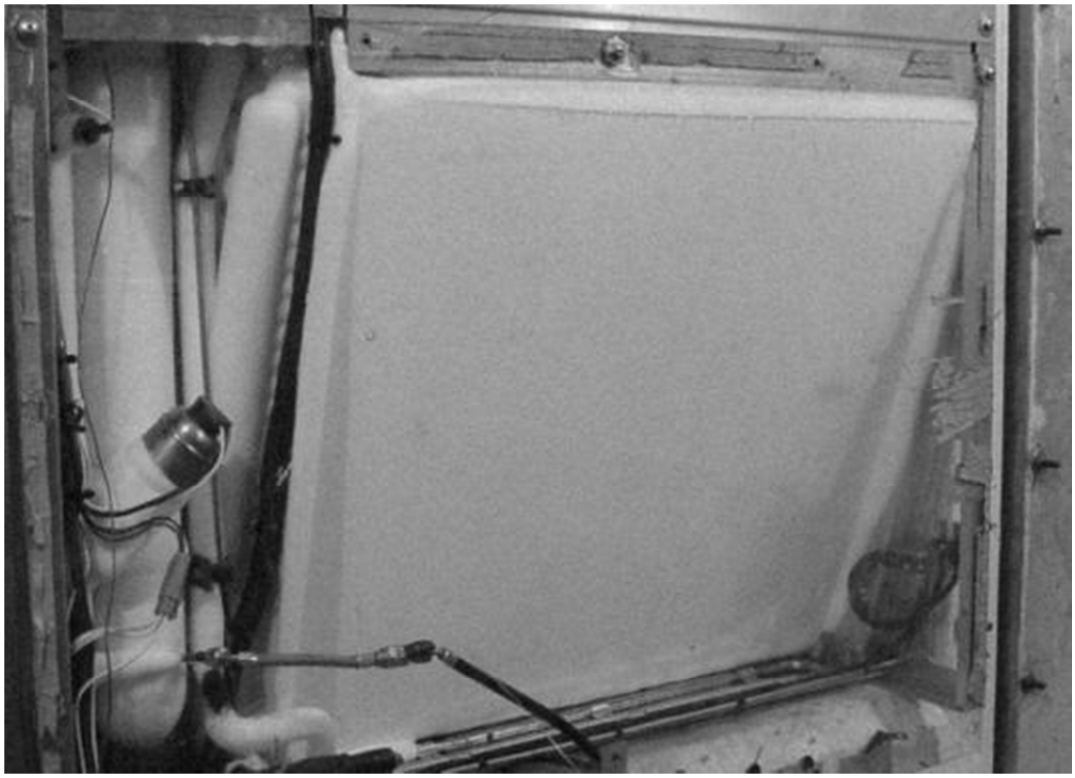

Figure 1-2. Severely frosted evaporator (Courtesy of Thermo King Corp.)

The frosting of low-temperature heat exchangers has a significant impact on refrigeration system performance and efficiency. The porous frost layer presents an insulating layer to the coil surface; increasing the overall resistance to the heat transfer in the coil. In addition, as the frost layer grows in depth, the free area for airflow across the frontal area of the heat exchanger is reduced, increasing the flow resistance, and thus decreasing the air mass flow rate through the coil. Figure 1-2 shows a severely frosted evaporator where the flow area has been completely obstructed by frost. The combined effect of the increased thermal resistance and reduced air mass flow rate causes a drop in the evaporator pressure of a vapor compression refrigeration system as the system rebalances to a new operating point. The drop in evaporator pressure causes a drop in the surface temperature of the coil.

A simple analysis of the idealized Carnot refrigerator shows the reduction of the system efficiency as frosting reduces the effectiveness of the evaporator. For the case

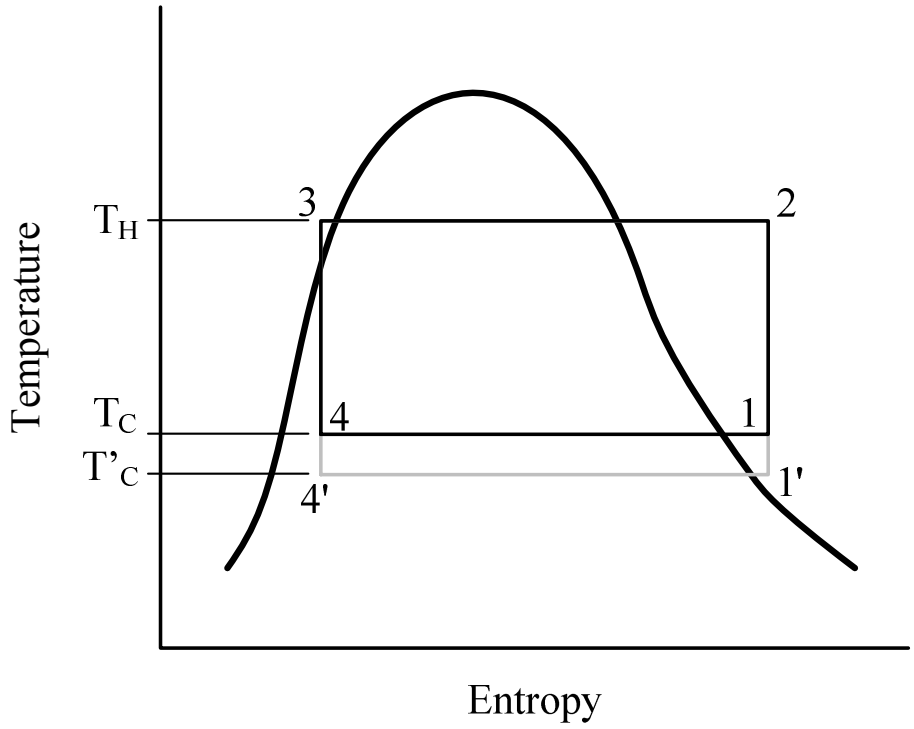

Figure 1-3. Ideal Carnot refrigerator.

shown in Figure 1-3, the system operates between temperature reservoirs T_H and T_C in an unfrosted condition. As the frost layer builds, the coil temperature drops to a new reservoir temperature T'_C. The efficiency of a Carnot refrigerator, as measured by the coefficient of performance (COP), is given by Equation (1.1). Take the case where the high temperature reservoir is at 35 °C and the low temperature reservoir moves from –10 to –15 °C as the coil frosts. The ideal Carnot COP shifts from a value of 5.84 to 5.16, a reduction of nearly 12% in refrigeration efficiency.

$$\mathrm{COP}=\frac{T_c}{T_h - T_c}. \tag{1.1}$$

1.1 Defrost

As the refrigeration system efficiency and performance decreases, it becomes inevitable that the frost layer must be removed through a defrost cycle. The intent of the defrost cycle is to return refrigeration performance to the pre-frosted condition.

1.1.1 Types of defrost

Several methods have been utilized to remove the frost layer from the coil during the defrost cycle (ASHRAE Fundamentals, 2006):

- *Natural Defrost* – A common method of defrosting for when the condition space temperature is near the freezing point of water is to simply turn off flow of coolant [i.e., glycol or refrigerant] to the coil, and allow the air temperature of the coil to naturally rise above the melting point of water. Typically, airflow through the coil is ceased and the process is dominated by free convection, though sometimes the airflow is continued to speed up the defrost process at the expense of return a portion of the moisture back into the control space. This method is commonly used for medium temperature display cases in retail applications.
- *Heated Coil Defrost* – When the condition temperature is well below the freezing point of water, it is necessary to add heat to melt the frost layer. A heat source is used to raise the coil surface temperature above the melting temperature of water, and is held there for a sufficient amount of time to clear the coil of frost. The water from the melt frost is collected and drained away from the conditioned space. To limit latent and sensible heat gain into the control spaces, the airflow through the coil is typically ceased. Several different heat sources have been employed:
    - Hot-Gas – Hot refrigerant gas from the compressor of the system is directed to the inlet of the coil. Diverting valves and tubing are required to direct the refrigerant from the compressor to the coil. A detailed description of the hot gas defrost method can be found in Appendix A.
    - Hot-Glycol – A hot fluid, such as glycol, is pumped through separate tubing circuits of the coil to heat the fin surfaces.
    - Electrical Heaters – The electrical resistance heaters supply heat to the coil. The common methods are to insert heater rods directly into the coil fin pack, or attached to the surface of the fins.
- *Mechanical Defrost* – A mechanical force, such as water or steam jet, is used to remove frost from coils. This method results in fast defrost, and is used in large scale, stationary systems.

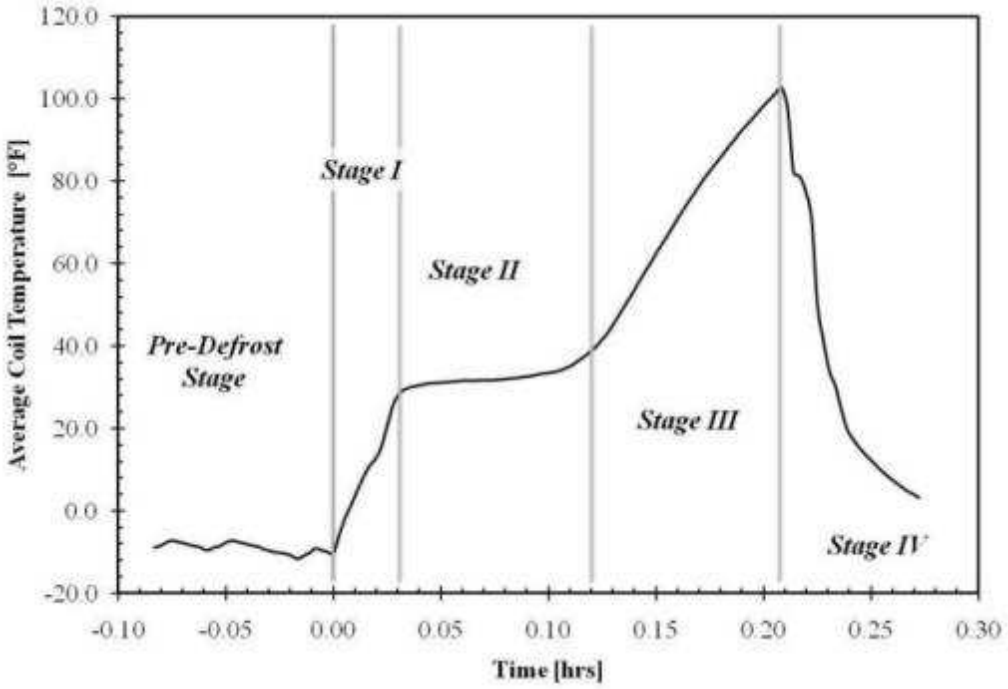

Figure 1-4. Stages of a hot gas defrost (Courtesy Thermo King Corp.)

1.1.2 Heated coil defrost process

As described previously, one of the most common methods of defrosting is to apply heat to the coil surface. The scope of the proposed study will focus on heated coil defrost. Previous studies have shown the defrost process to go through predictable stages (Muehlbauer, 2006; Donallen, 2007). Figure 1-4 shows the distinct stages of an actual process for a hot-gas defrost cycle. The average coil temperature is a fairly good indicator of the transition between the stages.

Pre-Defrost Stage - Prior to the defrost process, the refrigeration system is operating in the cooling mode, albeit at a reduce performance. The presence of the frost layer will cause average coil temperature to drop, compared to the un-frosted condition. Common indicators used to initiate the defrost cycle are: Air-side pressure drop across the coil, airside temperature differential, coil temperature, refrigeration pressure, optical sensor, timed.

Stage I: Pre-Heat - At the initiation of defrost, liquid refrigerant flow is terminated to the coil and replaced by a heat source (i.e., hot-gas refrigerant). Typically

the airflow across the evaporator is also stopped. This is done to limit the latent and sensible heat ingression into the control space. The applied heat is absorbed by the thermal capacitance of the heat exchanger and the frost layer, causing the temperatures to rise. Some of the supplied heat is lost through convective heat transfer from the frost surface, as well as conduction from the heat exchanger to the surrounding support structure of the system. In addition, a small portion of the water from the frost surface will be sublimed to the surrounding air.

Stage II: Melt - Once the interface temperature between the coil surface and frost layer rises above the freezing point of ice, the frost layer will begin to melt. The melt will propagate outward from the surface. Initially, the melt liquid is drawn into the porous frost layer aiding in the transport of heat into the frost layer. As the frost layer becomes saturated with liquid, some melt liquid will begin to drain from the coil. As the interface between the coil surface and frost layer is melted away, the adhesion of the frost layer is greatly reduced. This often leads to *slumping* of the frost layer, where large sections of the frost layer peel off of the coil and fall into the drain pan. Slumping aids in quick removal of the frost from the coil, and is more prevalent for frost grown at the tips of the fins. During the melting process the coil surface temperature is characterized by a nearly constant temperature as the majority of the supplied heat is absorbed by the melting frost layer. Some heat is lost to the surrounding environment through sensible and latent heat transfer.

Stage III: Dry-out - Once the bulk of the frost layer has become detached from the coil surface, the coil temperature will begin to rise. Some frost will remain loosely attached to the coil surface, and will continue to melt as heat is supplied to the coil surface. In this case the heat from the fin surface must transfer across the gap. During this stage, frost will continue to slump from the coil. Generally, the slump frost is caught in a heated drain pan, where it will continue to melt and the liquid drained. Retaining liquid water on the coil will be vaporized and lost to the surrounding air as latent heat.

Stage IV: Re-cool - By some measure (time, coil temperature, optical characteristics, etc), the coil will be judged to be sufficiently clear of frost and the defrost process is terminated. At the conclusion of the defrost process, hot-gas heating of the

coil is stopped, and liquid refrigerant is once again pumped to the evaporator. Typically, air flow over the coil is left off while the coil is pre-cooled. This is done to limit the rejection of sensible and latent heat to the control space. Any retained moisture on the coil is immediately frozen as ice to the coil surface. The remaining heat in the coil material is absorbed by the refrigerant and is an additional heat load on the refrigeration system.

1.1.3 Defrost efficiency

To understand the effectiveness of the defrost cycle it is convenient to express the experimental results in terms of a defrost efficiency, η_d. In its most basic form, defrost efficiency can be expressed as the ratio of the minimum energy required to melt the frost layer to the energy applied to actually melt the frost layer. The minimum energy to melt the frost layer is the combination of the sensible heat to warm the frost to the melt temperature plus the latent heat of fusion to melt ice. Thus the defrost efficiency is,

$$\eta_d = \frac{\text{Latent+Sensible Heat of frost layer}}{\text{Heat added to meltfrost layer}} \equiv \frac{m_f(\lambda_{if} + c_{p,i}\Delta T)}{E_d}, \tag{1.2}$$

where m_f is the mass of the frost layer, λ_{if}, is the latent heat of fusion for ice, c_p is the specific heat of ice, and ΔT is the difference of the frost temperature from the reference temperature.

The supplied energy, E_d , can further be evaluated as the heat required to warm and melt the frost layer plus the heat required to warm the coil material along with the heat that is lost to the surrounding ambient through conductive, convective, and radiated heat transfer during the defrost process,

$$E_d = m_f(\lambda_{if} + c_{p,i}\Delta T) + m_c c_{p,c}\Delta T_c + E_{loss}. \tag{1.3}$$

Combining Equations (1.2) and (1.3), the defrost efficiency can be calculated as,

$$\eta_d = \frac{m_f(\lambda_{if} + c_{p,i}\Delta T)}{m_f(\lambda_{if} + c_{p,f}\Delta T) + m_c \cdot c_{p,c}\Delta T_c + E_{loss}}. \tag{1.4}$$

The intent of the defrost process is to return the coil back to the pre-frosted condition. To return the coil to the cooling function, the sensible heat added to the coil material must be removed through the coiling medium. The energy penalty associated

with re-cooling the coil is equal to the heat added to heat the coil material. Thus Equation (1.4) can be modified to,

$$\eta_d = \frac{m_f(\lambda_{if} + c_{p,i}\Delta T)}{m_f(\lambda_{if} + c_{p,i}\Delta T) + 2 \cdot m_c c_{p,c} \Delta T_c + E_{loss}}. \quad (1.5)$$

From Equation (1.5) it is readily apparent that the defrost efficiency is always less the unity. The obvious ways to increase defrost efficiency is to limit the degree of overheating of the coil and limit heat losses during the defrost process, but generally this increases defrost time which can have other negative effects to the system.

To evaluate only the defrost efficiency at the surface level, it is worth ignoring the effects of heating and cooling of the surface mass. The surface defrost efficiency, η_d^*, is strictly attributed to the mass of the frost and the energy lost to the surroundings through heat and mass transfer.

$$\eta_d^* = \frac{m_f(\lambda_{if} + c_{p,i}\Delta T)}{m_f(\lambda_{if} + c_{p,i}\Delta T) + E_{loss}}. \quad (1.6)$$

1.1.4 Disadvantage of defrost

The primary disadvantages for all defrost cycles are,

- During the defrost event, the cooling system is unavailable to maintain the refrigerated space temperature, and temperature control is lost. The product temperature may raise above the optimal storage temperature, reducing shelf life, and in extreme cases increase the risk of pathogen growth.
- The heat that is added to defrost the coil is parasitic and must be removed from the control space, resulting in longer system run time and more energy consumed.

Defrost cycles timing and duration are typically chosen in an ad hoc manner. Commonly, the defrost events are periodically spaced (e.g., every 6 h) and have a set duration (e.g., 30 min). This cycle can result in either redundant defrost where minimal frost growth has occurred during the period between defrost cycles, or the defrost cycles is too short of a duration to adequately remove the frost altogether prior to termination. To prevent either too few or too short defrosts, it is common to design the defrost algorithm for what is considered the worst-case application, resulting in a defrost cycle that is either too frequent or too long in durations.

Figure 1-5. Transport Refrigeration Unit (Courtesy of Thermo King Corp).

1.2 Defrost cost

As a case example, the defrost process and cost of a transport refrigeration unit (TRU) will be considered. A TRU (Figure 1-5) is used to maintain product temperature as it is shipped from farms to distribution warehouses and on to retail centers. Such TRUs tend experience higher defrost loads compared, say, to stationary refrigeration system owing to larger latent cooling loads. Common sources of the latent cooling load include:

- Products, such as produce, tend to be loaded when they are warm and moist.
- Fresh produce naturally respire when latent heat is diffusing from the produce
- Door opening, especially for local product distribution, are frequent and lead to a large transfer of ambient air into the conditioned space.
- To save weight and cost, insulated cargo containers are typically poorly constructed, with significant leak paths between the conditioned and ambient space.
- General wear and tear of an over-the-road container leads to breakdown in door seals, causing leak paths.

Donnellan (2007) completed an experimental study of the defrost process of a TRU. He found that the defrost efficiency is largely effected by the frost growth conditions, which is primarily influence by the prevailing dry bulb temperature. Frost grown in a condition near 0°C tends to lead to a dense frost growth, which results in a more efficient melt process. Defrost efficiencies up to 80% were measured for frost grown at 0°C. Comparatively, defrost efficiency for frost grown at low temperature conditions, such as -20°C, were dramatically lower in the range of 5 to 10%. Donnellan concluded the reason for the significant difference in efficiency was due to the difference in frost density. He conducted an additional set of experiments at the low temperature condition, where he increased the time between defrost, which had the net effect of increasing the frost density, and saw the defrost efficiency rise to 20 to 30%. Unfortunately, the negative effect of the longer defrost interval was reduced system efficiency during the extended cooling period, which diminished the overall energy savings of the more efficient defrost.

Table 1-1 summarizes the annual economic cost of defrost for the North American population of semi-trailer refrigeration systems. ACT Research[1] estimates the North American population of TRUs to be 333,000 units. Thermo King Corporation conducted a field survey and found that approximately 78% of the systems operate in the fresh condition, while the remaining 32% of systems carry frozen loads. The average defrost frequency and defrost duration were found to be dependent on the condition of the space. The defrost frequency for fresh conditions is 0.14/h with an average duration of 0.09 h. Comparatively, defrost for frozen loads had a greater occurrence at 0.24/h and a longer duration of 0.18 h. Assuming an average run duration of 2500 h/system-y, a recovery period equal to the defrost duration, an average defrost fuel consumption of 0.6 gal/hr[2], and an average fuel cost of $3.44/gal[3], the total annual cost to defrost the population of systems is $76.5M.

[1] Market report of North American Reefer Van Population by Americas Commercial Transportation Research Co., LLC
[2] Internal test result, Courtesy of Thermo King Corporation, Bloomington MN
[3] 12 month average price (Nov 2011 to Oct 2012) for tax-exempt diesel fuel. Source: U.S. Energy Information Administration, Washington DC, http://www.eia.gov/dnav/pet/pet_pri_gnd_dcus_nus_w.htm

Table 1-1. Annual economic cost for defrosting North American semi-trailer TRU's.

	Frozen	**Fresh**
Trailer Population [Unit]	106,560	226,440
Average Run Cycle [Hr/unit]	2,500	2,500
Defrost per hour [Def/hr]	0.24	0.14
Average Defrost Duration [Hr]	0.18	0.09
Recovery Duration [Hr]	0.18	0.09
Total Duration [Hr]	0.36	0.17
Total Defrost Hours [Hr]	23,088,000	13,944,741
Fuel Consumption [Gal/hr]	0.6	
Total Defrost Fuel [Gal]	13,852,800	8,366,845
Fuel Cost [$USD/Gal]	$3.44	
Economic Cost [$USD/yr]	$47,695,190	$28,807,047
Total Economic Cost [$USD/yr]	$76,502,237	
Defrost efficiency [%]	10%	80%
Minimum defrost cost [$USD/yr]	$4,769,519	$23,046,637
Recoverable cost [$USD/yr]	$42,925,671	$5,761,409
Total Recoverable cost [$USD/yr]	$48,687,080	

A substantial portion of the energy utilized for defrost is wasted. Based upon the fresh and frozen defrost efficiencies measured by Donnellan, a total of $48.7M worth of fuel is wasted on system defrost. The majority of the total waste is for the frozen condition where defrost efficiency has been found to be substantially lower than the fresh condition. It is worth noting that transport refrigeration is estimated at less than 20% of the total refrigeration market[4], and the total economic cost of defrost for the entire refrigeration market would be several times larger.

1.3 Summary of research

Most of the recent research on heat and mass transfer in frost has been on characterizing frost growth and proprieties, investigating means to delay or prevent frost growth, and determining the impact of defrost on system capacity and efficiency. Multiple empirical and semi-empirical models have been proposed to model the time

[4] http://www.energymanagertoday.com/commercial-refrigeration-equipment-market-to-reach-46-6bn-in-2018-report-says-086455/

dependency of frost growth. There is a line of research that is investigating ways to delay frost growth through surface preparation with coatings or microstructures. There has been some work to evaluate defrost efficiency at the system level, looking at total cycle efficiency based on reduction of system efficiency due to the presence of the ice layer, as well as the water mass retention in the coil during successive defrost events. Proposals have been made to improve defrost frequency and shorter duration through improved sensing.

The present investigation focuses on measurements and modeling of the heated surface during the defrosting process. This work covers the gap that exists in the current body of research on the fundamental mechanism of melting at the fin level of a heat exchanger. Unknown are the energy required to melt frost of various properties and the mass removal rate of the melted liquid of various fin geometries. The research comprises both experimental and numerical studies of the frost melting process on fin-like geometries. A dedicated experimental apparatus has been built to take detailed measurements of the frost melting phenomena of a flat surface. Frost layers have been grown at various levels of temperature and humidity, comparable to published results of previous studies. The frost melt process has been evaluated for the case of rising surface temperature; though the test apparatus and model described could be used for air-heated defrost as well. Detailed measurements are made of the melting process, including the energy transfer and mass removal rates throughout the defrost process. Correlations have been generated to describe the heat and mass transfer throughout the defrost process. The results of the experimental work are compared to a proposed model framework to describe the melting process of a low temperature evaporator. This work will make it possible to optimize evaporator and defrost process to maximize system efficiency and availability.

2 Literature Review

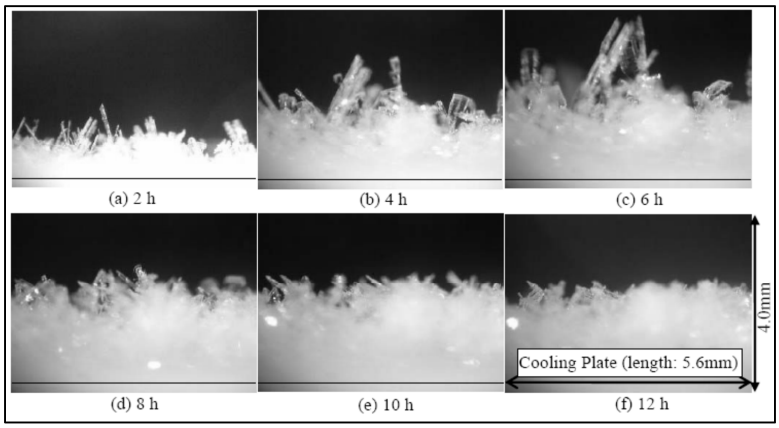

a) Chilled: 0°C Air, -10°C Surface, 72% RH.

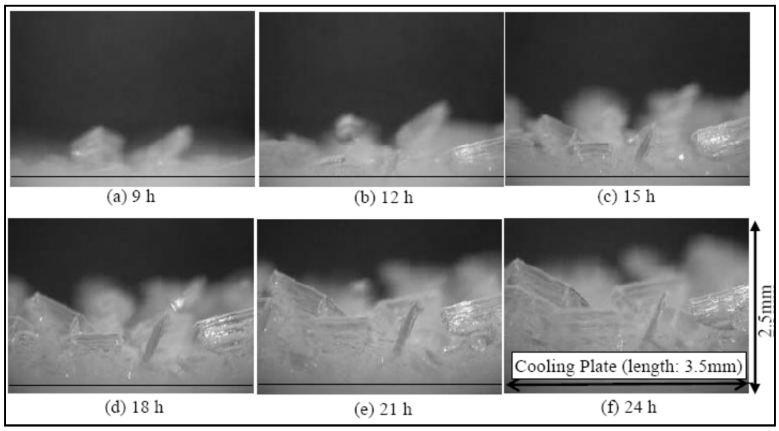

Frozen: -10°C Air, -29°C Surface, 50% RH.

Figure 2-1. Frost growth on cold plate (Yamashita et al., 2007).

The majority of the research conducted over the past five decades has concentrated on the description of the frost formation process. As seen in Figure 2-1, the prevailing air condition greatly influences the morphology of the frost layer. Several models have been proposed to describe the time-variant physical properties and growth of the frost layer. Several researchers have developed frosted fin models to predict the thermal performance of heat exchangers. Experimental studies have visualized the growth of frost on simple and finned surfaces, as well as, quantified the degradation of the system performance and efficiency under frosted conditions. Recently, several

studies have been completed to experimentally determine the heat load imposed on the system during defrosting and recovery cycles. There have been relatively few models proposed to predict the heat transfer in defrost, with nearly no work on examining the mass transfer aspects of the defrost cycle.

2.1 Fundamental frost models

Iragorry, Tao and Jia (2004) completed an extensive review of the research conducted on modeling frost growth and properties since the earlier review by O'Neal and Tree (1985). The intent of the review is to summarize the modeling work completed on frost formation and growth as it is applied to low-temperature evaporator application. Prior studies have shown that frost growth happens in distinct phases: drop-wise condensation (DWC), solidification and tip-growth (STG), densification and bulk growth (DBG). During the initial DWC period, water droplets condense as a sub-cooled liquid on the cold surface. The droplets form into ice particles after a characteristic time has been reached. The characteristic time is a function of ambient conditions (dry bulb temperature and dew point), cold surface temperature, and surface energy. Once the ice droplets form on the surface, the STG stage begins. The effect of the air movement across the surface is most pronounced during this stage. An increase in the bulk stream velocity causes tip growth to slow, but doesn't not affect the overall properties (i.e., density, conductivity, etc) of the layer. Once the DBG stage is reached, the frost layer resembles homogeneous porous medium, with its properties dependent upon ambient and surface conditions

The models reviewed for this study are generally empirical or semi-empirical, though the few fundamental models that exist are included. The property and parameter models are sub-divided into the following categories: thermal conductivity, frost density, frost thickness, and heat transfer coefficient. Experimental correlations for the thermal conductivity are generally correlated as a function of frost density, which is related to the porosity of the frost layer. The few theoretical models show that thermal conductivity of the frost layer is not a function of density alone and is also a function of the tortuous conduction path within it. Frost thermal conductivity in low temperature applications is typically ~0.15 to 1.0 W/m-K. Density correlations that have been developed are usually

a function of bulk air temperature, the temperature difference between the free air steam and surface, and the humidity ratio of the free stream. In general, higher defrost density (and lower porosity) is seen for lower bulk temperatures, and density increases with growth time. Frost density is typically in the range of 100 to 400 kg/m^3 in low temperature applications. Frost thickness, like density, is generally dependent upon the temperature difference and free stream humidity ratio.

Existing correlations for frost growth show rapid thickening of the frost layer during the initial growth period, and slower thickening as the layer becomes developed at later time periods. Heat transfer correlations often take two forms: those based on the energy exchange at the cold surface and those based upon the energy transfer at the frost-air interface. The first includes both the sensible and latent heat transfer effects and results in a higher heat transfer coefficients then for an unfrosted condition. The second reflects only sensible heat convection from the surface, and all models reviewed are from this category. Generally the heat transfer correlations are found to be time invariant, and are based upon the Reynolds number of the flow of the ambient (moist) air over the frost layer. Heat transfer rates on a frosted surface are higher than those on an unfrosted surface, and this increase is attributed to the surface roughness created by the frost.

In addition to the parametric models, a number of analytical growth models have been developed. These models take both integral and differential forms, and most of them solve the coupled energy and mass transfer equations to predict the growth of the frost thickness. Mass transfer is modeled as a vapor diffusion process wherein water molecules are directly sublimed to the growth region. These models can further be divided into those that assume the solid-vapor interface is at the saturation equilibrium condition defined by the Clausius-Clapeyron equation. Some recent studies (Sherif et al., 2001) have assumed super-saturation of the water vapor at the growth interface, but their results do not present strong evidence of improved accuracy compared to models that assume a saturated interface at the growth region. Most of the models presented in the literature are limited to the later tip growth and densification stages of frost growth phase, and require an initial guess of the nucleation growth stage.

In conclusion, the majority of the currently available parametric models have been

generated from a limited data set, narrowing the applicability of the resulting correlations. Most of them are also limited to conditions where the air temperature is above the freeze point of water and are not considered applicable for low-temperature refrigeration applications. Iragorry et al. (2004) does not indicate which of the analytical models reviewed produces the best results, though an absolute error of about 15% is common when comparing predictions to experimental results. The analytical models are typically limited to the later frost growth stages, and generally require some prior assumption about the nucleation process.

Recently, Lee and Ro (2005) proposed an updated model to predict the thickening and densification of the frost layer on a flat plate. The model assumes the frost layer is a porous medium, of uniform porosity, which is supported by observations of previous researchers. The model predicts the diffusion of water vapor into the frost layer and time variant growth of the frost. The model was evaluated for two boundary conditions at the frost-vapor interface. One assumed the frost surface was saturated and the gradient of the vapor pressure within the frost layer was in equilibrium with the vapor state equations (Clausius-Clapeyron equation). Results showed favorable comparison to experimental results (Lee and Ro, 2002), but only when the initial porosity was correctly chosen. To remedy the dependence on initial porosity, a modified model was evaluated where water vapor is assumed to be super saturated within the frost layer. Two parameters were reduced from the model: super saturation degree and the diffusion resistance factor. When compared to experimental results, a clear relationship between the saturation degree and porosity was seen, with a decrease in saturation degree for higher frost porosity. A correlation between frost porosity and diffusion factor was not seen, and further analysis was recommend by the researchers.

2.2 Frost effects on the heat exchanger and system

Kondepudi and O'Neal (1987) review the effects of frost growth on heat exchanger performance. They divide the reviewed papers by four key parameters that effect heat exchanger performance: fin efficiency, overall heat transfer coefficient, pressure drop, and surface roughness. At the time of their review article, limited results

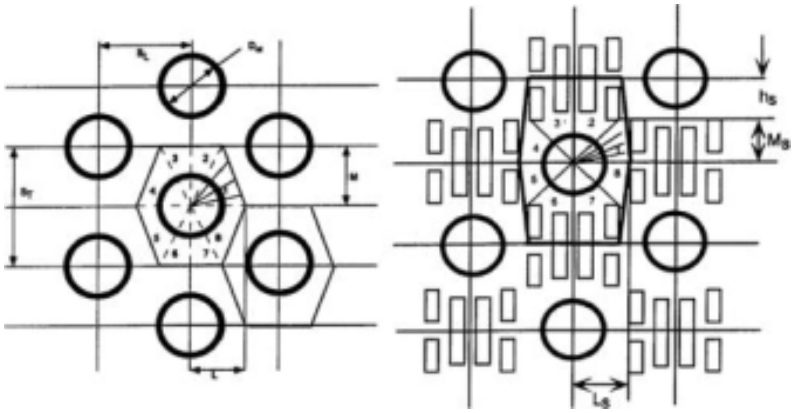

Figure 2-2. Hexagonal fin segmenation (Kondepudi and O'Neal, 1993a,b).

were available for frosted heat exchangers owing to the complexity and variety of the geometries of the heat exchangers commonly found in industry. Of the fin efficiency models they review, they felt the model proposed by Sanders (1974), developed analytically using an energy balance was the best, though it was not validated experimentally. They find a large variability in the overall heat transfer coefficient predicted by the models reviewed. Experimental studies have shown an increase in the overall heat transfer coefficient during the early frost formation stages, followed by a drop as the frost layer thickens and insulates the heat exchanger surfaces. Both analytical and empirical models are reviewed, but no definitive conclusion could be reached on which model most accurately captured the phenomena. The increase in airside pressure drop of the heat exchanger, due to a reduction of flow area caused by the growing frost layer, is found to be the most significant parameter in effecting heat exchanger performance. The performance reduction is mainly due to the decrease in airflow rate caused by the additional backpressure on the fan. There is limited discussion on the attempt to model the time dependency of frost growth as a function of area reduction, and there is no discussion on using flat surface correlations to build such a model. There is also limited discussion on the effect of a frost layer on surface roughness. The presumption is the frost layer is randomly distributed on the surface, and this should increase surface roughness. The increase in the overall heat transfer coefficient has been shown to be the result of this increased roughness, but as the layer thickens it appears to have a minimal effect on the heat exchanger performance.

Based upon the gaps found during their review, Kondepudi and O'Neal (1993a,b) completed a study to develop a comprehensive frosted direct expansion (DX) heat exchanger model and to validate it against experimental results. The heat exchanger model employs the frost fin efficiency model initially developed by Sanders for a flat plate. For the simulation, the heat exchanger is divided into elemental sections, where the frost and refrigerant properties are assumed constant. At each element the frost thickness and associated heat exchanger thermal performance and airside pressure drop are calculated in a quasi-steady state fashion. This procedure gives the advantage of hexagonal region around each tube (Figure 2-2). The temperature is assumed to vary allowing the frost thickness to vary depending upon the fin temperature. A disadvantage of the model is the need to assume an initial frost height and density on the heat exchanger at the start of the simulation, but these assumptions are needed for numerical stability. When compared to the experimental results, the model under predicts the rate of frost accumulation and airside pressure drop, which are directly related as a higher level of frost accumulation (thickness) reduces the air flow and increases the pressure drop. The model predicts the heat transfer rate of the heat exchanger fairly well, generally within 15 to 20%. The authors recommend further work to improve the mass transfer of the moisture in the frost layer.

Sommers and Jacobi (2006) analytically solve the problem of a frosted plane fins with round tubes (Figure 2-3). The sector method is used to solve for the frosted fin efficiency in the only in the radial direction within the fin, while the temperature in the frost layer is a function of the radial and axial directions. This assumption is supported by the fact that the conduction in the fin is substantially greater than in the frost layer, and the thickness of the fin is less than the frost layer. The infinite series solution allows for the computation of the fin efficiency and is within one percent of the exact solution for a non-frost case. The authors compare series solutions of one and four terms and find that a one-term solution over predicts the fin efficiency by a few percent in most cases. The model has advantages over earlier attempts, namely including two-dimensional heat

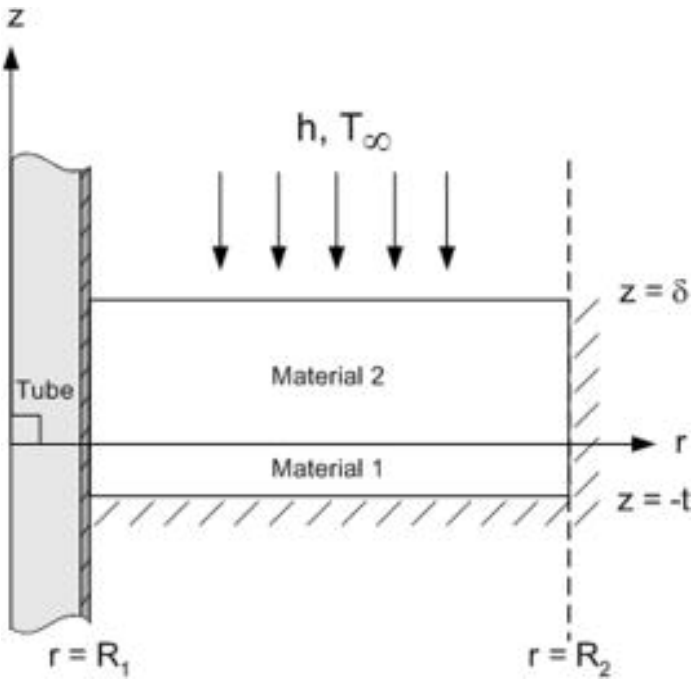

Figure 2-3. Frosted fin model (Sommers and Jacobi, 2006).

condition in the frost layer which allows the use of a modified airside heat transfer coefficient that includes effects of the latent and sensible heat transfer from the air to the frost layer. A disadvantage of the model is the need to assume the frost thickness and conductivity, which are typically not known a priori.

2.3 Defrost and melt models

Several fundamental models have been proposed for describing the mechanisms of the defrost process at the surface level. One of the earliest attempts to formulate the analytical solution to the defrost problem is that of Sanders (1974). Sanders' approach is to formulate the defrost problem as a simple one-dimensional heat balance at the surface. He considers the case where heat is applied to the wall, solving for the case of hot gas defrost (modeled as a constant surface temperature), as well as an electric defrost (modeled as constant heat flux). The key underlying assumption of Sanders' work is that the melt liquid is drawn into the porous frost layer. The solution of the model allows Sanders to determine the defrost time, heat input, and ultimately defrost efficiency for frost of varying thickness.

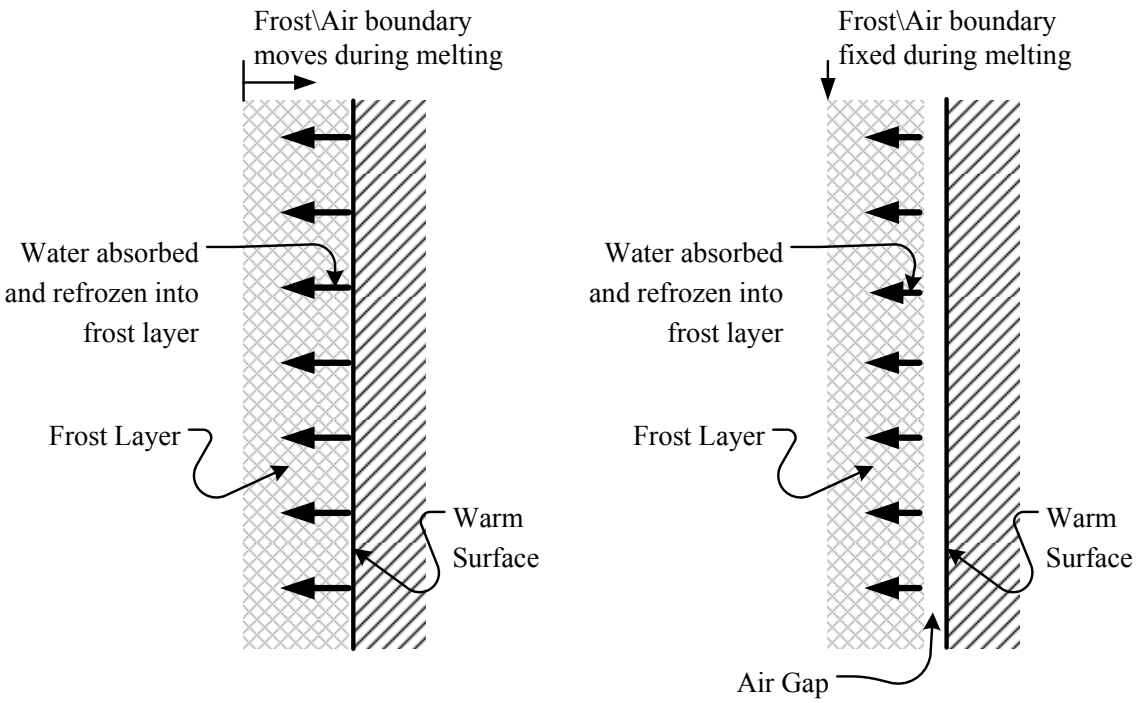

(a) Absorption Model (b) Air Gap Model

Figure 2-4. Sander's models of frost melting (1974).

Based upon the limited qualitative evidence available, Sanders proposed two models to describe the melting process. The first assumes that the frost layer remains attached to the heated surface throughout the defrost process. The melt water is absorbed into the frost layer and re-freezes (Figure 2-4a). For this model, the frost layer maintains contact with the surface and the exterior air-frost boundary moves towards the surface as the melting process proceeds. The second model (Figure 2-4b) assumes that melt liquid is drawn into the frost layer leaving behind an air gap at the boundary between the surface and frost. The exterior air-frost boundary stays fixed during the melting process, while the air gap increases as the melting process progresses. Heat is transferred across the gap by natural convection.

For each case, Sanders proposes two distinctive phases for the defrosting process. The first phase is the sensible heat gain of the wall and the frost layer. At the start of the simulation, the wall and frost temperature are assumed to be at some equilibrium

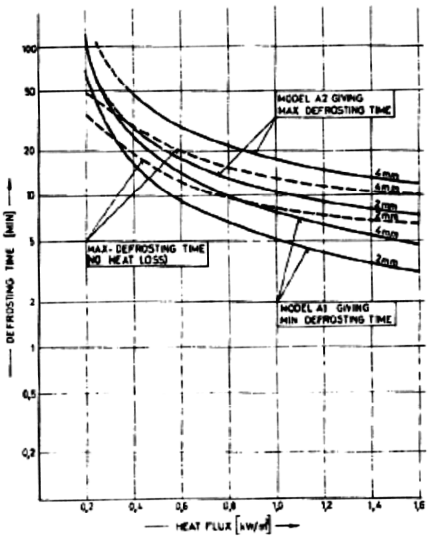

Fig. 7.6.

Defrosting time for defrosting with constant defrosting heat flux (Model B1 and B2). Frost layer thickness 2 and 4 mm.

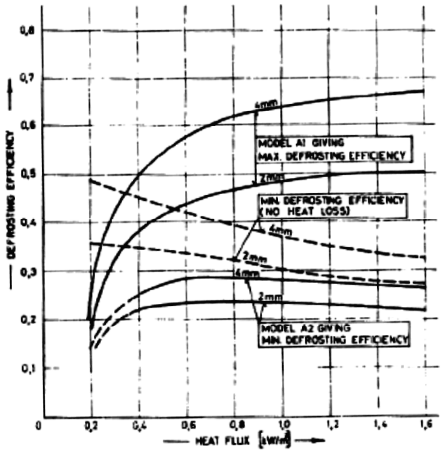

Fig. 7.7.

Defrosting efficiency for defrosting with constant defrosting heat flux (Model B1 and B2). Frost layer thickness 2 and 4 mm.

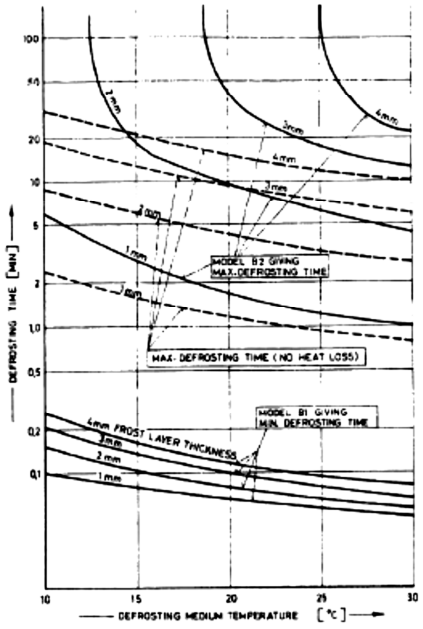

Fig. 7.4.

Defrosting time for defrosting with constant defrosting medium temperature (hot gas temperature)(Model A1 and A2). Frost layer thickness: 1, 2, 3 and 4 mm.

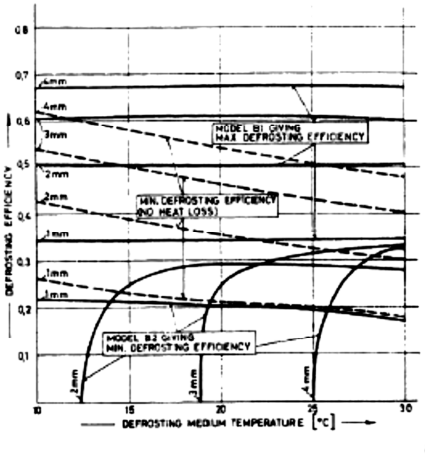

Fig. 7.5.

Defrosting efficiency for defrosting with constant defrosting medium temperature (hot gas temperature)(Model A1 and A2). Frost layer thickness: 1, 2, 3 and 4 mm.

Figure 2-5. Defrosting time and efficiency (Sanders, 1974).

temperature below the melt temperature of the frost layer. When heat is initially applied, most of the heat is absorbed by the fin material and frost layer, with some lost to the ambient via convection. At the moment the wall temperature reaches 0 °C, the frost will begin to melt, and the second phase of the process begins. As described before, the melt liquid is drawn into the porous frost layer, through capillary action. For the case where the frost layer remains in contact with the surface, only the heat transported by conduction is considered, and the air-frost front moves towards the wall, until it is completely melted. With the second case, where an air gap is formed, the model assumes the melt liquid is drawn into the porous frost layer and refreezes into ice at the air-frost interface away from the surface. Thus there is a shrinking frost front near wall, and a growing ice front. Eventually, the receding frost front will reach the growing ice front, at which point the ice layer begins to melt.

Through a simple heat balance, Sanders is able to generate a system of equations for solving the front location and defrost time through the entire defrost process. By applying either a constant temperature or heat flux boundary condition at the wall, results are obtained for defrost duration (time) and defrost efficiency. The results (Figure 2-5) indicate that an attached layer results in the shortest defrost time and maximum defrost efficiency. The air-gap model results in longer defrost time and lower efficiency, and can be directly attributed to the added resistance to heat transfer caused by the gap. From the results it is also obvious that the solutions for the two models represent the bounding limits of the problem with the actual solution lying between them. Sanders discuss the general limitations of the work. Namely, in real heat exchangers during the defrost process there appear to be regions of both contact and separation of the frost layer from the surface. The lack of experimental work at the time of his research made it difficult to draw further correlations, but it is noted that thin frost layers tend to stay attached to the surface while thicker frost layers have a tendency to separate. From the standpoint of optimizing the defrost process, it would be best to defrost before the layer reaches some critical thickness. The Sanders model largely neglects the mass and heat transfer effect of water transport. The model assumes no water is leaving the control volume which is clearly not true. It does not account for the heat leaving via the melt liquid, or water

vapor that would sublime from the frost surface to the surrounding ambient air. The effect of the heat transported by melt liquid into the frost layer by capillary forces is also neglected. In general Sanders questions the accuracy of the analysis but does provide a frame of reference for the problem.

Krakow, Yan, and Lin (1992a) proposes a model to describe the hot-gas defrost process of a refrigeration heat exchanger. From previous experimental work, it is noted that the defrost process has both a spatial and temporal component based on uneven frost thickness and uneven heating during defrost. A finite element heat exchanger model applies a mass and energy balance for each stage of the defrost process on a representative element. Latent heat effects of the melting process are combined with the sensible heat transfer through two conductance terms which are unknown. Additionally, other unknown parameters needed to complete the analysis are the retained mass of water on the heat exchanger surfaces and the water vaporization rate. The unknown terms are determined experimentally (Krakow, Yan, and Lin, 1992b) and are assumed to be constant for all time and heat exchanger geometries. The model produces reasonable agreement against previous experimental data, even though it largely ignores the effect of water drainage.

Krakow, Lin, and Yan (1993a,b) present another two-part paper applying the previously developed heat exchanger model in a full hot-gas defrost cycle simulation. In the first paper (1993a), the major component models (e.g., heat exchanger, compressor, receiver, and throttling device) of an idealized system are discussed. The second paper (1993b) focuses on the analysis and validation of the model. The experiment found that some parameters are indeterminable, such as saturated refrigerant states, a detailed refrigerant mass inventory, and heat storage in components. The simulation captures the overall trend of the hot gas defrost cycle and is useful in seeing relative changes rather than absolute values of pressure and mass flow. The model does not capture higher order dynamics, such as when the reversing valve is initially switched. The dynamics of the model are primarily influenced by the mass and energy storage of the high-side system components.

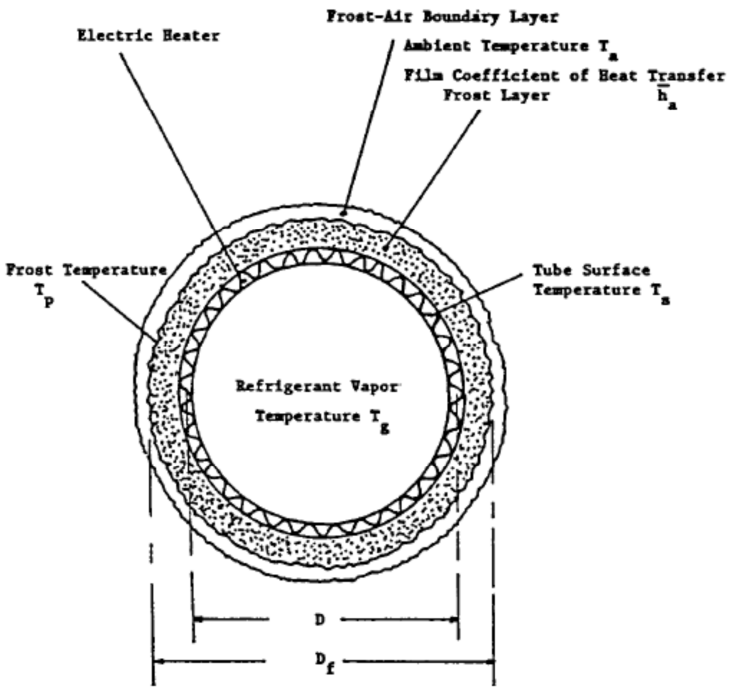

Figure 2-6. Model of frost melting due to Sherif and Hertz (1998).

Sherif and Hertz (1998) develop a model of the defrost process on an electrically heated cylindrical tube (Figure 2-6). The electrical heater is applied at the surface of the tube, and forms the boundary between the frost layer and refrigerant gas. Heat from the electrical heater is conducted into the frost layer and convected into the refrigerant, both of which must be given as input to the model. Resistance of the heat exchanger material is neglected in the analysis. In this model, the frost melt forms at the heated surface and is immediately drained, the frost layer remains attached to the surface, and the frost front moves towards the heated surface. Employing a quasi-steady-state procedure, the model calculates the transient change in frost thickness and frost surface temperature. The defrost process is assumed to be complete when the frost thickness reaches zero. In general, higher heat fluxes decrease the defrost time. The results of the model are greatly influenced by the selection of the heat flux, which is an input to the model. The model is not compared with experimental results, and the accuracy is not discussed (though intuitively it appears to be consistent with observations).

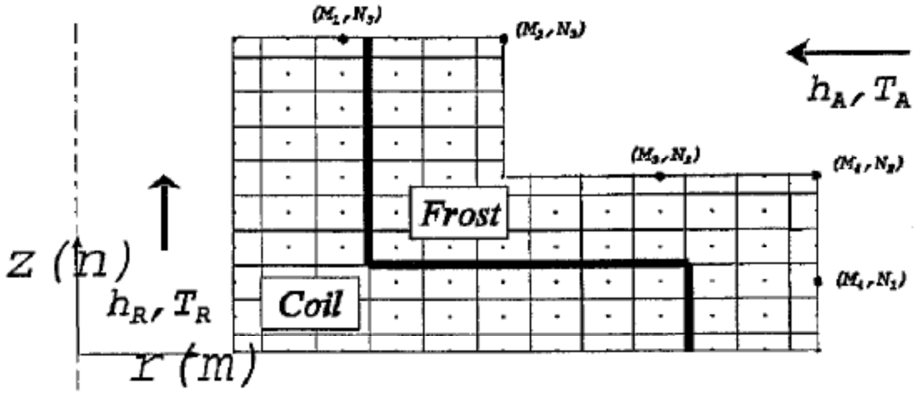

Figure 2-7. Two-dimensional fin model (Alebrahim and Sherif 2002).

Alebrahim and Sherif (2002) propose and numerically solve a two-dimensional defrost model of frosted disked fins on a tube. As with Sherif's earlier work, the surface is electrically heated to melt the frost. Energy from the heater is both conducted into the fin and frost, as well as convected to the refrigerant within the tube. The defrost process is divided into two stages. The first stage is the calculation of the steady-state temperature distribution within the frost layer. The frost layer is assumed to be uniformly distributed on the heat exchanger surfaces and has homogenous properties. The second stage is the defrost phase where heat is applied at the surface. This stage is further divided into two sub-phases; a pre-melt stage where the fin material and frost layer are heated, and a melt stage where the frost layer begins to melt. The enthalpy formulation of the energy equation is used to model the melting process in the frost layer, because it has the distinct advantage of being continuous model formation in both the solid and liquid phase domains of the computational domain. From the calculated enthalpy at each node, the temperature distribution and melt interface can be determined. The defrost process is assumed to be complete once the frost layer has melted along the entire heat exchanger\frost interface. Figure 2-7 shows the fin model and computational domain for the proposed model.

The model is an advancement of prior models allowing for the determination of the temperature distribution in both the fin and frost in two-dimensional space. The results of the model show that melt time can be greatly decreased by increasing the

supplied heat flux from the heater, but the rate of improvement decreases at extremely high heat fluxes. The total heat input is approximately constant, regardless of supplied heat flux and is dominated by the frost and air temperature. The temperature response and variation in the fin is less pronounced when compared to the frost layer, though the fin geometry used was a relatively short-fat fin, and a longer fin would be expected to have a greater temperature variation. The fin is found to be a significant heat sink due to its relatively large thermal capacitance. The results are not compared to any experimental studies, but are consistent with the findings of previous numerical studies indicating the enthalpy method should be able to be applied to defrost problem in more complex geometries.

Na (2003) expanded on Sanders' air gap model to include the effects of drying out of the heat exchanger. In this instance heat is continue to be added to the heat exchanger well after the frost has melted to vaporize any remaining moisture of the heat exchanger surfaces, thus resulting in a completely clean heat exchanger for the next cooling period. The model assumes that the mass of the retained moisture is known and at the same temperature as the heat exchanger surface. Na discussed that water retention is largely dependent on heat exchanger geometry (tube spacing, fin spacing, fin enhancements) and orientation. The addition of the dry-out phase greatly increases the calculated defrost time, and lowers the overall defrost efficiency. Na did not have experimental data to compare to the model results and was therefore unable to substantiate its accuracy. He recommends the model to be used as a general design tool which calculates the worst case defrost duration and energy input

Hoffenbecker, Klein, and Reindl (2005) develop a transient model to predict the heat and mass transfer effects associated with hot gas defrosting an industrial air-cooler. The predicted defrost duration compares favorably with experimental results of defrost of an evaporator heat exchanger of an industrial refrigeration system. Model predictions for defrost energy input also compare well to that reported in the literature. One interesting finding of the model is the increase in water vapor transport with a decrease in the inlet refrigerant gas temperature. The increase in water vapor transport is attributed to the prolonged defrost duration, which allows more time for the slower mass diffusion

process.

Dopazoa, Fernandez-Seara, Uhíaa, and Diza (2010) present a transient simulation for the defrost process of a round-tube plate fin heat exchanger. The defrost process is divided into six stages. Energy and mass balances are formulated for a representative tube and fin element for each stage of the defrost process. The model is capable of varying the inlet refrigeration condition to the heat exchanger. The model is validated against experimental data and shows excellent agreement in defrost duration. A parametric study shows that defrost time is inversely related to the refrigerant mass flow rate. Increasing the inlet refrigerant temperature is found to decrease defrost duration until it exceeds a critical temperature and then is found to have the opposite effect, resulting in an increase in defrost duration.

Aoki, Hattori, and Ujiie (1988) analytically and experimentally investigated the melt process of a porous snow layer that was heat from below. While the thickness of the snow layer is significantly greater than that of a frost layer, a number of significant physical phenomena are similar. First, the melt process of the snow layer proceeds through a number of distinct stages, also seen in the melting of a frost layer. In addition, the factors affecting the permeability of the melt liquid to be drawn into the porous layer are a result of the same capillary forces. The height of the permeability layer is directly related to porosity of the snow layer. Another phenomenon similar to what happens in the melt of a frost layer is the refreezing of the melt liquid into an ice layer, or ice lens. The factors affecting the refreezing of the melt liquid are thickness and porosity of the snow layer, heat flux at the heated surface, and surrounding air temperature. Intuitively, if the surrounding air temperature is significantly below the freeze point of water, one would expect a portion of the melt liquid to refreeze into ice. The capillary action of the melt liquid drawn into the porous snow layer increases the rate at which heat is transported from the heated surface but also causes a greater loss of heat to the surrounding air at the snow-air interface. The greater heat transfer rate is due to the larger temperature gradient between the surface and surrounding air. As seen in other frost melting studies, an increase in the supplied heat flux results in a decrease in the melt time, but at the expense of lower melt efficiency.

2.4 Defrost effects on the system

Al-Mutawa et al. (1998a,b,c,d,e) conducted an extensive experimental study to determine the heat load effect of defrosting of a typical low-temperature evaporator on the refrigeration system. The aim of the research was to provide insight into the system level effects of defrosting, from which improved guidelines can be developed for design engineers to accurately determine the defrost load on the refrigeration system. Previous researchers have found that defrost cycles can account for up to 15% of the total heat load on the refrigeration system. Furthermore current methods of defrost have been found to be inherently inefficient, with typically 15 to 25% of the supplied heat leaving with the melt liquid, and the remainder is parasitic heat loss.

Mago and Sherif (2002a,b) investigated the effect of defrosting of an industrial fan-heat exchanger with frost grown in a super saturation condition. Super saturated frost is formed when the moisture content of the air exceeds the saturation concentration at the prevailing air temperature. The frost is characterized by its snow-like appearance. This type of frost tends to form at fin tips on air entering side of the heat exchanger, and has minimal penetration into the heat exchanger. The test apparatus was constructed such that the heat exchanger inlet and outlet could be dampered shut during the defrost process. The intent of the dampers is to limit sensible and latent heat loss to the test room, thereby improving the defrost efficiency. A fully dampered defrost is found to have a 43% improvement in defrost efficiency relative to the undampered heat exchanger defrost. A partially dampered heat exchanger produces an 18% improvement over the undampered case.

Several studies have investigated the effect of defrost frequency and duration on both the defrost efficiency, as well as overall system efficiency. Sujau, Bronlund, Merts, and Cleland (2006) reported the effect of defrost frequency on the performance of a refrigerated cold store. In general defrost frequency is not found to have an appreciable effect on overall system energy use. A longer interval between defrost results in more frost accumulation on the evaporators, which is removed at a greater relative efficiency during the defrost cycle. However the larger interval has a negative effect on the temperature control of the refrigerated space. From the results, it appears the defrost

control sequence was not adjusted to attempt to improve the system efficiency. For the system studied, a defrost interval of 8 to 12 h appears optimal.

Muehlbaurer (2006) measures the performance degradation of a simple refrigeration system with a round-tube, plate fin evaporator through several frosting and defrosting cycles. He reports a drop in system capacity through successive defrost cycles and attributes the loss in performance to moisture retained on the heat exchanger surfaces at the conclusion of a defrost cycle. The retained moisture re-freezes on the subsequent cool cycle and acts as nucleation sites during the frost growth period speeding up the frosting process. He confirms the drop in system performance during the frosting period is attributed to the induced thermal resistance by the frost layer, and the additional flow resistance on the airside caused by the reduced flow area. A similar conclusion is experimentally confirmed by Xia, Zhong, Hrnjak, and Jacobi. (2006) for louvered fins.

Lohan, Donnellan and Gleeson (2005) study the defrost process of transport refrigeration units. Defrost efficiency is largely effected by the frost growth conditions with denser frost resulting in a more efficient defrost process. To facilitate a denser frost growth in frozen conditions, they recommend an adaptive defrost strategy where the time between defrost is a variable dependent upon the refrigerated space condition (i.e., temperature and humidity), system operation, and cooling demand.

2.5 Summary

This literature review has identified a number of studies that have investigated the effects of evaporator frosting on system performance. The common conclusion from them is that as frost accumulates on the evaporator coil, the free airflow space through the coil decreases thereby reducing the mass flow of air through the coil. The lower airflow rate reduces the cooling capacity of the system. Several models have been proposed to predict the rate of frost accumulation during the growth phase, as well as the thermophysical properties of the frost. The growth model are typically characterized by a relatively quick growth of the frost thickness during the initial stage, followed by a slower densification stage where mass is accumulated internally to the frost layer.

Experimental studies have found current defrost methods to be inherently inefficient, with up to 75% - 85% of the energy required to defrost the evaporator coil

lost to the refrigerated space as a parasitic heat load. Defrost efficiency appears to become worse as the coil and air temperature decrease. This reduction in efficiency can be largely attributed to the additional energy input to heat the coil mass from a lower start temperature. Studies have shown a drop in system performance after repeated defrost cycles can be attributed to the retained moisture on the coil at the conclusion of the defrost event.

Several defrost models have been compared. Most models use a one-dimensional approach to simplify the complexity of the problem. Early models, neglected the effect of mass transport in the defrost process, while later models combine the heat and mass transfer effects into lumped terms to simplify the equation set. Several studies demonstrated how the simplified defrost models could be used in larger system simulations to predict defrost energy input and duration.

3 Multi-Stage Defrost Model

It is apparent from the current literature that there is a need to advance the capabilities of accurately modeling the defrost process. At best, the current state of modeling can be used only as a general predictive tool for worst case scenarios and lacks the necessary accuracy to describe the defrost process. Generally current modeling is limited to one-dimensional heat transfer with simplified frost properties and neglects effects of latent heat through either melt drainage or sublimation. Gravitational effects on melt drainage and frost slumping are ignored as well. Finally current models are limited to a specific stage of the defrost process, and no current model is capable of predicting heat and mass transfer through the entire defrost process.

The model proposed in the present investigation will advance prediction of transient heat and mass transfer rates through the entire defrost process. Recall from earlier discussion that experimental observations have shown that the defrost process goes through predictable stages: pre-heat, melt, dry-out, and re-cool. Each stage is characterized by different thermal transport and fluid dynamic processes. A comprehensive model should therefore capture the combined heat and mass transfer effects in each stage.

The defrost model proposed here is a fundamental analysis specialized to defrost of a vertical plain fin. This geometry permits the formation of a tractable mathematical problem and forms a basic step toward modeling geometries that occur in application, e.g., a multi-fin condenser tube. The governing equations, along with the initial and boundary conditions, for each stage of the defrost process are described. In Chapter 6, the numerical solutions to the models are discussed. The numerical results of the model are compared against experimental results.

While the proposed model has the level of accuracy to predict heat and mass transfer rates for a single fin, it is too cumbersome to be applied to the analysis of an entire heat exchanger within a system simulation. The modeling framework for a frosted-defrosted heat exchanger is briefly discussed in Appendix C. Fin level effects are muted by the slower system level dynamics.

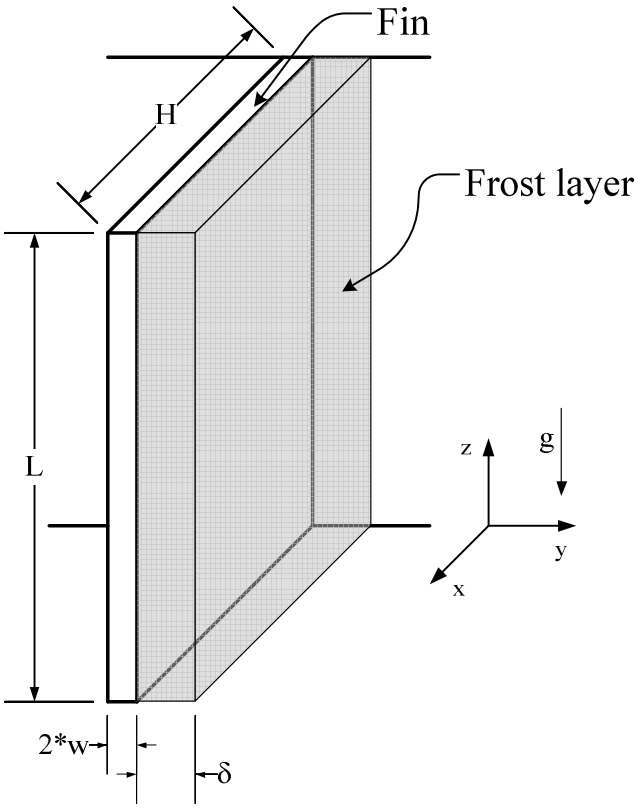

Figure 3-1. Frosted half fin.

3.1 Plain fin model

Figure 3-1 shows a simple plain half fin, which represents a single fin of a common evaporator coil. The fin is attached to a continuous base where the heat is supplied. The fin has a length L, and a half-thickness w. A frost layer of thickness δ is bonded to the fin surface. The frost is constructed of interlacing ice crystals with internal air pockets and has a porosity ε. There is some debate within the literature whether the porosity varies within the frost layer, and the present model is constructed such that either a constant or variable porosity can be evaluated. Initially the surface and surrounding air temperature are assumed to be below the melt temperature of ice. The temperature within the ice is assumed to vary linearly between the wall and frost surface temperatures. The water vapor pressure within air pockets in the frost is assumed to be at the saturation pressure of the local frost temperature. A thin fin approximation is used to

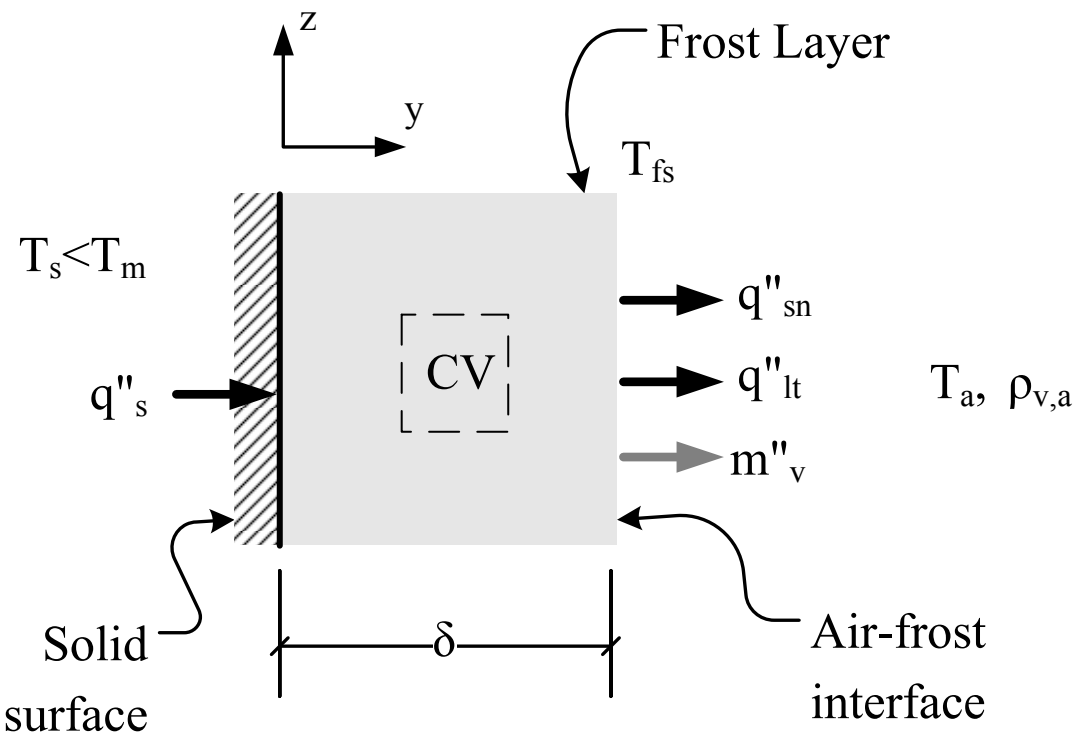

Figure 3-2. Defrost Stage I vapor diffusion model.

model heat transfer in the fin, with only temperature variations along the height of the fin assumed. The heat and mass transfer within the frost layer are assumed to occur predominately in the y-direction. This assumption is based upon the fact that the conductivity of the metal fin is several orders of magnitude greater than that of the frost layer. A summary of the multi-state defrost model is presented in Mohs and Kulacki (2011)

3.1.1 Stage I – Vapor diffusion model

Recall from Section 2.3.1, the defrost process has been shown to progress through several predicable stages. At a given moment of time, heat is applied to the fin causing the surface temperature to increase. The increase of the surface temperature causes a change in the internal temperature distribution of the frost layer. As heat is conducted through the frost, the change of temperature will also cause a change in the local vapor pressure within the air pockets. The small pressure difference will cause water molecules to sublimate. As the local vapor pressure increases above the prevailing bulk vapor

pressure, water will diffuse from the ice surface, through the frost layer, and escape into the surrounding air. Mass transport of the water vapor will carry latent heat from the frost layer and sensible heat is lost to the surrounding air through convective heat transfer. One would not expect the overall height of the frost layer to dramatically change during this stage, but instead see a slight decrease in the density of the frost layer. The energy balance of the control volume seen in Figure 3-2 is,

$$\left(\rho c_p\right)_f \frac{\partial T}{\partial t} = \frac{\partial}{\partial y}\left(k_f \frac{\partial T}{\partial y}\right) - \frac{\partial}{\partial y}\left(q''_v\right). \tag{3.1}$$

The left-hand term is the change in internal energy of the control volume, while the terms on the right-hand side are the energy transport by conduction and sublimation of the frost, respectively.

The volumetric heat capacity, $(\rho c_p)_f$, of the frost layer is determined by the arithmetic mean (volume) weighed, porosity, ε,

$$\left(\rho c_p\right)_f = \varepsilon\left(\rho c_p\right)_a + (1-\varepsilon)\left(\rho c_p\right)_i. \tag{3.2}$$

A common approximation for the thermal capacities of the frost is to ignore the capacitance of the air,

$$\left(\rho c_p\right)_f \approx (1-\varepsilon)\left(\rho c_p\right)_i. \tag{3.3}$$

Several models have been proposed to determine the effective conductivity of frost. Generally these models relate effective conductivity of the frost to bulk porosity. Auracher (1987) developed an empirical correlation for effective conductivity using a parallel and perpendicular plate frost structure,

$$\begin{aligned} &\frac{1}{k_f} = \frac{a}{k_{f,\perp}} + \frac{(1-a)}{k_{f,\parallel}}, \qquad a = 0.42\left(0.1 + 0.955^{\rho_f}\right), \\ &k_{f,\perp} = \left[\frac{\varepsilon}{k_a} + \frac{(1-\varepsilon)}{k_i}\right]^{-1}, \qquad k_{f,\parallel} = \varepsilon k_a + (1-\varepsilon)k_i\,. \end{aligned} \tag{3.4}$$

The latent heat leaving the frost layer is the product of the water vapor mass flux, m''_v, and the latent heat of sublimation, λ_{ig},

$$q''_v = \lambda_{ig} m''_v. \tag{3.5}$$

The water vapor transport within the frost layer is driven by molecular diffusion, which is formulated by Fick's Law,

$$m''_v = -D_v \frac{\partial \rho_v}{\partial y}. \tag{3.6}$$

In a porous medium, the diffusion path is obstructed by the pore structure, and in effect, lengthens the path along which the diffusion occurs. Na (2003) showed how an effective diffusion coefficient, $D_{v,eff}$, can describe the diffusion in a porous frost structure,

$$m''_v = -D_{v,eff} \frac{\partial \rho_v}{\partial y}. \tag{3.7}$$

Generally it is assumed that the water vapor within the pores of the frost layer is saturated at the local frost interface temperature. Applying the ideal gas law, Equation (3.7) becomes,

$$m''_v = -D_{v,eff} \frac{\partial}{\partial y}\left(\frac{p_v}{R_w T}\right). \tag{3.8}$$

The effective diffusion coefficient is related to the bulk diffusion coefficient by the bulk porosity and tortuosity factor, τ, which describes the path through the porous structure,

$$\tau = \frac{1}{\varepsilon}\frac{D_{v,eff}}{D_v}. \tag{3.9}$$

Lee and Ro (2005) recommend the following empirical equation for the diffusion coefficient and model for the tortuosity,

$$D_v = 9.26\times10^{-7}\frac{1}{p_a}\left(\frac{T^{2.5}}{T+245}\right), \tag{3.10}$$

$$\tau = \frac{\varepsilon}{1-(1-\varepsilon)^{0.5}}. \tag{3.11}$$

Combining Equations (3.1), (3.5), and (3.7) results in the following differential equation for the initial stage of the defrost process,

$$(\rho c_p)_f \frac{\partial T}{\partial t} = \frac{\partial}{\partial y}\left(k_f \frac{\partial T}{\partial y}\right) + \frac{\partial}{\partial y}\left(\lambda_{ig} D_{v,eff} \frac{\partial \rho_v}{\partial y}\right), \tag{3.12}$$

with the following boundary conditions,

$$\begin{aligned} &y=0,\ q''_s = -k_f \left.\frac{\partial T}{\partial y}\right|_{y=0}, \\ &y=\delta,\ k_f \left.\frac{\partial T}{\partial y}\right|_{y=\delta} = h(T_a - T_{fs}) + \lambda_{ig} h_m (\rho_{v,a} - \rho_{v,fs}), \end{aligned} \tag{3.13}$$

where q''_s is the supplied heat flux at the surface, T_a, and T_{fs} are the ambient air and frost surface temperatures, respectively. The convective heat transfer coefficient, h, and the mass transfer coefficient, h_m, can be estimated via the heat and mass transfer analogy, and are related by the Lewis number, Le_a, and the specific heat of air (Hao et al., 2005),

$$h_m = \frac{h}{\rho_a c_{p,a} Le_a^{2/3}}. \tag{3.14}$$

The last unknown is the change in density due to the sublimation. The change in density of the frost in the control volume can be expressed via conservation of mass as,

$$\frac{\partial \rho_f}{\partial t} = -\frac{\partial m''_v}{\partial y}. \tag{3.15}$$

Combining Equations (3.7) and (3.14), one obtains the final form of the mass balance with the following two boundary conditions,

$$\frac{\partial \rho_f}{\partial t} = -\frac{\partial}{\partial y}\left(D_{v,eff} \frac{\partial \rho_v}{\partial y}\right), \tag{3.16}$$

$$\begin{aligned} &y = 0;\ \left.\frac{\partial \rho_v}{\partial y}\right|_{y=0} = 0, \\ &y = \delta;\ m''_v = h_m (\rho_{v,a} - \rho_{v,fs}). \end{aligned} \tag{3.17}$$

The initial temperature distribution within the frost layer is determined through the solution of the steady state Fourier equation for a given heat flux and surface temperature. The vapor pressure within the frost layer is assumed to be at saturation to the temperature of the neighboring ice crystals and can be determined by Equation (D.2) in Appendix D.

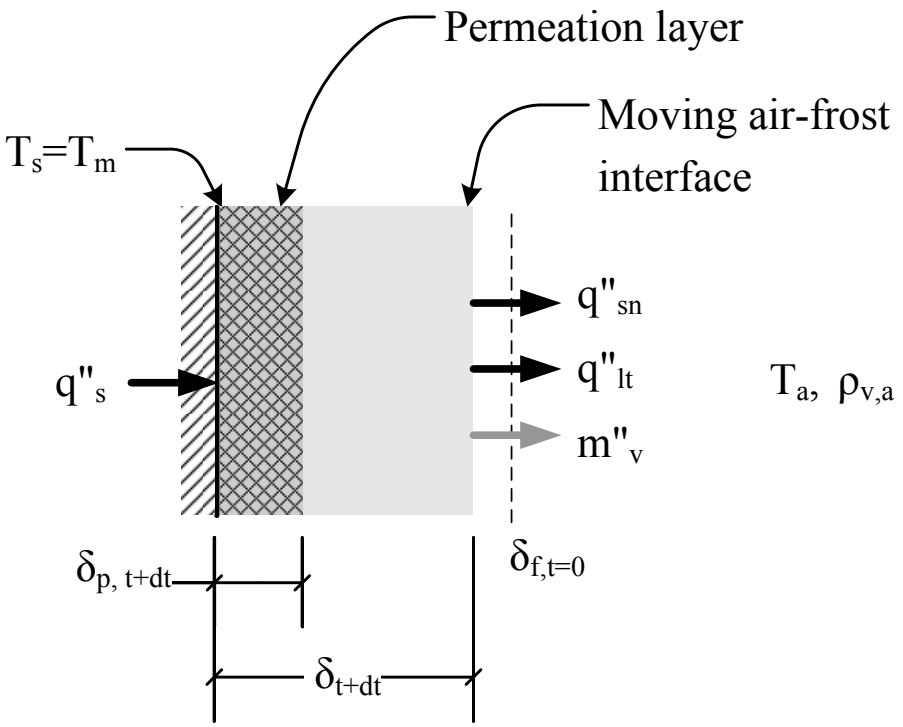

Figure 3-3. Defrost Stage II permeation model.

3.1.2 Stage II – Permeation model

At the moment the surface temperature reaches the melt temperature, ice attached to the surface will begin to melt. As liquid water accumulates, capillary forces draw the liquid into the small air pockets near the surface, causing a layer of water and ice (permeation layer) within the frost. Heat is transported into the frost layer by both the movement of the melt liquid and bulk conduction through the ice. The heat transported from the surface will reach a practical limit. That is to say the supplied heat flux is finite, and any heat supplied to the surface will be instantaneously absorbed by the melting frost layer causing the temperature within the permeation layer to be fixed at the melt temperature. As the ice melts and the liquid is drawn into the frost layer, the thickness of the frost layer will decrease. Within the permeation layer the water content would vary from almost completely water near the surface and decay to no water further into the frost layer. Thus one expects to see two fronts, a permeation front moving from the solid surface and the air-frost front moving towards the surface. A small portion of heat will escape the frost layer through both sensible and latent heat transfer.

Within the bulk frost layer, the conservation of energy equation will be very similar to the model described in the preceding section with an additional convective term to describe the heat transported by the bulk movement of the frost layer,

$$\left(\rho c_p\right)_f \frac{\partial T}{\partial t} = \frac{\partial}{\partial y}\left(k_f \frac{\partial T}{\partial y}\right) + \frac{\partial}{\partial y}\left(\lambda_{ig} D_{v,eff} \frac{\partial \rho_v}{\partial y}\right) + \left(\rho c_p\right)_f u \frac{\partial T}{\partial y}. \tag{3.18}$$

The convective velocity, u, occurs owing to the reduction in body volume due to the melting of the frost layer and can be written,

$$u = \frac{\partial \delta}{\partial t} = -\frac{q''_s}{\lambda_{if}\rho_f}. \tag{3.19}$$

The remaining terms in the energy equation are evaluated as described before. The mass balance for the zone is once again given by Equation (3.16). The boundary conditions for the region are,

$$y = \delta_p,\ T = T_m,\quad m''_v = 0,$$

$$y = \delta,\ k_f \left.\frac{\partial T}{\partial y}\right|_{y=\delta} = h(T_a - T_{fs}) + \lambda_{ig} h_m\left(\rho_{v,a} - \rho_{v,fs}\right), \tag{3.20}$$

$$m''_v = h_m\left(\rho_{v,a} - \rho_{v,fs}\right).$$

Aoki et al. (1988) developed a model to describe the penetration of the melt liquid into a porous layer. The water content ratio, S, describes the volume fraction of water. Near the heated surface the water content is nearly 100% and decays away from the surface. The time dependence of the water content in the permeation layer can be determined from,

$$\frac{\partial S}{\partial t} = -\frac{1}{\varepsilon \rho_w}\frac{\partial m''_{w,p}}{\partial y} - u\frac{\partial S}{\partial y}. \tag{3.21}$$

The terms on the right-hand side of the equation describe the contribution from the water permeation mass flux coming up from the surface and the bulk movement of the frost layer towards the surface. The water permeation mass flux, $m''_{w,p}$, in the frost layer will be dependent upon the structure of frost and capillary and gravitational forces. The rate of the change in the location of the water permeation front is equal to the rate that water permeates in the frost, the rate at which the water refreezes, and the rate at which the frost

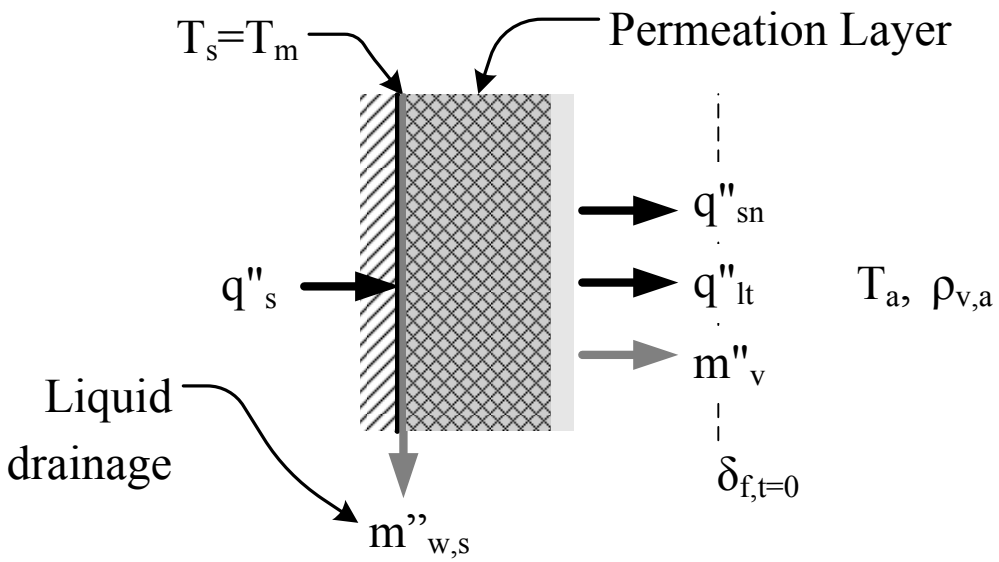

Figure 3-4. Defrost Stage II permeation and drainage model.

is moving towards the surface,

$$\frac{\partial \delta_p}{\partial t} = \frac{m''_{w,p}\big|_{y=\delta_p}}{\varepsilon \rho_w S_c} + \frac{1}{\varepsilon \rho_w S_c}\frac{k_p}{\lambda_{if}}\frac{\partial T}{\partial y}\bigg|_{y=\delta_p} + u, \tag{3.22}$$

where S_c is the limited water content, k_p and ρ_p are the conductivity and density in the permeation layer, respectively. The change in density in the permeation layer due to refreezing can be represented as,

$$\delta_p \frac{\partial \rho_p}{\partial t} = -\frac{k_p}{\lambda_{if}}\frac{\partial T}{\partial y}\bigg|_{y=\delta_p}. \tag{3.23}$$

As the ice crystals in the vicinity of the wall are melted, and the permeation layer becomes fully saturated, a liquid layer will form at the solid surface interface. By gravitational force, some of the liquid will drain from the surface, as seen in Figure 3-4. The mass flux of the melt liquid leaving the surface, $m''_{w,s}$, is equal to the difference between the mass flux of the melt liquid at the surface, $m''_{w,t}$, and the water permeation mass flux,

$$m''_{w,s} = m''_{w,t} - m''_{w,p}. \tag{3.24}$$

The total mass flux at the surface is the sum of liquid generated through the melt

process, plus the mass flux of liquid carried with the bulk movement of the frost layer towards the surface,

$$m''_{w,t} = -u\left(\rho_p + \varepsilon\rho_w S_{y=0}\right). \tag{3.25}$$

Combining Equations (3.24) with (3.23) and (3.18), one obtains the melt drainage mass flux,

$$m''_{w,s} = \frac{q''_s}{\lambda_{if}\rho_f}\left(\rho_p + \varepsilon\rho_w S_{y=0}\right) - m''_{w,p}. \tag{3.26}$$

Boundary conditions for the permeation layer are,

$$\begin{aligned} &y = 0,\ q''_s = -k_w \left.\frac{\partial T}{\partial y}\right|_{y=0}, \\ &y = \delta_p,\ T = T_m,\ \ S = S_c. \end{aligned} \tag{3.27}$$

The initial temperature and vapor distribution are inherited from the end of Stage I. As recommended by Aoki (1988), the initial water content ratio at the surface is assumed to be equal to the limiting value of 0.1.

Melting continues until either the entire frost layer has melted or the frost pulls away from the surface in a bulk movement, also called *sloughing*. The tendency to melt or slough is dependent upon the adhesion forces governed by the surface tension forces at the frost-solid interface. One would expect the likelihood of sloughing to be greater for thick, dense frost wherein the weight of the frost layer is greater than the adhesion force to the surface. At this time the model will be evaluated for frost layers that stay in contact with the surface, but if experimental work shows evidence of sloughing, a further evaluation of the phenomena will be needed.

3.1.3 Stage III – Dry out model

After the frost layer has melted or sloughed away, a small portion of the liquid will adhere to the surface through surface tension forces. The amount of retained liquid mass on the surface will be a function of inclination angle and the surface wettability. Wettability is determined by a force balance between adhesive and cohesive forces of a

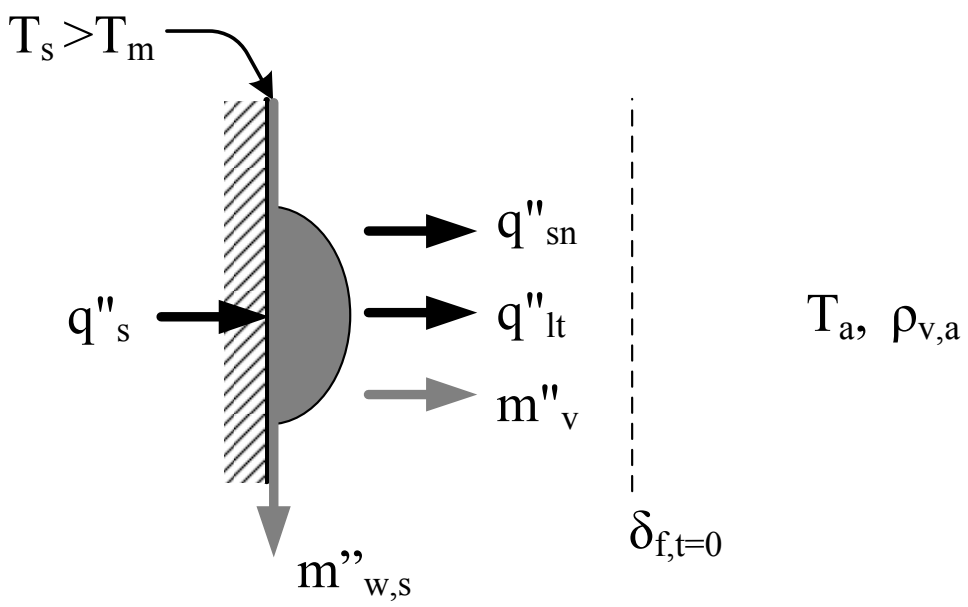

Figure 3-5. Defrost Stage III dry out model.

water droplet. Surfaces that have a high degree of wettability, tend to form a thin layer of water, and are called hydrophilic surfaces. Low wetting surfaces, or hydrophobic, tend to form individual droplets of water on the surface. Liquid water will continue to shed from the surface as a falling film, while heating of the surface will cause some of the water to be vaporized to the surrounding air. The following analysis is a simplified approach to the model presented by Yan and Lin (1990) for a coupled heat and mass transfer of falling film evaporation.

From a mass balance on the control volume in Figure 3-5, the change rate of mass (per unit area) is equal to the net mass flux of the melt liquid falling down the surface and the mass flux of the moisture that is vaporized into the surrounding air,

$$\frac{\partial}{\partial t}\left(\frac{m}{A}\right) = m''_{w,s} + m''_v. \tag{3.28}$$

The mass flux leaving the surface is a simple evaporation process. Assuming the liquid layer is sufficiently thin, temperature variations within the film can be neglected, and in addition, the film temperature is the same as the wall temperature. The mass flux can then be expressed as,

$$m''_v = h_m(\rho_{v,a} - \rho_{v,w}), \tag{3.29}$$

where h_m is the mass transfer coefficient, $\rho_{v,a}$ and $\rho_{v,w}$ are the water vapor density of the free stream air and saturated at the liquid surface respectively. The mass flux of the liquid stream can expressed as the product of the film velocity, u_w, and density, ρ_w,

$$m''_{w,s} = u_w \rho_w. \tag{3.30}$$

Assuming laminar film flow and negligible inertia effects, the film velocity can be determined by the in-plane momentum equation,

$$\frac{\partial}{\partial y}\left(\mu_w \frac{\partial u_w}{\partial y}\right) + \rho_w g = 0. \tag{3.31}$$

The motion of the water film is strictly dependent upon the balance of the viscous and gravitational forces. Assuming the no slip condition at the wall and equally small velocity at the frost interface, the mean velocity can be determined by integrating Equation (3.31).

$$\overline{u_w} = -\frac{\rho_w g}{12\mu_w}\delta_w^2, \tag{3.32}$$

where δ_w is the thickness of the water stream, and μ is the viscosity of water. Combining Equations (3.28), (3.29), (330) and (3.32), one obtains the following equation for the change in film thickness,

$$\frac{\partial \delta_w}{\partial t} = -\frac{\rho_w g}{12\mu_w}\delta_w^2 + \frac{h_m}{\rho_w}(\rho_{v,a} - \rho_{v,w}). \tag{3.33}$$

Assuming the temperature variation in the film is negligible, a lumped analysis can be applied to the control volume. The change rate of temperature of the film is equal to the heat leaving with the liquid drainage, as well as, the sensible and latent heat exchange to the ambient air,

$$\delta_w(\rho c_p)_w \frac{\partial T}{\partial t} = q''_{ws} + q''_v + q''_s. \tag{3.34}$$

Energy leaving with the liquid steam, q''_{ws}, can be expressed,

$$q''_{ws} = m''_{w,s}\Delta h_w = \overline{u_w}\rho_w \Delta h_w, \tag{3.35}$$

where Δh_w is the change in enthalpy of the water at the film temperature, and $\overline{u_w}$ is the mean water stream velocity. Similar to earlier analysis, the heat leaving the surface is the sum of the sensible and latent heat transfer, where the convective heat and mass transfer coefficients are analogous via the Lewis number,

$$q''_v = h(T_a - T_w) + \lambda_{ig} h_m (\rho_{v,a} - \rho_{v,w}). \quad (3.36)$$

Combining Equations (3.34), (3.35), and (3.36), gives the following partial differential equation for the energy governing equation,

$$\delta_w (\rho c_p)_w \frac{\partial T}{\partial t} = \overline{u_w} \rho_w \Delta h_w + h(T_a - T_w) + \lambda_{ig} h_m \left(\rho_{v,a} - \rho_{v,w}\right) + q''_s. \quad (3.37)$$

The initial conditions for the model are the initial surface temperature and film thickness. The initial film thickness can be estimated from the retained liquid mass. Factors that affect retention are surface wettability, due to coating and surface finish, obstruction (e.g., louvers and other fin geometries) and fin spacing which can lead to bridging. El Sherbini and Jacobi (2006) developed a detailed retention model where contact angle is used to calculate the volume of an individual droplet. Employing a size-distribution function they find the retained mass for the entire heat exchanger can be determined. Applying the model to a plane-fin heat exchanger, they find the retained mass to be about 120 gm/m^2, which compares favorably with their measurements.

The most notable assumption in this stage of the model is the neglect of the effect of water surface tension on the water hold up phenomena. In reality, Equation (3.30) should include a term to describe the resistive force caused by surface tension effects. As mentioned earlier, surface tension effects will cause an adhesion force to the surface that will tend to impede water drainage. Also the current model does not capture the dynamics of a bulk frost movement. A sloughing model will be closely tied to surface tension effect, as this would be the primary adhesion force acting of the frost.

3.1.4 Summary of governing equations

Table 3-1 summarizes the governing equations and boundary conditions for each stage and region of the defrost process. As structured, each stage of the model will be solved separately. The final state of each stage model is the initial condition for the subsequent stage.

Table 3-1. Governing equations and boundary conditions for each defrost stage.

Defrost Stage	Frost Region	Energy		Mass	
		Eq.	BC	Eq.	BC
I	Vapor diffusion	3.12	3.13	3.16	3.17
II	Vapor diffusion	3.17	3.20	3.16	3.17
II	Permeation	3.21	3.27	3.22	3.27
II	Drainage	3.21	3.27	3.25	3.27
III	Dry-Out	3.37		3.33	

3.2 Non-dimensional and scaling analysis

To gain a better insight into the relative magnitude of each term in the governing equations, dimensional analysis is a useful tool. By applying the appropriate dimensionless parameters to the physical dimensions of the problem, the governing equation is reduced to a simpler form, where the magnitude of terms is expressed by a dimensionless group. Applying the appropriate physical values to these dimensionless groups aids in determining which terms of the equation maybe negligible, allowing for further simplification of the governing equations

3.2.1 Stage I

The first stage of the defrost process is dominated by the sensible heating of the frost layer, and sublimation of the ice into the air stream. Recall, the energy equation for the initial stage is represented as

$$\left(\rho c_p\right)_f \frac{\partial T}{\partial t} = \frac{\partial}{\partial y}\left(k_f \frac{\partial T}{\partial y}\right) + \frac{\partial}{\partial y}\left(\lambda_{ig} D_{v,eff} \frac{\partial \rho_v}{\partial y}\right). \tag{3.38}$$

Applying the chain rule to expand the terms on the right-hand,

$$\left(\rho c_p\right)_f \frac{\partial T}{\partial t} = k_f \frac{\partial^2 T}{\partial y^2} + \frac{\partial k_f}{\partial y}\frac{\partial T}{\partial y} + \lambda_{ig} D_{v,eff} \frac{\partial^2 \rho_v}{\partial y^2} + \lambda_{ig} \frac{\partial D_{v,eff}}{\partial y}\frac{\partial \rho_v}{\partial y}. \tag{3.39}$$

Define the following dimensionless parameters:

$$\theta = \frac{T - T_s}{T_m - T_s} = \frac{T - T_s}{\Delta T}, \qquad \tau = \frac{\alpha_f t}{{\delta_f}^2}, \qquad \alpha_f = \frac{k_f}{(\rho c_p)_f},$$

$$\phi = \frac{\rho_v - \rho_{v,s}}{\rho_{v,m} - \rho_{v,s}} = \frac{\rho_v - \rho_{v,s}}{\Delta \rho_v}, \qquad \eta = \frac{y}{\delta_f}, \tag{3.40}$$

$$\pi = \frac{D_{v,eff} - D_{v,eff,s}}{D_{v,eff,fs} - D_{v,eff,s}} = \frac{D_{v,eff} - D_{v,eff,s}}{\Delta D_{v,eff}}, \quad \kappa = \frac{k_f - k_{f,s}}{k_{f,fs} - k_{f,s}} = \frac{k_f - k_{f,s}}{\Delta k_f}.$$

Combining into Equations (3.39) and (3.40) yields,

$$\frac{\partial \theta}{\partial \tau} = \frac{\partial^2 \theta}{\partial \eta^2} + \left(\frac{\Delta k_f}{k_f}\right)\frac{\partial \theta}{\partial \eta}\frac{\partial \kappa}{\partial \eta} + \left(\frac{\lambda_{ig}}{c_{p,f}\Delta T}\right)\left(\frac{D_{v,eff} c_{p,f} \Delta \rho_v}{k_f}\right)\frac{\partial^2 \phi}{\partial \eta^2} + \left(\frac{\lambda_{ig}}{c_{p,f}\Delta T}\right)\left(\frac{D_{v,eff} c_{p,f} \Delta \rho_v}{k_f}\right)\left(\frac{\Delta D_{v,eff}}{D_{v,eff}}\right)\frac{\partial \pi}{\partial \eta}\frac{\partial \phi}{\partial \eta}, \tag{3.41}$$

and several dimensionless parameters emerge,

$$\frac{\partial \theta}{\partial \tau} = \frac{\partial^2 \theta}{\partial \eta^2} + \left(\frac{\Delta k_f}{k_f}\right)\frac{\partial \theta}{\partial \eta}\frac{\partial \kappa}{\partial \eta} + \Gamma_1 \frac{\partial^2 \phi}{\partial \eta^2} + \Gamma_1 \left(\frac{\Delta D_{v,eff}}{D_{v,eff}}\right)\frac{\partial \pi}{\partial \eta}\frac{\partial \phi}{\partial \eta}, \tag{3.42}$$

where Γ_1 is defined as the reciprocal of the Stefan and Lewis numbers for the first stage,

$$\Gamma_1 = \left(\frac{\lambda_{ig}}{c_{p,f}\Delta T}\right)\left(\frac{D_{v,eff} c_{p,f} \Delta \rho_v}{k_f}\right) = \left(\frac{1}{St_1}\right)\left(\frac{1}{Le_1}\right). \tag{3.43}$$

Similarly the conservation of mass from Equation (3.16) can be expressed,

$$\frac{\partial \rho_f}{\partial t} = \frac{\partial}{\partial y}\left(D_{v,eff}\frac{\partial \rho_v}{\partial y}\right). \tag{3.44}$$

Applying the chain rule to expand the terms on the right-hand side results in,

$$\frac{\partial \rho_f}{\partial t} = D_{v,eff}\frac{\partial^2 \rho_v}{\partial y^2} + \frac{\partial D_{v,eff}}{\partial y}\frac{\partial \rho_v}{\partial y}. \tag{3.45}$$

Recall the porosity of the frost layer is defined as

$$\varepsilon = \frac{\rho_i - \rho_f}{\rho_i - \rho_a} = \frac{\rho_i - \rho_f}{\Delta \rho_{i,a}}. \tag{3.46}$$

Substituting the dimensionless parameters into Equation (3.45),

$$\frac{\partial \varepsilon}{\partial \tau}=\left(\frac{D_{v,eff}c_{p,f}\Delta\rho_v}{k_f}\right)\left(\frac{\rho_f}{\Delta\rho_{i,a}}\right)\frac{\partial^2\phi}{\partial\eta^2}+\left(\frac{D_{v,eff}c_{p,f}\Delta\rho_v}{k_f}\right)\left(\frac{\rho_f}{\Delta\rho_{i,a}}\right)\left(\frac{\Delta D_{v,eff}}{D_{v,eff}}\right)\frac{\partial\pi}{\partial\eta}\frac{\partial\phi}{\partial\eta}. \tag{3.47}$$

Again a number of dimensionless parameters are found,

$$\frac{\partial \varepsilon}{\partial \tau}=\left(\frac{1}{Le_1}\right)\left(\frac{\rho_f}{\Delta\rho_{i,a}}\right)\frac{\partial^2\phi}{\partial\eta^2}+\left(\frac{1}{Le_1}\right)\left(\frac{\rho_f}{\Delta\rho_{i,a}}\right)\left(\frac{\Delta D_{v,eff}}{D_{v,eff}}\right)\frac{\partial\pi}{\partial\eta}\frac{\partial\phi}{\partial\eta}, \tag{3.48}$$

where the first stage Stefan and Lewis numbers are defined,

$$St_1=\frac{c_{p,f}\Delta T}{\lambda_{ig}}, \tag{3.49}$$

$$Le_1=\frac{\alpha_v}{D_{v,eff}}=\frac{k_f}{D_{v,eff}c_{p,f}\Delta\rho_v}. \tag{3.50}$$

Applying the dimensionless parameters to the boundary conditions,

$$\begin{aligned}
&\left.\frac{\partial\theta}{\partial\eta}\right|_{\eta=0}=-\frac{\delta_f\, q''_s}{k_f\Delta T}=-Bi_{1,s},\ \left.\frac{\partial\phi}{\partial\eta}\right|_{\eta=0}=0,\\
&\left.\frac{\partial\theta}{\partial\eta}\right|_{\eta=1}=\left(\frac{\delta_f\, h}{k_f}\right)\left(\frac{T_a\text{-}T_{fs}}{\Delta T}\right)+\left(\frac{\lambda_{ig}}{c_{p,f}\Delta T}\right)\left(\frac{D_{v,eff}c_{p,f}\Delta\rho_v}{k_f}\right)\left(\frac{\delta_f\, h_m}{D_{v,eff}}\right)\left(\frac{\Delta\rho_{v,a\text{-}fs}}{\Delta\rho_v}\right)\\
&\qquad=Bi_{1,fs}\left(\frac{\Delta T_{a\text{-}fs}}{\Delta T}\right)+\ \Gamma_1\left(\frac{\delta_f\, h_m}{D_{v,eff}}\right)\left(\frac{\Delta\rho_{v,a\text{-}fs}}{\Delta\rho_v}\right),\\
&\left.\frac{\partial\phi}{\partial\eta}\right|_{\eta=1}=\left(\frac{\delta_f\, h_m}{D_{v,eff}}\right)\left(\frac{\Delta\rho_{v,a\text{-}fs}}{\Delta\rho_v}\right).
\end{aligned} \tag{3.51}$$

3.2.1.1 Special case for constant porosity

Experimental images suggest that the porosity of the frost layer does not vary appreciably in the thickness of the frost layer. Assuming a constant porosity, it can be shown there will be no change in the local value of the diffusion coefficient and conductivity from the wall to the frost-air interface.

$$\begin{aligned}
&\Delta D_{v,eff}=D_{v,eff,fs}-D_{v,eff,s}\xrightarrow[\frac{\partial\varepsilon}{\partial y}=0]{}0,\\
&\Delta k_f=k_{f,fs}\text{-}k_{f,s}\xrightarrow[\frac{\partial\varepsilon}{\partial y}=0]{}0.
\end{aligned} \tag{3.52}$$

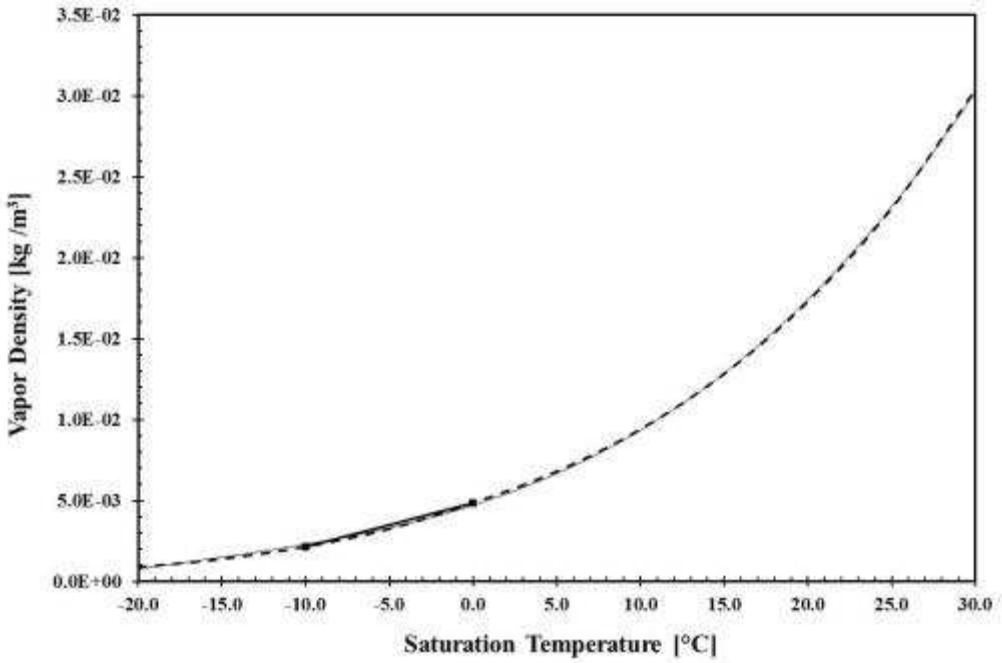

Figure 3-6. Water vapor density as a function of staturation temperature (Eq. (D.2)).

Applying to the Equations (3.42) and (3.48), the non-linear terms drop off to give,

$$\frac{\partial\theta}{\partial\tau}=\frac{\partial^2\theta}{\partial\eta^2}+\Gamma_1\frac{\partial^2\phi}{\partial\eta^2}, \tag{3.53}$$

$$\frac{\partial\varepsilon}{\partial\tau}=\left(\frac{1}{\mathrm{Le}_1}\right)\left(\frac{\rho_f}{\Delta\rho_{i,a}}\right)\frac{\partial^2\phi}{\partial\eta^2}. \tag{3.54}$$

3.2.1.1 Vapor density relationship

Using known phenomena of water vapor, it is possible to decouple the relationship of temperature and vapor density in the energy Equation (3.53). The first assumption is that the temperature of the water vapor is equal to the local frost temperature. Secondly, the water vapor density varies primarily with the saturation temperature of the gas (Figure 3-6). Furthermore, over small ranges of temperature the vapor density can be approximated with a linear relation,

$$\rho_v=mT+B. \tag{3.55}$$

Differentiating both sides of Equation (3.55) with respect to y, the following relation between vapor density and temperature can be developed,

$$\frac{\partial^2 \rho_v}{\partial y^2} = m \frac{\partial^2 T}{\partial y^2}. \tag{3.56}$$

Applying the non-dimensional parameters for vapor density, temperature, and y-direction,

$$\frac{\partial^2 \phi}{\partial \eta^2} = m \frac{\Delta T}{\Delta \rho_v} \frac{\partial^2 \theta}{\partial \eta^2}. \tag{3.57}$$

The value of m is the local slope of the vapor pressure-versus-temperature relation. Using the same value as chosen for the non-dimensional variable reduces the equation to,

$$\frac{\partial^2 \phi}{\partial \eta^2} = \frac{\partial^2 \theta}{\partial \eta^2}. \tag{3.58}$$

Applying this relationship to Equation (3.53), the energy equation can be expressed,

$$\frac{\partial \theta}{\partial \tau} = (1+\Gamma_1) \frac{\partial^2 \theta}{\partial \eta^2}. \tag{3.59}$$

Similarly, the change in porosity can be related to changes in temperature field by,

$$\frac{\partial \varepsilon}{\partial \tau} = \left(\frac{1}{Le_1}\right)\left(\frac{\rho_f}{\Delta \rho_{i,a}}\right) \frac{\partial^2 \theta}{\partial \eta^2}. \tag{3.60}$$

3.2.1.1 Scaling analysis of Stage I

With the governing equations in the non-dimensional form, it is straight forward to calculate the dimensionless parameters to determine the relative weight of each term in the differential form of the equation. When evaluating Equation (3.59), it is clear that the diffusion of vapor is an enhancement to the overall heat transfer from the surface, and it is scaled to the Stefan and Lewis numbers,

$$St_1 = \frac{c_{p,f} \Delta T}{\lambda_{ig}}, \tag{3.61}$$

$$Le_1 = \frac{\alpha_v}{D_{v,eff}} = \frac{k_f}{D_{v,eff} c_{p,f} \Delta \rho_v}. \tag{3.62}$$

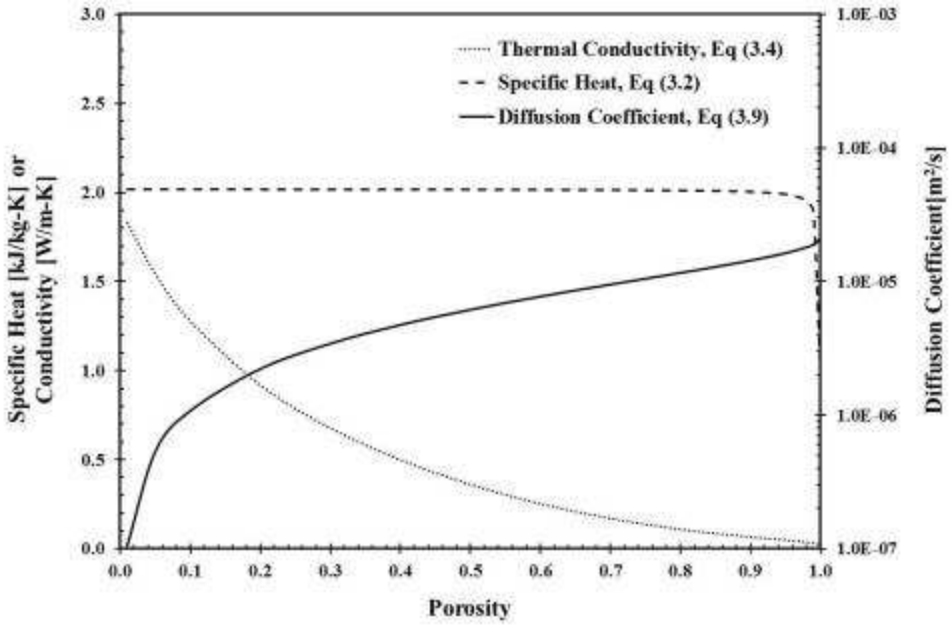

Figure 3-7. Frost properties as a fuction of porosity (T_f = -10°C).

Recall from Equations (3.2), (3.4), and (3.10) the specific heat, thermal conductivity, and diffusion coefficient are all proportional to the porosity of the frost layer. Furthermore the specific heat and thermal conductivity are primarily driven by the properties of ice. Figure 3-7 shows the variability of specific heat, conductivity and diffusion coefficient as a function of porosity at a frost temperature of -10°C.

Applying the physical properties, the Lewis and Stefan numbers as a function of porosity for the first stage of the defrost process are shown in Figure 3-8. For typical frost layers, with porosity in the range of 0.4 to 0.6, the Lewis number will be on the order of 10,000. This is obvious when evaluating Equation (3.59), because transport due to thermal diffusion (i.e., the numerator) is significantly greater than that of mass diffusion (i.e., the denominator). The Stefan number is nearly constant for all values of porosity, and is on the order of 0.01. From Equation (3.61), it is seen that the Stefan number is dominated by the large value of heat of sublimation of ice (2604 kJ/kg). Γ_1, defined as the reciprocal of the product of Stefan and Lewis numbers (Equation (3.43)), is found to vary from 0 to 1 over the whole range of porosity. From Equation (3.60), the effect of vapor diffusion can be negligible for extremely small values of Γ_1. From Figure

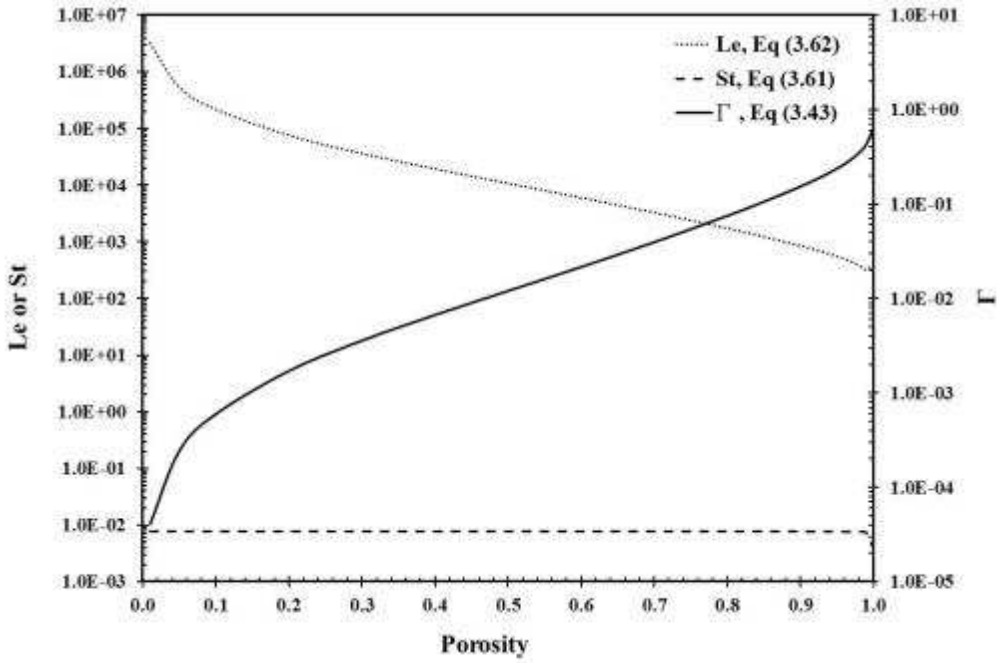

Figure 3-8. Lewis and Stefan number for Stage I (T_f = -10°C).

3-8, heat transfer due to vapor diffusion would only be about one percent for a porosity of 0.5, and less than five percent for a porosity of 0.7. For significantly small value, the mass transport due to vapor diffusion in the first stage of defrost can be assumed negligible for values of porosity about 0.5. Applying the energy and mass conservation Equations, (3.59) and (3.60) respectively, reduce to,

$$\frac{\partial \theta}{\partial \tau} = \frac{\partial^2 \theta}{\partial \eta^2}, \tag{3.63}$$

$$\frac{\partial \varepsilon}{\partial \tau} = 0. \tag{3.64}$$

With the following boundary conditions,

$$\left.\frac{\partial \theta}{\partial \eta}\right|_{\eta=0} = \mathrm{Bi}_{1,s},$$
$$\left.\frac{\partial \theta}{\partial \eta}\right|_{\eta=1} = \mathrm{Bi}_{1,fs}\left(\frac{\Delta T_{a\text{-}fs}}{\Delta T}\right). \tag{3.65}$$

From the scaling analysis, it is apparent that mass diffusion during first stage of

defrost is insignificant in the overall energy transport for dense frost layers. Equation (3.63), the energy equation, is reduced to the non-dimensional diffusion equation. For frost layers with high porosity (i.e., low density), the effect of vapor transport cannot be neglected, and Equations (3.59) and (3.60) should be used to describe the first stage of the defrost process.

3.2.2 Stage II

The second stage of the defrost process is dominated by the physics of melting. As discussed in Section 3.1.2, the stage is dominated by the frost front moving towards the surface, and a permeation front moving away from the surface. A similar set of the dimensioning parameters are proposed for the second stage,

$$\theta = \frac{T - T_m}{T_a - T_m} = \frac{T - T_a}{\Delta T_{a-m}}, \qquad \tau = \frac{u_o t}{\delta_{f,o}},$$
$$M = \frac{m''_{w,p}}{u_o \varepsilon \rho_w}, \qquad \eta = \frac{y}{\delta_{f,o}}. \tag{3.66}$$

Appling Equation (3.66) to the equations governing the permeation layer, the concentration gradient (Equation (3.21)) and permeation layer thickness (Equation (3.22)) become,

$$\frac{\partial S}{\partial \tau} = -\frac{\partial M}{\partial \eta} - U\frac{\partial S}{\partial \eta}, \tag{3.67}$$

$$\frac{\partial \eta_p}{\partial \tau} = \frac{M_{\eta_p=1}}{S_c} + \frac{St_{2,p} Le_{2,p}}{S_c}\frac{\partial \theta}{\partial \eta}\bigg|_{\eta=1} + U. \tag{3.68}$$

where the velocity ratio, Stefan number, and Lewis number of the permeation layer are,

$$U = \frac{u}{u_o}, \tag{3.69}$$

$$St_{2,p} = \frac{c_{p,f}\Delta T}{\lambda_{if}}, \tag{3.70}$$

$$Le_{2,p} = \frac{k_p}{u_o \varepsilon c_{p,w} \rho_w \delta_{f,o}}. \tag{3.71}$$

Here the Lewis number has a slightly different form, providing the ratio of the heat flow

due to thermal transport to the bulk movement of the water within the frost layer. Applying the scaling parameters and the vapor density approximation in section 3.2.1.1, the temperature distribution in the vapor diffusion layer becomes,

$$\frac{\partial\theta}{\partial\tau} = \mathrm{Le}_{2,f}[1+\Gamma_2]\frac{\partial^2\theta}{\partial\eta^2} + \mathrm{U}\frac{\partial\theta}{\partial\eta}, \tag{3.72}$$

where Γ_2 is defined,

$$\Gamma_2 = \frac{1}{\mathrm{St}_{2,v}\mathrm{Le}_{2,v}}. \tag{3.73}$$

The Stefan and Lewis numbers are defined for both the frost and vapor as,

$$\mathrm{St}_{2,v} = \frac{c_{p,f}\Delta T}{\lambda_{ig}}, \tag{3.74}$$

$$\mathrm{Le}_{2,v} = \frac{k_f}{D_{v,eff}c_{p,f}\Delta\rho_v}., \tag{3.75}$$

$$\mathrm{Le}_{2,f} = \frac{k_f}{u_o\varepsilon c_{p,f}\rho_f\delta_{f,o}}. \tag{3.76}$$

The boundary conditions become,

$$\left.\frac{\partial\theta}{\partial\eta}\right|_{\eta=0} = -\frac{q''_s\delta_{f,0}}{k_f\,\Delta T_{a\text{-}m}} = -\mathrm{Bi}_{2,s}\,, \quad S_{\eta=\eta_p} = 1,$$
$$\theta_{\eta=\eta_p} = 0, \quad S_{\eta=\eta_p} = S_c, \tag{3.77}$$
$$\left.\frac{\partial\theta}{\partial\eta}\right|_{\eta=1} = \mathrm{Bi}_{2,fs}\left(\frac{T_a - T_{fs}}{\Delta T_{a\text{-}m}}\right) + \left(\frac{1}{\mathrm{St}_{2,v}}\right)\left(\frac{1}{\mathrm{Le}_{2,v}}\right)\left(\frac{\delta_f\,h_m}{D_{v,eff}}\right)\left(\frac{\Delta\rho_{v,a\text{-}fs}}{\Delta\rho_v}\right).$$

3.2.2.1 Scaling analysis of Stage II

As shown in Figure 3-8, for most values of porosity, the heat transport due to vapor diffusion can be neglected. Thus Equation (3.72) can be approximated by,

$$\frac{\partial\theta}{\partial\tau} = \mathrm{Le}_{2,f}\frac{\partial^2\theta}{\partial\eta^2} + \mathrm{U}\frac{\partial\theta}{\partial\eta}. \tag{3.78}$$

with boundary conditions,

$$\theta_{\eta=\eta_p} = 0,$$
$$\left.\frac{\partial\theta}{\partial\eta}\right|_{\eta=1} = \mathrm{Bi}_{2,fs}\left(\frac{T_a - T_{fs}}{\Delta T_{a\text{-}m}}\right). \tag{3.79}$$

3.2.2.2 Special case for constant heat flux input

Recall from Equation (3.19) that the velocity of the front is related to the heat input at the surface, latent heat of fusion and frost density. If the input heat, q''_s, is held constant, by definition the front velocity will be constant, with U=1.

3.2.2.3 Special case for no draining

For thin frost layers, surface tension effects prevent draining of the melt liquid from the surface. Assuming the melt water flux is negligible, the permeation mass flux can be approximated as,

$$m''_{w,p} = \frac{q''_s}{\lambda_{if}\rho_f}\left(\rho_p + \varepsilon\rho_w S_{y=0}\right). \tag{3.80}$$

3.2.3 Stage III

The non-dimensional parameters for the third stage are defined,

$$\theta_w = \frac{T_w - T_{w,0}}{T_a - T_{w,0}} = \frac{T_w - T_{w,0}}{\Delta T_{a\text{-}w,0}}, \qquad \eta_w = \frac{y}{\delta_{w,0}},$$
$$\tau = \frac{\alpha_w t}{{\delta_{w,0}}^2}, \qquad \alpha_w = \frac{k_w}{\left(\rho c_p\right)_w}. \tag{3.81}$$

Applying the non-dimensional parameters to the mass and energy Equations (3.33) and (3.37), one obtains,

$$\frac{\partial\eta_w}{\partial\tau} = \frac{\delta_{w,0}}{\alpha_w}\overline{u_w} + \frac{h_m\delta_{w,0}}{\alpha_w\rho_w}\Delta\rho_{v,a\text{-}w}, \tag{3.82}$$

$$\frac{\partial\theta}{\partial\tau} = \frac{\rho_w\Delta h_w\delta_{w,0}}{k_w\Delta T_{a\text{-}w,0}}\overline{u_w} + \frac{h\delta_{w,0}}{k_w}\theta + \frac{\lambda_{ig}h_m\delta_{w,0}}{k_w\Delta T_{a\text{-}w,0}}\Delta\rho_{v,a\text{-}w} + \frac{q''_s\delta_{w,0}}{k_w\,\Delta T_{a\text{-}w,0}}. \tag{3.83}$$

Thus the rate change of the thickness and temperature of the water film is a coupled set of equations. The equations are a function of the film velocity, temperature potential, water vapor density potential, and supplied heat flux. Using Equation (3.55), it is possible to expresses the vapor density by the water film temperature. The modified equations are,

$$\frac{\partial\eta_w}{\partial\tau} = \frac{\delta_{w,0}}{\alpha_w}\overline{u_w} + \frac{h_m\delta_{w,0}}{\alpha_w\rho_w}m\theta, \tag{3.84}$$

$$\frac{\partial\theta}{\partial\tau} = \frac{\rho_w\Delta h_w\delta_{w,0}}{k_w\Delta T_{a\text{-}w,0}}\overline{u_w} + \left[\frac{h\delta_{w,0}}{k_w} + \frac{\lambda_{fg}h_m\delta_{w,0}}{k_w\Delta T_{a\text{-}w,0}}m\right]\theta + \frac{q''_s\delta_{w,0}}{k_w\,\Delta T_{a\text{-}w,0}}, \tag{3.85}$$

where m is the local slope of the vapor density line seen in Figure 3-6.

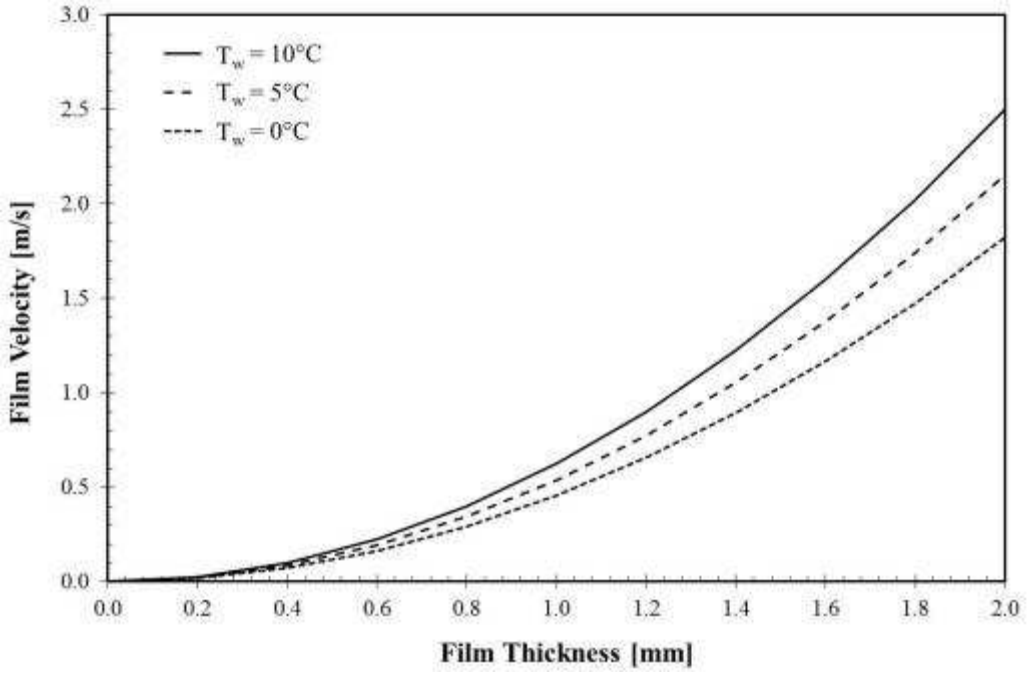

Figure 3-9. Water film velocity, Eq (3.32).

3.2.3.1 Special case for no film flow

From Equation (3.32), the film velocity will vary with the square of the film thickness. As seen in Figure (3-9), the film velocity quickly decays to a small value for thin films. Furthermore, surface tension effects, which were neglected in Equation (3.32), will further act to retard the flow of the film. For most practical cases, when the film thickness is small, the film velocity can be assumed to be negligible. Neglecting film velocity, and grouping the constant into dimensionless parameters, the governing equations become,

$$\frac{d\eta_w}{d\tau} + \frac{1}{Le_3}\theta = 0, \tag{3.86}$$

$$\frac{d\theta}{d\tau} - \left[Bi_{3,w} + \frac{1}{St_3}\frac{1}{Le_3}\right]\theta = Bi_{3,s}, \tag{3.87}$$

where the dimensionless groups are defined,

$$Le_3 = \frac{k_w \rho_w}{h_m \delta_{w,0} c_{p,w} m}, \tag{3.88}$$

$$St_3 = \frac{c_{p,w}\Delta T_{a\text{-}w,0}}{\lambda_{fg}}, \tag{3.89}$$

$$Bi_{3,w} = \frac{h\delta_{w,0}}{k_w}, \tag{3.90}$$

$$Bi_{3,s} = -\frac{q''_s \delta_{w,0}}{k_w \, \Delta T_{a\text{-}w,0}}. \tag{3.91}$$

From Equation (3.86), the change in film thickness is driven by the evaporation of the liquid from the surface, and is proportional to the temperature potential. The energy equations, Equation (3.87), is expressed by an ODE, and is a function of the sensible heat transfer from the surface, and the combined sensible and latent heat transfer at the air-water interface.

3.3 Summary

In this chapter, a fundamental defrost model has been described. The model has been developed by analysis of heat and mass transfer during each stage of the defrost process. The multistage model describes the sublimation and melting phenomena for the case of a heated vertical surface. A dimensional analysis reduces the governing equations to dimensionless form, resulting in a number of dimensionless parameters. The dimensionless parameters are the Lewis number, which relates the thermal to mass diffusion, the Stefan number, which is the ratio of the sensible to latent heat transfer, and the Biot number, which relates the external to internal thermal conductance. The dimensionless parameters for each stage are slightly different, owning to the difference in the dominate heat or mass transfer mechanism. By analyzing the magnitude of the dimensionless groups, it is possible to determine the relative weight of each term. From this scaling analysis it is proposed to neglect the effect of mass transport due to sublimation for the first and second stage of the defrost process. The effects of several limiting cases on the governing equations are evaluated, with simplified equations sets proposed for them. The method and solution for the multistage defrost model is discussed in Chapter 6.

4 Apparatus and Procedure

Within the current literature, there is a gap in knowledge of the effects of frost morphology on the defrost process at the surface level. The majority of the experimental defrost work has been conducted at the system level (Al-Mutawa et al., 1998a-e, Muehlbauer, 2006, Donallen, 2007). These works have characterized the performance cost of defrost on system operation.

One finding of system level defrost research is that defrost efficiency, which is supposed to be a function of the frost morphology, is related to growth conditions of the frost layer. To the knowledge of the author, there has been no experimental research on the effect of frost morphology on the defrost process. The experimental facility provides the first direct measurements of the heat and mass transfer during the melting of a porous frost layer.

The overall goals of the experimental program are:

- Design and build a dedicated test facility that controllably builds and melts the frost layer on reference surfaces.
- Capture high-resolution video at the microscopic level of frost formation.
- Capture high-resolution video at the microscopic level of the morphological changes in the frost layer during defrost.
- Correlate the effect of frost morphology on melt rate and efficiency.
- Measure heat and mass transfer rates during defrosting.
- Provide a data set to compare against existing formation models.

The results of the experiment are meant to validate the model proposed in Chapter 3, specifically, the evaluation of the distinct stages of the defrost process. Additionally, the test facility provides a test bed where alternate surface geometries or finishes can be evaluated.

4.1 Facility description

Figure 4-1 is a schematic of the facility design. The main elements of the facility are the test chamber, test surface, humidity generator, hygrometer, chiller, digital video camera with zoom microscopes, data acquisition system, and a computer. The facility is

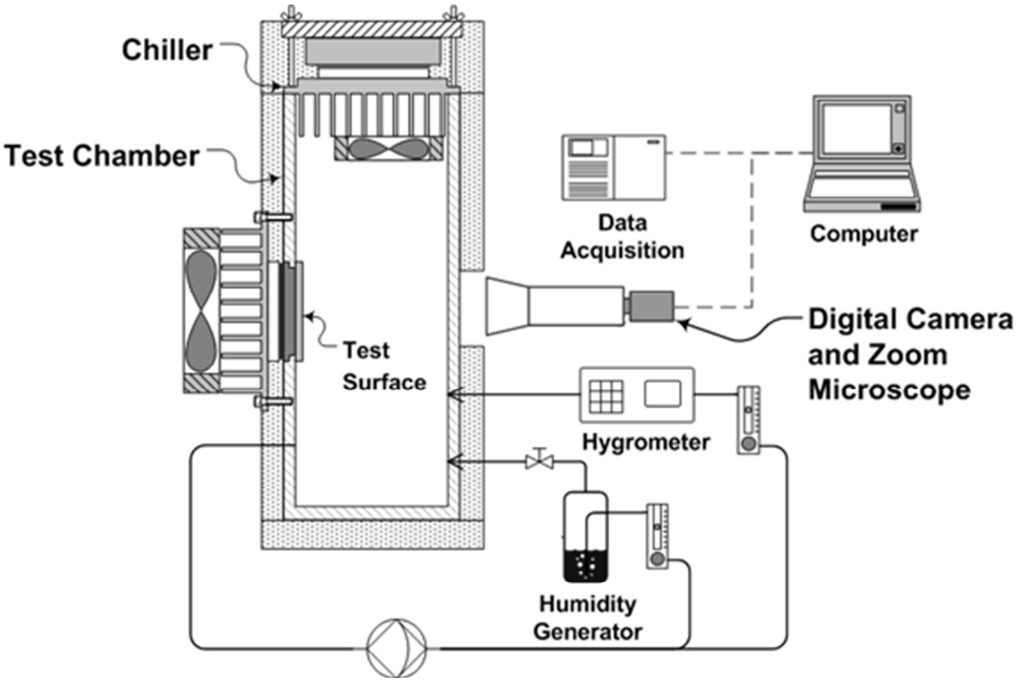

Figure 4-1. Frost-defrost test facility schematic.

capable of controlling chamber temperatures in the range of 10 to –15°C, chamber dew points in the range of 0 to -20°C, and test surfaces' temperatures down to –20°C. Figure 4-2 shows the actual test facility.

Figure 4-2. Frost-defrost test facility.

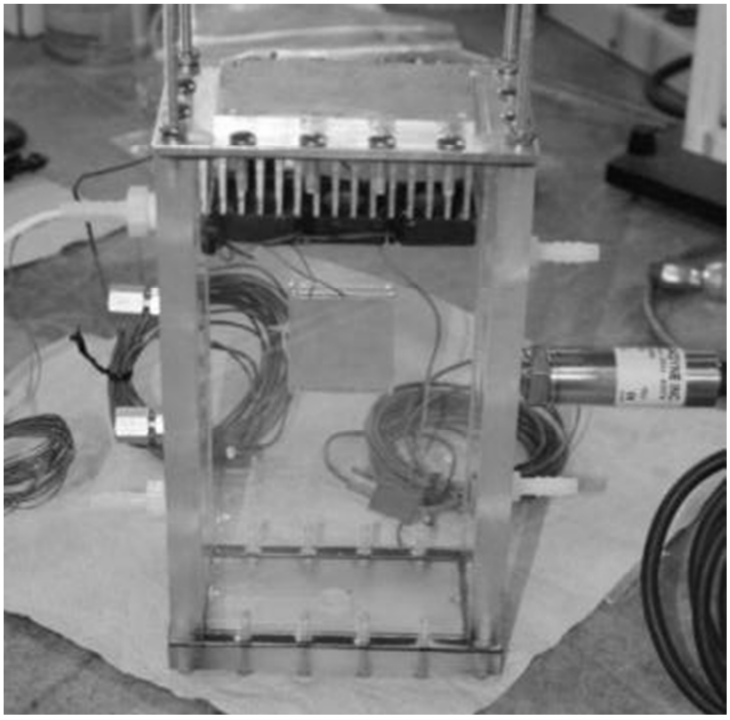

Figure 4-3. Test chamber with chiller.

4.2 Test chamber

The test chamber is a well-insulated enclosure that houses the chilled surface. The chamber is constructed of clear 12 mm polycarbonate. This material was chosen for its excellent visibility, reasonable thermal insulation properties, and excellent machining properties. The chamber isolates the test surface from the ambient space and prevents air and moisture exchange. To further limit the heat gain from the ambient to the chamber, a shell of 25 mm polyisocyanurate foam insulation is included.

The approximate interior dimensions of the chamber are 20 cm high x 10 cm wide x 5 cm deep. The gross interior volume of the chamber is 1050 cm^3. Neglecting the space occupied by the chiller, the net interior volume is 980 cm^3. Complete piece part drawings of the test chamber, and details of the assembly process are in Appendix E. All access points into the chamber are sealed to limit the ingression of air and moisture from the ambient space. Upon completion of the test chamber, an air leak test was conducted. It was evacuated using a vacuum pump down to 500 mbar. With the pump access sealed, it takes nearly 10 min for the pressure in the chamber to rise to atmospheric pressure.

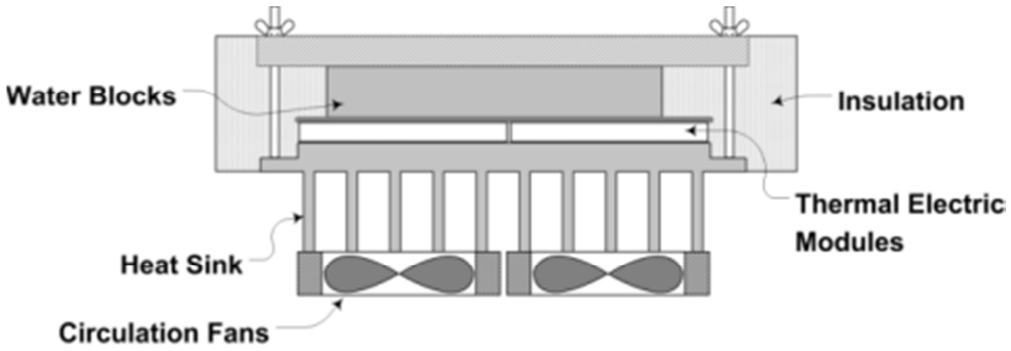

Figure 4-4. Chiller assembly.

4.2.1 Chiller

The function of the chiller is to remove the sensible heat from the test chamber. The chiller also forms the top of the test chamber (Figure 4-3). Two thermoelectric modules (Figures 4-4) are used to extract heat from the heat sink. The extracted heat is removed by a water block using the laboratory water supply, as the cooling fluid. Three 30 mm circulation fans are used to move air across the heat sink to enhance performance and circulate the air in the chamber to promote mixing. The fans are estimated to provide 20 air exchanges/min in the chamber with a mean velocity of 0.9 m/s. The sides of the chiller are well insulated to prevent heat exchange to the ambient air. The temperature of the chiller is measured by several thermocouples mounted within the heat sink. The temperature is controlled by adjusting the supply voltage to the TE modules from a digital power supply (BK Precision Power Supply, Model No. 1696). During the frost build stage of the experiment, the temperature of the cold plates is maintained above the dew point of the air to avoid condensation and/or frost formation.

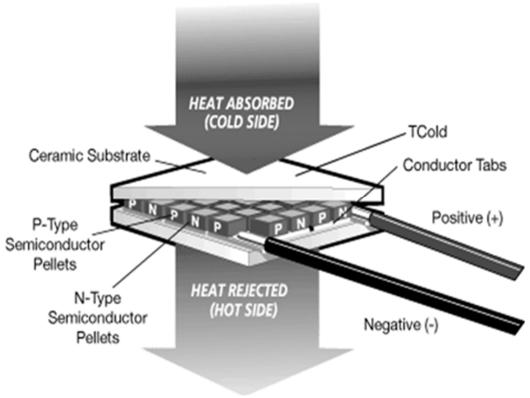

Figure 4-5. Thermoelectric module (Tellurex Corporation).

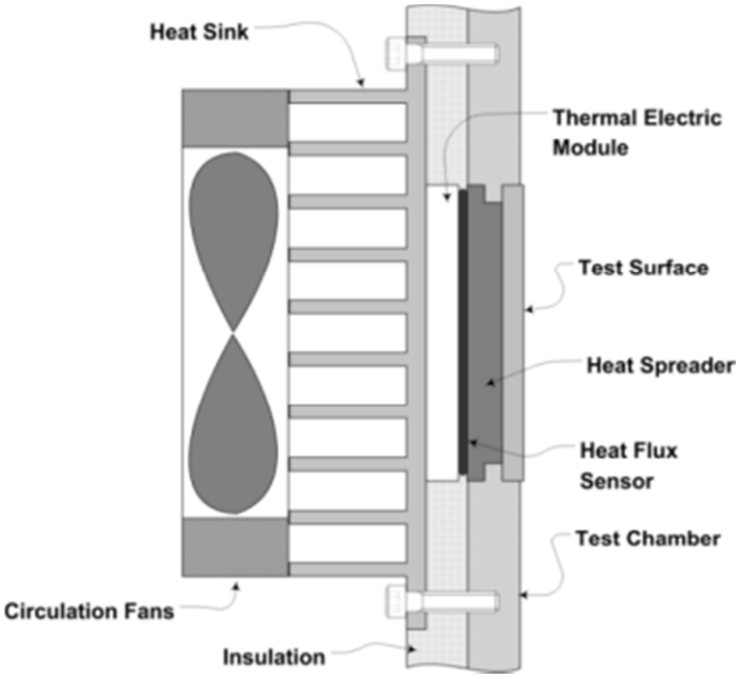

Figure 4-6. Test surface assembly.

4.2.1.1 Thermoelectric (TE) module

The thermoelectric (TE) module is a Peltier device (Tellurex Corporation, Model C1-1.4-127-1.14, Traverse City, MI, http://www.tellurex.com). The function of the TE module is to extract heat from a surface. By adjusting the voltage, the surface temperature is precisely controlled, which affects the rate and properties of the frost layer. In addition, by reversing the voltage potential, the base plate is controllably heated and used to melt the frost layer. Heat flow through the TE module is inferred from the known heat pumping capacity of the module (Figure 4-5).

4.2.2 Test surface assembly

The primary function of the test surface assembly (Figure 4-6) is to provide for the controlled growth and melting of a frost layer. The design of the assembly allows for interchangeable test surfaces to be attached to the base plate. Heat is extracted from the test surface via a TE module and is rejected through a finned heat sink. Thin wired thermocouples embedded in the test surface measure the temperature near the frosting surface. A heat flux sensor measures the heat flow into, or out of, the assembly. Temperatures and heat flux sensor are continuously monitored, and feedback signals provide control of the test surface temperature.

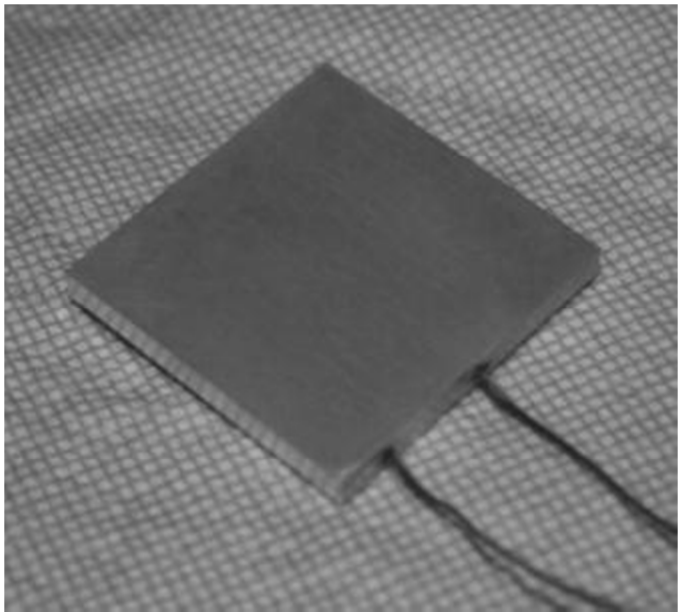

Figure 4-7. Test surface.

4.2.2.1 Test surface

The test chamber is designed such that the test surfaces are interchangeable. The test surface evaluated in this experimental program is a flat aluminum surface (Figure 4-7). The test surface is made from 3.88 mm (0.153 in.) thick aluminum sheet stock. The alloy used is aluminum 5052, temper H32. The ANSI properties for the alloy are shown in Table 4-1. The nominal size of surface is 38 mm x 38 mm and the measured mass of the surface is 15.29 gm. The thermal capacitance of the test surface is calculated to be 14.72 J/K. Two 30 GA Type-T special-limit thermocouples are embedded in the surface. One thermocouple in located in the center of the plate and the other is located in one corner, 6mm from each edge. The thermocouples are installed in 0.8 mm holes with conductive epoxy. The test surface was lapped using 600 grit wet-dry paper.

Table 4-1. Density, thermal conductivity, and specific heat of test surface material.

Property	**Aluminum 5052-H32**	**Copper D110**
Density (kg/m^3)	2680	8933
Thermal Conductivity (W/m-K)	138	388
Thermal Specific Heat (J/kg-K)	936	385

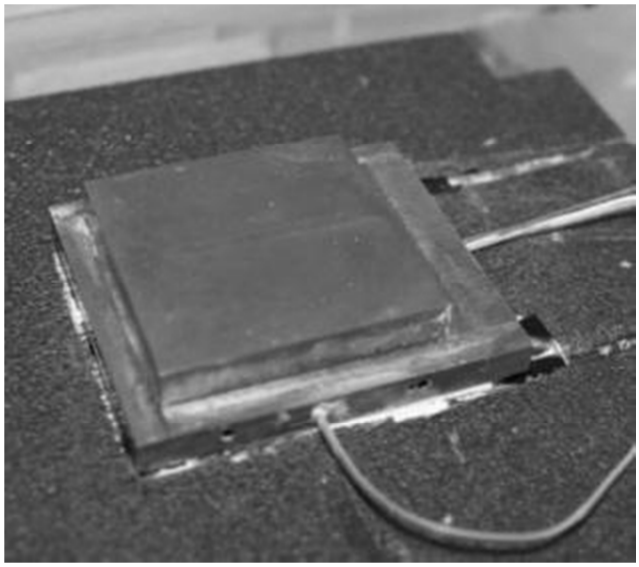

Figure 4-8. Test surface assembly.

4.2.2.2 Heat spreader

The function of the heat spreader is to conduct the heat from the thermoelectric module to the test surface. The heat spreader is made from 99.9% copper (D110 alloy). The nominal size of the spreader is 45 mm x 40 mm and 9.5 mm thick. The measured mass of the spreader is 117.5 grams. The ANSI properties for the alloy are shown in Table 4-1. The calculated thermal capacitance of the test surface is 45.26 J/K. A single 30 GA Type-T special limit thermocouple is embedded near the center of the spreader. During the assembly process, all heat conducting surfaces were coated with thermal conductive grease to minimize contact resistances.

4.2.2.3 Heat sink

The function of the heat sink is to reject heat from the test surface. The heat sink is sized to reject both the heat of the test surface plus the supplied power to the TE module. Analysis of the test carriage found that an active heat sink (i.e., forced convection) was required for the design. The heat sink is a pin fin style with fins of 2 mm x 2 mm x 40 mm (Alpha Novatech Inc. Model FS10040PU, Santa Clara, CA). The overall dimension of the base is 100 mm x 100 mm and includes an integral cooling fan. The resistance of the heat sink is 0.15 C/W. Closed cell foam insulation (6mm thick) is mounted to the underside of the heat sink to limit heat ingression into the test chamber. Figure 4-9 shows the heat sink with the insulation and heat spreader installed.

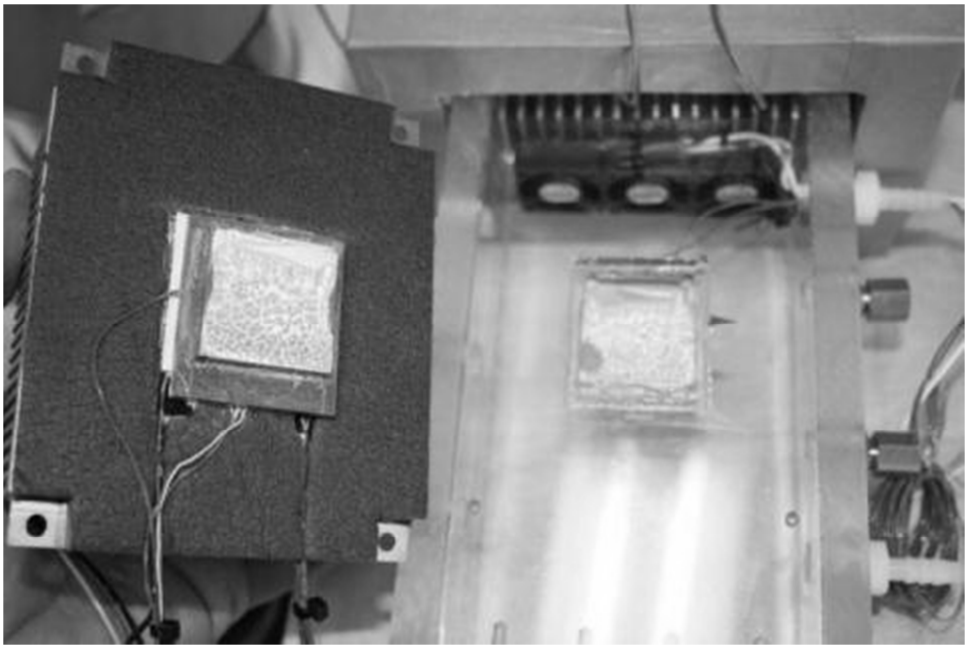

Figure 4-9. Heat sink with heat spreader assembly.

4.3 Humidity generator

The humidity generator is based upon the NIST frost-point generator (Scace, Huang, Hodges, Olson, and Whetstone, 1997). It comprises a pump, control valves, saturator, and interconnecting tubing. Air is drawn from the test chamber into the humidifier by an oil-less diaphragm air pump. The flow stream is split into two paths. One stream is directed to the saturator where moisture is absorbed by the air stream. The other air stream bypasses the saturator and is directed to the hygrometer to measure the dew point temperature. The flow to saturator and hygrometer are controlled by a variable flow rotameter. Both air streams are returned to the test chamber. By controlling the amount of bypass airflow and the temperature of the saturator, a precise level of moisture can be returned to the test chamber. The total volumetric flow through the humidifier is measured by an inline flow meter.

The function of the saturator is to add moisture to the airstream. The saturator comprises of a 500 ml taper flask partially filled with distilled water. Air is pumped into the saturator through a stainless steel tube below the water level and is returned by a side

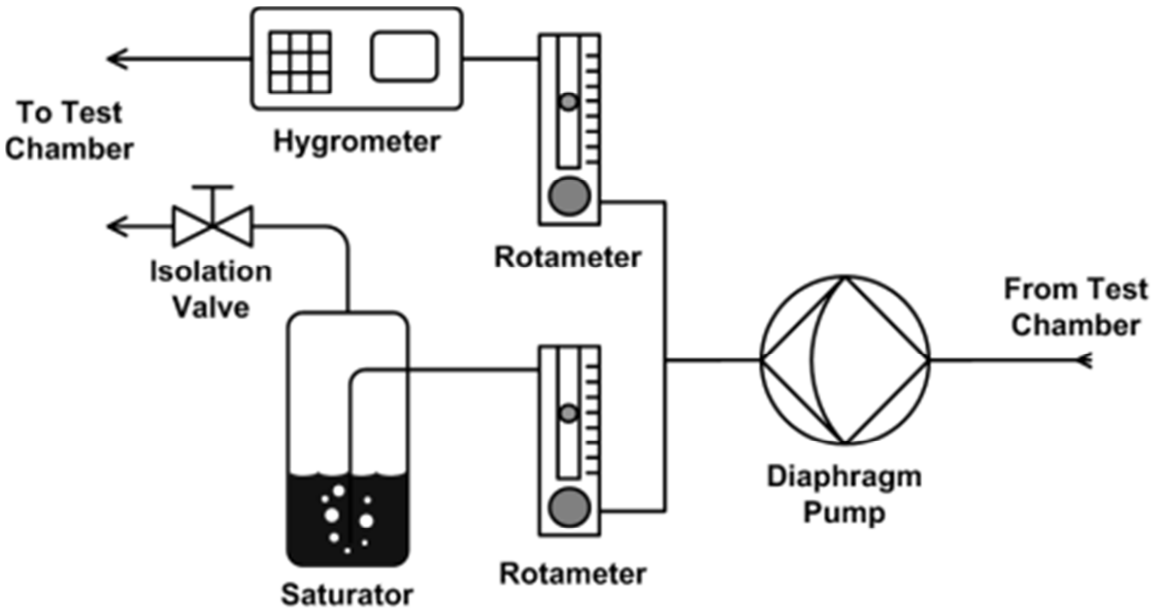

Figure 4-10. Humidity generator.

port on the flask. The outlet moisture content of the saturator, as measured by the hygrometer, is controlled by adjusting the flow through the saturator. The mass of saturator with the charge of distilled water is measured at the start of an experimental run and again at the end of the run. The difference between mass is the amount of water added to the test chamber.

At the conclusion of the test, the saturator is isolated from the test chamber by closing an isolation valve. In place of the saturator, a second flask containing silica gel desiccant is added. The chamber air is pumped through the desiccant and the moisture in the chamber is absorbed by the desiccant. By weighing the mass gain of water in the desiccant, and a second independent measurement of the total water mass added to the chamber during the run is captured. Additionally, the desiccant prepares the chamber for the run by removing any residual moisture, thus removing a source of uncertainty.

4.4 Measurements

Numerous measurements are made during the frosting and defrosting portions of the test. These measurements allow for feedback of the control during the test, and they provide a record of the test that is used for further analysis to determine the heat and mass transfer during the frost and defrost process.

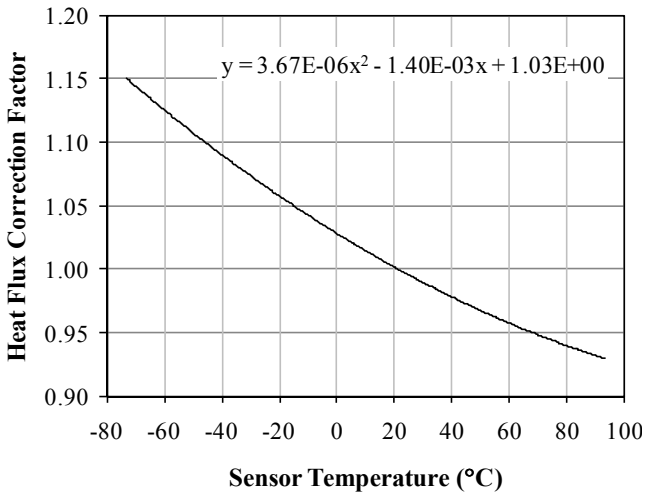

Figure 4-11. Heat flux sensor temperature compensation factor (Omega Engineering).

4.4.1 Temperature

Surface and air temperatures are measured by special-limit type-T thermocouples. Type T thermocouples have a measurement range of -250 to 350°C with a measurement accuracy of ±0.5°C, and are ice-point calibrated. Embedded thermocouples are installed with a high conductivity epoxy to minimize contact resistance. Air thermocouples are shielded to prevent radiation effects. The thermocouples are measured by the data acquisition hardware. The output of the thermocouples is continuously measured by the data acquisition system (DAS).

4.4.2 Pressure

The pressure of the test chamber is measured via an absolute pressure transducer that is mounted directly to the test chamber. The transducer is an Omega Engineering Model PX409-030AI, with a measurement range of 0 to 210 kPa and an accuracy of ±0.05% full scale. A certificate of calibration is provided by the manufacturer. The 4 to 20 mA output of the run is digitally recorded.

4.4.3 Heat flux

The primary method to measure the heat transfer from the test surface is a thin-film heat flux sensor (Omega Engineering, Model HFS-4), placed in series between the TE module and the heat spreader. The Schmidt-type heat flux sensor is a 50-junction thermopile arranged across a polyimide film barrier. The sensor produces a small voltage

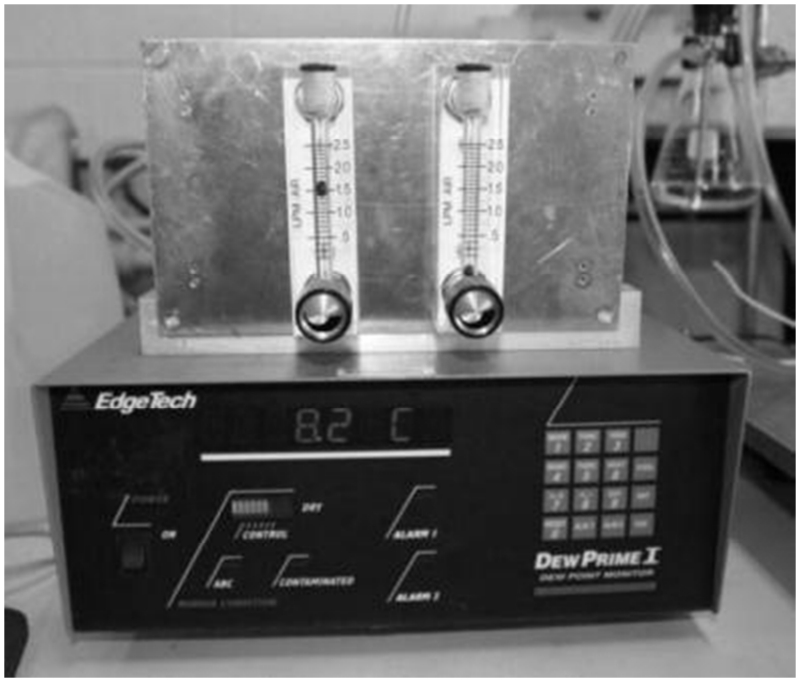

Figure 4-12. Hygrometer with rotameters.

signal that is proportional to the heat flux. The maximum measured heat flux of the sensor is ±30,000 W/m^2 and has a measurement sensitivity of 1.83 μV/W/m^2. A Type-K thermocouple is incorporated into the sensor for measurement of the sensor's temperature, which is used for temperature compensation of the sensor (Figure 4-11). The accuracy of the sensor is ±0.5%. A certificate of calibration is provided by the manufacture. The heat flux output and temperature is continuously monitored by the DAS system.

4.4.4 Chilled mirror hygrometer

A chilled mirror hygrometer is used to measure the dew point of the air within the test chamber for the required accuracy of the humidity measurement. See Appendix D for a further discussion of humidity measurement methods and devices. The hygrometer used for these experiments is an EdgeTech DewPrime I with an S2 sensor (calibration in October 2010). The measurement range of the device is -50°C to 90°C with a measurement accuracy of ±0.2°C and a repeatability of ±0.05°C Air is supplied to the sensor from the chamber through the same diaphragm air-pump as used for the saturator. A rotameter is used to control the flow to the chilled mirror at the manufacturer

specification of 1 to 2 L/min. The air stream after the sensor is returned to the chamber. The 0 to 5 V DC analog output is proportional to the dew point measurement, and is continuously measured.

4.4.5 Rotameters

The flow through the saturator and hygrometer are measured and controlled by inline variable flow rotameters (Omega Engineering, Model RMA-26). The rotameters are a tapered tube containing a steel ball that acts as a float. The position of the ball is proportional to the flow rate with the reading made from the graduated scale on the meter. The accuracy of the flow meter is ±5% full scale, with a measurement range of 0.5 to 5 l/min. A correction factor, as specified by the manufacture, is used to adjust the flow rate for fluid temperature. Integrated valves allow the flow to be adjusted through the meter, allowing for precise control of the flow to the hygrometer and saturator. The reading from the flow meters is manually recorded during the test.

4.4.6 Digital scale

A digital scale (Acculab NA, Model ALC-320.3, Edgewood, NY) is used to measure the mass of the water change, melt of the frost during the defrost process, and residual charge in the saturator. The range of the scale is 320 g with a measurement resolution of 1 mg. The scale is calibrated by a two-point method using a certified 200 g mass (Class U).

4.4.7 Current and voltage

For reference, the current and voltage to the thermoelectric modules used for both the test surface and chiller are measured. The current measurement is made using a 25-amp shunt (Deltec Company). The shunt produces a millivolt signal which is proportional to the current. The accuracy of the shunt is ±0.25%.

4.4.8 Data acquisition hardware

Output of the thermocouples, pressure transducer, heat flux sensor, power supply voltage and current, and the humidity transmitter are measured by an Agilent 34970A Data Acquisition/Switch Unit through a 34901A Multiplexer. This multiplexer accommodates 20 channels and with a scan rate of 60/s. Agilent BenchLink

Table 4-2. Summary of instrument accuracy and range.

Measurement	Instrument	Accuracy	Range
Dew point	EdgeTech DewPrime	±0.2°C	-50 to 90°C
Flow	Omega FL2012	±5%	0.5 to 5.0 LPM
Temperature	Special Limit Type T	±0.5°C	-250 to 350°C
Heat Flux	Omega HFS-4	±0.5%	±30 kW/m^2
Pressure	Omega PX409-03AI	±0.05%	0 to 210 kPa
Mass	Acculab ALC320.3	±3 mg	0 to 320 g
Voltage	Agilent 34970A	± 0.03%	0 to 10 Vdc
Current	Deltec 25-Amp Shunt	±.25%	±25 Amps

software is used to collect and display results. The results are exported as comma space delimited files for further analysis.

4.4.9 Summary of instrumentation accuracy and resolution

Table 4-2 summarizes the accuracy and range of all of the instruments used for the testing phase of this study. Instruments were selected with high accuracy for any measurements that are subsequently used to calculate the heat and mass transfer of the frost and defrost process.

4.5 Data reduction

The following sections summarize the data reduction of the measurements to determine the heat and mass transfer coefficients for steady-state and transient conditions.

4.5.1 Chamber heat balance

The heat balance on the test chamber is,

$$Q_{ts} + Q_{ch} + Q_{cp} + Q_{hu} = 0, \tag{4.1}$$

where Q_{ts} is the heat extracted by the test surface, Q_{ch} is the heat leakage into the test chamber, Q_{cp} is the heat extracted by the chiller, and Q_{hu} is the heat added by the humidifier. The heat extracted by the test surface is directly measured by the heat flux sensor. The heat leakage from the chamber is determined by multiplying the chambers overall heat transfer coefficient, UA_{ch}, by the temperature difference between the interior and exterior of the chamber. The overall heat transfer coefficient is determined by a calibration test and is calculated by,

$$UA_{ch} = \frac{Q_{ch,c}}{(T_\infty - T_{ch})}, \tag{4.2}$$

where $Q_{ch,c}$ is the sensible heat added to the chamber during calibration, T_∞ and T_{ch} are the average exterior and interior air temperatures. Heat extracted by the chilled plates is estimated by the input power into the thermoelectric and heat pumping efficiency, η_{TE}.

$$Q_{cp} = P \cdot \eta_{TE}. \tag{4.3}$$

Heat addition by the humidifier is calculated by the change in air enthalpy across the device,

$$Q_{hu} = \dot{V}_a \rho_a (h_{a,o} - h_{a,i}), \tag{4.4}$$

where $\dot{V}_a$ is the volumetric flow rate, ρ_a is the average density, and $h_{a,o}$ and $h_{a,i}$ are the outlet and inlet moist air enthalpies, respectively. The properties of moist air are calculated using the equations discussed in Appendix D.

4.5.2 Water mass balance

The global mass balance of water in the test chamber can be expressed as,

$$m_{l,hu} = m_{f,ts} + m_{v,ch}, \tag{4.5}$$

where $m_{l,hu}$ is the total mass of water vapor introduced by the humidifier during the test, $m_{f,ts}$ is the mass of the frost adhered to the test surface, and $m_{v,ch}$ is the mass of the water vapor in the air of the chamber. The mass of the frost is estimated by,

$$m_{f,ts} = \rho_i V_{f,i} = \rho_i V_{f,t}(1 - \varepsilon), \tag{4.6}$$

where ρ_i is the density of ice, $V_{f,i}$ is the volume of the ice in the frost layer that is related to the total volume of frost, $V_{f,t}$ and by the frost porosity, ε. The total volume of the frost layer is determined by the product of the test surface area, A_{ts} and the frost average thickness, δ,

$$V_{f,t} = A_{ts}\delta. \tag{4.7}$$

The mass of the water vapor in the chamber is determined by the ideal gas law,

$$m_{v,ch} = \frac{p_v V_{ch}}{R_w T_{ch}} \tag{4.8}$$

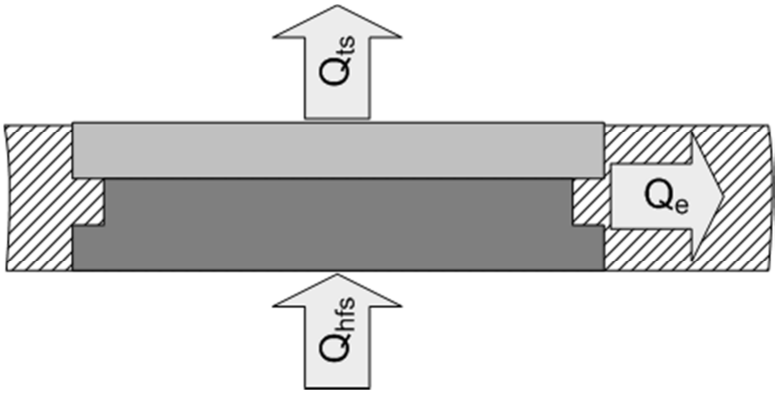

Figure 4-13. Heat flow in the test apparatus.

where p_v is the vapor pressure of water in the chamber, V_{ch} is the volume of the chamber, T_{ch} is the chamber temperature in Kelvin, and R_w is the gas constant for water vapor (461.5 J kg^{-1} K^{-1}). The mass transfer rate can be estimated as the change in the water vapor mass over the duration of the test,

$$\dot{m}_{v,ch} = \frac{\Delta m_{v,ch}}{\Delta t} \tag{4.9}$$

4.5.3 Test Surface Energy Balance

The defrost process is an inherently transient event. It is necessary to determine the net heat flow at the test surface to complete the analysis. The heat flow at the test surface, Q_{ts}, is a function of the heat flow into the heat spreader, Q_{hfs}, the heat flow at the edges, Q_e, and the internal energy changes of the test surface and heat spreader. A lumped analysis approach is developed to simplify the governing equations. For a lumped analysis, temperature variations within the body are neglected, and Bi < 0.1, where,

$$Bi = \frac{hL_c}{k}. \tag{4.10}$$

The heat spreader and test surface have small characteristic length (2.6 mm and 1.6 mm respectively) and high thermal conductivities (388 and 138 W/mK respectively). As long as the heat transfer coefficient is below 8000 W/m^2K, a lumped analysis will be valid. Figure 4-14 is the equivalent resistance-capacitance circuit for the heat spreader and test surface.

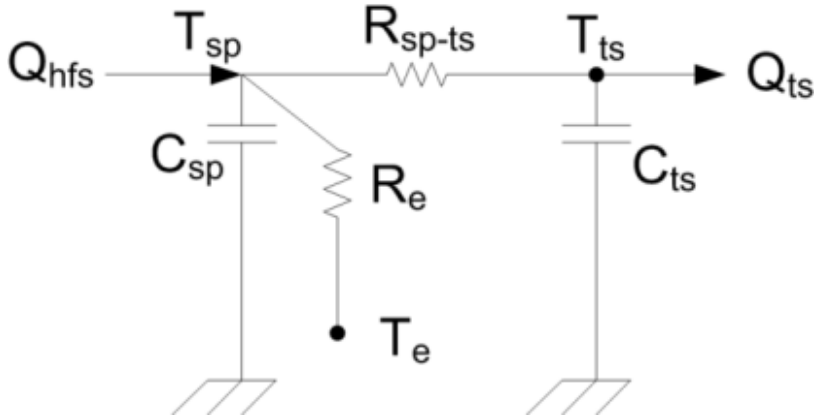

Figure 4-14. Lumped capacitance model of test surface.

The transient energy balance at node T_{sp} is,

$$\frac{dT_{sp}}{dt} = \frac{1}{C_{sp}}\left[\frac{1}{R_{sp,ts}}\left(T_{ts} - T_{sp}\right) + \frac{1}{R_e}\left(T_e - T_{sp}\right) + Q_{hfs}\right]. \tag{4.11}$$

The thermal capacitance of the heat spreader C_{sp} is defined as,

$$C_{sp} = m_{sp}c_{p,sp}, \tag{4.12}$$

where m_{sp} is the mass of the spreader and $c_{p,sp}$ is the specific heat of the spreader and is calculated to be 45.26 J/K. The thermal resistance, $R_{sp,ts}$, is defined as the contact resistance between the heat spreader and test surface. The edge thermal resistance, Re, is the resistance between the heat spreader and the chamber walls. The mean wall temperature, T_e, is assumed to be the average of the inner and outer chamber temperatures. The thermal resistances, $R_{sp,ts}$ and R_e are determined through steady-state test. Similarly, the energy balance at node T_{ts} is,

$$\frac{dT_{ts}}{dt} = \frac{1}{C_{ts}}\left[\frac{1}{R_{sp,ts}}\left(T_{sp} - T_{ts}\right) + Q_{ts}\right], \tag{4.13}$$

where C_{ts} is the thermal capacitance of the test surface and is calculated to be 14.72 J/K. The heat transfer coefficient at the surface is defined as,

$$h_{ts} = \frac{Q_{ts}}{A_{ts}(T_{ch} - T_{ts})}. \tag{4.14}$$

4.5.4 Defrost efficiency

Recall from section 1.1.3, defrost efficiency is defined as the ratio of the minimum energy required to melt the frost layer to the total energy supplied to melt the frost,

$$\eta_d^* = \frac{E_f}{E_d}. \tag{4.15}$$

The minimum energy to melt the frost, E_f, is the sum of the latent and sensible heat of the frost layer. The defrost energy, E_d, is the time integrated heat flow during the defrost process. In practice the supplied energy is approximated by the numerical integration of the measured heat flux, q''_{ts}, over the recording interval, Δt,

$$E_d = \sum A_{ts} q''_{ts} \Delta t. \tag{4.16}$$

The defrost efficiency during the defrost test can be calculated by,

$$\eta_d^* = \frac{m_f(\lambda_{if} + c_{p,i}\Delta T)}{\sum A_{ts} q''_{ts} \Delta t}. \tag{4.17}$$

4.6 Digital video camera and zoom microscope

Two digital cameras with zoom microscopes are used to capture frontal and side pictures and movies of the frost growth and defrost processes. The cameras are positioned outside of the test chamber and access ports through the insulation allow for viewing of the test surface. The test surface is illuminated with by a fiber optic light ring and light source from an Edmund Optics MI-150 High-intensity Illuminator. The light source has a 150W EKE Quartz Halogen lamp with a variable light control that ranges the intensity from 0 to 100%. The light ring is attached to the frontal camera lens, and provides the necessary illumination for the side camera as well.

4.6.1 Front profile lens and camera

Frontal images are captured by a 5.1 megapixel CMOS color camera (BigCatch™ DCM510C) pared with a zoom imaging lens (Edmund Optics VZM 450i) (Figure 4-15). The lens has a maximum magnification of 4.5X. The camera and lens are capable of

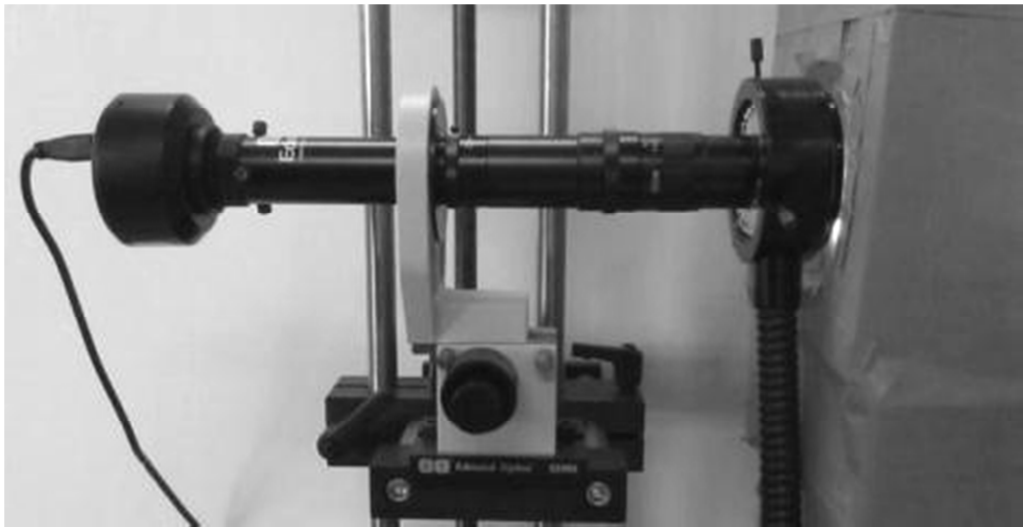

Figure 4-15. Front profile camera and lens with light ring.

resolving frost structures down to 1 μm at the maximum magnification and resolution. Table 4-3 summarizes the image resolution in pixels/mm and μm for various camera resolutions and lens magnifications. The camera is connected to the computer via a USB port, and the camera is controlled and images are recorded by the supplied viewer software.

4.6.2 Side profile lens and camera

The side profile of the frost build and defrost process is captured by a second USB camera (Edmund Optics model EO-1312M) with a zoom imaging lens (Navitar Zoom 7000) (Figure 4-16). The camera has a 0.5 inch CCD monochrome sensor, which

Table 4-3. Image resolution (pixel/mm and μm) for frontal camera and lens.

Magnification	**Camera Resolution (pixels)**							
	2592 × 1944		1280 × 960		1024 × 768		640 × 480	
1x	406	4.92	201	9.97	201	9.97	100	19.94
2x	765	2.61	378	5.29	378	5.29	189	10.59
3x	1308	1.53	646	3.10	646	3.10	323	6.19
4x	1753	1.14	866	2.31	866	2.31	433	4.62
4.5x	2112	0.95	1043	1.92	1043	1.92	521	3.84

Figure 4-16. Side profile camera and lens.

is capable of capturing images at a resolution of 1280 × 1024 at frame rates of 25 s^{-1}. The camera is capable of capturing higher frame rates (up to 50 s^{-1}) with reduced resolution. The zoom imaging lens has a maximum magnification of 6.0X and minimum field of view of 6.4 mm. The maximum image resolution for this camera and lens is 133 pixels/mm which allows for resolving frost structures down to 15 μm.

4.6.3 Resolution verification

The resolution of both camera and lens sets were verified using a calibrated test target. The test target is based upon the 1951 USAF resolution test chart and conforms to MIL-STD-150A. Figure 4-17 is an enlarged photo of the test target. Figure 4-18 shows the calibration photos taken for the front camera and lens at the minimum and maximum resolution of the inner most test pattern (Group 2 and 3).

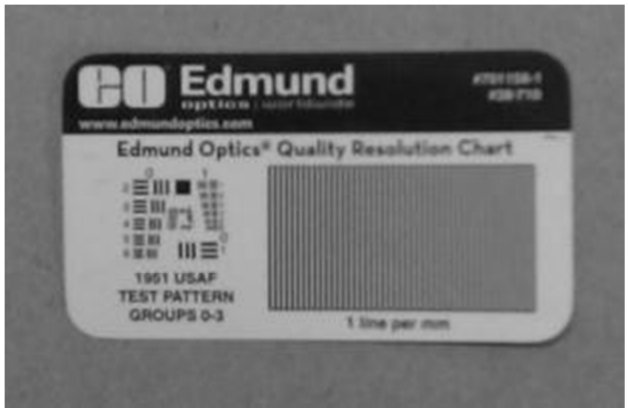

Figure 4-17. Calibration test target.

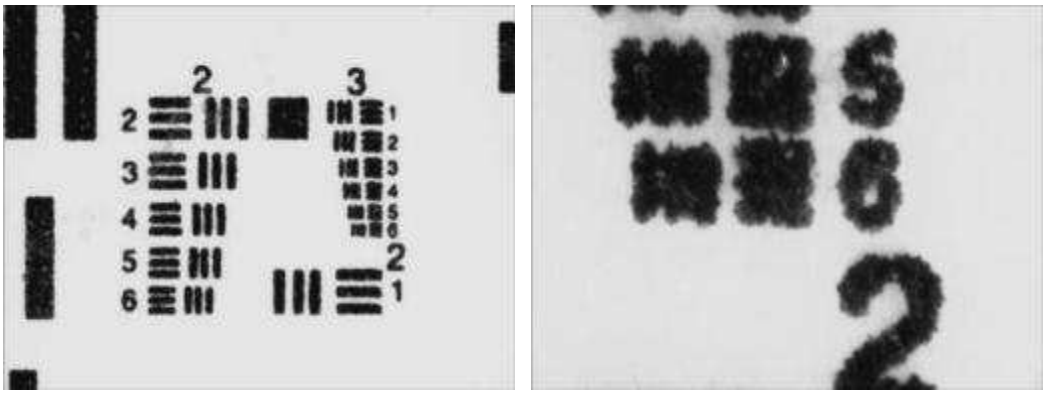

Figure 4-18. 1X and 4X magnification of USAF test pattern.

4.6.3.1 Imaging software

Several software packages are used to post-process the images for visual inspection and detailed measurements. Image enhancement typically required increasing the contrast between the ice crystals and open voids. For some analysis, such as droplet size measurements, it is necessary to cancel out the background image to allow for a clearer view of the boundaries. Table 4-4 summarizes the software used for the visual analysis.

4.6.4 Visual analysis techniques

From the post analysis of the images, it is possible to determine a number of physical characteristics of the frosting and defrosting process. These characteristics are sometimes used for indirect calculations. For example, the porosity of the frost is needed to calculate the mass of the ice at the beginning of the defrost process. The melt rate can

Table 4-4. Image enhancement and analysis software.

Software	Purpose
Adobe Photoshop Elements 8	General enhancement and editing of photos.
Mean Avidemux	Editing of videos length, capturing individual frames.
ScopeTek ScopePhoto	Scaled measurement of frost structure.
Mathworks MATLAB with Image Processing Toolbox	Detailed enhancement of images and automated measurement of frost thickness, porosity, and droplet size

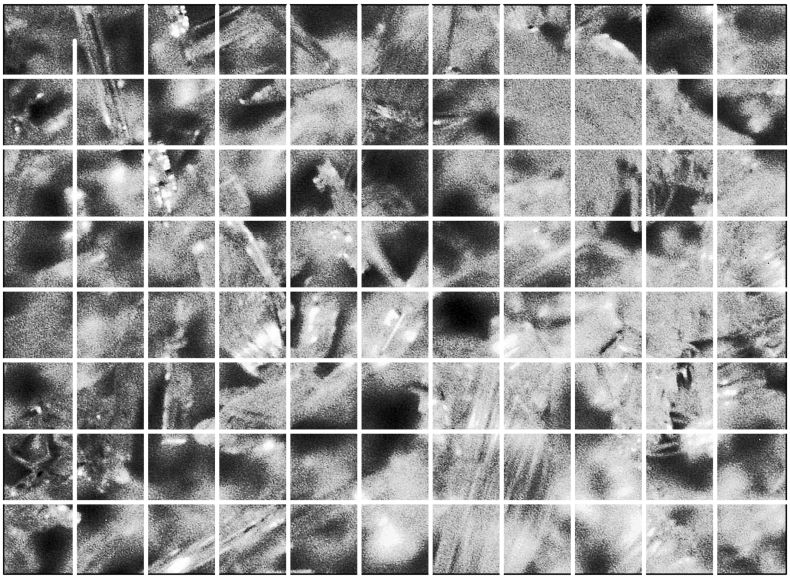

Figure 4-19. Enhanced frost image parallel to test surface.

be determined from the change in the frost front location. The mass transfer of the water vapor during the dry-out stage can be seen as a reduction in the volume of the droplets. The following section describes the formulation and calculations for the visual analysis techniques. Further discussion of the visual analysis technique is presented in Janssen, Mohs and Kulacki (2012b).

4.6.5 Frost porosity

The porosity (also called the void fraction), ε, of the frost layer is defined as the ratio of the volume occupied by ice to the total volume,

$$\varepsilon = 1 - \frac{V_i}{V_t} \tag{4.18}$$

Assuming the ice crystals are evenly dispersed in the frost layer, the porosity can be determined along any two-dimensional plane within the frost,

$$\varepsilon = 1 - \frac{V_i}{V_t} = 1 - \left(\frac{A_i}{A_t}\right)\left(\frac{L_i}{\delta}\right) \approx 1 - \frac{A_i}{A_t}, \tag{4.19}$$

where A_i is the area occupied by the ice crystals and A_t is the total area. Assuming the length scale of the ice crystal, L_i, is approximately the same as the thickness of the frost, δ, the relationship can be approximated by the ratio of the occupied area to the total area.

The porosity can be estimated through a visual technique. As seen in Figure 4-19, the in-plane ice crystals can be enhanced against the in-plane voids. By gridding the enhanced photo and counting the occupied squares, N_i, then dividing by the total number of squares, N_t, the porosity can be estimated as,

$$\varepsilon \approx 1 - \frac{N_i}{N_t}. \tag{4.20}$$

To automate and improve the accuracy of the calculation, the digital photo can be evaluated at the pixel level. The image is converted to a binary black and white image, and a simple MATLAB subroutine is used to calculate the porosity by counting the number of pixels that are white (pixel value of 1) and dividing by the total number of pixels. A copy of the MATLAB code can be found in Appendix F.

The method is calibrated through a process where the accumulated mass of the ice is measured directly. By measuring the total volume of the frost layer, it is possible to calculate the porosity from equations in section 4.3.2. The MATLAB™ program uses the "graythresh" toolkit to automatically select the grayscale intensity. Any pixel intensity with a value greater than this level is converted to white, and below is converted to black (considered to be a void).

4.6.6 Frost thickness

From the side profile images, it is possible to capture the time rate of change of the frost thickness during the formation and melting processes. The image is converted into a black and white image. The MATLAB function "bwboundaries" is used to capture the pixel location of the frost-air front by using the ratio of pixels to spatial dimension for the photo. A detailed description of the technique can be found in Janssen (2011). A copy of the MATLAB code can be found in Appendix F.

4.6.7 Droplet area and volume

To determine the water vapor mass transfer during the final stage of the defrost process it is necessary to determine the size, shape, and distribution of the water droplets that are left on the surface at the end of the melt process (Figure 4-20). The mass flux of water vapor leaving the droplets surface can be expressed as,

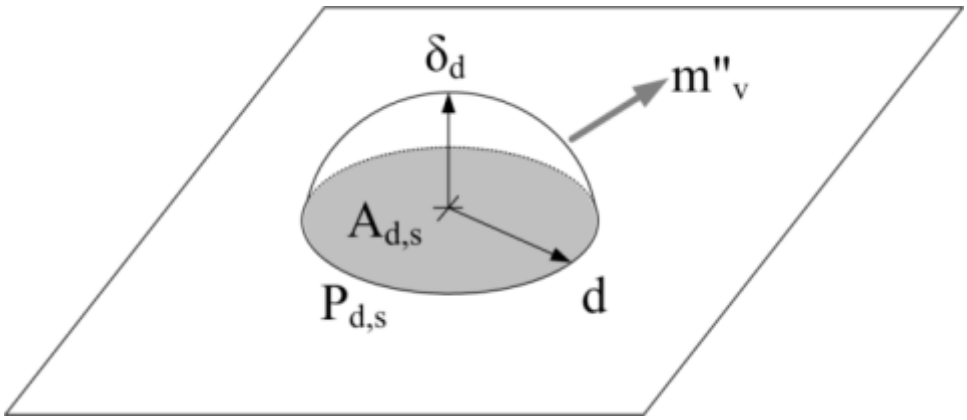

Figure 4-20. Idealized water droplet on surface.

$$m''_v = \frac{\partial}{\partial t}\left(\frac{m_d}{A_d}\right). \tag{4.21}$$

where m_d is the mass of a droplet, and A_d is the surface area of the droplet. Assuming the water density varies minimally over time, it can be moved outside of the derivate,

$$m''_v = \rho_w \frac{\partial}{\partial t}\left(\frac{V_d}{A_d}\right). \tag{4.22}$$

Assuming the droplets can be modeled as a spherical dome, the surface area and volume are,

$$A_d = 2\pi r_c \delta_d\,, \tag{4.23}$$

$$V_d = \pi\delta_d\left(r_c\delta_d - \frac{1}{3}{\delta_d}^2\right), \tag{4.24}$$

where δ_d is the height of the droplet, and r_c is the radius of curvature, which is a function of the droplet height and diameter, d, and is calculated as,

$$r_c = \frac{{\delta_d}^2 + \left({}^{d}/_{2}\right)^2}{2\delta_d}. \tag{4.25}$$

On a real surface, the water droplets tend to have an irregular shape. An equivalent droplet diameter is calculated as the hydraulic diameter at the solid-liquid interface,

$$d = \frac{4A_{d,s}}{P_{d,s}}, \tag{4.26}$$

where $A_{d,s}$ is the contact area and $P_{d,s}$ is the perimeter of the droplet at the solid surface interface. The characteristic diameter of the droplet, d_c, is defined as the ratio of the droplet volume to surface area,

$$d_c = \frac{V_d}{A_d} = \frac{r_c\delta_d - \frac{1}{3}{\delta_d}^2}{2r_c}. \tag{4.27}$$

The characteristic diameter is a function of the droplet height, contact area, and perimeter. Using time-lapse photography, these three factors can be determined. The droplet height can be measured directly from the side profile photographs. The droplet contact area and perimeter can be determined from the frontal photographs. The images are enhanced to provide a clear boundary of the droplet. A MATLAB program is used to capture the droplet boundary and then the program calculates the average droplet area and perimeter. A copy of the MATLAB code can be found in Appendix F.

The mass flux can be determined from the rate of change of the characteristic diameter,

$$m''_v = \rho_w \frac{\partial}{\partial t}(d_c) \approx \rho_w \frac{\Delta d_c}{\Delta t}. \tag{4.28}$$

Finally with vapor mass flux, the mass transfer coefficient, $h_{m,v}$, can be determined from

$$h_{m,v} = \frac{m''_v}{\left(\rho_{v,a} - \rho_{v,s}\right)}, \tag{4.29}$$

where $\rho_{v,a}$ and $\rho_{v,s}$ are the water vapor density of the free stream air and saturated liquid interface respectively.

4.7 Summary of combined uncertainty

Table 4-5 summarizes the combined uncertainty of the dependent variables. The combined uncertainty is calculated using the uncertainty calculator function in Engineering Equation Solver (EES).

Table 4-5. Combined uncertainty of dependent variables.

Dependent variable	Combined Uncertainty
Chamber water vapor mass, $m_{v,ch}$	±2.5%
Frost mass, $m_{f,ts}$	±5%
Thermal resistances, R_e	±2%
Test surface heat flow, Q_{ts}	±8%
Heat transfer coefficient, h_{ts}	±8%
Defrost efficiency, η_d	±12%
Frost height, δ_f	±5%
Frost porosity, ε	±10%
Melt velocity, u	±8%
Droplet height, δ_d	±5%
Vapor mass flux, m''_v	±6%
Vapor mass transfer coefficient, $h_{m,v}$	±8%

4.8 Experimental procedure

To limit sources of bias error in the experiment, structured test procedures were adopted for the frosting and defrosting tests. A test matrix based upon the critical factors was implemented to provide a wide range of test results for analysis.

4.8.1 Frosting Process

1. Remove residual moisture in chamber by pumping chamber air through desiccant bed until the dew point temperature is below -20 °C.
2. Start data logger
3. Use chiller to cool test chamber to target testing temperature.
4. Charge saturator with distilled water, measure mass of saturator with water, isolate desiccant and remove. Install charged saturator, but keep isolated.
5. Cool test surface to desired test temperature. Adjust chiller cooling as required to maintain target testing temperatures.
6. Once chamber temperature has stabilized, cool test surface to target temperature.
7. Stabilize chamber and test surface temperatures.
8. Open valves to saturator. Adjust flow through saturator to maintain desired humidity level.
9. During frosting, monitor and adjust chiller and test surface to maintain target test temperatures.
10. Allow frost layer to build for 4 hours.
11. Capture time elapsed photograph of the frosting process at periodic intervals.
12. Isolate saturator from test chamber by closing valves.

13. Stop data logger and cameras image capture.

4.8.2 Defrost test process

1. Reset data logger for new scan rate. Start scanning.
2. Reset digital cameras for video capture. Start video capture.
3. Adjust voltage to test surface TE module to heat surface
4. Monitor defrost process, stop video capture after frost has melted and drained.
5. Allow remaining surface moisture to be vaporized from test surface.
6. Stop data logger, turn off power to chiller and test surface
7. Remove isolated saturator and weigh mass.
8. Weigh desiccant bed, install in system.
9. Remove moisture in chamber by pumping chamber air through desiccant bed until the dew point temperature is below -20 °C.
10. Isolate, remove and weigh desiccant.

4.8.3 Frosting test conditions

The key outputs of the tests are the time-dependency of the frost thickness and porosity. The frost porosity is affected by the shape and compactness of the ice crystals. Prior research shows the primary factors controlling the crystal shape are the bulk air temperature and the degree of super-saturation. Super-saturation is measured by the delta temperature between the air dew point and the surface temperature. In the low-temperature range of 0 to -20 ^{o}C, the primary crystalline structures are: needles, dendrites, and plates. The factors that primarily effect rate of frost growth are the difference between the air and surface temperature and the degree of super-saturation, air humidity, and the surface temperatures. Thus, the type and rate of frost growth is dependent upon the ambient air temperature and dew-point, and the surface temperature. Given the physical nature of the problem, the dew point temperature is always bounded by the air temperature and the surface temperature.

$$T_{ch} > T_{dp} > T_{ts} \tag{4.30}$$

The region of interest in this study is the fresh to frozen condition, commonly used for the storage and transportation of foodstuff, which is from air temperature of 0°C to -20°C. For a direct expansion air-cooler, the typical delta between the air and surface

Table 4-6. Frosting test matrix. All entries are in ^{o}C.

Air temperature	Air dew point temperature	Surface temperature	Degree of super-saturation	Surface to air temperature delta
0	-5	-10	5	-10
0	-10	-20	10	-20
-5	-10	-15	5	-10
-5	-15	-20	5	-15
-10	-15	-20	5	-10
-10	-15	-25	10	-15

temperature is in the range of 10 to 20 °C. The degree of super-saturation can vary over a large range and for this study is varied from 0 to 15 °C. Table 4-6 summarizes the nominal test conditions for the frost formation.

4.8.4 Defrost test condition

For each frost formation test, there is a corresponding defrost test. The only factor that is controlled during defrost is the supplied heat flux, q''_{hfs}. By adjusting the voltage of the TE module, different heat fluxes can be supplied to the surface. Two levels of heat flux levels were tested for each frost formation condition in Table 4-6.

4.9 Summary

This chapter provides a detailed description of the experimental test facility, including the instrumentation and digital video equipment. The fundamentals of the data reduction are described and the measurement uncertainties are summarized. A detailed discussion of the visual analysis is presented. The sequential test procedure for the frost formation and defrosting portion of the test program are discussed along with the matrix of test conditions.

5 *Experimental Results*

In this chapter, the results of the experimental program are analyzed and discussed. A set of calibration experiments establish the accuracy of the experimental method. An analysis of the frost formation process is conducted with the results compared against proposed growth models. A complete analysis of the defrost process is presented; wherein the heat and mass transfer of each defrost stage is calculated. The results are compared against the fundamental model described in Chapter 3. Complete experimental results are in Appendix G

5.1 Calibration of the experimental apparatus

A set of steady-state heat transfer experiments were conducted on a dry test surface to determine the internal thermal resistances of the laboratory apparatus. Free and forced convection heat transfer coefficients are compared against known correlations for flow over a vertically heated plate. Additionally, measurements of transient heating of the test surface were conducted to validate the lumped capacitance model proposed in section 4.3.2.

5.1.1 Dry surface steady state results

Recall from section 4.3.3 that to determine the heat flow at the test surface, two internal thermal resistances within the apparatus need to be determined. At steady-state, Equations (4.10) and (4.12) can be combined and reduce to,

$$Q_{ts} = Q_{hfs} - \frac{1}{R_e}\left(T_e - T_{sp}\right). \tag{5.1}$$

The heat transfer at the test surface for a constant heat flux can be expressed as,

$$Q_{ts} = hA_{ts}(T_{ch} - T_{ts}). \tag{5.2}$$

For the calibration tests, the heat flow from the test surface is effectively negated by controlling the temperature difference between the chamber air and test surface to a value close to zero. The wall thermal resistance R_e is calculated from Equation (5.1) and varies with the mean wall temperature (Figure 5-1). From a least square regression of the data,

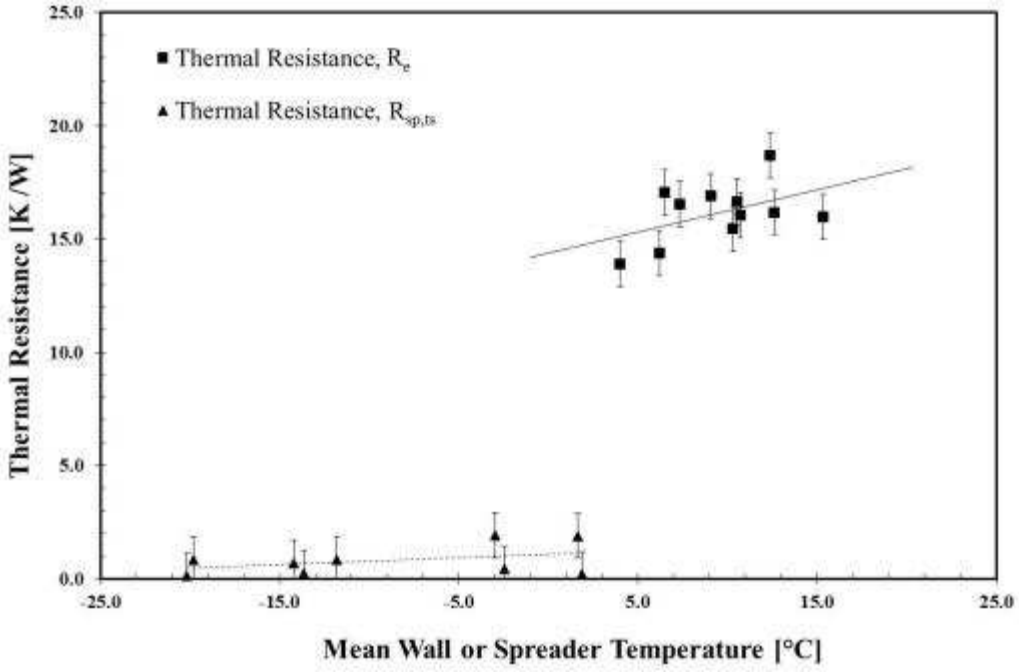

Figure 5-1. Estimation of thermal resistances.

the wall thermal resistance is estimated as,

$$R_e = 0.186T_e + 14.377. \quad (5.3)$$

Similarly, the contact resistance between the heat spreader and test surface can be estimated from steady-state test where an appreciable amount of heat is transferred across the joint. The thermal resistance as a function of the spreader temperature is,

$$R_{sp,ts} = 0.031T_{sp} + 1.080. \quad (5.4)$$

Once the heat flow at the test surface is determined, the air side heat transfer coefficient can be determined from Equation (5.2). Table 5-1 summarizes measured heat

Table 5-1. Heat transfer coefficent for steady-state calibration test.

Chamber air temperature [°C]	**Surface Temperature [°C]**	**Heat transfer coefficient [W/m^{2}K]**		**Test Condition**
		Measured	Correlation	
19.9	1.7	5.9 ±0.6	6.5	Free
19.4	-3.0	6.1 ±0.6	6.9	Free
-1.7	-11.8	16.3 ±1.3	18.5	Forced
-4.9	-14.2	18.9 ±1.5	18.5	Forced

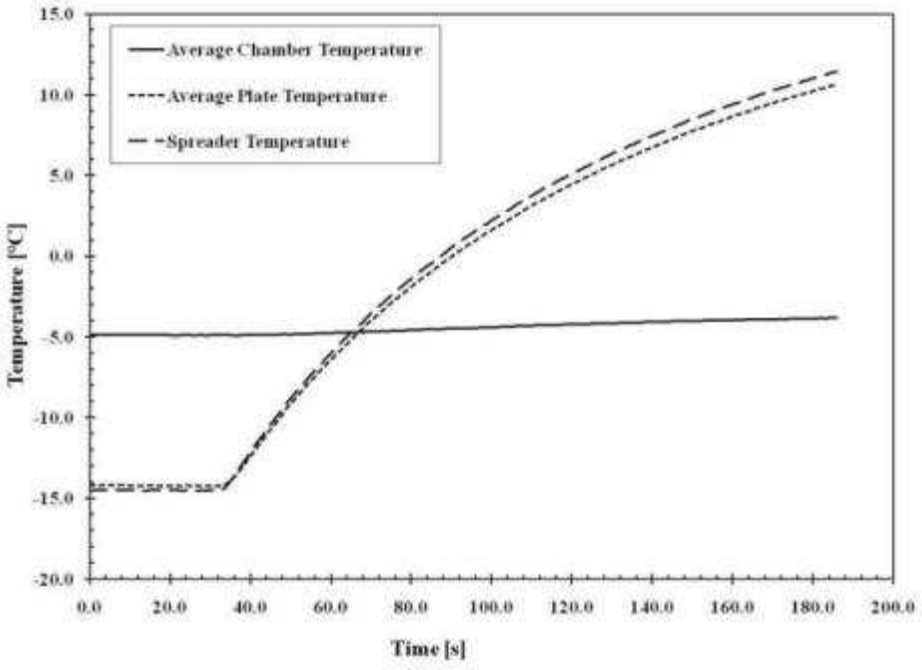

Figure 5-2. Temperatures during a "pull-up" experiment.

transfer coefficients for free and forced convection calibrations. The results compare favorably to coefficients predicted by standard correlations for a vertical plate with a constant heat flux boundary condition (Holman, 2002).

5.1.2 Dry surface transients results

Defrost is a dynamic process. To calculate the time-dependent heat flow, it is necessary to solve the transient energy balance (Equations (4.10) and (4.12). Figure 5-2 shows measured temperature for a "pull-up" experiment, wherein the test surface is heated from a stable low temperature to above the frost melt temperature. Figure 5-3 shows the heat flow during the test. The solid line is the supplied heat flow at the base of the spreader. The dash-dot line is the heat lost through the edges of the test apparatus. The dash line is the change of the stored thermal energy of the heat spreader and test surface. The dot line is the net heat flow at the test surface.

For the first 35 s of the test the plate temperature is held steady. The heat flow at the surface is from the chamber ambient air via forced convection with an estimated average heat transfer coefficient of 20 W/m^2K. When heat is applied to the surface, a

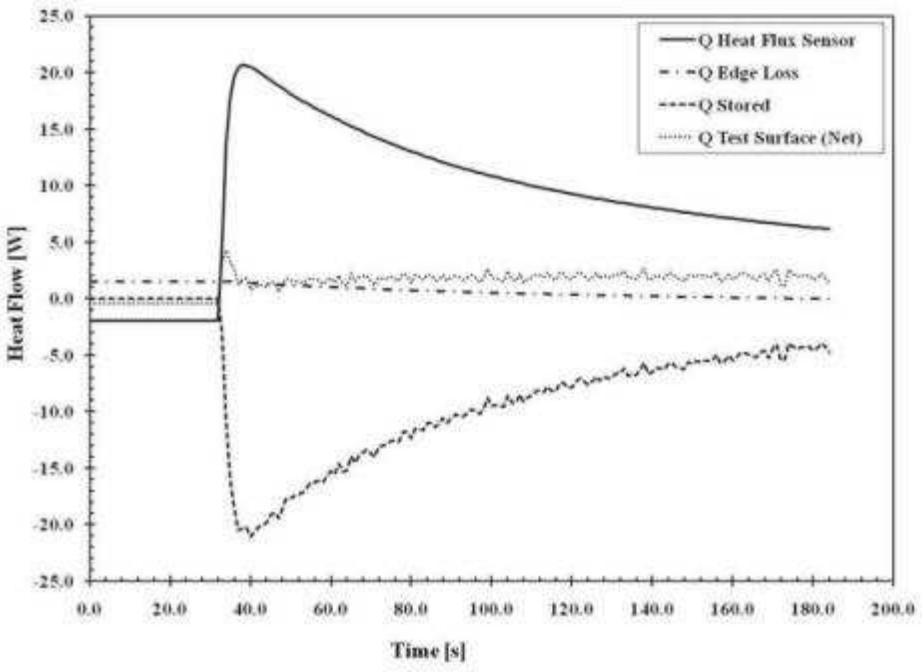

Figure 5-3. Heat flow a during "pull-up" experiment.

large heat flow into the test surface is measured by the heat flux sensor. Correspondingly, a large amount of the heat is absorbed by the heat spreader and test surface. The net heat flow is found to be nearly constant during the heating test at 1.9 W. These results provide a basis of comparison for the defrost test.

5.1.3 Simulation of dry surface transient heat transfer

To validate the lumped capacitance model presented in section 4.3.3, a numerical simulation was developed. Equations (4.10) and (4.12) can be readily stacked using the linear state space notation,

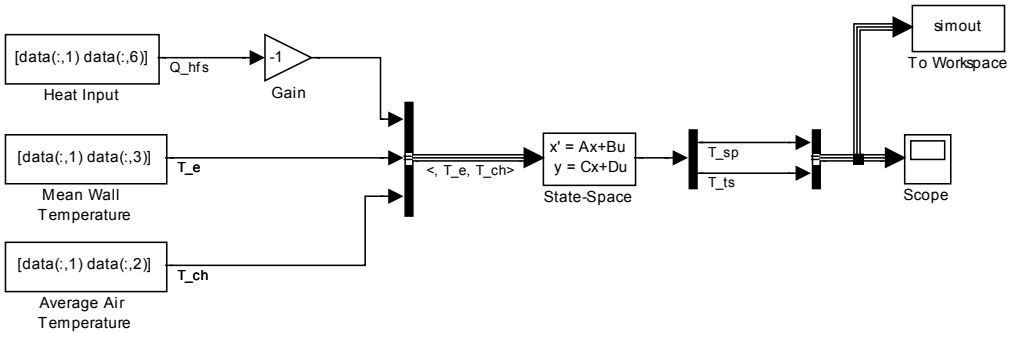

Figure 5-4. State space model.

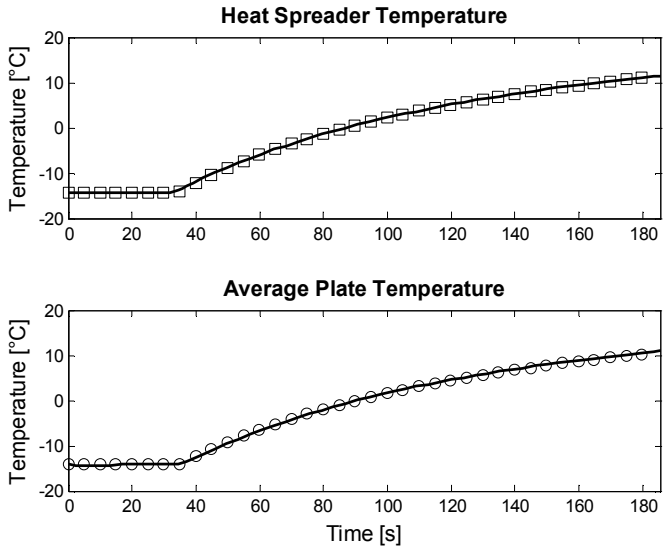

Figure 5-5. State space temperature results.

$$\dot{\mathbf{T}} = \mathbf{AT} + \mathbf{Bi}, \tag{5.5}$$

where $\dot{\mathbf{T}}$ is the vector of the time derivatives, **A** and, **B** are matrices of coefficients, **T** is a vector of states, and **i** is a vector of inputs. Substituting Equations (4.10) and (4.12), the system of equations in Equation (5.5) can be expressed as,

$$\begin{bmatrix} \dot{T}_{sp} \\ \dot{T}_{ts} \end{bmatrix} = \begin{bmatrix} -\left[\frac{1}{C_{sp}R_{sp,ts}} + \frac{1}{C_{sp}R_e}\right] & \frac{1}{C_{sp}R_{sp,ts}} \\ \frac{1}{C_{ts}R_{sp,ts}} & -\left[\frac{1}{C_{ts}R_{sp,ts}} + \frac{UA_a}{C_{ts}}\right] \end{bmatrix} \times \begin{bmatrix} T_{sp} \\ T_{ts} \end{bmatrix} + \begin{bmatrix} \frac{-1}{C_{sp}} & \frac{1}{C_{sp}R_e} & 0 \\ 0 & 0 & \frac{UA_{ts}}{C_{ts}} \end{bmatrix} \times \begin{bmatrix} Q_{hfs} \\ T_e \\ T_{ch} \end{bmatrix} \tag{5.6}$$

A state space model can be readily solved using a MATLAB/Simulink simulation. The inputs are the coefficients for the A and B matrices and the input vector I (Figure 5-4). The code for initializing the model block is in Appendix F. Figure 5-5 compares the model output (lines) to the reference data sets (markers) for the heat spreader and plate temperatures respectively. The simulation confirms that the one-dimensional lumped capacitance model is adequate to capture the dynamics of the test.

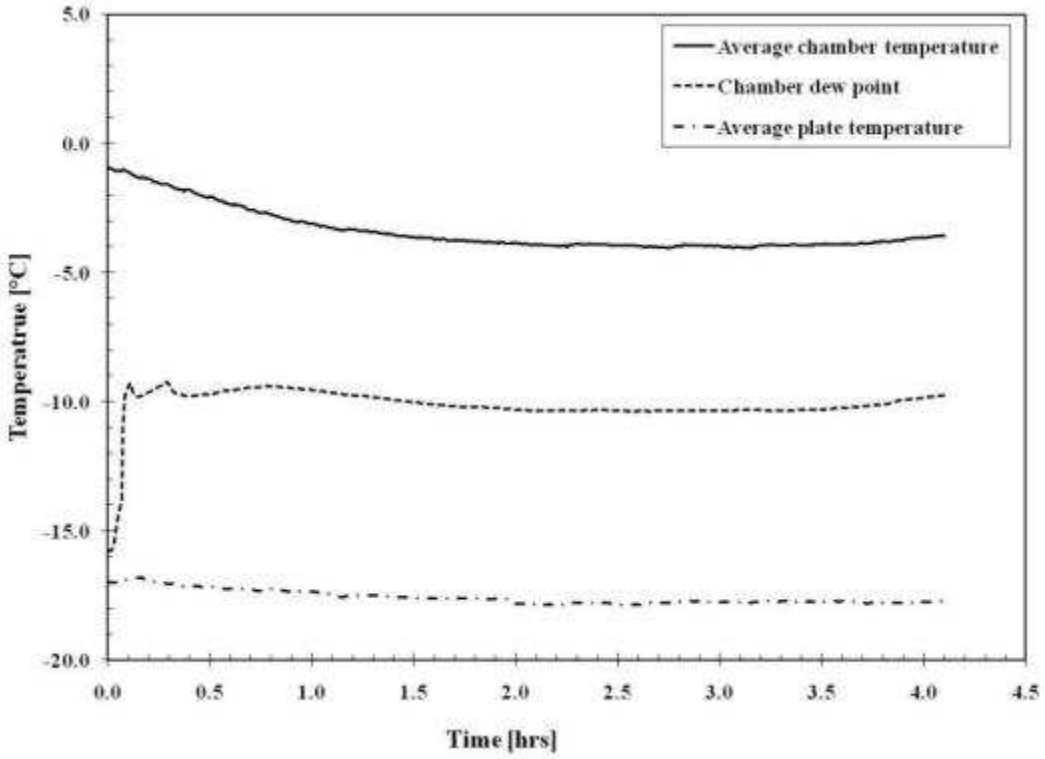

Figure 5-6. Temperatures during frost formation test (Test ID 12).

5.2 Frost formation results

A series of frosting experiments were conducted. Digital images of the front and side profiles of the frost layer were captured. The test surface temperature, chamber temperature, humidity, and pressure, along with the input heat flux were recorded over the four hour period of each run. Results of an experiment are discussed in detail below, and the results of all runs in Appendix G.

5.2.1 The frost formation process

Figure 5-6 shows a plot of the average chamber ambient air, dew point and surface temperatures during the frost formation process. Temperatures are held nearly constant during each run, and humidity is added to the chamber ambient at ~10 min. The average plate, dew point, and chamber temperatures during the reference test shown in Figure 5-6 are -3.4°C, -10.0 °C, and -17.6 °C, respectively.

Figures 5-7 and 5-8 shows the side and frontal images of the frost layer during

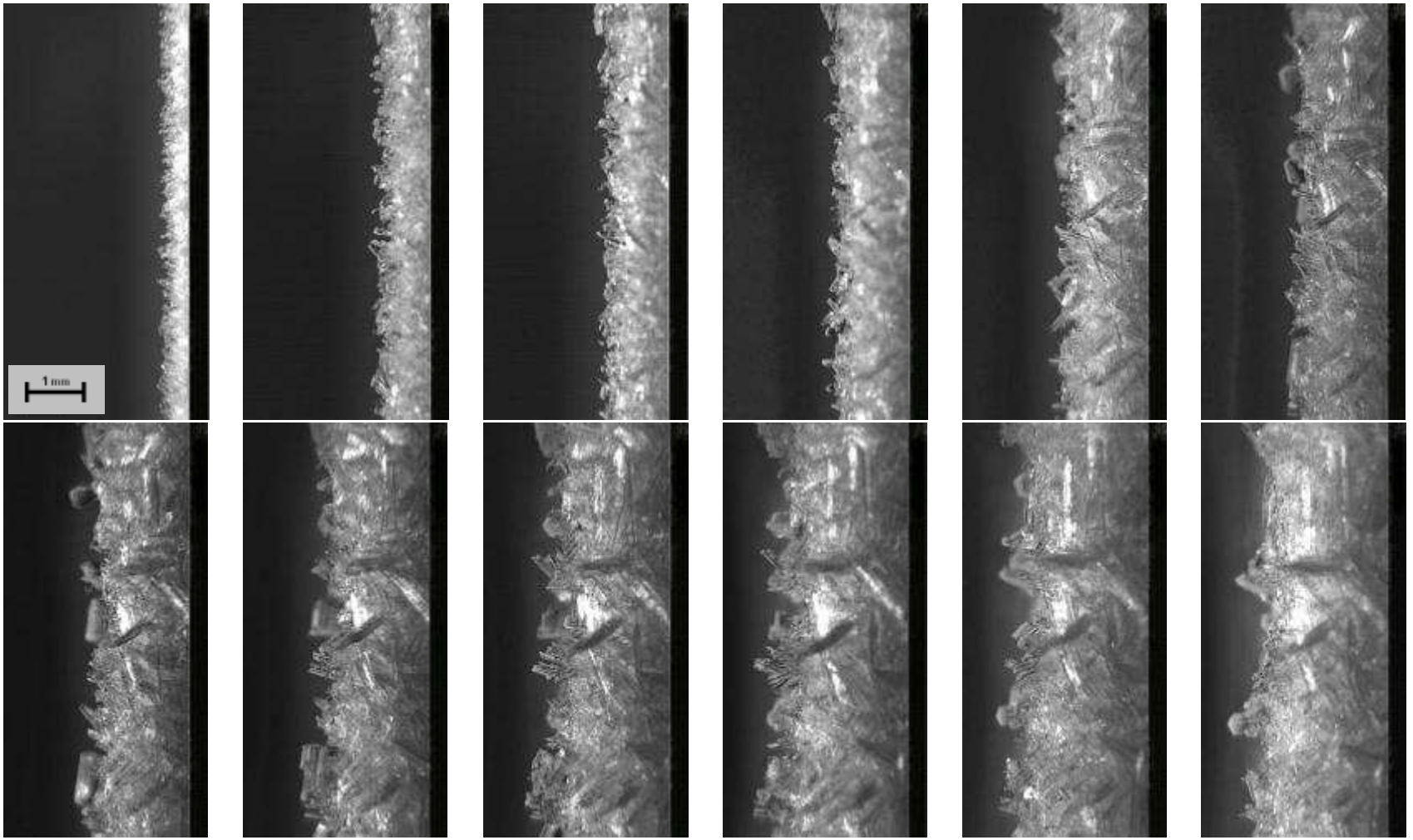

Figure 5-7. Side images of frost formation process at 20 min intervals (ID 3).

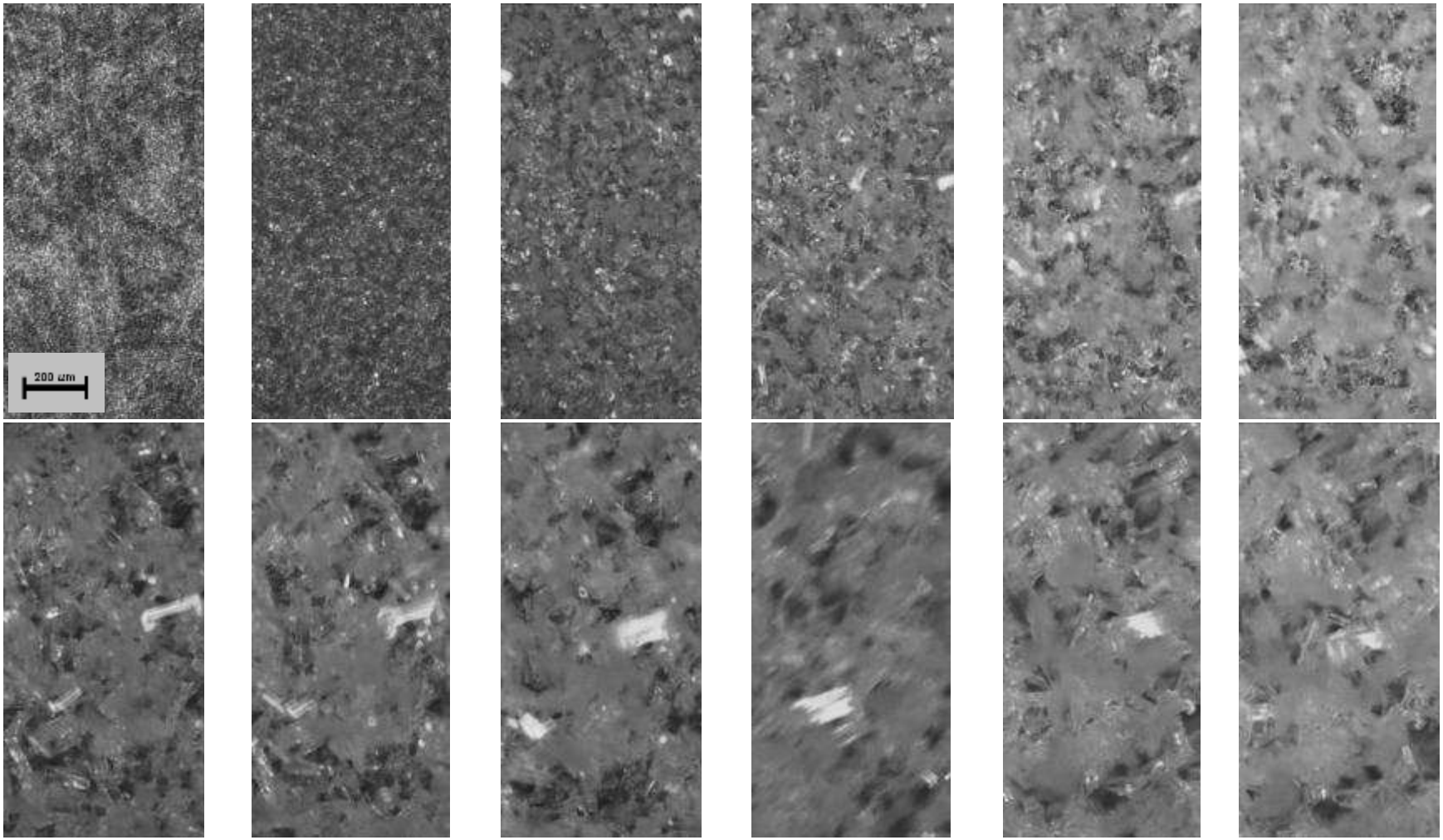

Figure 5-8. Frontal images of frost formation process at 20 min intervals (ID 3).

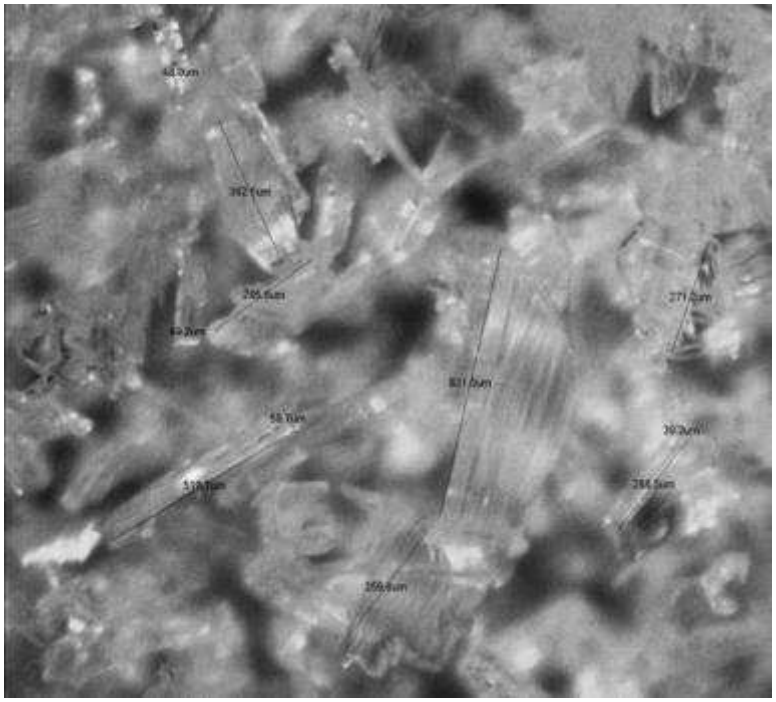

Figure 5-9. Close-up of ice crystal at 240 min (ID 3).

formation. The first image was taken approximately 10 min after humidity was added to the chamber. The interval between the images is ~20 min. For the run shown, the frost crystals formed as flat plates and frost thickness changes rapidly during the initial stages of the formation process (Figure 5-7). The accelerated growth at the tip is driven by the high concentration gradient of water vapor between the crystal and ambient air. As the crystal grows in thickness, away from the surface, the internal temperature gradient causes the local vapor pressure at the tip to be closer to that of the bulk airstream, which causes a reduction of the water vapor concentration, reducing the rate of tip growth. The majority of the crystal growth in thickness occurs during first 60 min of the run.

As seen in Figure 5-8, frost crystals grow from nucleation sites on the surface. Previous studies have found that nucleation sites are minor imperfections in the surface where the surface energy is slightly less than the neighboring region (Na, 2003). As time progresses, ice crystals grow as flat plates that branch from the nucleation sites. As the ice crystals form, the frost layer forms a structure of randomly orientated plates. The plates grow in thickness and length, until neighboring plates touch. When two

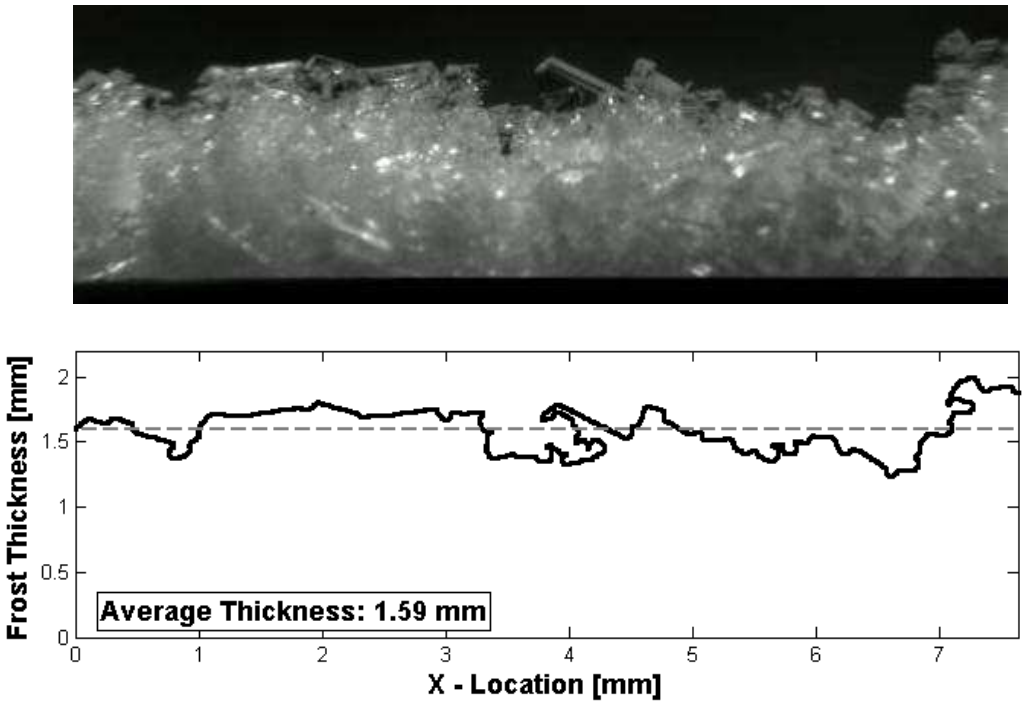

Figure 5-10. Comparison of digital image and edge capture (Janssen 2011).

neighboring plates touch, a new nucleation site forms for the growth of subsequent ice crystal branches. The rate of change in thickness growth slows as the tip temperature approaches the dew point of the air. Once this point is reached, crystal growth is dominated by an increase in the overall size of ice crystals. The overall porosity of the frost layer decreases as time progresses.

Figure 5-9 shows a close-up of the ice crystals at the 240 min duration of the run. The crystals form as flat plates. A survey of the reference image found the tip-to-tip length of the crystals is ~390 μm, and the average thickness is ~52 μm. The primary factors controlling the type of crystal growth are the temperature and humidity differential between the chamber air and surface (Hobbs, 1974). These are also the same factors that affect the rate of growth of the frost layer.

5.2.2 Frost thickness

As described in Section 4.6.4, a MATLAB program is used to analyze the digital images of the frost growth. The program calculated the minimum, maximum, and average frost layer thickness. Figure 5-10, is an example of the edge capture technique.

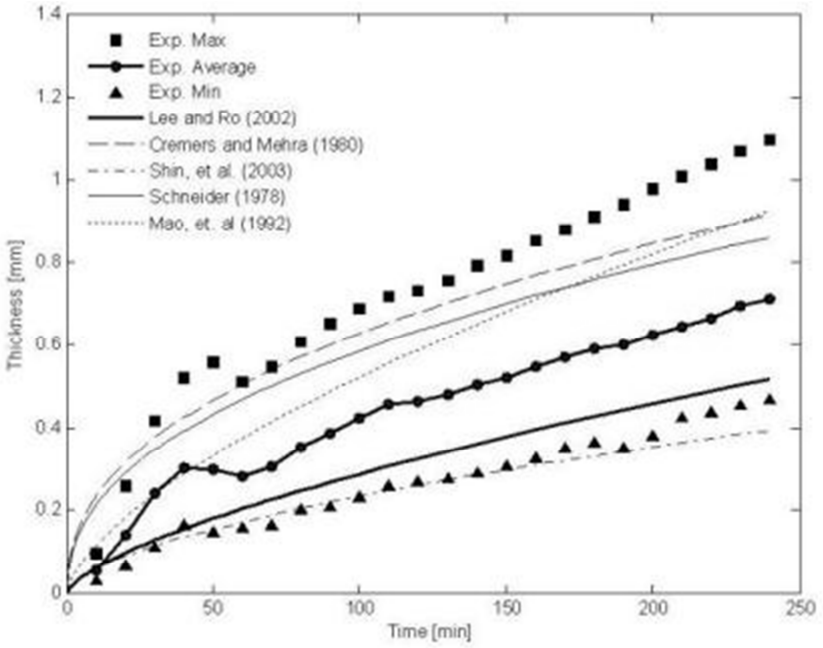

Figure 5-11. Frost growth rate (Janssen, Mohs, and Kulacki, 2012a).

The final frost thicknesses for the tests are in Table 5-2. A copy of the MATLAB code is in Appendix F.

Janssen, Mohs, and Kulacki (2012a) compare the result of the frost thickness to several published growth models. Figure 5-11 is the change in frost thickness for growth conditions of T_{ch} = -1.2 °C, T_{dp} = -8.5 °C, and T_{ts} = -10.0 °C. When compared against other models, Janssen finds that some models correlate well to maximum measured thickness, while others agree more closely with the minimum measured thickness. None of the models he reviewed accurately predict the average measured thickness. The inconsistency in them maybe due to differences either in the technique used to measure frost layer thickness or in the estimation of the frost surface temperature which is a derived value. When comparing all of the measured growth results, Janssen found the model proposed by Lee and Ro (2002) gives the best agreement to his data.

Based upon the growth results of his experiments, Janssen proposes a simplified growth model,

$$\delta_f = 0.0036 t^{\theta} \theta^{(\theta - 4.939)}, \tag{5.7}$$

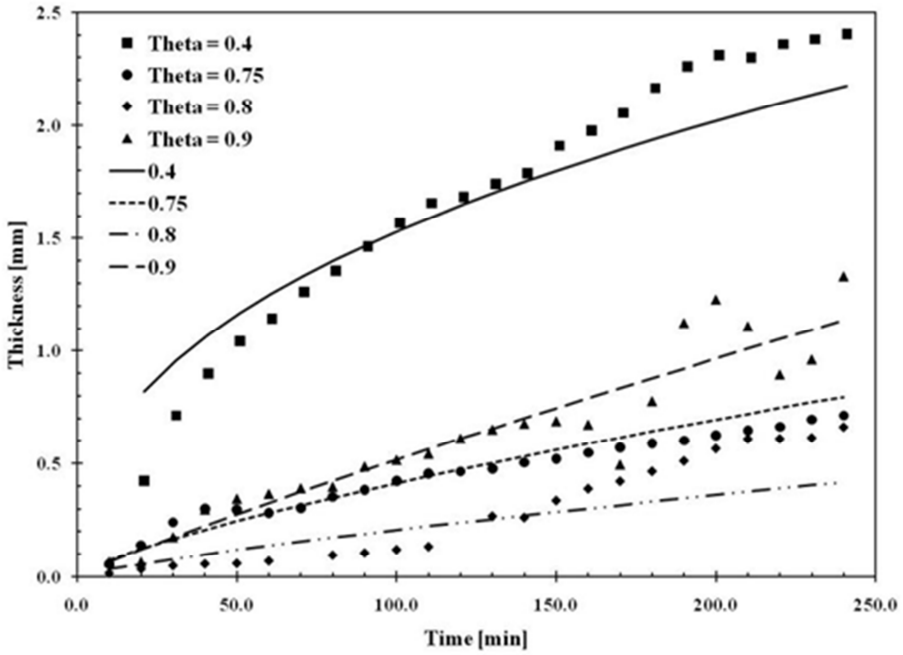

Figure 5-12. Frost growth model (Janssen, 2011).

where t is time in min, and θ is defined as the ratio of the latent temperature potential to the sensible temperature potential,

$$\theta = \frac{T_{ch} - T_{dp}}{T_{ch} - T_{ts}}. \tag{5.8}$$

In Figure 5-12 Janssen's model is compared with the experimental results and reasonable agreement is seen over a wide range of conditions. Janssen also reports a more complex form of the growth equation, which showed even better agreement with the test results of this study. The simplified form growth equation (5.7) will be used as the representative growth equation for the remainder of this analysis, but in fact any growth equation could be used and would be compatible to the equation sets described hereafter.

5.2.3 Frost porosity and mass transfer

As described in section 4.5.1, the porosity of the frost layer can be determined from the frontal view of the frost layer. The contrast of the image is enhanced to aid in detection of the ice crystals and voids and he image is converted to a binary black and

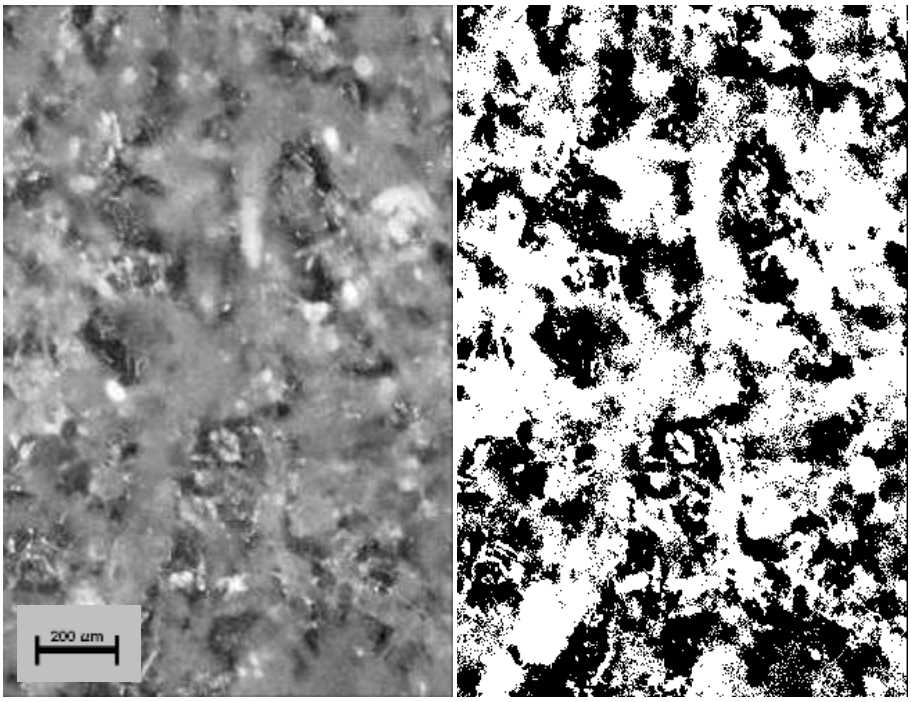

Figure 5-13. Frontal image and enhanced image (ID 3).

white image (Figure 5-13). Pixels that are occupied by ice (white, +1 value) are counted, and the porosity is calculated by dividing the occupied pixels by the total pixel count (Equation 4.19). The final frost porosities for the test are found in Table 5-2. A copy of the MATLAB code can be found in Appendix F.

Figure 5-14 shows the change in frost porosity, thickness, and mass during the frost layer growth for test conditions T_{ch} = 0.0°C, T_{dp} = -8.3°C, and T_{ts} = -19.2°C. Initially, the frost layer has a porosity of unity and quickly decreases as the layer grows. From thickness and porosity, the accumulated mass of the ice layer can be readily determined by,

$$m_f = A_{ts}\delta_f(1-\varepsilon)\rho_i, \tag{5.9}$$

where A_{ts} is the area of the test surface, and ρ_i is the density of ice, which is assumed to be 920 kg/m^3. As seen in Figure 5-15, the porosity of the frost layer is linearly proportional to the frost thickness. This relationship is understandable, as the factors controlling thickness are the same as expected to control the porosity. The porosity can

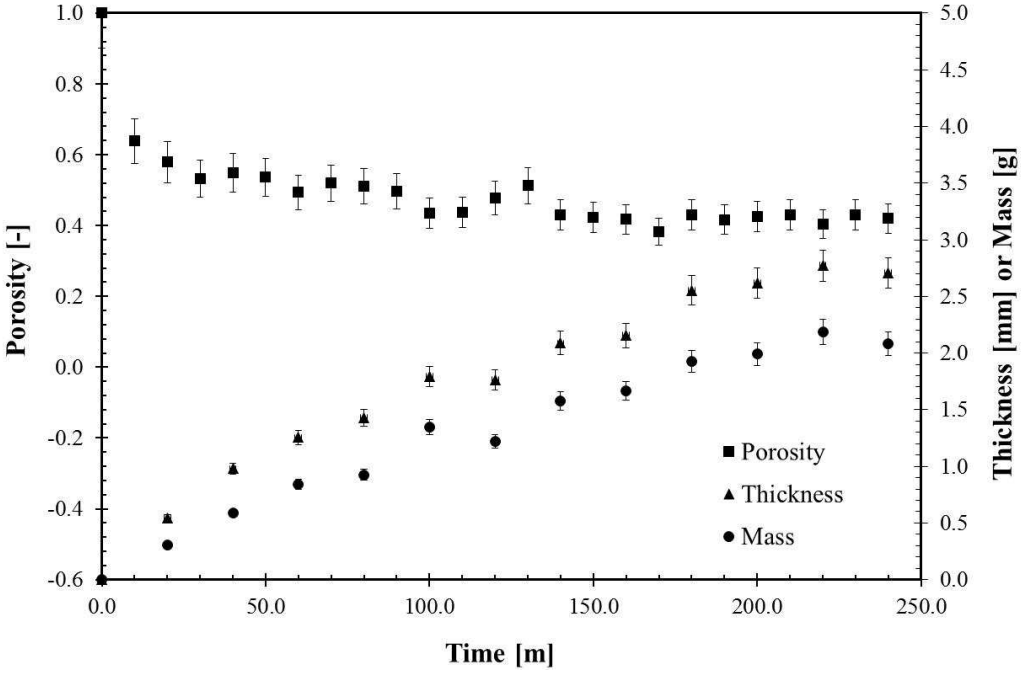

Figure 5-14. Change in frost prosity and thickenss during growth (ID 3).

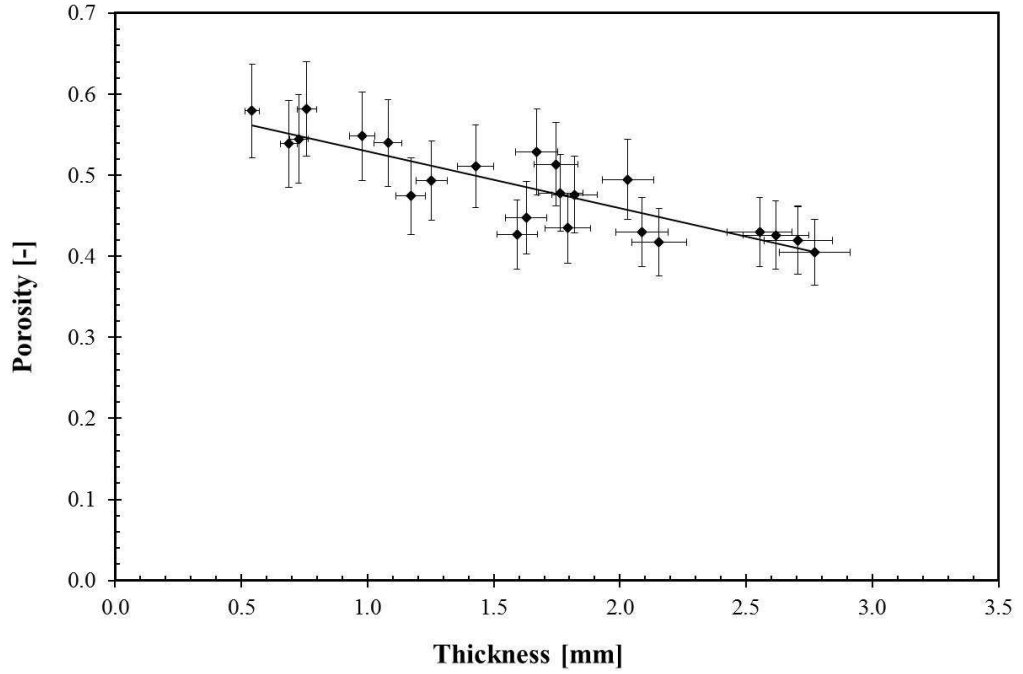

Figure 5-15. Frost porosity as a function of thickenss (ID 3).

Table 5-2. Summary measurements for of frost conditions at the end of build period.

Test ID	Test Conditions $T_{ch}/T_{dp}/T_{ts}$ [°C]	Frost Thickness [mm]	Porosity [-]	Mass [g]
1	-8.5/-19.0/-20.2	1.08	0.54	0.68
2	-1.2/-8.5/-10.0	0.76	0.58	0.43
3	0.0/-8.3/-19.2	2.68	0.42	2.13
4	-7.9/-18.1/-19.4	1.82	0.48	1.31
5	-0.6/-8.4/-9.6	0.73	0.54	0.45
6	-7.2/-16.8/-19.5	1.75	0.51	1.16
7	-5.6/-13.2/-18.9	2.03	0.49	1.41
8	-5/-12.5/-18.4	1.67	0.53	1.08
9	-8.6/-16.2/-18.9	1.17	0.47	0.84
10	-4.7/-13.9/-17.8	0.69	0.54	0.43
11	-4.6/-12.1/-18.8	1.59	0.43	1.25
12	-3.4/-10.0/-17.5	1.63	0.45	1.19

be estimated as,

$$\varepsilon = -0.0701\delta_f + 0.5992. \tag{5.10}$$

Combining Equations (5.9), (5.7) and (5.10), it is possible to determine the time dependent accumulated frost mass by,

$$m_f = A_{ts}\rho_i\left(1.443 \times 10^{-3} t^{\theta}\theta^{(\theta-4.939)} + 9.085 \times 10^{-9} t^{2\theta}\theta^{2(\theta-4.939)}\right). \tag{5.11}$$

5.2.4 Frost properties at end of build stage

Table 5-2 summarizes the final frost thickness, porosity, and accumulated mass at the conclusion of the frost growth period. Frost thickness and porosity are determined by the visual techniques described in Sections 4.5.2 and 4.5.1. The accumulated mass is directly measured by the method described in Section 4.3. The thickest layer (ID 3) is grown at the largest temperature differentials between the chamber ambient air and test surface temperatures. This layer also has the lowest porosity and the most accumulated mass (2.13 g). The frost layer with the highest porosity (ID 12) is grown at the smallest temperature difference between the chamber dew point and test surface temperatures.

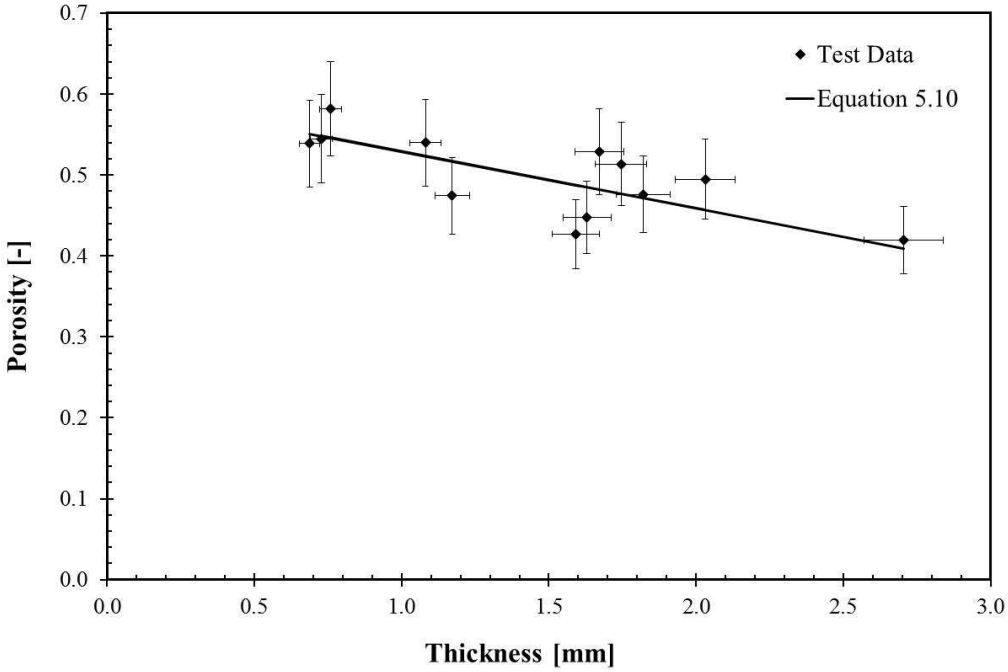

Figure 5-16. Porosity at conclusion of frosting process.

Figure 5-16 shows the comparison between the final measured porosity against thickness, as well as, the correlation proposed in Equation (5.10). Equation (5.10) is found to provide a reasonable estimate of the frost porosity over a wide range of growth conditions. This result implies that a good estimate of the frost porosity can be made from a direct measurement of the frost thickness, or by using an appropriate correlation for frost thickness, such as Janssen (2011). The conclusion of the frosting process is the beginning of the defrost process. The values presented in Table 5-2 are the starting conditions for the defrost test to be discussed in Section 5.3. If the properties of the frost are not directly measured, the thickness, porosity, and mass can be estimated from Equations (5.7), (5.10), and (5.11).

5.2.5 Heat transfer during frosting process

Figure 5-17 shows the surface heat flux and temperature during the frost growth process for run ID 12 where T_{ch} = 0.0 °C, T_{dp} = -8.3 °C, and T_{ts} = -19.2 °C. When humidity is injected into the chamber, a corresponding increase in the heat flux is seen at surface. The heat transfer at the surface is a combination of both sensible and latent heat

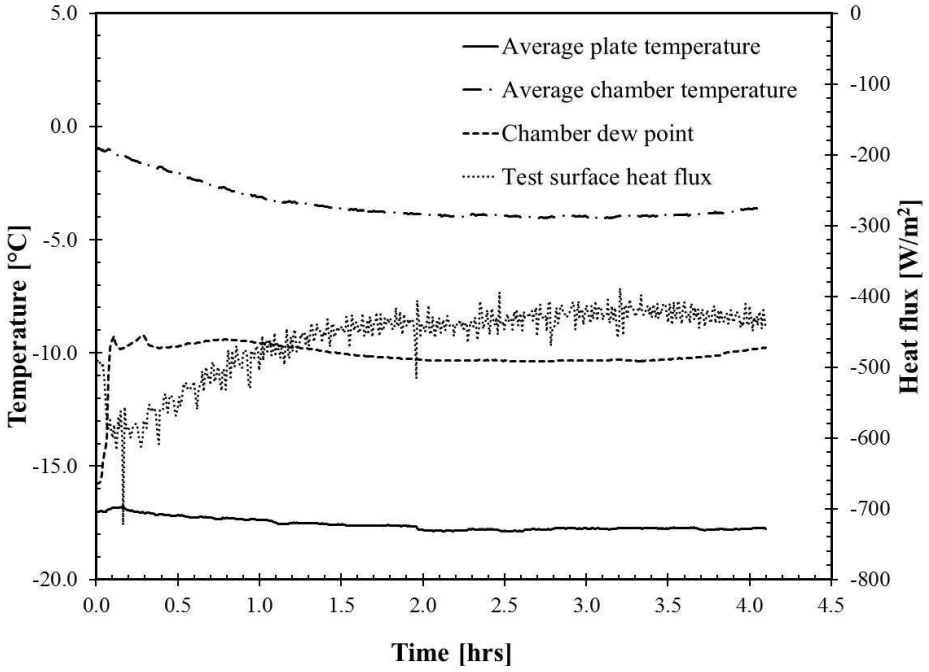

Figure 5-17. Heat flux during the frosting process (ID 12).

transfer. The increase in heat flux is due to the latent heat transfer as water molecules in the air freeze on the surface as ice crystals. The heat flux correlates well with the mass transfer results. The highest gradient of the heat flux is seen early in the frost growth process where mass transfer is the highest. As the frost formation process continues a reduction in both the heat and mass transfer are measured. The final heat flux is similar to that measured for a dry (unfrosted) surface at same conditions, which would be the sensible heat transfer.

The effect of the frost growth on heat transfer is clearly seen in Figure 5-18. The frosted heat transfer coefficient is plotted as a function of time. For comparison, the heat transfer coefficient for an equivalent dry surface is also plotted Equation (5.2). The frosted heat transfer coefficient quickly rises, and is seen as an enhancement to the heat transfer coefficient for an equivalent dry surface. The frosted heat transfer coefficient quickly decays as the frost layer thickens. Also seen in Figure 5-18 is a prediction of the heat transfer coefficient via a new model. When the total heat flux at the surface is

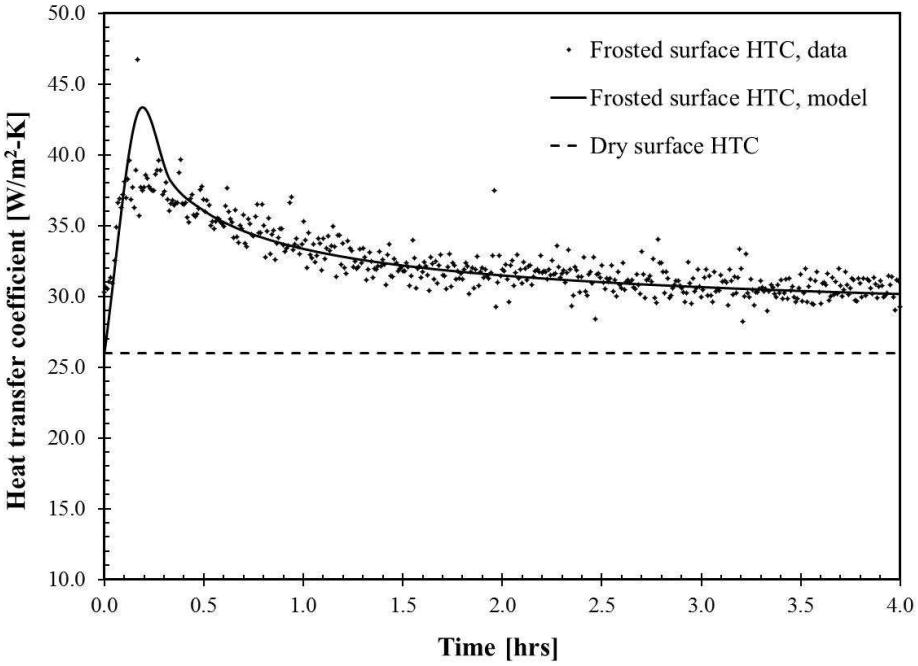

Figure 5-18. Heat transfer coefficient during frosting process (ID 12).

defined as the sum of the sensible and latent heat transfer, it is possible to define the frosted heat transfer coefficient as,

$$h_f = \frac{q''_{f,s} + q''_{f,l}}{(T_{ch} - T_{ts})}, \tag{5.12}$$

or,

$$h_f = h_{f,s} + h_{f,l}, \tag{5.13}$$

where h_s and h_l are the sensible and latent heat transfer coefficient, respectively. Latent heat transfer is determined by the rate of sublimation of water vapor from the ambient air into the frost layer expressed as,

$$q''_{f,l} = \lambda_{ig} \frac{\partial m_f}{\partial t}, \tag{5.14}$$

where λ_{ig} is heat of sublimation of ice, and is assumed to be 2604 J/g. The rate of change of the mass of the frost layer is determined by differentiating Equation (5.11) with respect to time,

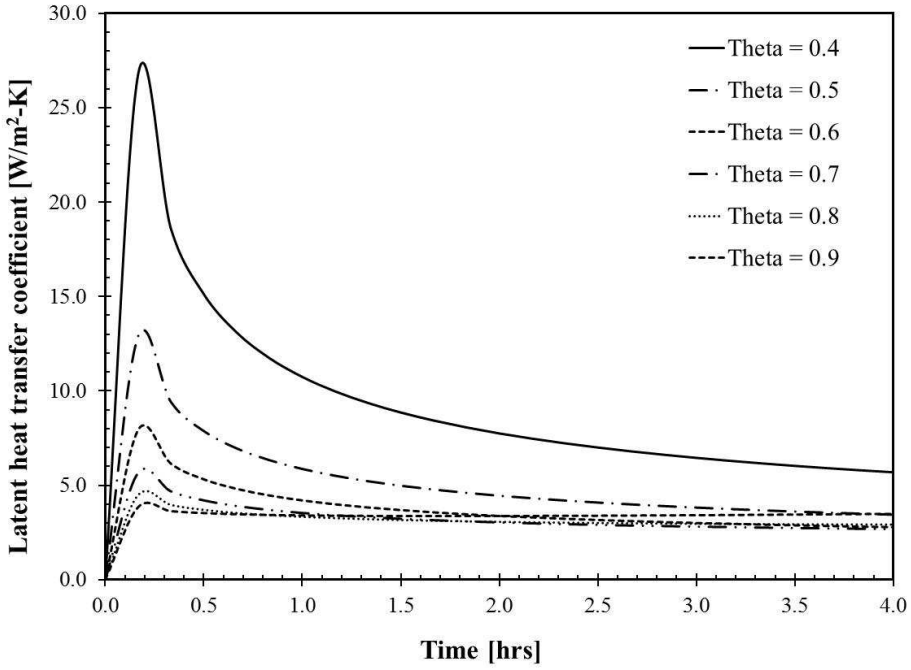

Figure 5-19. Latent heat transfer for various θ (ΔT = 15°C).

$$\frac{\partial m_f}{\partial t} = \frac{A_{ts}\rho_i}{60}\left(1.443\times10^{-3}t^{(\theta-1)}\theta^{(\theta-3.939)} + 1.961\times10^{-9}t^{(2\theta-1)}\theta^{2(\theta-4.439)}\right). \quad (5.15)$$

Combining Equations (5.12), (5.14), and (5.15), the latent frosted heat transfer coefficient is defined,

$$h_{f,l} = \frac{\lambda_{ig}A_{ts}\rho_i}{60(T_{ch} - T_{ts})}\left(1.443\times10^{-3}t^{(\theta-1)}\theta^{(\theta-3.939)} + 1.961\times10^{-9}t^{(2\theta-1)}\theta^{2(\theta-4.439)}\right). \quad (5.16)$$

Figure 5-19 shows the effect of varying θ (over the range of values seen in this study) on the latent heat transfer coefficient. The greatest enhancement is seen for low values of θ, where the potential for heat transfer is the greatest.

5.2.6 Summary frost growth results

A single test case of the frost formation process is reviewed in detail. The visual images confirm earlier studies, confirming the frost formation process progress through consistent stages. Two new visual image analysis techniques are used to calculate the frost thickness and porosity. Utilizing Janssen's (2011) empirical thickness correlation, new simplified mass and heat transfer models are proposed. The semi-empirical models estimate the time dependent heat and mass transfer of the frost formation process. The

models are dependent upon a new parameter, θ, which is the ratio of the latent to sensible temperature potential. The form of the proposed heat transfer model is compatible with current methods of calculating heat transfer performance for heat exchanges.

5.3 Defrost results

Following the frost formation experiments, a series of defrost experiments were conducted. Again, digital profile images capture the front and side of the frost layer. The results of an individual defrost test are discussed below. The images and data traces of all defrost experiments are in Appendix G.

5.3.1 Observations of the defrost process

Figures 5-20 and 5-21 show images of the defrost process for run ID 3. These images clearly show the changes in structure of the frost layer through the melting process. The field of view for the side images is 3.0 mm x 6.5 mm and for the front view is 3.0 mm x 2.0 mm. The side images are shown for an even interval of 4.7 s, and the front images are every 5.0 s.

From the side images, minimal changes in frost structure are seen in the first few images at the initiation of the defrost process. By the third image (~15 s), the air-frost front is seen moving towards the solid surface. The melt liquid is absorbed by the frost layer. By the fifth image water is migrating through the crystal structure. At this point, one sees a steady progression of the air-frost front moving toward the surface. The shape of the air interface does not change, and this characteristic indicates that the frost is melting at the surface. By the seventh frame (~35 s) a visible deformation of the frost surface is seen and all the voids in the frost layer are saturated. From this point forward, the bottom of the image is showing that there is a gravity effect of the melt water draining off the surface and a suction force is pulling the frost layer towards the surface.

Even up until the last melt process ice crystals are visible in the water, and frontal images illustrate this. For this frost layer, a bulk downward movement of the frost layer off the surface is not seen. It is theorized that surface tension is holding the water and frost to the solid surface. For the front images, the tip crystals do not deform until fully saturated, and remain in place on water droplets. Water drained off surface sheds quickly

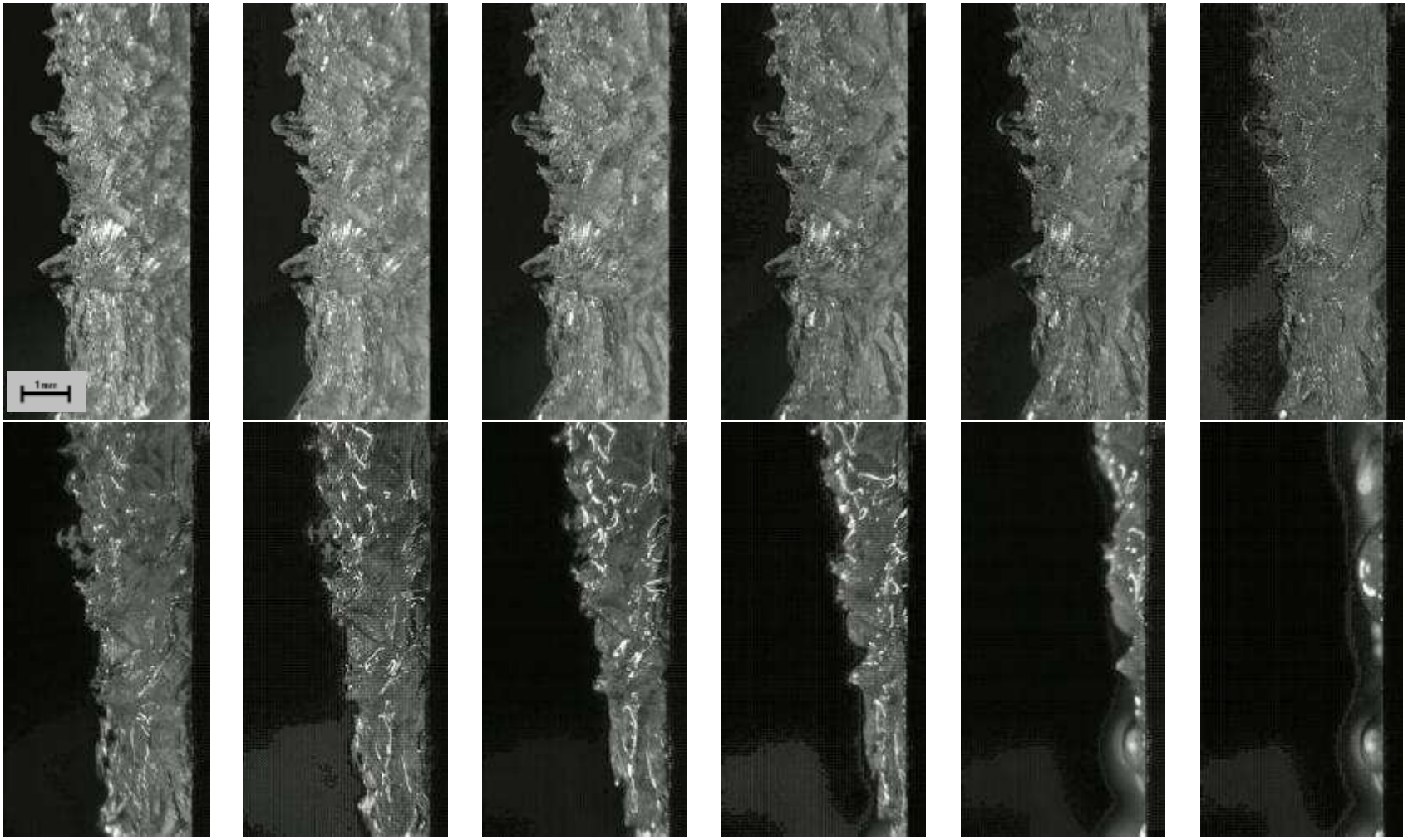

Figure 5-20. Side images of defrost at 4.7 s intervals (ID 3).

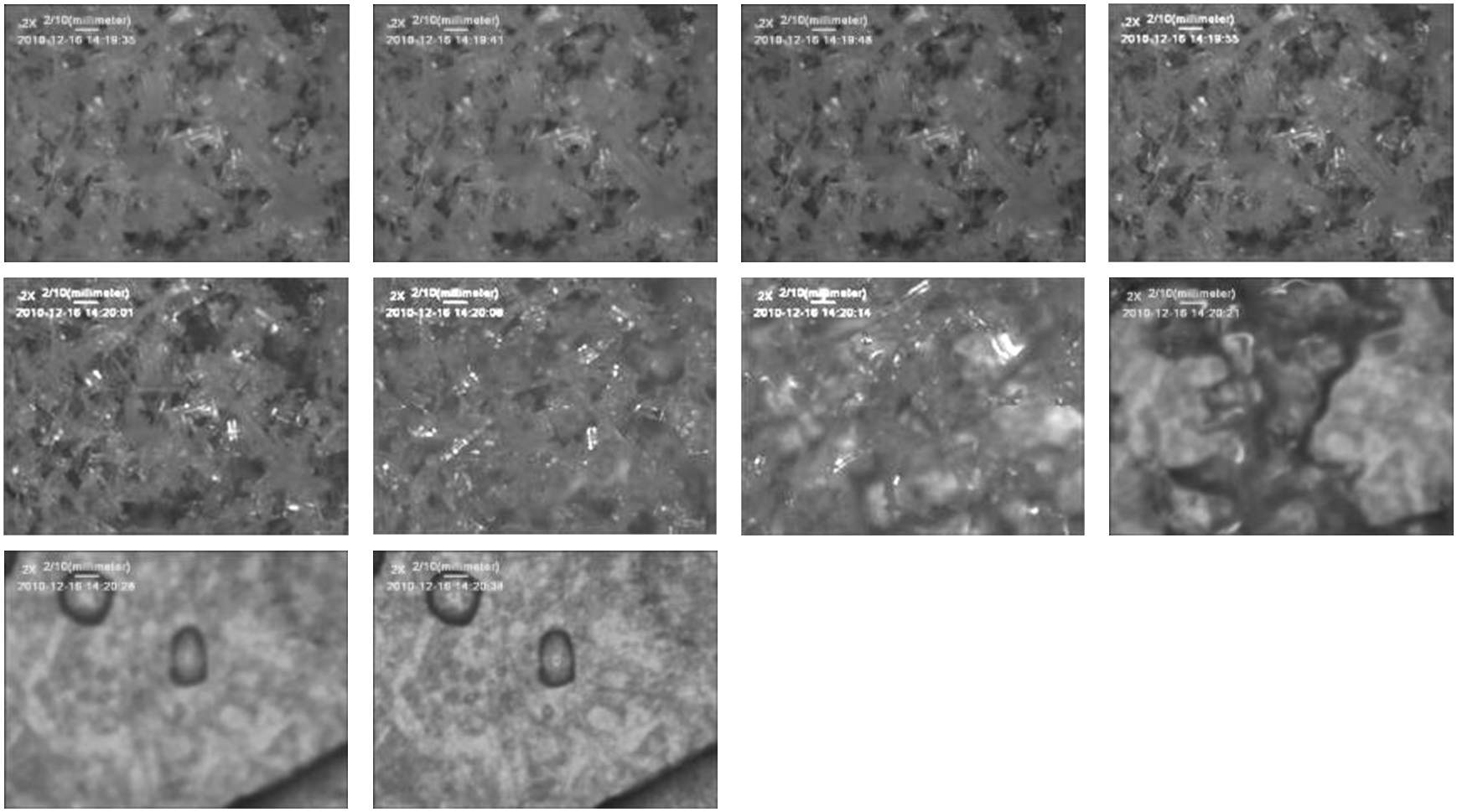

Figure 5-21. Frontal images of defrost 5.0 s intervals (ID 3).

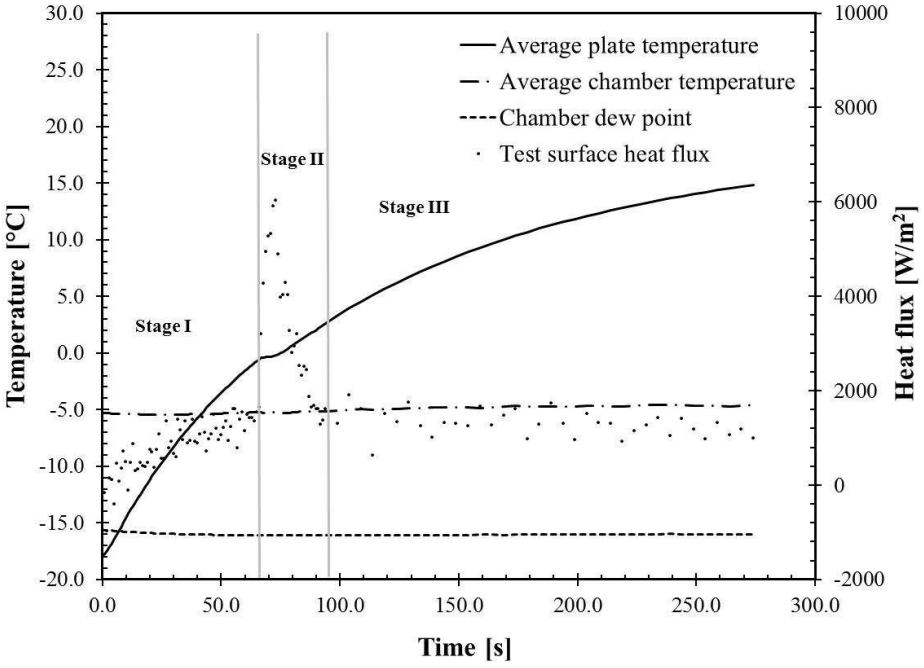

Figure 5-22. Temperature and heat flux during defrost (ID 9).

and water droplets stay in place until evaporated. From the images, it is possible to measure structural changes in the frost layer, which can be used to determine the mass transfer during the defrost process. The time-lapse images provide a basis of reference to compare the temperature and heat flux measurements.

Figure 5-22 shows the temperature and heat flux during a typical defrost. From this figure, it is possible to see the frost melt between the stages of the defrost process. As heat is applied to the test surface, the surface temperature rises until it reaches the melt temperature of the frost. At 65 s, a transition is seen in the surface temperature as it levels off at ~0°C. The surface temperature remains constant at the melt temperature until the ice crystals at the surface have melted. At this time the surface temperature begins to rise, due to heat transfer across the water film layer between the solid surface and the frost layer. The next transition is when frost completely melts, leaving only liquid film and droplets on the surface. The temperature continues to rise as heat is applied to the surface, and the water droplets evaporate. The highest heat flux is seen during the melting stage. The heat flux during the final dry out stage is nearly constant.

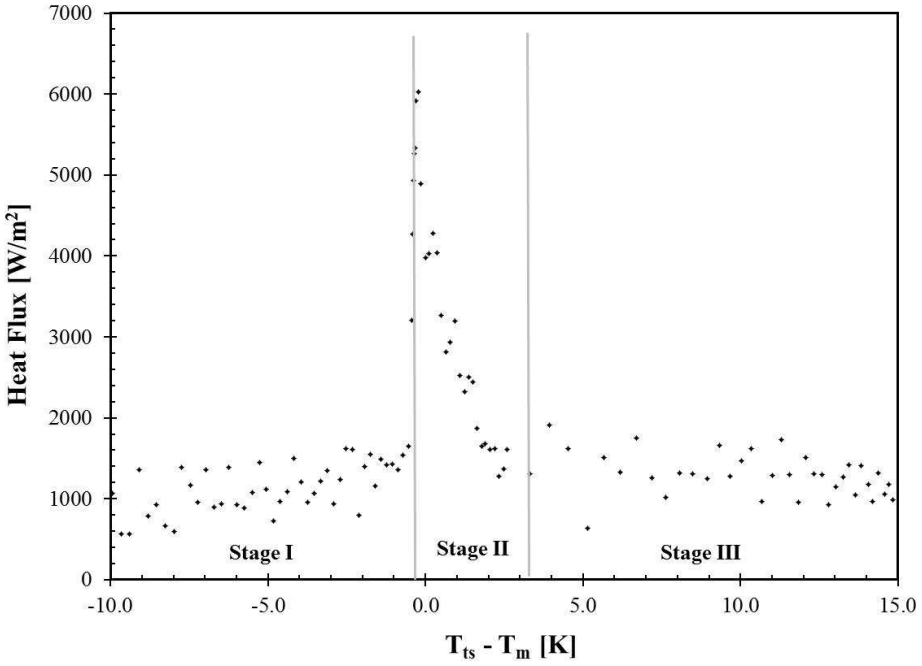

Figure 5-23. Heat flux versus temperature differential during defrost (ID 9)

From the time series plot alone, it is difficult to determine the transitions between the different stages of the defrost process. The heat flux plotted against the temperature differential with respect to the melt temperature at the surface appears to be a better indicator of the defrost process Figure 5-23. When the temperature difference of the surface reaches about zero, melting begins, and a dramatic increase in the heat flux at the surface is measured. During the initial melt process, it is similar to if an infinite heat sink has been applied to the surface. Any heat applied to the surface is quickly absorbed by the melting frost layer. The transition between the melting (Stage II) and dry-out (Stage III) processes of defrost is less defined, but appears to happen when the surface temperature is about 2.5°C above the melt temperature. The change in temperature indicates a short melt period, but the heat flux indicates a longer melting stage. The video images support the longer melt period indicated by the heat flux measurement.

5.3.2 Mass transfer during Stage I defrost

One objectives of this study was to definitively determine the mass transfer during

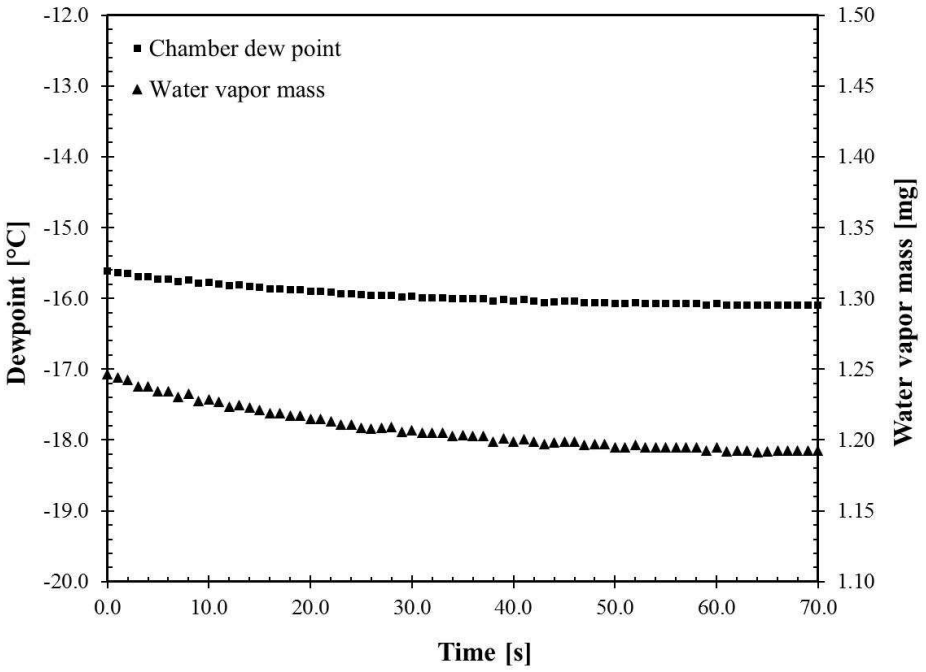

Figure 5-24. Stage I dew point and water vapor mass (ID 9).

each stage of the defrost process. Most prior studies assume that mass transport via sublimation during the first stage is negligible. The apparatus used for this study is capable of making measurements of the chamber dew point temperature during the defrost tests. As seen in Figure 5-24, the chamber dew point is found to vary slightly during the test with a small reduction in dew point temperature. Using Equation (4.8), it is possible to calculate the mass of the water vapor in the test chamber at any given time. For the data shown in Figure 5-24, the initial mass is 1.192 mg and a final mass 1.238 mg for a total mass change of 0.046 mg in the frost layer. By comparison, the total mass of the frost layer is ~820 mg. Relatively speaking only 0.01% of the mass was transferred by sublimation. Using Equation (4.9), the mass transfer rate was calculated as 0.51 mg/m^2s for ID 9. Table 5-3 summarizes mass transfer rates for this investigation, which are exceedingly small, generally on the order of milligrams per second.

Also listed in Table 5-3, is the first stage Stefan and Lewis numbers as calculated by Equations (3.49) and (3.50). As shown in Section 3.2.1, Γ_1, the reciprocal of the Stefan and Lewis number, is a key parameter in the mass and energy conservation

Table 5-3. Mass transfer for Stage I defrost.

Test ID	Mass transfer rate [mg/m^{2}s]	St_1 Eq. (3.49)	Le_1 Eq. (3.50)	Γ_1 Eq. (3.43)
1	5.01	0.0155	5885	0.0110
2	1.39	0.0077	6544	0.0197
3	2.04	0.0147	12074	0.0056
4	0.38	0.0149	8459	0.0080
5	1.61	0.0074	8485	0.0159
6	0.10	0.0149	7091	0.0094
7	0.27	0.0145	8052	0.0086
8	1.34	0.0140	6453	0.0110
9	0.51	0.0144	9065	0.0077
10	0.15	0.0135	6178	0.0120
11	0.11	0.0144	11462	0.0061
12	0.32	0.0135	10440	0.0071

equations. A value of $\Gamma_1 << 1$ allows the simplification of the governing equations by neglecting the effect of latent heat and mass transfer through sublimation. The results of this analysis imply that mass transfer effects can be neglected for the types of frost layers tested.

5.3.3 Heat transfer during Stage I defrost

Figure 5-25 shows the temperatures and supplied heat flux during the first stage. The start of the defrost process begins when heat is added to the surface. For the case shown, the surface temperature at the start of defrost is approximately -17 °C, with an air temperature of -5 °C. For the first 40 s of defrost, the plate temperature is well below the air temperature, during which time heat will be absorbed by the frost layer from the air. Heat loss during this stage only happens when the frost surface temperature is above the local air temperature, which is only the last 20 s of the stage. In general, the closer the air temperature is to melt temperature a beneficial heating from the air will occur, and less of the heat supplied to the surface will be lost to the air. This compares well to the observation of other researchers who found substantially better defrost efficiency as the air temperature approaches the melt temperature.

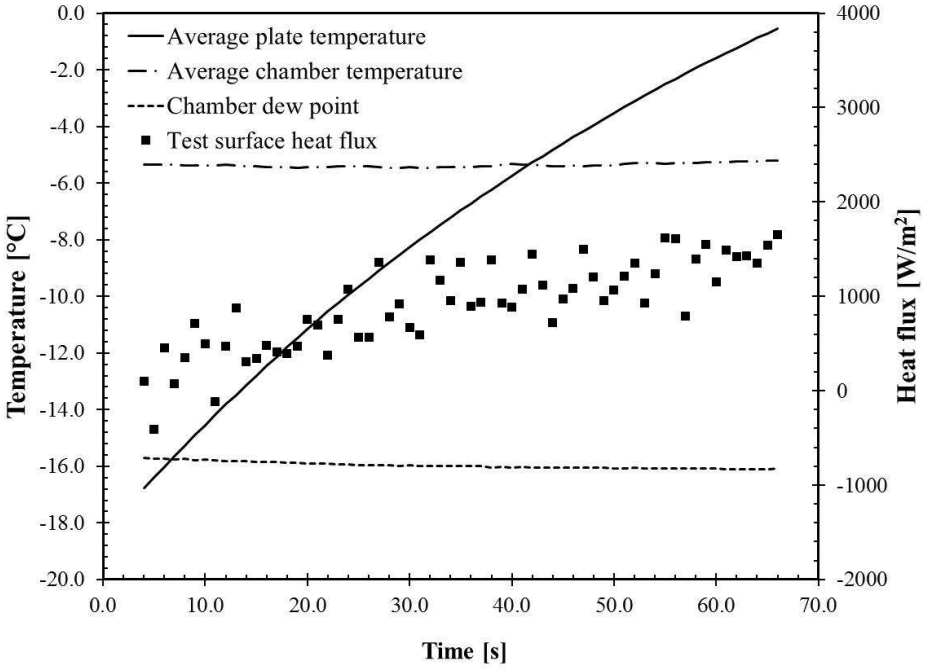

Figure 5-25. Temperatures and heat flux during Stage I (ID 9).

Table 5-4. Summary of energy transfer during Stage I defrost.

Test ID	Heat Input [J]	Heat Stored [J]	Duration [s]	Average Heat Flux [W/m^2]	Sublimation Heat Flux [W/m^2]
1	108.1	9.2	36	1852	1.30E-02
2	51.8	7.7	113	285	3.63E-03
3	133.7	78.6	157	533	5.30E-03
4	121.2	45.4	159	476	9.79E-04
5	67.6	8.3	44	970	4.20E-03
6	99.0	43.9	74	836	2.49E-04
7	90.2	51.3	70	805	7.16E-04
8	101.8	37.4	65	978	3.50E-03
9	83.9	26.6	62	846	1.33E-03
10	75.4	12.0	30	1570	3.87E-04
11	75.4	45.2	39	1209	2.96E-04
12	61.5	42.1	43	893	8.38E-04

Table 5-4 summarizes heat input, stored energy, duration, average heat flux, and sublimation heat flux for first stage of the defrost experiments conducted. Recall from Chapter 3, the initial stage of the defrost process is dominated by the sensible heating of the frost layer. Sensible heat storage during the first stage is,

$$E_{d1} = m_f c_{p,i}(T_m - T_{ts}|_{t=0}), \quad (5.17)$$

where m_f is the mass of the frost, $c_{p,i}$ is the specific heat of ice, T_m is the melt temperature, and T_{ts} is the surface temperature evaluated at the start of the defrost process. From the test record, the first stage defrost time is taken as the value from the moment heat is applied to the surface and terminates at the point when the surface temperature reaches the melt temperature Figure 5-22. By integrating the supplied heat flux with respect to time, the input energy for the defrost process is calculated Equation (4-16). Dividing the input energy by the defrost time and test surface area calculates the average heat flux during this portion of the test. From the mass transfer rate Table 5-3, it is possible to estimate the heat transferred by sublimation using Equation (3.5). As seen in Table 5-4, the heat transferred by sublimation is insignificant when compared with the total heat transfer. Thus the mass and energy transfer by sublimation in the first stage of the defrost process is negligible to the overall mass and energy balance.

5.3.3.1 Stage I Defrost Efficiency Model

Recall from Section 1.1.3, defrost efficiency is defined as the minimum heat input, divided by the total heat input. Using Equation (4-15), the defrost efficiency from the first stage is displayed in Table 5-5. A wide range of defrost efficiency occurs, 16.3% to 67.0%. When compared to all of the factors e.g., input heat flux, degree of sensible heating, chamber air temperature, frost thickness, mass, and porosity, defrost efficiency correlates most strongly with frost porosity Figure 5-26. Interestingly, a relatively small change in porosity appears to produce a significant change in defrost efficiency. A less defined correlation with air temperature was also seen. Higher air temperatures tend to have higher defrost efficiency. This compares well to the results of other studies (Donnellan, 2007 and Muehlbaurer 2006).

Table 5-5. Summary of defrost efficiency during Stage I defrost.

Test ID	Porosity [-]	Average Chamber Temperature [^{o}C]	Sensible Temperature Change [K]	Defrost Efficiency [%]
1	0.54	-8.5	7.16	23.9
2	0.58	-1.2	9.18	16.3
3	0.42	0.0	19.32	58.4
4	0.48	-7.7	18.38	39.5
5	0.54	-0.6	9.46	18.1
6	0.51	-6.9	20.00	43.4
7	0.49	-5.5	19.26	55.6
8	0.53	-5.0	18.27	36.9
9	0.47	-8.2	16.63	36.2
10	0.54	-4.6	14.51	17.9
11	0.43	-4.6	19.13	58.9
12	0.45	-3.4	18.00	67.0

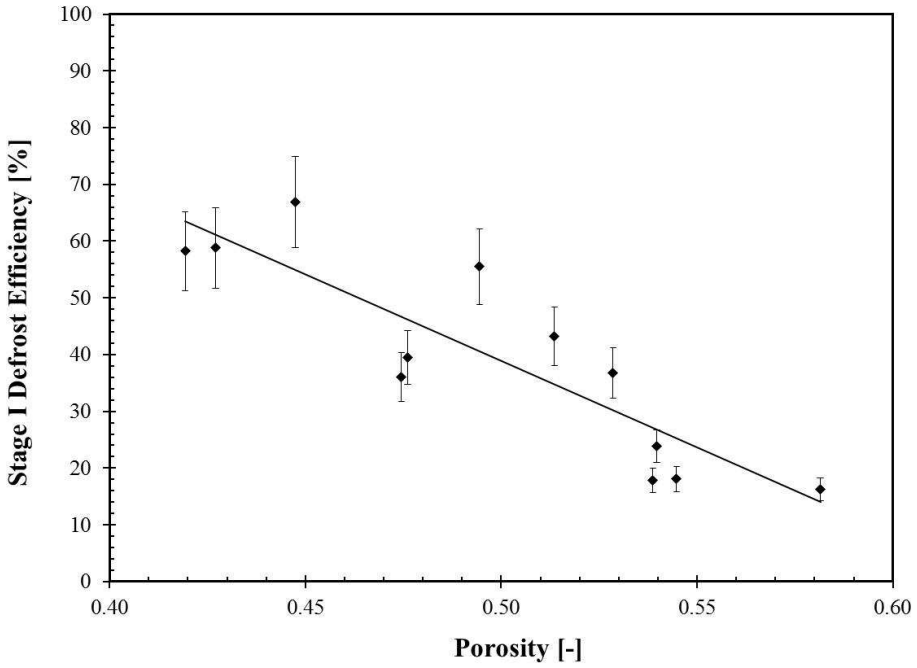

Figure 5-26. Stage I defrost efficiency.

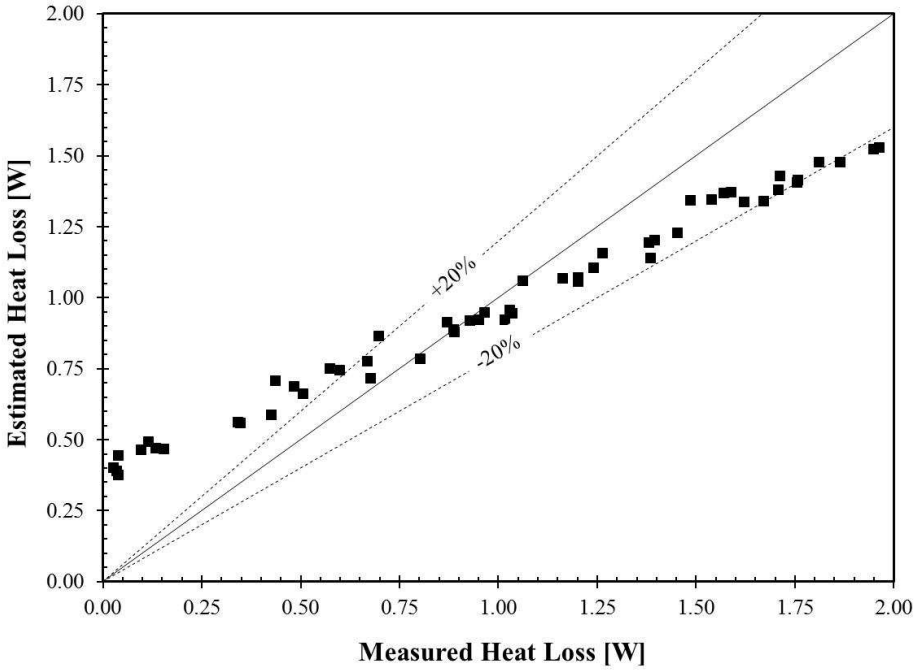

Figure 5-27. Comparison of measured to estimate heat loss (Equation 5.19).

Using the strong dependency of defrost efficiency to porosity, a new heat transfer model is proposed. If the defrost efficiency is assumed to be constant during the entire stage, Equation (4.17) can be reordered and differentiated with respect to time to give,

$$\frac{dE_{d1}}{dt} = Q_{f,d1} \approx \eta_{d1} Q_{ts}, \tag{5.18}$$

where $Q_{f,d1}$ is the stored heat absorbed by the frost layer. Applying an energy balance at the frost-air interface, the lost heat, $Q_{l,d1}$, is,

$$Q_{l,d1} = Q_{ts} - Q_{f,d1} = (1 - \eta_{d1}) Q_{ts}. \tag{5.19}$$

Figure 5-27 compares the measured heat loss to the estimated heat loss using Equation (5.19) for the case where the defrost efficiency is 31.6% (ID 9). The model over predicts the heat loss for low heat flux, and under predicts it for high heat flux. These results imply that defrost efficiency is not a constant over the heat process. While the model has questionable accuracy for determining the instantaneous heat loss from the surface, it could be useful for providing an approximation of the total energy lost from the surface during the entire first stage.

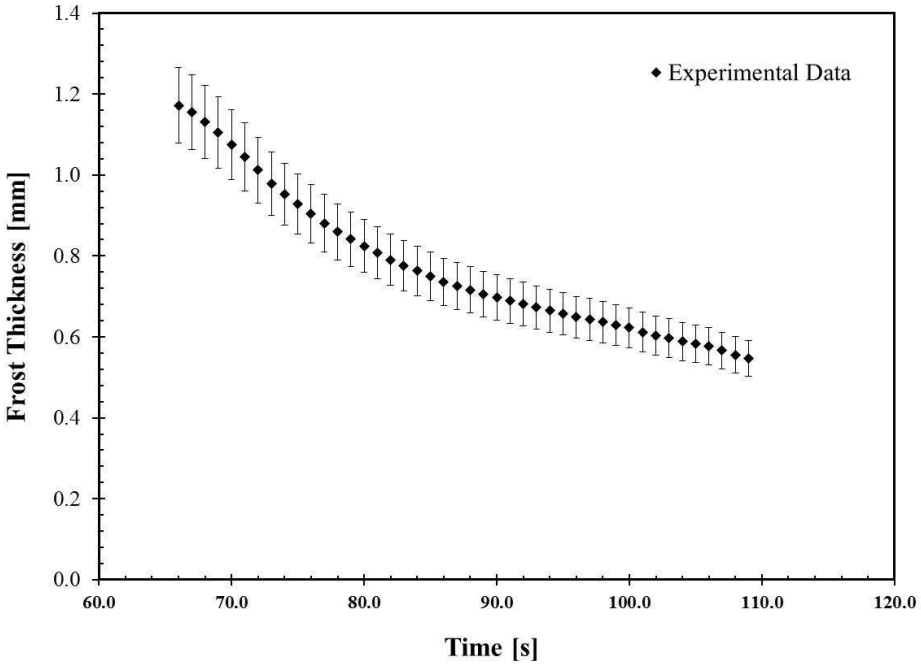

Figure 5-28. Change in frost thickness (ID 9).

5.3.4 Melt rate and mass transfer during Stage II defrost

The second stage of defrost is dominated by the melting of the frost layer. As seen in the series of images in Figure 5-20, the front position changes during defrost. Using the visual technique described in Section 4.5.2, the location of the frost front can be determined at any moment in time. Figure 5-28 shows the change in front position for a typical test case. Once the temperature at the surface reaches the melt temperature, the frost thickness reduces as the melting occurs at the surface. A higher rate of change in the front position was observed during the first 10 s of the melting process, followed by a smaller rate of change for the remaining melt process.

Numerical differentiating the front position with respect to time, an instantaneous front velocity can be calculated. Figure 5-29 shows the difference between the measured and calculated front velocity Equation (3.19). A larger front velocity is seen during the initial portion of time for the melt period. This is followed by a slower velocity until all of the frost is completely melted. The larger initial front speed is due to the direct contact

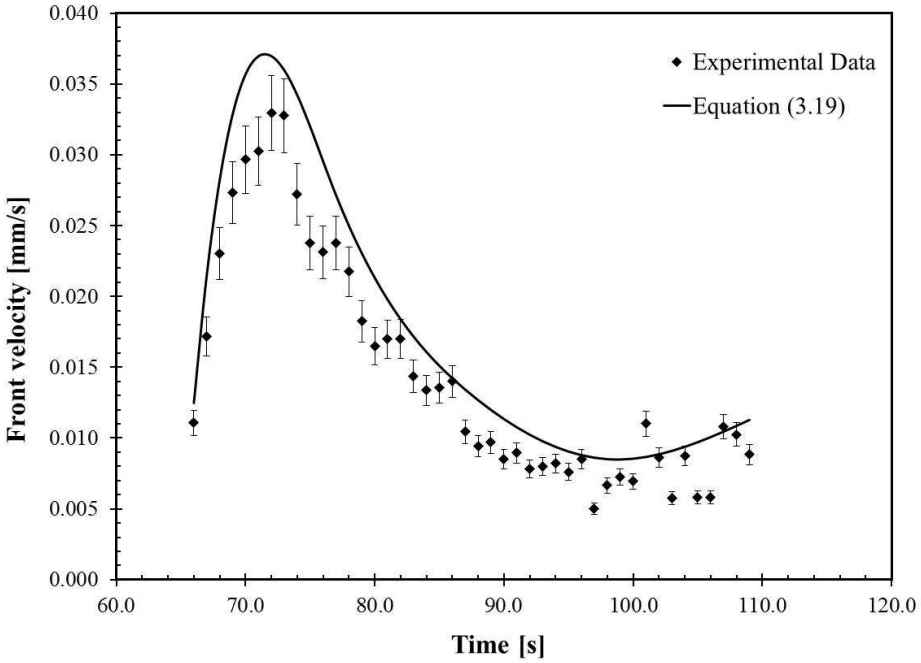

Figure 5-29. Measured and modeled front velocity (ID 9).

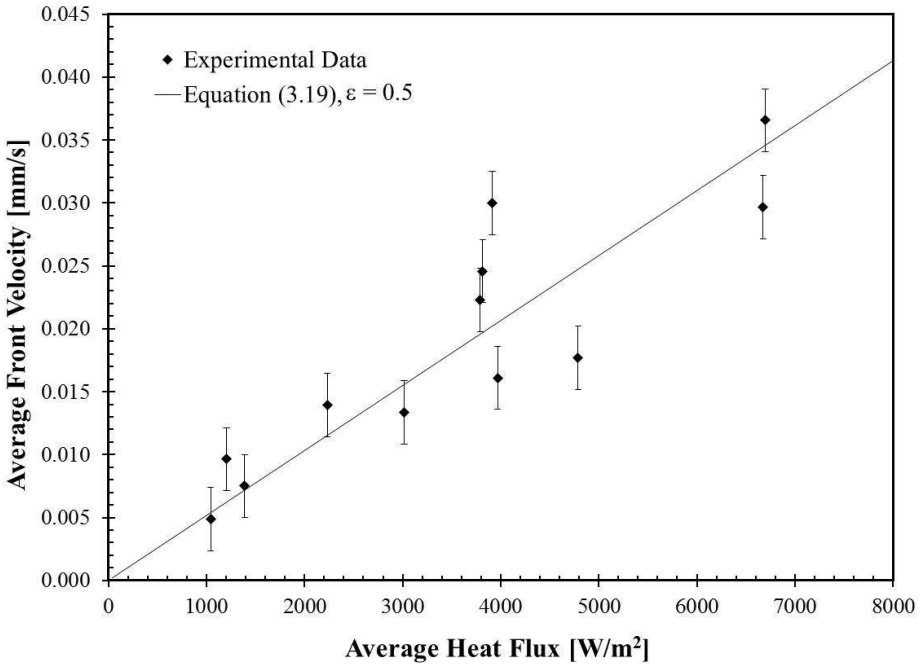

Figure 5-30. Average front velocity vesus average heat flux.

of the frost crystals with the heated surface, which aids in heat transport from the surface to the ice. As the melt progresses heat is transported into the frost layer due to permeation of the melt liquid. As the frost layer becomes fully saturated, a liquid layer forms at the surface, and the front velocity decreases as heat has to conduct through the liquid film. The excellent agreement between the measured and modeled front velocity shows that melt rate is primarily influenced by the frost porosity and supplied heat flux. Figure 5-30 shows the time-average front velocity for all of the experiments. The time-average velocity is defined as the change in front location from the beginning and end of the stage, divided by the elapsed time. As expected, the average front velocity is strongly influenced by the magnitude of heat flux at the surface. With a higher supplied heat flux resulting in a faster front velocity. For comparison, a line of the average front velocity for a constant frost porosity of 0.5, as calculated by Equation (3.19), is compared to the experimental results. The limited range of porosities achieved during this study, prevent a complete analysis of the impact of porosity on the effect of melt rate, but the strong influence of the supplied heat flux is confirmed.

Similar to Stage I, a small portion of water will escape from the surface as water vapor. Using Equation (4.9), the mass transfer rate for each experiment was calculated, and is summarized in Table 5-6. The measured mass transfer rates were exceeding small, and would have an insignificant effect of the mass transfer during this stage. Additionally in Table 5-6 are the Stefan and Lewis numbers for this Stage, as calculated by Equations (3.74), (3.75), and (3.76). When compared to Stage I, it is observed that the vapor Stefan number is smaller, while the Lewis number is larger, but the parameter Γ_2 is about the same order. A value of $\Gamma_2 << 1$ was shown to allow the simplification of the governing equations to neglect the effect of latent heat and mass transfer through sublimation. The results of this analysis imply that mass transfer through sublimation can be neglected for the types of frost layers tested.

Table 5-6. Mass transfer for Stage II defrost.

Test ID	Mass transfer rate [mg/m^{2}s]	St_{2v} Eq. (3.74)	Le_{2v} Eq. (3.75)	Le_{2f} Eq. (3.76)	Γ_2 Eq. (3.73)
1	7.08	6.50E-03	9.68E+03	28.9	0.016
2	1.32	9.29E-04	4.03E+04	158.5	0.027
3	2.22	7.66E-05	1.20E+06	48.3	0.011
4	2.94	5.89E-03	1.47E+04	46.2	0.012
5	6.32	4.65E-04	9.93E+04	71.9	0.022
6	0.43	5.28E-03	1.34E+04	14.4	0.014
7	0.79	4.21E-03	1.80E+04	16.0	0.013
8	1.28	3.83E-03	1.54E+04	26.5	0.017
9	0.01	6.28E-03	1.48E+04	35.4	0.011
10	2.27	3.53E-03	1.55E+04	55.2	0.018
11	2.46	3.52E-03	2.96E+04	21.1	0.010
12	1.61	2.61E-03	3.40E+04	15.5	0.011

Table 5-7. Defrost time and heat transfer for Stage II.

Test ID	Defrost time [Sec]	Peak heat flux [W/m^2]	Average heat flux [W/m^2]	Sublimation Heat Flux [W/m^2]
1	26	6456	3792	9.97
2	91	2663	1042	3.42
3	152	3227	1389	5.75
4	90	2898	1203	7.62
5	30	5452	3015	8.91
6	30	6400	3914	1.12
7	41	7036	3818	2.05
8	55	8093	3969	3.31
9	26	6031	3432	3.98
10	21	9437	4788	5.89
11	23	13051	6676	6.39
12	20	9773	6699	4.19

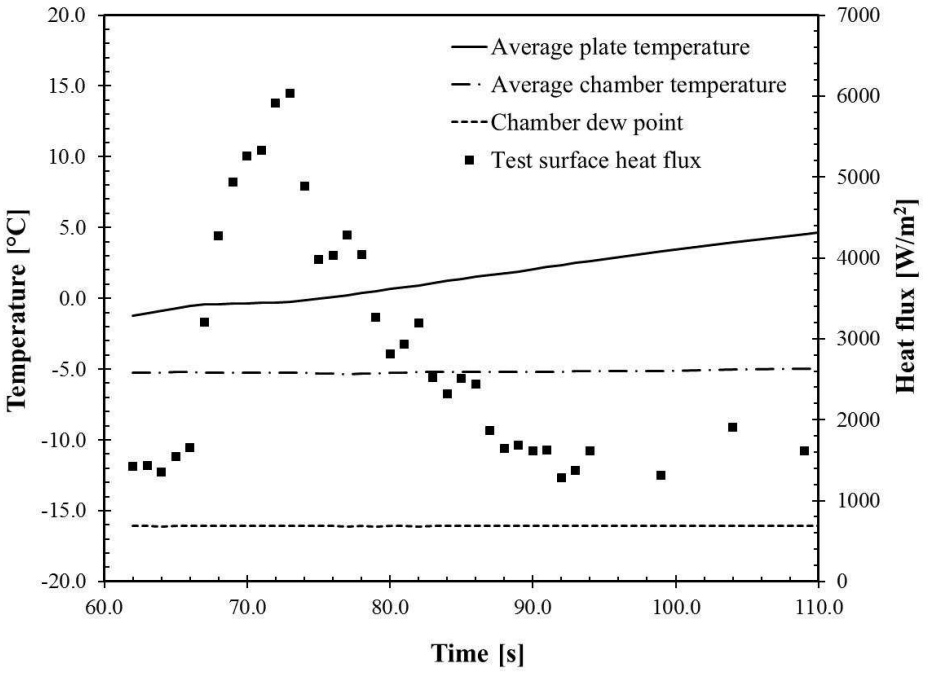

Figure 5-31. Temperatures and heat flux during Stage II (ID 9).

5.3.5 Heat transfer during Stage II defrost

Figure 5-31 shows the heat flux, surface, dew point, and chamber temperatures during the second stage of the defrost process. During the initial moments of the stage, the surface temperature is found to remain nearly constant at 0°C for 8 to 9 seconds, after which the temperature rises at a nearly constant rate. The length of the dwell time is proportional to the amount of frost in contact with the surface and the supplied heat flux. As the thin film of water is formed at the surface, heat is conducted into the water film and then carried into the frost layer. The ice crystals of the frost layer do not maintain contact with the solid surface.

Table 5-7 summarize the average and peak heat flux measured during Stage II. Using the sublimation mass flux in Table 5-6, it possible to calculate the sublimation heat flux. The rate of heat transfer due to sublimation is found to be insignificant when compared to the overall heat transfer rate, accounting for less than 0.5 percent of the total heat transfer. As with the first stage of the defrost process, the amount of mass and heat

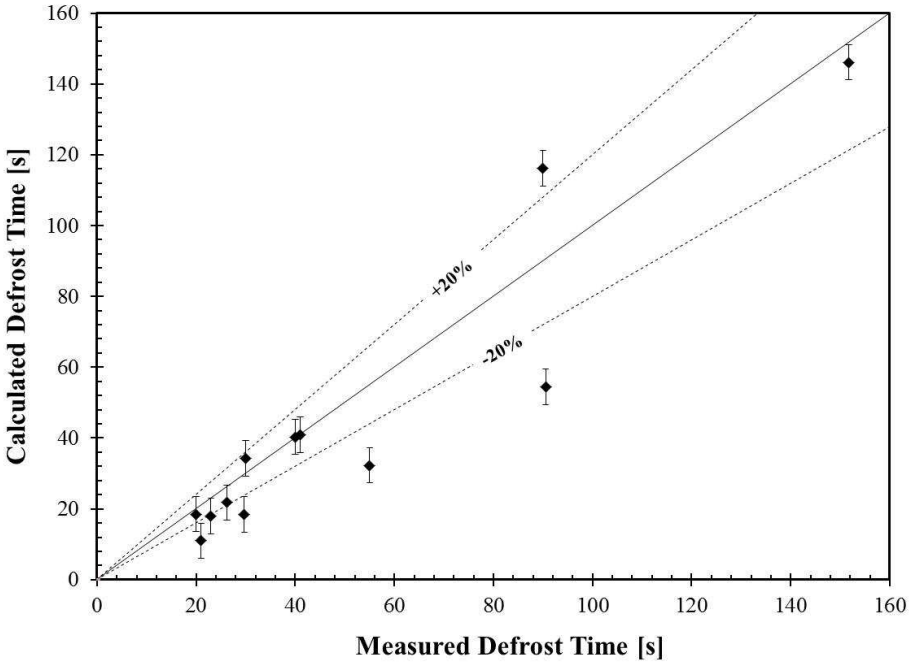

Figure 5-32. Temperatures and heat flux during Stage II.

transported through sublimation is negligible to the overall energy transfer. Any heat supplied to the surface is absorbed by the melting frost layer.

The length of the second stage is difficult to determine from the temperature data. From the temperature data in Figure 5-30, it appears the length of the stage is very brief, only 8 to 9 seconds, while the heat transfer data implies a longer second stage, about 25 to 30 seconds. The digital photographs agree with the longer length of time for the stage. Table 5-7 shows the length of second stage defrost time as measured by the heat flux data. Recall from Equation (3.19), the front velocity is proportional to the frost density, supplied heat flux, and latent heat of fusion. Integrating Equation (3.19), the second stage melt time can be estimated,

$$\Delta t \approx \frac{\lambda_{if}\rho_{f,o}}{q''_s}\Delta\delta, \tag{5.20}$$

where density of frost is taking at the start of the melt, and the heat flux is averaged. Figure 5-32 shows the comparison of the calculated and measured defrost time. The

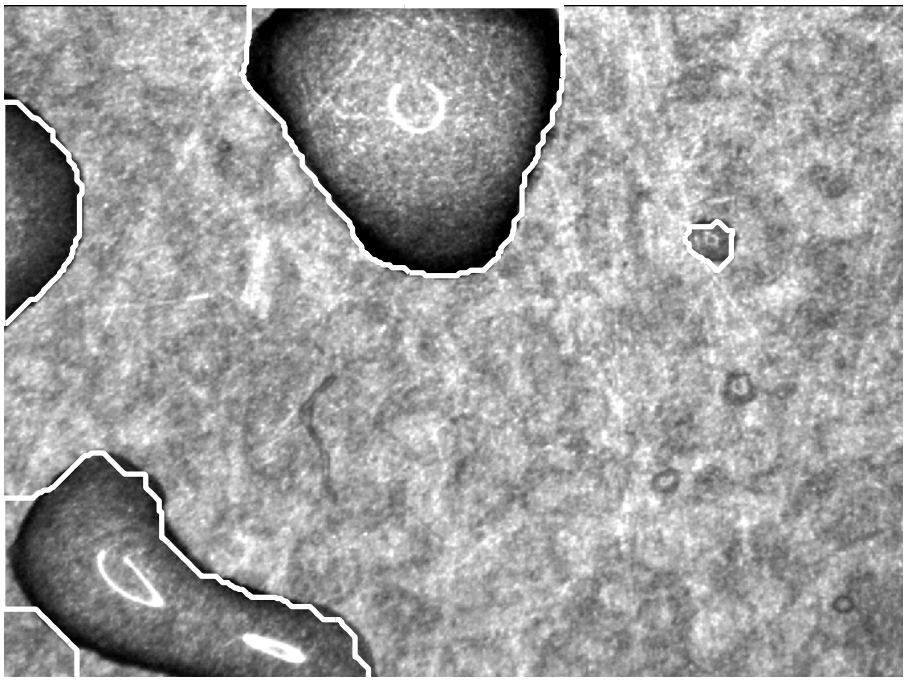

Figure 5-33. Drop size analysis.

simple model provides an acceptable estimation of the defrost time, with most of the calculated times falling within a ±20% tolerance band.

The defrost efficiency of the second stage is defines as,

$$\eta_{d,2} = \frac{\lambda_{if} m_{f,o}}{E_{d3}}, \tag{5.21}$$

Where m_f is the mass of the frost, λi_f is the heat of fusion, and E_d is the supplied heat flux. The measured defrost efficiency were on the order of 95-98%, which was the highest of the three stages. The reason for the high defrost efficiency are the temperature difference between the air and frost surface is small, limiting the heat transfer rate, and the stage is brief, limiting the amount of time for heat to escape. As mentioned earlier, as heat is supplied to the surface, it is readily absorbed by the melting frost layer.

5.3.6 Mass transfer during Stage III defrost

For the dry-out phase of defrost, the mass transfer of the melt liquid through draining and evaporation from the surface dominates the stage. From the visual test

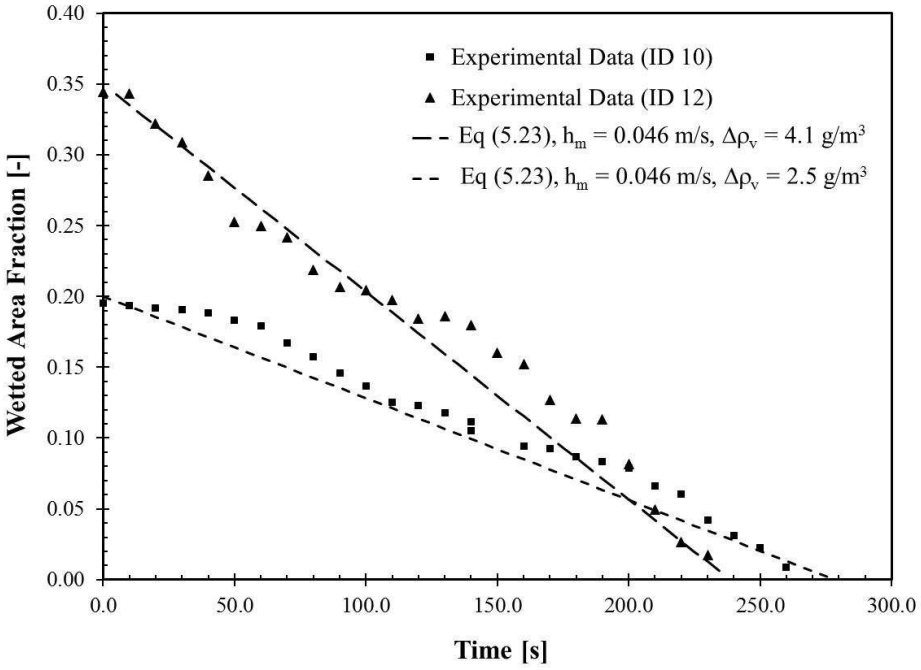

Figure 5-34. Change in wetted area during Stage III.

records, the film flow is a relatively quick process taking just a few seconds. At the conclusion of the draining process, the surface is wetted with stationary water droplets. Using the visual analysis technique described in Section 4.6.8, the mass transfer rate through evaporation can be determined by measuring the change in volume of the water droplets of the surface. The measurements made in this study did not make it possible to quantify the effect of drainage on the overall mass transfer.

Figure 5-33 shows an example of an image from the dry-out process with the edges of the droplets detected using the visual analysis algorithm. By tracking the number and size of the droplets during the dry-out phase, the total water mass on the surface can be calculated as a function of time. Figure 5-34 shows the change in wetted area for two different test cases. The data shows that the rate of change of the retained mass is dependent on a number of factors. The primary factor affecting the evaporation process is the water vapor pressure difference between the surface and the ambient air. As expected, a higher vapor pressure difference results in a greater rate of change and

Table 5-8. Mass transfer for Stage III defrost.

Test ID	Mass transfer rate [mg/m^{2}s]	Mass transfer coefficient [m/s]
1	0.56	0.051
2	0.26	0.030
3	0.50	0.055
4	0.41	0.039
5	0.61	0.064
6	0.55	0.052
7	0.50	0.047
8	0.56	0.051
9	0.51	0.048
10	0.94	0.083
11	0.98	0.083
12	0.72	0.070

shorter dry-out time. The other observation from the test records is the duration of the third stage is significantly longer than the other two stages, on the order of 200 to 300 seconds. This is due to the slower nature of the evaporation process. Using the instantaneous mass data, the mass flux of water leaving the surface is calculated as,

$$m''_{v,3} \approx \frac{\Delta m''}{\Delta t}. \tag{5.22}$$

Besides a reduction in the mass of water on the surface, the contact area of the droplets decreases. As discussed in Section 4.6.7, the change in volume and area can be expressed by a characteristic diameter Equation (4.27). The change in wetted area is proportional to the change in mass. Figure 5-35 shows the change in wetted area during the dry-out phase for the two test cases.

Mass transfer only occurs across the wetted area of the surface (e.g., at the drops). The mass transfer from the wetted surface can be calculated from the whole surface mass transfer coefficient by,

$$m''_{v,w} = m''_{v,3} \frac{A_s}{A_w} = m''_{v,3} \frac{1}{f}. \tag{5.23}$$

where f, is the ratio of the wetted and total area of the surface. Combining Equations (5.22), (4.21), and (4.29), the time dependent change in wetted area fraction can be estimated by,

$$f = f_o\left(1 - \frac{h_m \Delta\rho_v}{m_o/A_s}t\right), \tag{5.24}$$

where, f_o and m_o are the initial wetted area fraction and retained mass at the start of the dry-out. The initial wetted area and mass are a function of wettability of the surfaces, and for the surface tested are discussed in Section 5.3.8. In Figure 5-34, Equation (5.23) is compared against the experimental results for two cases. The model has reasonable agreement to the measured data.

Once the mass transfer from a drop is known, the mass transfer coefficient can be estimated using Equation (4.29). Table 5-8 summarizes the measured mass transfer and mass transfer coefficients that occurs across the wetted area of the surface for all of the experiments. By comparison, the mass transfer coefficient estimated by the heat and mass transfer analogy Equation (3.14), is around 0.045 to 0.060 m/s for condition of the experiment, which is close to the measurements made during this study.

5.3.7 Heat transfer during Stage III defrost

Figure 5-35 shows the change of temperature for the third stage of the defrost process. This stage of the defrost process is dominated by the evaporation of the water from the solid surface. From the temperature plot it is impossible to determine the exact transition from the second to third stage when all of the frost crystals have melted. Using the visual record for the reference test case it appears all of the ice crystals melt around 120 seconds into this experiment. Over the course of the dryout stage, the heat flux remains approximately constant, while the surface tempeature increses at an almost constant rate.

In this stage both sensible and latent heat transfer occurs. As discussed in the previous section, the surface is wetted with small water droplets. The water droplets reduce in size as water evaporators, exposing more of the dry surface to the air. Thus the

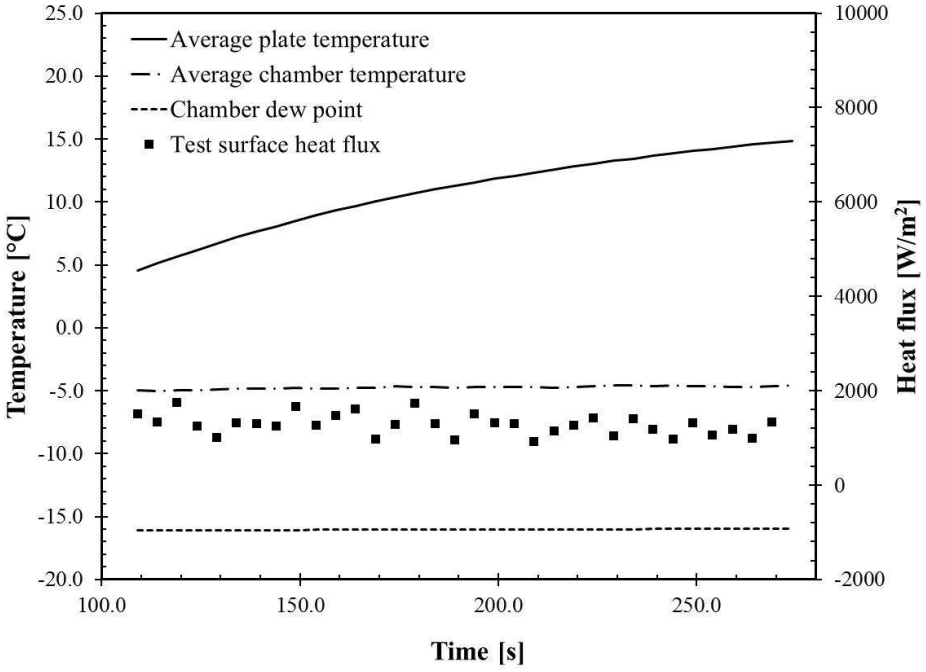

Figure 5-35. Temperatures and heat flux during Stage III (ID 9).

heat transferred from the surface will be a combination of the latent heat from the evaporating water droplets and sensible heat from the dry surface.

$$Q_3 = Q_{3,sn} + Q_{3,lt}, \tag{5.25}$$

Assuming the water dropets are at the same temperature as the surrounding surface, the sensible heat exchange will be across the entire surface, A_s, while the latent heat trasfer would be across the wetted area of the surface, A_w. Thus, the heat flux from the surface can be expressed as,

$$q"_3 = q"_{3,sn} + \frac{A_w}{A_s} q"_{3,lt} = q"_{3,sn} + f\, q"_{3,lt}, \tag{5.26}$$

where $q"_{3,sn}$ is the heat flux of sensible heat exchange, $q"_{3,lt}$ is the heat exchange due to latent heat transfer, and f is the wetted area fraction given by Equation (5.24).

Using the definition of the heat transfer coefficient from Equation (4.14), a total surface heat transfer coefficient, h^*_3 can be defined as,

$$h^*_3 = h_{3,sn} + f\, h_{3,lt}, \tag{5.27}$$

where $h_{3,sn}$ and $h_{3,lt}$ are the heat transfer coefficient for sensible latent heat exchange. The

Latent heat transfer coefficient can be expressed as,

$$h_{3,lt} = \frac{q''_{3,lt}}{\Delta T} = \frac{\lambda_{fg} m''_{v,3}}{\Delta T} = \frac{\lambda_{fg} h_m \Delta \rho_v}{\Delta T}, \tag{5.28}$$

where λ_{fg} is the latent heat of evaporation, $\Delta\rho_v$ and ΔT are the vapor and temperature potentials between the surface and ambient air stream. Substituting Equations (5.23) and (5.27) into Equation (5.26), results in the following relationship for the total surface heat transfer coefficient,

$$h_3^* = h_{3,sn} + f_o \left(1 - \frac{h_m \Delta \rho_v}{m_o / A_s} t \right) h_m \lambda_{fg} \frac{\Delta \rho_v}{\Delta T}, \tag{5.29}$$

From Equation (5.28), it is seen that the total surface heat transfer coefficient is related to a sensible heat transfer coefficient, and a time-dependent latent heat transfer coefficient. Furthermore, the latent heat transfer coefficient decays at a quadratic rate. Figure 5-36 shows a comparison of the measure heat transfer coefficient of an experiment to the results from Equations (5.28), with $h_{3,sn}$ = 40 W/m^{2}K, f_o = 0.45 , m_o = 0.05 kg/m^2 , h_m = 0. 48 m/s. Excellent agreement is seen between the measured and calculated heat transfer coefficient.

Table 5-9 summarizes the defrost time and heat transfer rates to raise the test surfaces to 20°C, which is at a temperature that most of the melt liquid is evaporated from the surface. An observation is that even with high supplied heat fluxes most of the heat is transported through sensible heat exchange with only 2-10% of the heat transported through sensible heat transfer.

Defrost efficiency of the third stage is inherently the worse of the three stages. The primary mechanism for removing moisture from the surface is evaporation of the moisture into the surrounding air stream. Besides the latent heat transfer, there is significant sensible heat lost to the ambient air, which in a refrigerated container, would be the condition air space. Furthermore, as discussed in Section 1.1.3, prolong heating of the heat exchanger mass requires a greater amount of cooling to reduce the coil temperature during defrost recover. Rearranging Equation (5.23), the length of the defrost time for the third stage is approximately,

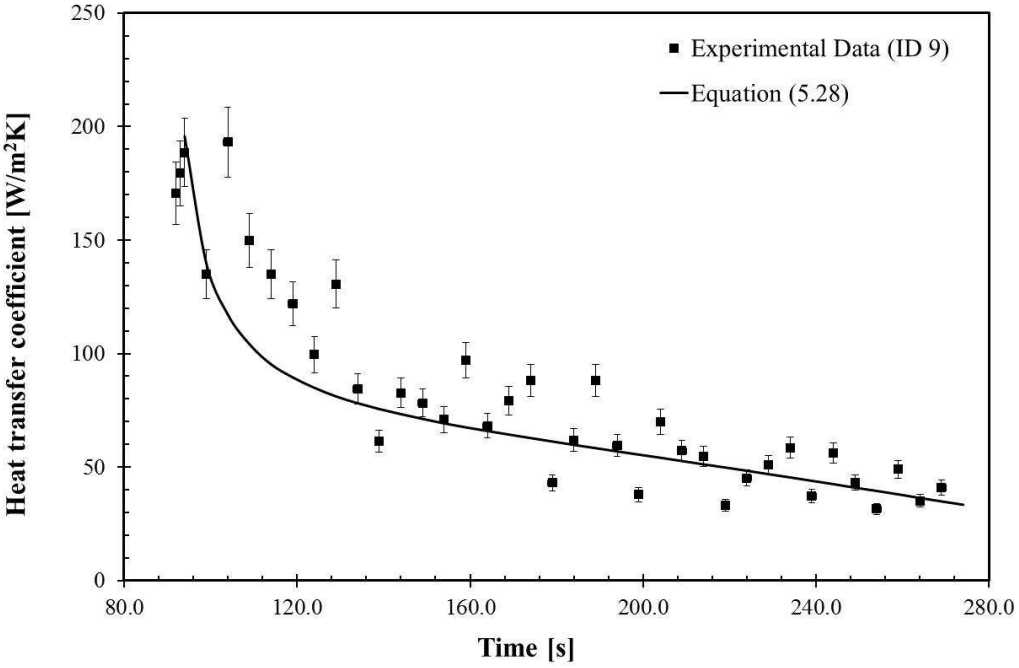

Figure 5-36. Stage III Heat transfer coefficient (ID 9).

Table 5-9. Defrost time and heat transfer for Stage III defrost.

Test ID	Defrost time [s]	Average heat flux [W/m^2]	Latent heat transfer [W/m^2]	Ratio of latent heat transfer [%]
1	153	1755	34.3	2.0%
2	101	245	21.7	8.8%
3	125	1469	26.6	1.8%
4	178	532	32.8	6.2%
5	77	1388	20.2	1.5%
6	166	1467	24.1	1.6%
7	175	535	28.7	5.4%
8	181	1643	29.1	1.8%
9	180	1338	18.1	1.4%
10	75	2492	30.8	1.2%
11	201	2847	41.9	1.5%
12	195	2837	34.0	1.2%

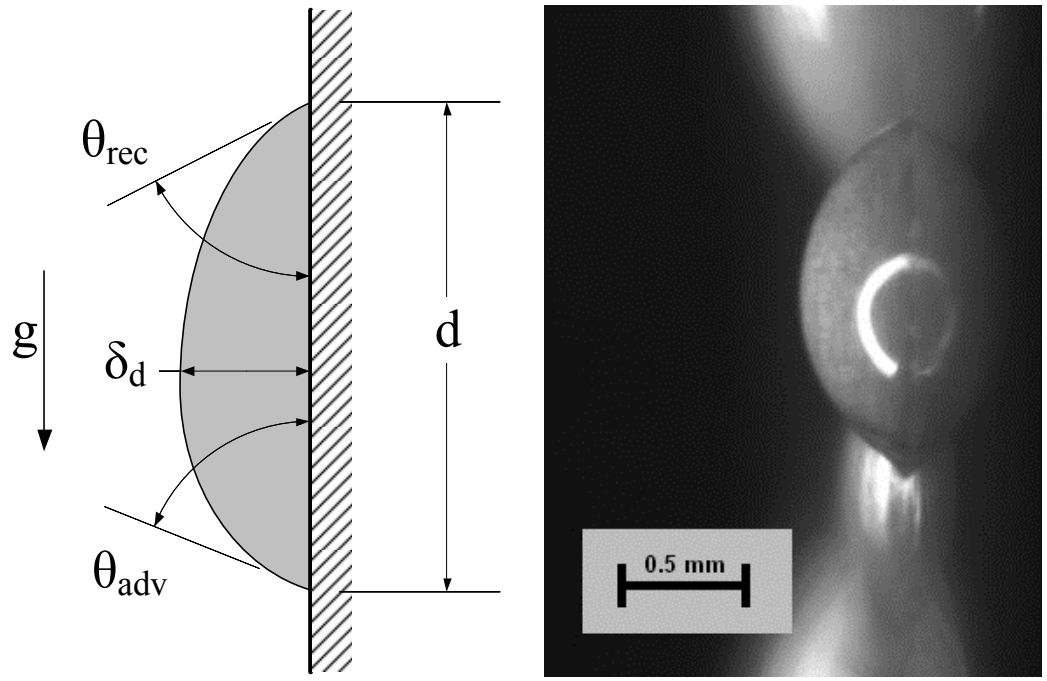

Figure 5-37. Drop contact angle analysis.

$$t = \left(1 - \frac{f}{f_o}\right)\frac{m_o}{h_m \Delta\rho_v}, \tag{5.30}$$

Practically speaking, if the intent is to minimize defrost time and maximize defrost efficiency; decreasing the initial mass of the retained melt liquid on the plate will have the largest impact. The only way to affect the retained mass is to control the surface wettability. Another way to decrease the defrost time is to leave residual moisture on the surface, which is a common practice in the industry. The retained liquid refreeze during the subsequent cooling cycle and generally does not have a negative effect on system performance, other than the frozen droplets can act as a nucleation site, for subsequent frosting cycles. This may lead to more frequent defrost cycles.

5.3.8 Surface wettability during Stage III defrost

Surface wetting is the ability of a liquid to maintain contact with a surface. The wettability of a surface is the balance between adhesion of the water molecules to the surface and the cohesion between individual water molecules. The wettability of a surface is determined by measuring the contact angle of the water droplet on the surface.

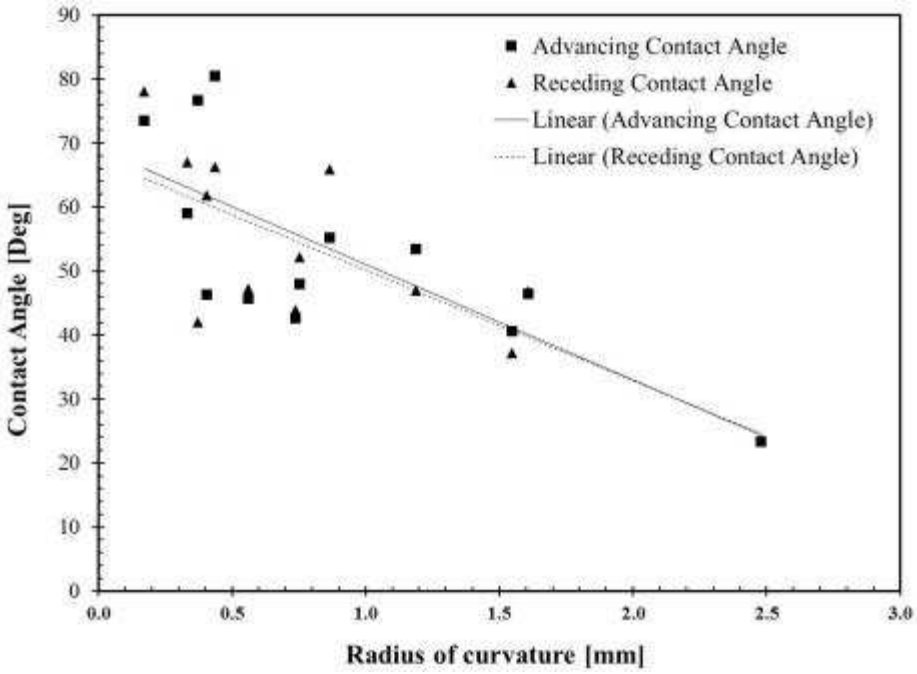

Figure 5-38. Measured contact angle (ID 9).

As seen in Figure 5-37, the contact angle is measured at the solid-fluid interface. Surfaces with contact angles <90° are considered to have high wettability, and are called hydrophilic. A surface with a contact angle equal to 0° is a perfectly wetted surface, and would exhibit no droplet of liquid water, but only a continuous water film. Surfaces with contact angles > 90° are considered to have low wettability, and are called hydrophobic. On a vertically orientated plate, the liquid droplet will have an advancing contact angle, θ_{adv}, on the downward side of the drop, and a receding contact angle, θ_{rec}, on the top of the drop. The difference between the contact angles denotes the drop contact hysteresis. Contact angle hysteresis is dependent on surface finish and gravitational. High levels of hysteresis imply less force to start motion of the drop, which is favorable for shedding of the drop. The contact angle is optically measured using the Sessile drop technique. The advancing and receding contact angles are directly measured on the digital images of the water droplets attached to the surface at the conclusion of the melt process Figure 5-41. Figure 5-38 summarizes the measured contact angles as a function of the radius of

Table 5-10. Summary of defrost efficiency.

Test ID	Mass [g]	Melt energy [J]	Energy Input [J]	Defrost Efficiency [%]
1	0.68	247	721	34.3
2	0.43	149	359	41.6
3	2.13	775	1012	76.6
4	1.31	471	598	78.8
5	0.45	155	499	31.1
6	1.16	420	448	93.7
7	1.41	506	605	83.6
8	1.08	387	630	61.5
9	0.84	303	569	53.4
10	0.43	155	607	25.6
11	1.25	449	570	78.9
12	1.19	441	562	78.4

curvature Equation (4.24). The surface used in this investigation, lapped aluminum alloy 5052-H32, has moderate wettability. The lowest contact angle (highest wettability) is observed for drops with large radius of curvature and is found to increase as drop radius decreases. Low contact angle hysteresis was also measured, which implies that drops did not have a tendency to move. This is supported by the time-lapsed images, where little drop motion is observed. Once a drop forms, it remains in place during the vaporization process.

5.3.9 Defrost Efficiency

Table 5-10 summarizes the defrost efficiency for the various test conditions. The defrost efficiency is defined as the minimum heat required to melt the frost layer, divided by the total heat input. The defrost efficiency can be calculated from Equation (1.2), where the mass of the frost layer is known, and the heat input is calculated by integrating the heat flow at the test surface during the defrost test. For this analysis, defrost was assumed to be completed when the test surface temperature reached 20°C. This results in a higher calculated defrost efficiency when compared to the literature results of defrost

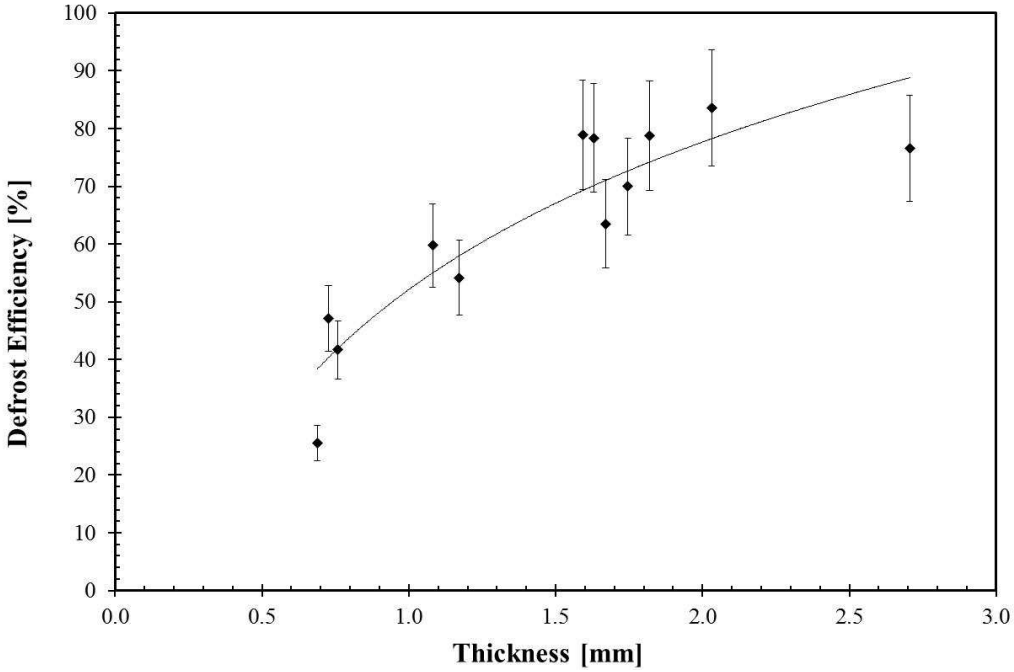

Figure 5-39. Defrost efficiency as a function of frost thickness.

efficiency for a heat exchanger. A wide range of defrost efficiencies were measured, with the minimum at 25.6% and the maximum at 93.7%. Of all of the factors measured (mass, porosity, thickness, θ, etc.), the frost initial thickness was found to have the strongest correlation to defrost efficiency.

As seen in Figure 5-39, the defrost efficiency is found to increase with thicker frost layers. It is inconclusive if there is an optimal frost thickness, as there is not enough data to determine if the defrost efficiency decreases for exceedingly thicker frost layers. It appears that thicker frost layers have better defrost efficiency due to the insulative properties of the frost itself. For the thicker layer, a substantial temperature gradient is formed in the layer. While the crystals near the surface are melting, there is still ice at the air-frost interface, limiting the heat loss. For thin layers, a more uniform temperature gradient in the frost layer results in a greater losses to the ambient air. This conclusion is supported by the visual record, for melting of thick frost layers melt liquid is seen at the surface, while the crystals at the air interface remain solid for several seconds (Figure H-24). Comparatively, for thin layers the entire frost layer appears to melt instantaneously (Figure H-47). From these results, it appears the optimal defrost efficiency occurs for

frost thickness around 1.5 to 2.0mm

5.4 Summary

As part of this study, a new experimental apparatus was constructed. The apparatus consisted of a test chamber with a thermoelectric chiller to cool the ambient air space, a humidity generator with pump to introduce moisture, and a test surface. The test surface consisted of another thermoelectric module to control the surface temperature, which was read by embedded thermocouples and a heat flux sensor to measure the heat transfer rate into and out of the test surface. Steady-state tests were conducted to measure the heat conduction losses from the surface. To validate the apparatus for transient experiments, a number of dry surface cooling and heating tests were conducted and compared favorably to standard head transfer correlations for flow over a flat plate.

A series of frosting experiments were conducted to provide data to validate the visual image analysis techniques, and record the condition of the frost, prior to defrost. The results of this study were compared against several published growth models. A new model for a frosted heat transfer coefficient was proposed. The model has the advantage over previous models, as it combines both the latent and sensible heat transfer effects into a single heat transfer coefficient and correlates this heat transfer coefficient to the growth condition of the frost was measured.

The key contribution of this study are the images and measurements of the defrost process. The heat and mass transfer for each stage of the process is discussed in detail. The primary factor effecting the first stage of defrost is the porosity of the frost layer at the start of the process. A large portion of the applied heat to the surface is absorbed by the frost layer. Frost layers with lower porosity (aka high density) absorbed more of the heat, allowing for less to escape. A rudimentary defrost efficiency model was proposed to calculate the heat lost during this stage. Heat and mass transfer through sublimation during this stage was found to be insignificant.

The second stage of defrost is dominated by the melting of the frost layer. Using a digital analysis technique, the front velocity was measured. The measured front velocity was found to vary with the supplied heat transfer rate and frost porosity. Higher heat transfer rates resulted in faster melt velocity, and thus shortened defrost times.

While lower frost porosity had the effect of increasing the defrost time. Like the first stage, the effects of sublimation were found to be negligible to the overall heat and mass transfer. Defrost efficiency for this stage is nearly 100% with little heat lost to the surroundings.

Evaporation of the melt liquid dominates the final stage. This stage is inherently the worst for defrost efficiency, as most of the supplied heat is lost through sensible heat exchange with the ambient air. A new heat transfer model for the wetted surface is proposed. The model captures both the sensible and latent heat exchange effects. The latent heat exchange is correlated to an area reduction of the water droplets, which is expressed by a mass transfer coefficient.

The overall defrost efficiency was measured for each of the experiments. A wide range of defrost efficiencies was measures, and found to be primarily dependent on frost thickness. It appears that a thicker frost layer is able to trap heat at the surface for the initial stages, aide in the process and limiting the heat loss. A thicker layer also tends to result in more droplets adhering to the surface at the end of the melt and beginning of the third stage. A general improvement in the defrost efficiency can be achieved by limiting the duration of the final stage, but this can result in residual moisture on the surface that will be refrozen in the subsequent cool cycle.

6 *Defrost Models*

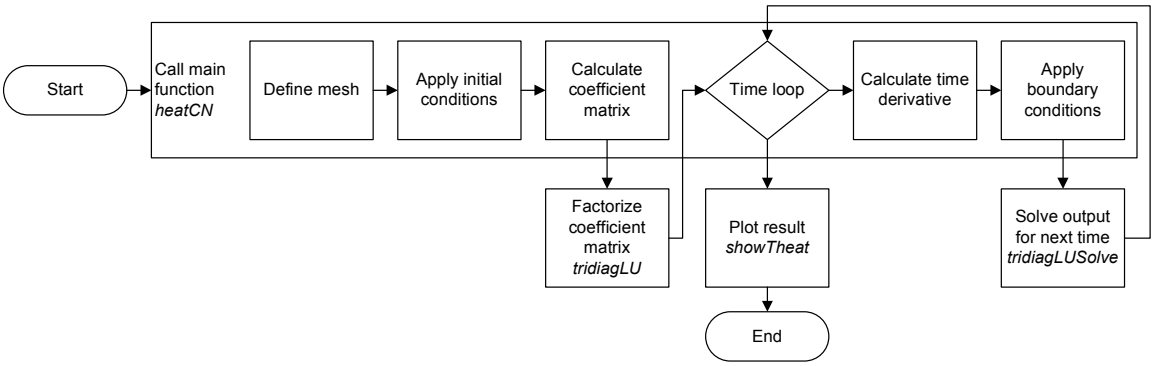

Figure 6-1. Model numerical method.

6.1 Numerical method

As shown in Chapter 3, non-linear differential equations describe the heat and mass transfer during each stage of the defrost process. In most cases, a direct analytical solution is impossible. Of the several finite difference numerical methods available, the Crank-Nicolson (C-N) scheme has been used to solve the fundamental equations. The implicit C-N scheme has the benefit of being second order accurate in time and unconditionally stable, as compared to explicit schemes such as the forward time, centered space (FTCS) or backward time, centered space (BTCS) formulations. Programmatically, C-N method is very similar to the BTCS method (Recktenwald, 2011). The C-N method is the result of applying a center difference to the space derivative, and the trapezoidal rule to the time derivative. The CN method results in a sparse tridiagonal coefficient matrix, which is solved through the LU decomposition method. The sequence of the numerical method is shown in Figure 6-1. All code was written in MATLAB, and copy of the code can be found in Appendix F.

6.2 Stage I

The fundamental equation for the first stage of the defrost process were described in Section 3.2.1. The energy equation is given by Equation (3.59). Applying the numerical method described earlier, the time-dependent temperature distribution and

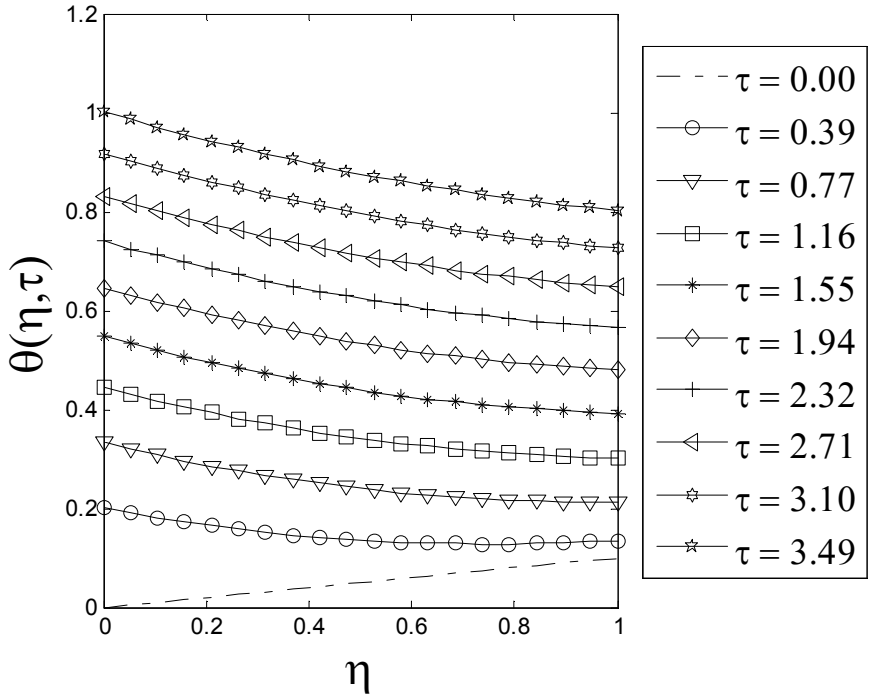

Figure 6-2. Change in frost temperature distribution for Γ_1=0.01, Bi_s = 0.2, Bi_{fs} = 0.1, $\theta_{fs,0}$=0.1, θ_a=0.75.

stage duration can be determined. Figure 6-2 shows the change in non-dimensional can be determined. Figure 6-2 shows the change in non-dimensional temperature distribution within the frost layer for a typical simulation. The boundary condition for this simulation where constant Neumann type. The inner boundary condition of Bi_s = 0.2, an outer boundary condition of Bi_{fs} = 0.1, and a dimensionless air temperature of θ_a = 0.75. The simulation starts with a steady-state temperature distribution that would be found at the end of the frosting process. The simulation end when the surface temperature reaches θ_s = 1.0, which is the point where melting would begin at the surface. In the figure, the temperature profile is shown for equaled spaced time increments. A significant change in shape is seen early in the process. Here most of the heat applied is absorbed by the frost layer. As time progresses, the temperature profile approaches the linear, steady-state, shape.

The two factors that have the large effects on Stage I duration are porosity and boundary condition at the solid surface. Figure 6-3 shows the effect of each of these factors on defrost time. Recall from Section 3.2.1, it was shown that as porosity increase

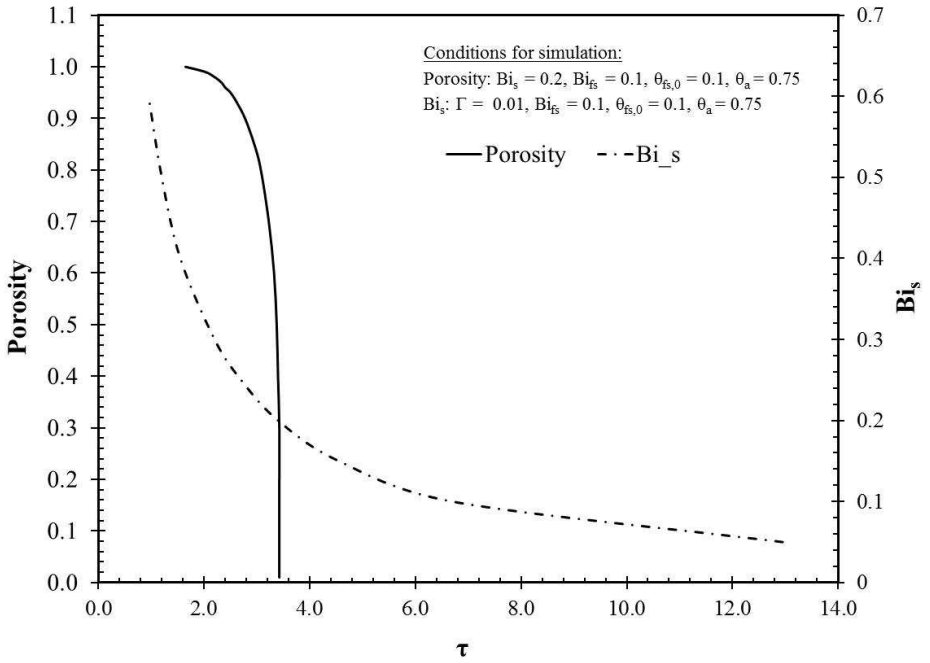

Figure 6-3. Effect of porosity and surface boundary condition on Stage I defrost time.

there is a greater potential of heat transport due to sublimation. The greater heat transport reduces the time it takes for the surface to reach the melt temperature. This effect is most pronounced at large values of porosity. For most frost layers, the porosity is typically in the range of 0.4 to 0.6, and the effect heat transport by sublimation is minimal. Changes at the boundary are found to have a greater effect on the duration of Stage I. Increasing Bi_s, such as raising the heat flux at the surface, can dramatically reduce the time.

Table 6-1 summarizes the inputs and results for the simulations that are compared to the experiments for completeness. The effect of Γ_1 was included in the simulation, but had a minimal effect on the results. In general, the model underpredicted the defrost time, but followed the trend of higher surface Biot number resulting in a shorter duration. The disagreement is due to a number of factors. The model assures 1-D heat transfer, while in the experiment 2-D affects were observed. The model assumed a constant heat transfer rate at the interface, while there was difficulty in maintaining a constant heat flux at the surface during the defrost experiments.

Table 6-1. Summary of simulation results for Stage I.

Test ID	Γ_1	Bi_s	Bi_{fs}	$\theta_{fs,0}$	θ_a	τ Experiment	τ Model
1	0.01	0.28	0.07	0.10	0.58	11.5	2.7
2	0.02	0.07	0.06	0.11	0.88	38.3	10.6
3	0.01	0.14	0.12	0.13	1.00	9.4	4.8
4	0.01	0.10	0.09	0.05	0.60	19.4	8.3
5	0.02	0.21	0.05	0.08	0.94	30.4	3.6
6	0.01	0.19	0.10	0.07	0.65	9.3	4.1
7	0.01	0.21	0.11	0.10	0.71	6.8	3.5
8	0.01	0.24	0.10	0.11	0.73	8.8	3.0
9	0.01	0.12	0.06	0.04	0.56	18.5	7.1
10	0.01	0.17	0.04	0.05	0.74	23.3	4.8
11	0.01	0.20	0.07	0.08	0.76	6.7	3.8
12	0.01	0.17	0.08	0.09	0.80	6.8	4.5

Using the results from the simulation, it is possible to calculate the defrost efficiency of the first stage. Recall, the first stage defrost efficiency was defined as,

$$\eta_{d1}^{*} = \frac{\text{Energy absorbed by frost}}{\text{Total energy input}} = \frac{\sum(Q_s - Q_{fs})\,\Delta t}{\sum Q_s\,\Delta t}. \tag{6.1}$$

Applying the relationship define for the first stage Biot numbers at the surface and frost-air interface, equation 6.1 can be expressed as,

$$\eta_{d1}^{*} = 1 - \frac{Bi_{fs}}{Bi_s}\sum(\theta_{fs} - \theta_a)\,\Delta\tau. \tag{6.2}$$

The first stage defrost efficiency will be less than one when the frost surface temperature is greater than the air temperature, and greater than 1 when the air temperature is higher than the frost surface temperature. In the first case, heat from the surface will be lost from the frost and into the air, and in the second case heat from the air will be absorbed by the frost layer from the air stream, which will aid the defrost process. In most situations, at the start of the defrost process, the temperature of the frost surface will be below the air temperature, resulting in a high defrost efficiency. As time progresses, the frost surface temperature will exceed the air temperature resulting in a loss of heat to the

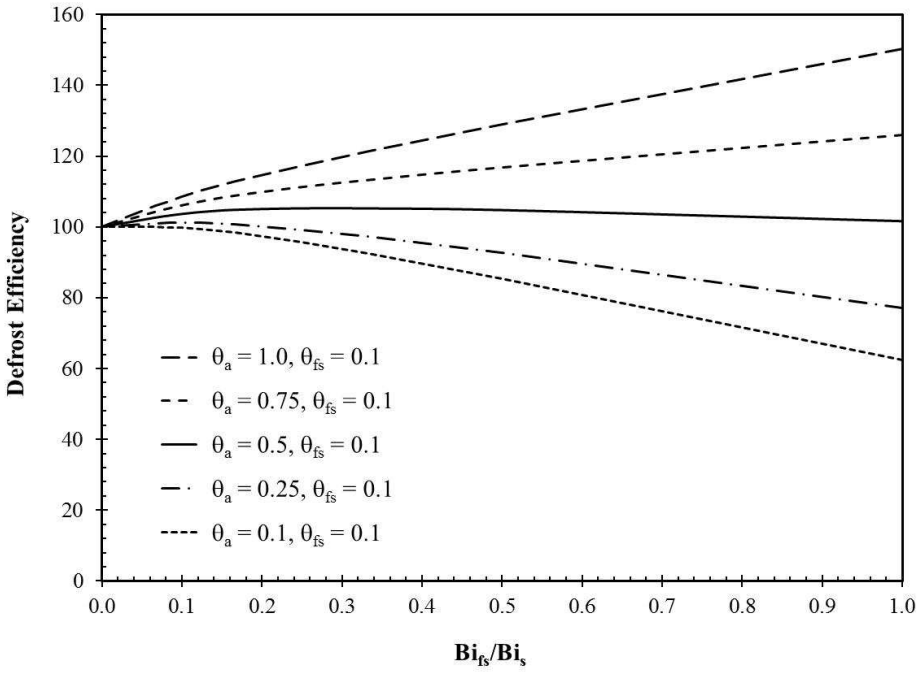

Figure 6-4. Effect of boundary conditions on Stage I defrost efficiency.

ambient air, and a reduction of the defrost efficiency. The temperature difference is scaled by the ratio of the Biot numbers at the air-frost and frost-solid interfaces. A higher surface Biot number results in a lower ratio, reducing the temperature effects on the defrost efficiency.

Figure 6-4 shows the effect the ratio boundary conditions have on the defrost efficiency of the first stage for various air temperatures. When the air temperature is near the melt temperature, defrost efficiencies greater than 100% can be achieved. Once the temperature falls below 0.5, defrost efficiency is below 100%, but can be positively improved by having a high heat transfer rate at the surface interface relative to the air interface. Ways to maximize the defrost efficiency are by selecting heat sources that can be supplied at a high rate, such as electrical resistance and reduce the air heat transfer rate by limiting convective or radiated heat transfer.

6.3 Stage II

As discussed in Section 3.2.2, the second stage is modeled as the melting of the frost at the heat surface. When the surface temperature exceeds the melt temperature, the frost melts. The melt liquid is drawn into the open pores of the frost layer, and the thickness of the frost layer will decrease. The rate of change of the frost layer is given by Equation (3.19). Applying an upwind finite difference approximation the position of the front can be given as,

$$\eta_i^m = \eta_i^{m-1} - U\Delta\tau. \tag{6.3}$$

where the velocity ratio, U, is equal to 1 for a constant supplied heat.

As the melt liquid is absorbed back into the frost layer, a wetted permeation layer grows away from the surface. The growth of the permeation layer is described by Equation (3.68), with a water content that is govern by Equation (3.67). Applying a linear upwind approximation, the water content ratio, S, is given by,

$$S_i^m = S_i^{m-1} + \frac{\Delta\tau}{\Delta\eta}[1 - U(S_i^{m-1} - S_{i-1}^{m-1})]. \tag{6.4}$$

Initially, the content ratio throughout the frost layer is assumed to be equal to 0. Once melting starts, the water content at the surface is assumed to be equal to the critical water content value, Sc, equal to 0.1. By definition the water content cannot exceed 1. The location of the permeation front can be estimated as the point where the content ratio is less than the critical water content. Within the permeation layer, the temperature is assumed to be at the melt temperature. The temperature of the remainder of the frost layer is described by Equation (3.72) with the boundary conditions given by Equation (3.77). The initial temperature profile is given by the profile at the conclusion of the first stage.

Due to the change in the frost height, a moving mesh is applied to the numerical method. Figure 6-5, shows the changes to the algorithm specified in Section 6.1. The mesh is initialized for the starting height, and grid spacing. As the grid spacing is changed each time step, the coefficient matrix must be updated, prior to calculating the derivative matrix. This does impose a computational penalty, as the coefficient matrix

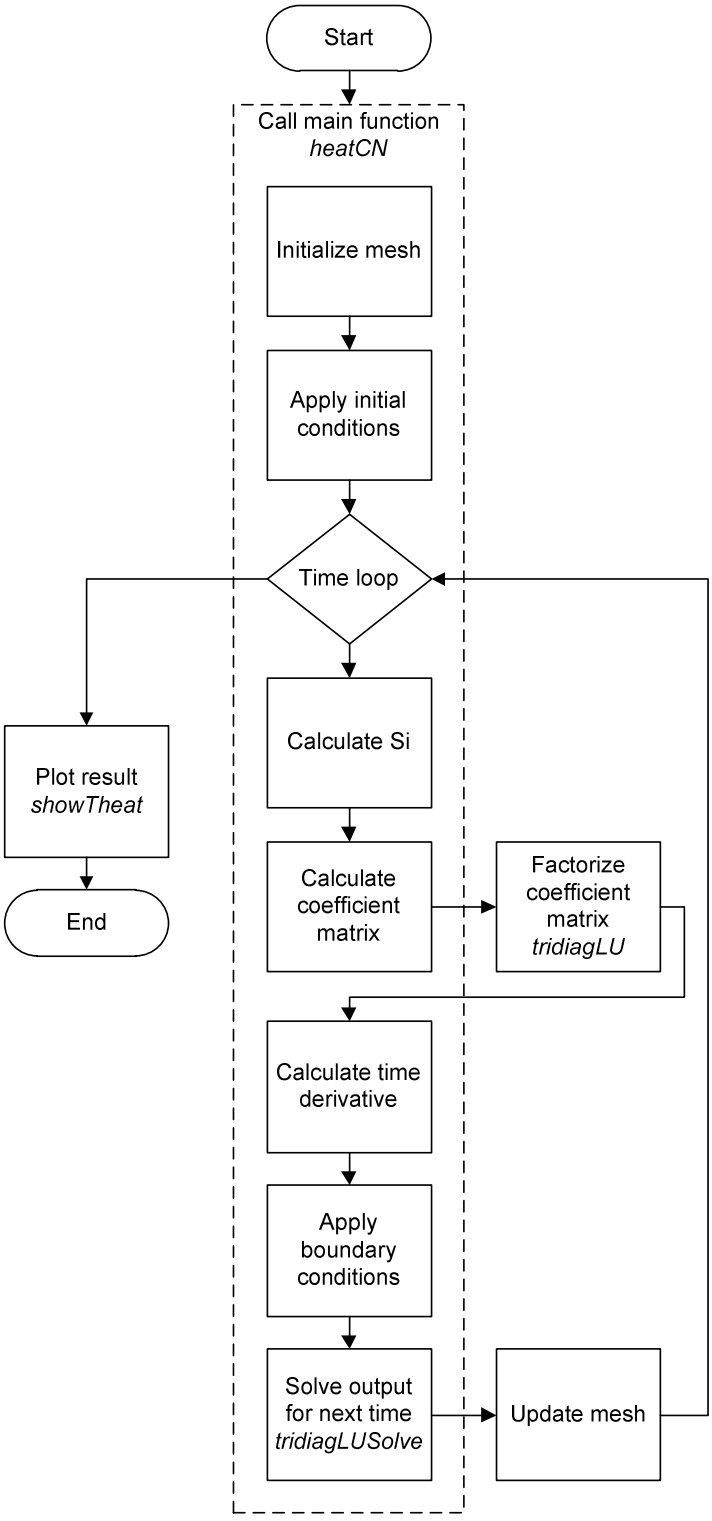

Figure 6-5. Stage II Model numerical method.

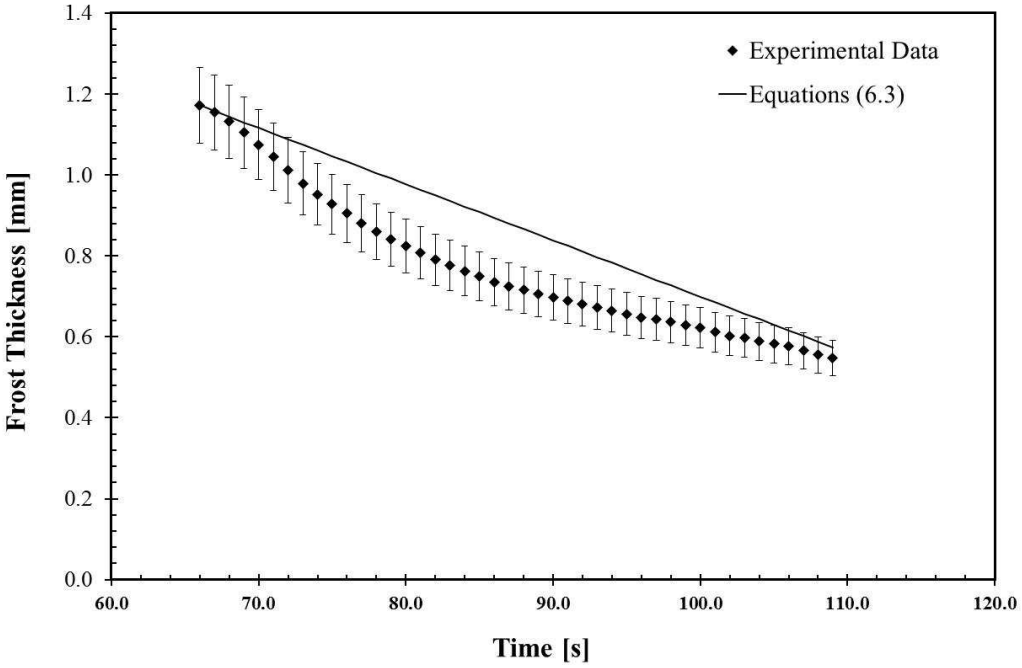

Figure 6-6. Comparison of front location from model to experimental results.

must be factored for each time step. The water concentration gradient is calculated every time step, as it impacts the calculation of the temperature profile. The mesh is update as the last calculation for each time step. The MATLAB code is found in Appendix F.

Figure 6-6 shows a comparison of the front position for an experimental data set (Test ID 9) and simulated results by Equations (6.3). The model predicts a linear change in front position becase a constant velocity ratio was used. During the experiment the front velocity was not constant (Figure 5-29). The non-linear shape of the experimental front position is due to the variability of the supplied heat flux during the test. While a constant velocity ratio doesn't match the data over the whole range, the final front position is predicted fairly accuately. The reason the final precidtion is acceptable is due to the intergral nature of the phase change process, where most of the supplied energy is absorbed by the frost layer, resulting in a fairly uniform melt rate. Using a non-unifrom heat flux for the simulation results in a closer match to the experimental results.

Table 6-2 summarizes the simulation results using the experimenal derived inputs. The model predicts the melt duration within 20% of the measured value, with most of the

Table 6-2. Summary of simulation results for Stage II.

Test ID	u_o [mm/s] Eq. (3.19)	Le_{2f} Eq. (3.76)	Γ_2 Eq. (3.73)	Bi_{2s}	Bi_{2fs}	τ Experiment	τ Model
1	0.022	28.9	0.016	1.50	0.07	0.54	0.45
2	0.005	158.5	0.027	2.35	0.06	0.58	0.55
3	0.008	48.3	0.011	7.61	0.12	0.42	0.41
4	0.010	46.2	0.012	0.70	0.09	0.48	0.52
5	0.013	71.9	0.022	1.93	0.05	0.55	0.54
6	0.030	14.4	0.014	2.77	0.10	0.51	0.59
7	0.025	16.0	0.013	3.69	0.11	0.50	0.50
8	0.016	26.5	0.017	3.94	0.10	0.53	0.51
9	0.014	35.4	0.011	0.78	0.06	0.48	0.48
10	0.018	55.2	0.018	2.21	0.04	0.54	0.48
11	0.030	21.1	0.010	4.80	0.07	0.43	0.43
12	0.037	15.5	0.011	7.06	0.08	0.45	0.42

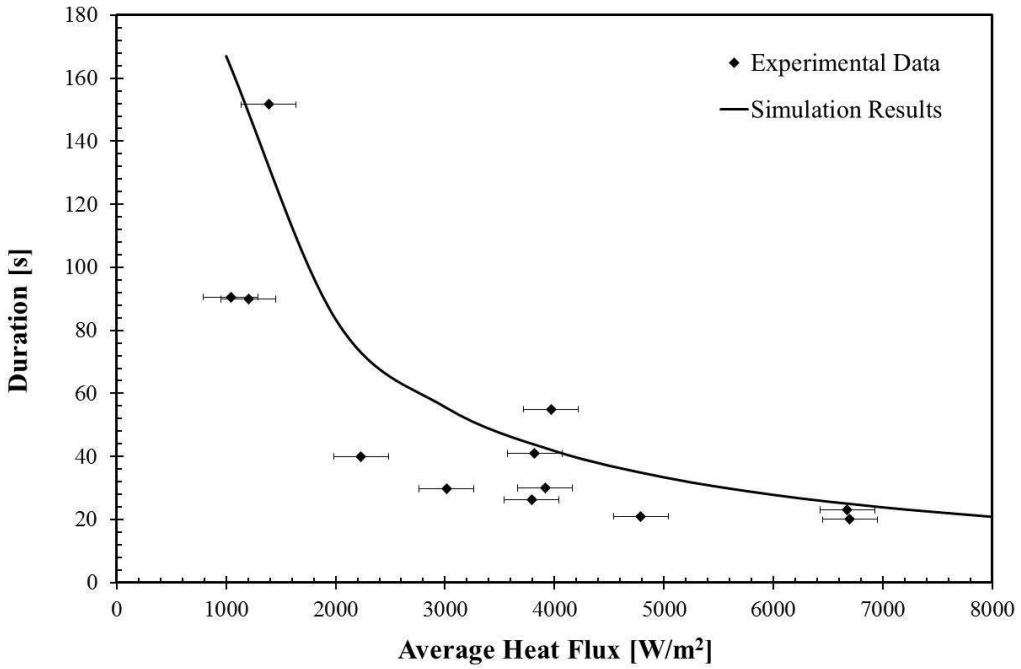

Figure 6-7. Comparison of duration from model to experimental results.

data within 10%. From the dimesionless time, it is difficult to infer the effect of the boundary condition on the defrost time. Converting the model back to engineering units a better correlation can be seen. Figure 6-7 shows the comparison of the experimental results to simulation output for a constant frost thickenss and porosity. A strong relationship between the stage duration and supplied heat flux was confirmed. A higher heat flux results in a shorter duration, but as the heat flux is dramatically increased the effect on shortening the duration is dimished. From the figure it appears a optimal heat flux would be about 5000 W/m^2.

6.4 Stage III

As discussed in Section 3.2.3, the third stage is modeled as the evaporation process of a thin water film on the heated surface. The heat and mass transfer of the third stage are expressed by the coupled ordinary differential Equations (3.86) and (3.87). Equation (3.87) have the solution,

$$\theta = \frac{C_2}{C_1}(e^{C_1\tau} - 1), \tag{6.5}$$

where, C_1 and C_2 are defined,

$$C_1 = \left[Bi_{3,w}, + \frac{1}{St_3}\frac{1}{Le_3}\right], \tag{6.6}$$

$$C_2 = Bi_{3,s}. \tag{6.7}$$

The constant C_1 represents the sum of the sensible and latent heat transfer from the film surface, while C_2 is the heat into the film from the surface. Substituting Equation (6.3) into (3.86) and integrating, film thickness is,

$$\eta_w = 1 - \frac{C_2}{{C_1}^2 Le_3}\left((e^{C_1\tau} - 1) - C_1\tau\right), \tag{6.8}$$

As discussed in Section 5.3.7, the magnitude of the heat transfer at the surface has a large effect on the duration of the third stage. Figure 6-8 shows the film thickness, Equation (6.6) and the temperature Equation (6.5) during the dry-out process for various supplied heat fluxes with all other factors held constant. Like the experimental results an

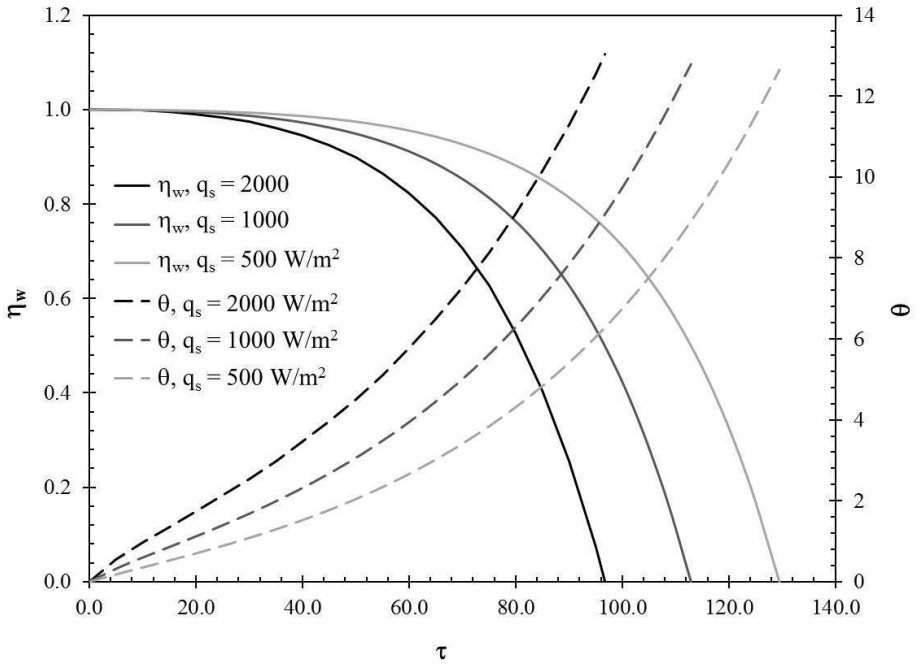

Figure 6-8. Effect of surface heat flux on Stage III defrost.

increase in heat flux shortens the defrost time. An important observation from the simulation is the slow rate of change in the film thickness for a substantial period of the dry-out process. For example, the first 20% of reduction in film thickness takes over60% of the total time. This is due to the evaporation process, as the vapor pressure at the water surface needs to exceed the partial pressure of water in the air. For evaporation to occur, the second observation is the final temperature at dry-out is nearly the same, regardless of the rate of heat transfer.

Figure 6-9 shows the effect of the air temperature when other factors are held constant. Lower air temperatures are found to result in a longer dry-out process. The reason for the longer time is due to the diminished capacity of the colder air to hold moisture, slowing the evaporation process.

Table 6-3 summarizes the simulation results using the inputs from the experiments discussed in Chapter 5. Both the measured and modeled defrost times are reported. In all cases, the model under predicts defrost time. A number of reasons for this difference is likely First, the model assumes that the surface is fully wetted with a thin water film, while in reality it is wetted with small water droplets (i.e., partially dry).

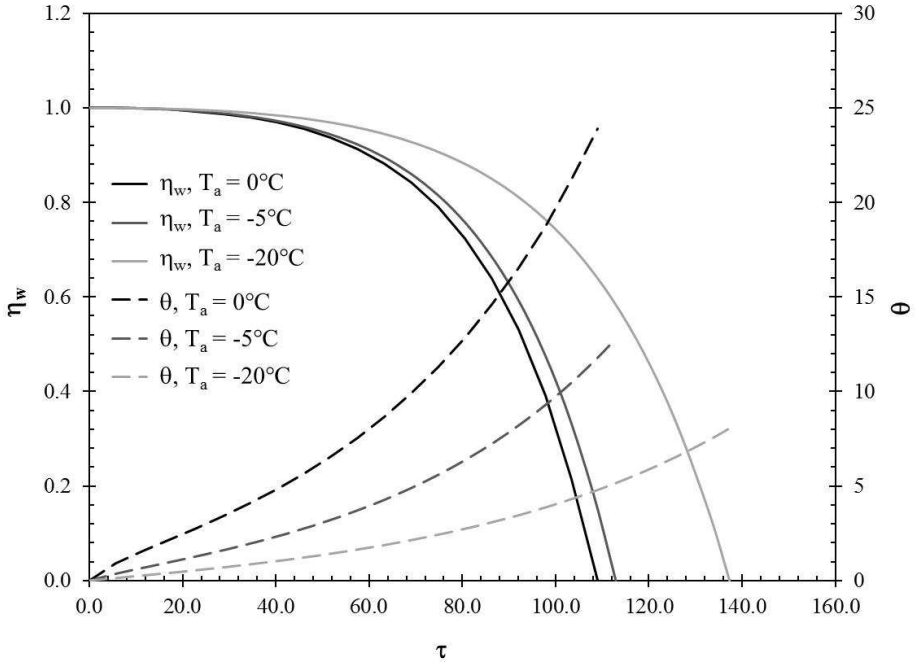

Figure 6-9. Effect of air temperature on Stage III defrost.

Table 6-3. Summary of simulation results for Stage III.

Test ID	Bi_{3s}	Bi_{3w}	Le_3	St_3	τ Experiment	τ Model
1	0.008	0.025	294	0.26	173.6	108.3
2	0.002	0.018	470	0.10	210.8	145.2
3	0.024	0.033	334	0.09	77.37	63.9
4	0.004	0.033	226	0.22	109.7	97.3
5	0.009	0.019	562	0.14	149.9	133.7
6	0.010	0.032	195	0.22	112.5	75.6
7	0.011	0.035	184	0.22	100.4	70.8
8	0.010	0.030	204	0.23	136.1	78.6
9	0.006	0.028	297	0.27	163.7	110.1
10	0.009	0.018	311	0.22	159.6	114.2
11	0.017	0.032	168	0.25	132.9	63.6
12	0.021	0.032	212	0.20	127.5	64.3

For the simulation, an equivalent film thickness is calculated by taking the total water volume of the droplets and dividing by the plate surface area. This results in a film thickness that is significantly smaller than the true height of the drops. Increasing the film thickness results in a longer defrost time. The other difference is the inputs for the simulation are held constant, while in the experiment both the heat transfer rate and air temperature vary owing to difficulty in controlling them. While the model under-predicts, it demonstrates similar trends to those seen the experiments, and can be useful as a tool to understand the factors effecting the defrost process.

6.5 Summary of results

In this chapter, the fundamental models described in Chapter 3 were solved and compared against the experimental results. The governing equations of Stages I and II were numerically solved using the Crank-Nicolson scheme. A custom C-N solver was coded in MATLAB. The model allows for detailed analysis of the defrost process, and an evaluation of parameters which can be controlled to effect defrost performance. The governing equations for State III are analytically solved.

The first stage model showed that porosity of the frost layer had minimal effect on the defrost duration. The rate at which heat is supplied at the surface, had a more significant effect, but very high rates had a diminishing effect on reducing defrost duration. Confirming the experimental study, heat and mass transfer through sublimation was shown to be insignificant to the overall transfer processes. The defrost efficiency of the first stage was found to have some interesting effects. A defrost efficiency greater than 100% is achievable when the air temperature is near the melt temperature. This is primarily due to heat transfer from the ambient air into the frost layer, aiding the heating process. Another interesting conclusion is that for lower air temperatures the defrost efficiency can be favorably improved by increasing the heat transfer rate into the frost layer. Thus one can conclude that to optimize the defrost duration and efficiency of the first stage a high heat transfer rate at the surface is highly desirable. The second stage of defrost is dominated by the melting of the frost layer. The model is capable of tracking the change in both the thickness of the frost layer and the location of the permeation front. The front velocity varies with the supplied heat transfer rate and frost porosity.

Higher heat transfer rates at the surface resulted in faster melt velocity, and thus shortened stage duration. Similar to the first stage, the effects of sublimation was shown to be negligible to the overall heat and mass transfer. An analytical solution for third stage has been evaluated. The effects of both the heat transfer rates and air temperature were investigated. Similar to the earlier stages, a high heat transfer rate is favorable to reducing the defrost duration. Lower ambient air temperatures lengthen the duration of the melt.

7 Conclusion

Frosting and defrosting is an important problem in the refrigeration industry. Frost directly diminishes the performance and efficiency of the entire refrigeration system by presenting resistances to the airflow and heat transfer in the air cooler. Current defrost methods are inefficient and cause great disruption to the operation of the refrigeration unit. Improving defrost efficiency will have a measurable improvement on the overall system energy usage. The aim of this research is develop a firm understanding of the fundamentals of the defrost process at the surface level. This work quantifies the heat and mass transfer during the phase-change process. The specific goals of the research were:

- Capture the definitive experimental data set on the effect of frost morphology on the defrost process.
- Develop a multi-stage defrost model that includes all of the relevant heat and mass transfer parameters

Both the experimental facility and model have uses beyond the research presented in this study. The experimental facility may be used by future researchers to investigate the effect of surface finishes and coatings on the frost formation and defrost process. Another possible research topic could be the evaluations of frost detection techniques, as well as, an interesting shedding technology using piezoelectric actuators to fracture the ice crystals from the surface. While the model may be used as a tool to optimize coil geometry and defrost algorithms so as to maximize system efficiency.

7.1 Frosted heat and mass transfer analysis

To validate the experimental apparatus, a series of frost accumulation tests were conducted. The test conditions were for a typical refrigerated frozen application. The heat and mass transfer were measured for the frosting process. Digital images were taken of the growing frost layer. A digital image analysis technique was used to determine the time dependent change in frost thickness and porosity. The frost growth results compared favorably to other published studies.

A new heat transfer model was proposed. The model combined the latent and

sensible heat exchange into a single model. The total heat transfer was shown to be proportional to the growth rate of the frost layer. Any frost growth model can be used. For a representation case, the frost model proposed by Jansen (2011) was evaluated. The model showed a quick increase in the heat transfer rate at the inception of the frost layer, and a diminishing enhancement as the frost layer grew thicker. This was the exact behavior measured during the experiments.

7.2 Visual analysis techniques

A major contribution of this study is the development of digital analysis techniques of the images captured during the frost and defrost experiments. Using an algorithm based approach allowed for higher accuracy and greater repeatability when compared with a subjective manual analysis. The software code allowed for automation of the analysis, which greatly increases the number of images that were analyzed. A copy of the software code for the visual analysis is found in Appendix F.

The visual analysis techniques were used to measure the change in frost thickness and porosity during frost growth, the change in frost thickness during melting, and the change in the water droplet size during the dry-out stage. Combining the visual records with the temperature and heat flux measurements allowed for a detailed analysis of the frost and defrost processes. New heat and mass transfer models were constructed from these measurements.

7.3 Defrost heat and mass transfer analysis

The key contribution of this study is the evaluation of the defrost process through the defined stages. Detail images and measurements of the defrost process were made, allowing for the evaluation of the heat and mass transfer for each stage. A fundamental model of the defrost process was developed and compared against the experimental results. The porosity of the frost at the start of defrost has a significant impact on the initial stage. A large portion of the applied heat to the surface is absorbed by the frost layer. Frost layers with lower porosity (aka high density) absorbed more of the heat, allowing for less to escape and resulting in a higher defrost efficiency. Heat and mass transfer through sublimation during this stage was found to be insignificant.

The second stage of defrost is dominated by the melting of the frost layer. Using a digital analysis technique, the front velocity was measured. The measured front velocity was found to vary with the supplied heat transfer rate and frost porosity, which compared will to the visual measurement. Higher heat transfer rates resulted in faster melt velocity, and thus shortened defrost times. While lower frost porosity had the effect of increasing the defrost time. Like the first stage, the effects of sublimation were found to be negligible to the overall heat and mass transfer. Defrost efficiency for this stage is nearly 100% with little heat lost to the surroundings.

Evaporation dominates the final stage. This stage inherently has the worst defrost efficiency, because most of the supplied heat is lost through sensible heat exchange with the ambient air. A new heat transfer model for the wetted surface is proposed, which captures both the sensible and latent heat exchange effects. The latent heat exchange is correlated to an area reduction of the water droplets, which is expressed by a mass transfer coefficient.

7.4 Recommendations

As discussed in Section 1.1, defrost is an inherently inefficient process. During defrost the air-cooler must be turned off, preventing conditioning of the space. To which can result in loss of temperature control. Furthermore heat is applied to the frosted surface to melt the frost. Some of this heat is lost into the conditioned space resulting in a parasitic load. Thus the objective of the design engine is to have short defrost durations with minimal heat loss. This study showed that high defrost efficiency for Stage I and Stage II are achievable. Efficiency and duration improves with higher supplied heat fluxes. The measured defrost efficiency at the surface far exceeds that of a real heat exchanger. There are a couple of reasons for this difference. In this work, the stored energy of the solid surface was not included in the defrost efficiency. A real heat exchanger has several kilograms of metal that must be heated to part of the defrost process. The second difference from a real heat exchanger is the uniformly and completeness of frost cover. During the experiment, a uniform frost layer was grown on the test surface. On a real heat changer, there are portions of the coal which have little to no frost. During defrost this uncovered area provides a direct path of heat transfer.

By definition, the final stage of defrost can only reduce the defrost efficiency. Any heat applied to the surface will be lost of the air either through sensible or latent heat exchange. Thus, the aim of the design engineer should be to design well-draining surfaces that leave minimal moisture on the coil at the conclusion of the second stage. While outside of the scope of this work, several recent studies have shown that surface coatings and finishes can improve the draining characteristics.

8 Recommendation for future work

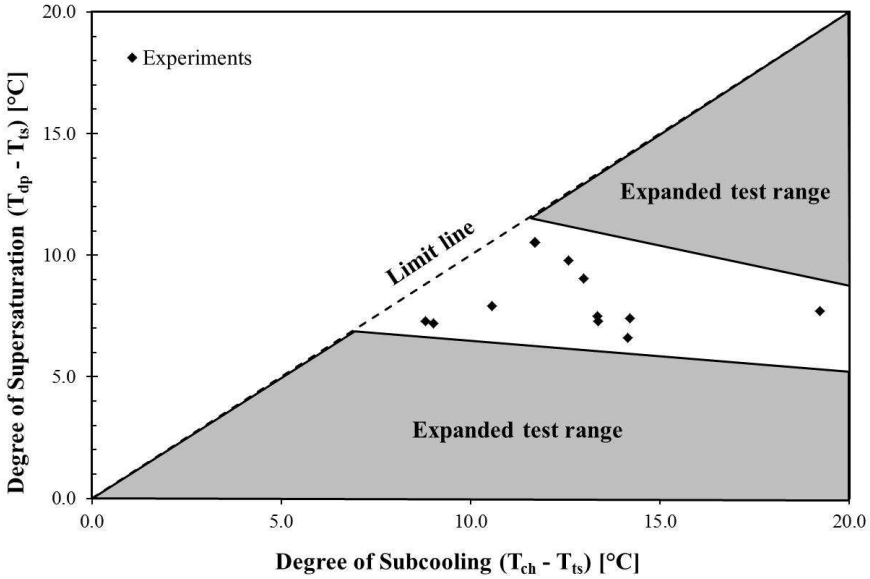

Figure 8-1. Test coverage of current study.

This study addresses a number of unknowns in the heat and mass transfer mechanism of the defrost process on a heated flat plate, but there is still a number further studies that are required to fully understand the defrost process. The experimental study is limited by both the capabilities of the apparatus and the available test. Both can be improved and extended. The model described in Chapter 3 has a number of simplifying assumptions that impact the accuracy of the simulation as discussed in Chapter 6. Modeling should be extended to look at the multidimensional aspect of the problem, as well as, a closer evaluation of the effect of mass and heat transfer through the movement of liquid water. In this chapter, several follow-up studies are recommended.

8.1 Expand test range

Figure 8-1 show the experiments conducted in the current study as a function of degree of super saturation to subcooling of the test surface with respect to the air dew point and dry bulb temperature. The current tests covered moderate degrees of super saturation, which is most commonly encountered in typical refrigeration application. Two expanded test regions should be evaluated, low super saturation and high super

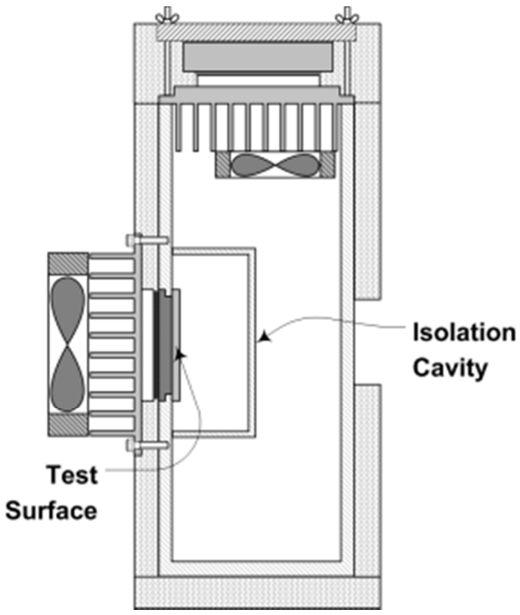

Figure 8-2. Modified test chamber.

saturation. For the current test chamber design, the chamber air dew point was limited by the temperature of cold sink of the chiller. If the chiller temperature is below the dew point of the air, condensate or frost formed on the chiller. This limited the lower range of super saturation that could be tested. Additional, the moisture accumulation on the chiller, induced a large error on the mass measurement.

To decouple the sensible cooling and humidity control of the chamber, a slight modification to the test chamber is required. A small isolation cavity could be constructed around the test surface. The exterior of the cavity would be cooled by the chiller, while humidity is only introduced to the cavity. Figure 8-2 shows a schematic of the proposed design. This enhancement would require re-routing of the instrumentation connections for the humidity, temperature, and pressure. A wider range of test conditions could be evaluated with the modified chamber.

8.2 Effect of fin efficiency on defrost

The current study investigated the heat and mass transfer effect of defrost on a flat surface. Most heat-exchangers employ extended surfaces (fins) to enhance the air-side heat transfer by increasing the area. A number of researchers have investigated wet and frost fin efficiency (Lin and Jang, 2001, Xia and Jacobi, 2005, Sommers and Jacobi,

2006, Zhou et al., 2007). Generally, the updated fin-efficiency model lumps the sensible and latent heat transfer effects into a single term. This technique is attractive as it is compatible to the common UA-LMTD heat exchanger performance calculation. To knowledge of the author, there has been no experimental work conducted on defrosting of finned surface for the development of defrost fin efficiency. This work would require the fabrication of new finned test surfaces. Thermocouples imbedded within the fins could measure the temperature distribution, and thus the fin efficiency during defrost.

8.3 Vapor diffusion in finned surfaces

Additionally, in a typically heat exchanger the fins are closely spaced resulting in parallel channels. As the channels pack with frost, the flow path for vapor diffusion will be significantly restricted. The resistance to the molecular diffusion of water vapor from the frost will decrease the rate of mass transfer by vapor transport. As shown in this study, vapor diffusion is most significant during the final stage of defrost, which also happens to be the slowest stage of the process. One would expect the fin pack to have a slower mass transfer, and thus a slower overall defrost process.

8.4 Multi-dimensional defrost model

The conduction along the fin will cause a temperature gradient at the frost-surface interface, resulting in a multi-dimensional temperature distribution in the frost layer. The heat flow and vapor mass diffusion will be influenced by the two-dimensional temperature distribution. Additionally, the melt front would tend to propagate from the fin base towards the tip. Alebrahim and Sherif (2002) developed a simple multi-dimensional model for the first and beginning of the second stage of the defrost process. The model stops being valid once continuous water is formed at the surface. In the current study, a multi-stage defrost model has been developed for the one-dimensional surface. This model can be extended to the multi-dimensional fin, and be used asa basis of validation of a fin efficiency model for defrost.

8.5 Effect of surface wettability on defrost heat and mass transfer

Recently, there have been several studies to investigation the effect of surface wettability on condensate and frost formation on cooled surfaces (Na, 2003, Xia et al.,

2006, Liu and Jacobi, 2009). The studies have found that super hydrophilic surfaces require a higher degree of super saturation for frost to form on the surface. Thus it is practical to delay the temperature at, which frost forms. Additionally, the frost that grows on super hydrophilic surfaces appears to have a higher porosity. The effect of surface wettability on the heat and mass transfer has not been thoroughly investigated. System level testing has pointed to enhance drainage for super hydrophobic surfaces, which should reduce the time and energy input during the third stage of the defrost process.

8.6 Water permeation mass flux

The understanding of the water permeation mass flux is limited. Currently no model for the water permeation mass flux was developed as part of this study. A preliminary review of the literature has pointed towards empirical correlations that exist for melt propagation in snow layers. Further research is required to determine the applicability of these correlations. From the video microscopy a water front moving from the surface was observed. The contrast of the water front was not clear enough to make measurements of the changes in the permeation front as it changed with time. A possible test could use a non-melting matrix structure of similar structure to the frost layer that a dyed water layer could permeate through. The captured video images can then be used to calculate the front velocity.

8.7 Dynamic frosted-defrosted heat exchanger model

As described in Appendix C, the defrost process is an inherently dynamic process. Of key interest would be to model the frosting and defrosting process of a vapor compression system. A dynamic system model can be used within a model-base control design process to develop improved algorithms for the detection and control of the defrost process to improve the overall system efficiency. As described earlier, the defrost efficiency is directly related to the frost morphology. An improved detection algorithm could use knowledge about the growth condition to predict the type of frost on the coil surface. Then with proper control, the defrost control algorithm would add the specific amount of heat, at the proper rate to maximize the defrost efficiency.

References

Alebrahim, A.M., and Sherif, S.A. (2002). Electric defrosting analysis of a finned-tube evaporator coil using the enthalpy method. Proceedings of the Institution of Mechanical Engineers Part C Journal of Mechanical Engineering Science, 216(6), 655-673.

Al-Mutawa, N.K., & Sherif, S.A. (1998e). Determination of Coil Defrosting Loads: Part V Analysis of Loads (RP-622). ASHRAE Transactions, 104, 344-355.

Al-Mutawa, N.K., Sherif, S.A., & Mathur, G.D. (1998c). Determination of Coil Defrosting Loads: Part III Testing Procedures and Data Reduction (RP-622). ASHRAE Transactions, 104, 303-312.

Al-Mutawa, N.K., Sherif, S.A., Mathur, G.D., Steadham, J.M., West, J., Harker, R.A., & Tiedeman, J.S. (1998b). Determination of Coil Defrosting Loads: Part II Instrumentation and Data Acquisition Systems (RP-622). ASHRAE transactions, 104, 289-302.

Al-Mutawa, N.K., Sherif, S.A., Mathur, G.D., West, J., Tiedeman, J.S., & Urlaub, J. (1998a). Determination of Coil Defrosting Loads: Part I Experimental Facility Description (RP-622). ASHRAE transactions, 104, 268-288.

Al-Mutawa, N.K., Sherif, S.A., & Steadham, J.M. (1998d). Determination of Coil Defrosting Loads: Part IV Refrigeration/Defrost Cycle Dynamics (RP-622). ASHRAE transactions, 104, 313-343.

Aoki, K., Hattori, M., & Ujiie, T. (1988). Snow Melting by Heating from the Bottom Surface. JSME International Journal, 31(2), 269-275.

ARI. (2001). ARI Standard 410-2001: Forced-Circulation Air-Cooling and Air-Heating Coils. Arlington, VA: Air-Conditioning, Heating, and Refrigeration Institute.

ASHRAE. (2005). ASHRAE Handbook – Fundamentals: Chapter 6 Psychrometrics. Atlanta, GA: American Society of Heating, Refrigeration, and Air Conditioning Engineers, Atlanta.

ASHRAE. (2006). ASHRAE Handbook – Refrigeration. Atlanta, GA: American Society of Heating, Refrigeration, and Air Conditioning Engineers, Atlanta.

Auracher, H. (1987). Effective thermal conductivity of frost. Proceedings of International Symposium on Heat and Mass Transfer in Refrigeration and Cryogenics - Dubrovnik, Yugoslavia, 1 - 5 September, 1986, 285-302.

Donnellan, W., Lohan, J., Gleeson, K., (2005). Development of Efficient Defrosting Strategies for Refrigerated Transportation Systems, Part II Test Procedure and Results, Proceeding International IIR Conference on Latest Developments in Refrigerated Storage, Transportation and Display of Food Products Amman, Jordan, 28 – 30 March.

Donnellan, W. (2007). Investigation and Optimization of Demand Defrost Strategies for Transport Refrigeration Systems. Unpublished Doctoral Dissertation, Galway-Mayo Institute of Technology, Galway, Ireland.

Dopazoa, J.A., Fernandez-Seara, J., Uhíaa, F.J., and Diza, R., (2010). Modeling and experimental validation of the hot-gas defrost process of an air-cooled evaporator. International Journal of Refrigeration, 33(4), 829-839.

El Sherbini, A.I., and Jacobi, A.M. (2006). A model for condensate retention on plain-fin heat exchangers. Transaction ASME, Journal of Heat Transfer, 128, 427-433.

Fossa, M. and Tanda, G. (2002). Study of free convection frost formation on a vertical plate. Experimental Thermal and Fluid Science, 26(7), 661-668.

Hao,Y.L., Iragorry,J., and Tao,Y.-X. (2005). Frost-Air interface characterization under natural convection. Transaction ASME, Journal of Heat Transfer, 127(10), 1174-1180.

Hobbs, P.V. (1974). Growth of Ice from the Vapour Phase. In Ice Physics (pp. 524-571). Oxford: Clarendon Press.

Hoffenbecker, N., Klein, S.A., and Reindl, D.T. (2005). Hot gas defrost model development and validation. International Journal of Refrigeration, 28(4), 605–615.

Holman, J.P. (2002). Principals of Convection. In Heat Transfer, 9th ed. (pp. 205-263). New York: McGraw-Hill.

Iragorry, J., Tao, Y.-X., and Jia, S. (2004). A critical review of properties and models for frost formation analysis. HVAC&R Research, 10(4), 393-420.

Jain, N. (2009). Dynamic modeling and validation of a commercial transport refrigeration system. Unpublished Master Thesis, University of Illinois at Urbana-Champaign, Urbana.

Janssen, D.D., Mohs, W.F., and Kulacki, F.A. (2012a). Modeling Frost Growth – A Physical Approach, Proceedings, 2012 ASME Summer Heat Transfer Conference, Paper No. HT2012-58054.

Janssen, D.D., Mohs, W.F., and Kulacki, F.A. (2012b). High Resolution Imaging of Frost Melting, Proceedings, 2012 ASME Summer Heat Transfer Conference, Paper No. HT2012-58061.

Janssen, D.D. (2011). Experimental Strategies for Frost Analysis, Unpublished Master Thesis, University of Minnesota, Minneapolis.

Keir, M.C. (2006). Dynamic modeling, control and fault detection in vapor compression systems. Unpublished Master Thesis, University of Illinois at Urbana-Champaign, Urbana.

Kondepudi, S.N., and O'Neal, D.L. (1987). The effects of frost growth on extended surface heat exchanger performance: a review. ASHRAE transactions, 93(2), 258-274.

Kondepudi, S.N., and O'Neal, D.L. (1993a). Performance of finned-tube heat exchangers under frosting conditions: Part I Simulation model. International Journal of Refrigeration, 16, 175-180.

Kondepudi, S.N., and O'Neal, D.L. (1993b). Performance of finned-tube heat exchangers under frosting conditions: Part II Comparison of experimental data with model. International Journal of Refrigeration, 16, 181-184.

Krakow, K.I., Lin, S., Yan, L. (1993a). An idealized model of reversed-cycle hot gas defrosting - Part 1: Theory. ASHRAE Transactions, 99 (1), 317-328.

Krakow, K.I., Lin, S., Yan, L. (1993b). An idealized model of reversed-cycle hot gas defrosting - Part 2: Experimental Analysis and Validation. ASHRAE Transactions, 99(2), 329-338.

Krakow, K. I.; Yan, L.; Lin, S. (1992a). Model of hot-gas defrosting of evaporators-part 1: heat and mass transfer theory. ASHRAE Transactions, 98(1), 451-461.

Krakow, K. I.; Yan, L.; Lin, S. (1992b). Model of hot-gas defrosting of evaporators-part 2: experimental analysis. ASHRAE Transactions, 98(1), 462-474.

Lee, Y.B., and Ro, S.T. (2005). Analysis of the frost growth on a flat plate by simple models of saturation and super saturation. Experimental Thermal and Fluid Science, 29(6), 685-696.

Lohan, J., Donnellan, W., and Gleeson, K., (2005). Development of Efficient Defrosting Strategies for Refrigerated Transportation Systems Part I, Experimental Test Facility, Proceedings. International IIR Conference on Latest Developments in Refrigerated Storage, Transportation and Display of Food Products, Amman, 28 – 30 March.

Mago, P.J., and Sherif, S.A. (2002a). Modeling the cooling process path of a dehumidifying coil under frosting conditions. Transactions ASME, Journal of Heat Transfer, 124, 1182-1191.

Mago, P.J., and Sherif, S.A. (2002b). Dynamics of coil defrosting in supersaturated freezer air. Proceedings of the Institution of Mechanical Engineers, Part C, Journal of Mechanical Engineering Science, 212, 949-958

Mohs, W.F., and Kulacki, F. A., (2011). Heat and mass transfer in the defrost process, A new modeling paradigm, Proceedings, International Conference on Refrigeration, Prague, Paper No. 158.

Muehlbauer, J. (2006) Investigation of Performance Degradation of Evaporator for Low Temperature Refrigeration Applications. Unpublished Master Thesis, University of Maryland, College Park.

Na, B. (2003). Analysis of Frost Formation in an Evaporator. Unpublished Doctoral Dissertation, Pennsylvania State University, University Park.

Recktenwald, G.W. (2011). Finite-Difference Approximations to the Heat Equations. Retrieved from http://www.f.kth.se/~jjalap/numme/FDheat.pdf.

Sanders, C.T. (1974). The Influence of Frost Formation and Defrosting on the Performance of Air Coolers. Unpublished Doctoral Dissertation, Delft University of Technology, Delft.

Scace, G.E., Huang, P.H., Hodges, J.T., Olson, D.A., and Whetstone, J.R., (1997). The new NIST low frost-point humidity generator. Proceeding 1997 NCSL Workshop and Symposium, Atlanta.

Sherif, S.A., and Hertz, M.G. (1998). A semi-empirical model for electronic defrosting of a cylindrical coil cooler. International Journal of Energy Research, 22(1), 85-92.

Sherif, S.A., Mago, P.J., Al-Mutawa, N.K., Theen, R.S., and Bilen, K. (2001). Psychometrics in the supersaturated frost zone. ASHRAE Transactions, 107(2), 753-767.

Sommers, A.D., and Jacobi, A.M. (2006). An exact solution to steady heat conduction in a two-dimensional annulus on a one-dimensional fin: Application to frosted heat exchangers with round tubes. Transactions ASME, Journal of Heat Transfer, 128, 397-404.

Sujau, M., Bronlund, J. E., Merts, I., and Cleland, D. J. (2006). Effect of defrost frequency on defrost efficiency, defrost heat load, and coolstore performance. Refrigeration Science and Technology Series, 1, 525-532.

Wiederhold, P.R. (1997). Water Vapor Measurement: Methods and Instrumentation. New York: Marcel Dekker.

Xia, Y. and Jacobi, A.M. (2005). Air-side data interpretation and performance analysis for heat exchangers with simultaneous heat and mass transfer: Wet and frosted surfaces. International Journal of Heat and Mass Transfer, 48, 5089-5102.

Xia, Y., Zhong, Y., Hrnjak, P.S., and Jacobi, A.M. (2006). Frost; defrost; and refrost and its impact on the air-side thermal-hydraulic performance of louvered-fin; flat-tube heat exchangers. International Journal of Refrigeration, 29, 1066-1079.

Yamashita, K., Hamada, M., Ise, S., and Ohkubo, H. (2007). Study of frost properties in a low temperature environment. Proceedings, 22nd International Congress of Refrigeration, Beijing, August 21-26, 2007.

Yan, W.M., and Lin, T.F. (1990). Combined heat and mass transfer in natural convection between vertical parallel plates with film evaporation. International Journal of Heat and Mass Transfer, 33(3), 529-541.

Zhou, X., Braun, J.E., and Zeng, Q. (2007). An improved method for determining heat transfer fin efficiencies for dehumidifying cooling coils (RP-1194). HVAC&R Research, 13(5), 769-783.

Zhou, X. and Braun, J.E. (2007). A simplified dynamic model for chilled-water cooling and dehumidifying coils, Part 1 Development (RP-1194). HVAC&R Research, 13(5), 785-804.

Appendix A. Vapor Compression Refrigeration Cycle

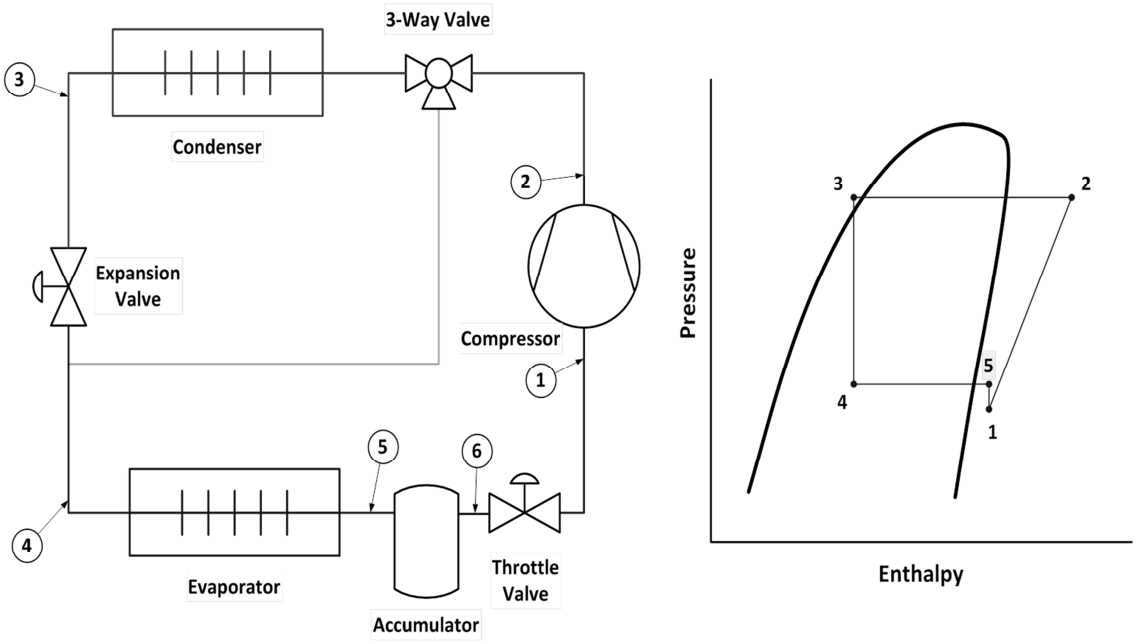

Figure A-1 Vapor compression refrigeration cycle

A.1 Cooling cycle

Figure A-1 shows a schematic and pressure-enthalpy diagram of a typical vapor compression refrigeration system. The primary components of the system are: compressor, condenser coil, expansion device, and evaporator coil. The system also contains an accumulator and throttle valve whose function is to protect the compressor in heat mode operation. Refrigerant enters the compressor at (1) as low-pressure, superheated vapor. Across the compressor, the pressure and enthalpy of the refrigerant is raised by the work of the compressor and leaves at state (2). The three-way valve directs the refrigerant to the condenser coil, where the superheated vapor enters the condenser coil is condensed into a saturated liquid (3). The liquid refrigerant is adiabatically expanded as it passes through the thermostatic expansion valve (TXV) and enters the evaporator as a two-phase refrigerant at a lower pressure (4). The refrigerant absorbs heat and boils as it passes through the evaporator coil and exits as a superheated vapor (5). The superheated vapor passes through the accumulator and throttle valve, which controls the outlet pressure, and finally back to the compressor (1).

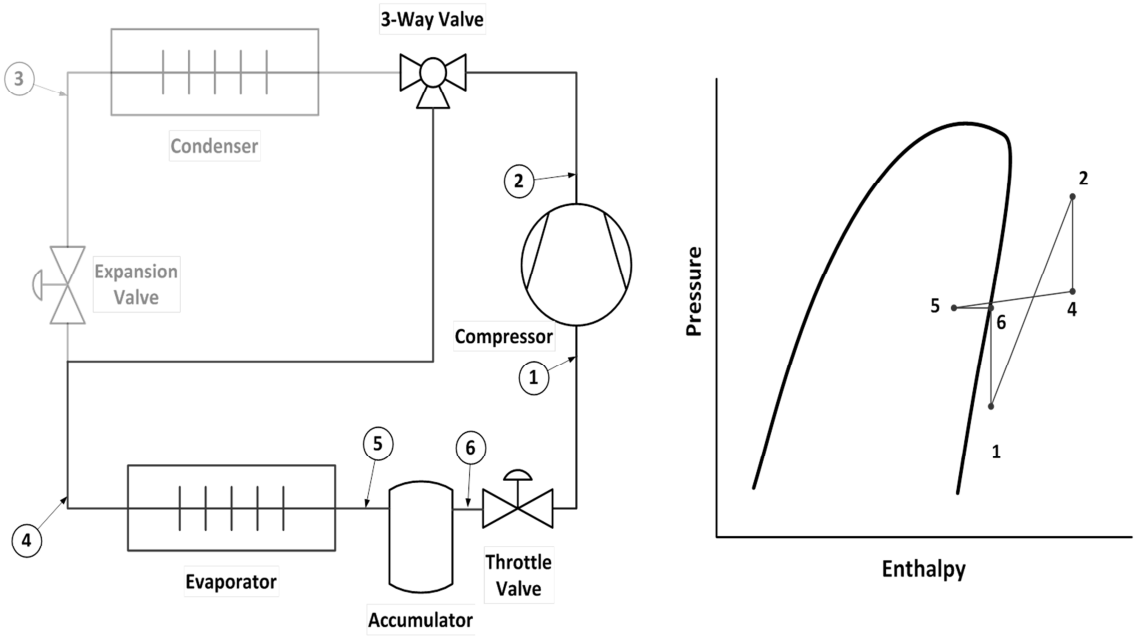

Figure A-2 Hot gas heating refrigeration cycle.

A.2 Hot gas defrost cycle (Reverse cycle)

A hot gas defrost cycle uses the heat generated by the work of the compressor to warm the coil evaporator and melt the frost. As with the cool cycle superheated vapor enters the compressor (1) and the work added raises the enthalpy and pressure of the refrigerant (2). The three-way valve is shifted to direct the high-temperature, high-pressure refrigerant to the inlet of the evaporator coil, downstream of the TXV (4). The three-way valve and TXV are closed so as to trap the refrigerant sitting between the inlet of the condenser and the outlet of the expansion valve, and thus the condenser and TXV are no longer a part of the refrigeration system. The evaporator coil now behaves like a condenser, taking superheated vapor in and condensing it into a two-phase fluid (5). The two-phase flow enters the accumulator, which separate the liquid refrigerant from the vapor. The liquid refrigerant is held in the accumulator, while the refrigerant vapor exits the accumulator (6), passes through the throttle valve, and finally returns to the compressor (1).

Appendix B. Preliminary Experimental Results

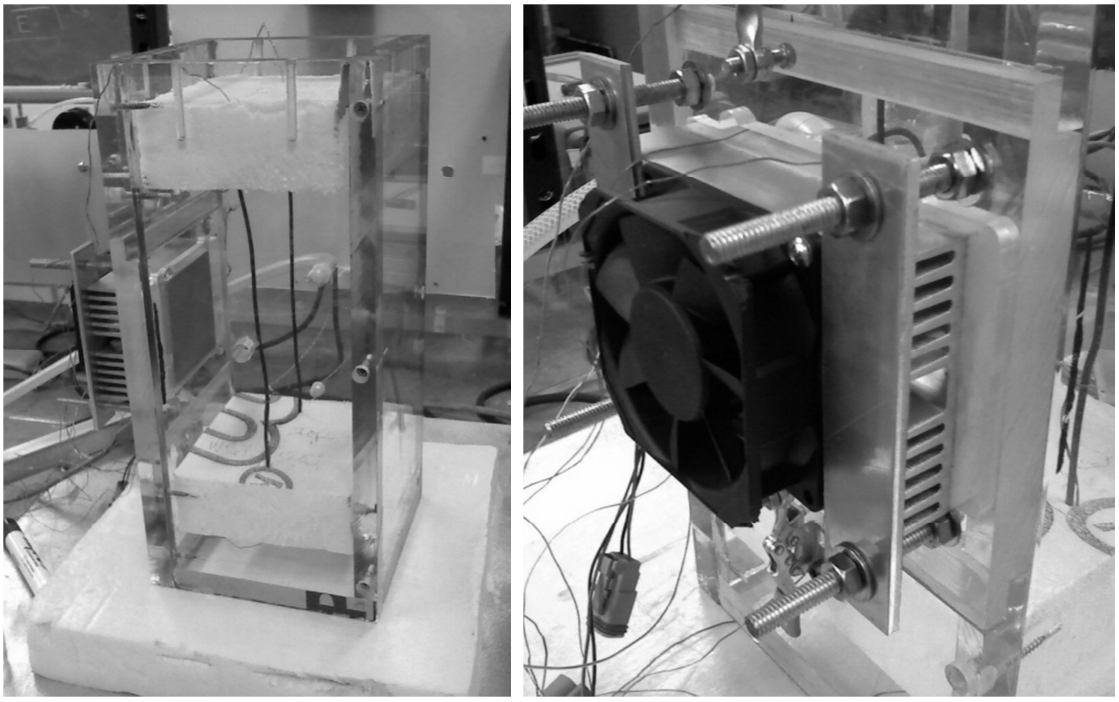

Figure B-1 Summer 2009 test chamber.

B.1 Introduction

A preliminary set of frost and defrost experiments were completed during the summer of 2009 through the support of a REU student. The aim of the experiment was to generate a base set of a data to understand the raw scale of the frost and defrost process. Additionally, knowledge gained from the experiment was used to improve the design of the final test facility

B.2 Test facility

Figure B-1 shows the test chamber used for the test. The test chamber was a 5 by 7.5 inch rectangular, Plexiglas box. The top and bottom of the test chamber was insulated to limit heat gain. Humid air was allowed to enter the chamber through small holes on the side of the chamber. As a result, the relative humidity, which was not controlled, generally stayed between 30 and 60%. The humidity was measured by a HyCal Humidity Transmitter. The temperature inside the test chamber, measured by four type-E thermocouples, was not regulated.

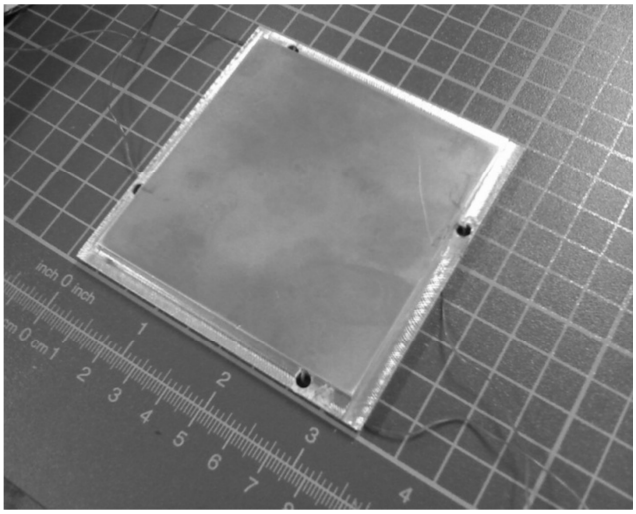

Figure B-2 Test surface.

The test surface (Figure B-2) was a 3 by 3 inch aluminum plate. The surface was progressively lapped up to 2000 grit wet-dry sandpaper. Four type-E thermocouples were embedded in the test surface in order to measure its temperature. The test surface was cooled and heated by a Thermal Electric module. The temperature was regulated by adjusting the input voltage through a BK Precision 1696 Power Supply. Heat from the TE module was transferred to the ambient space through a finned heat sink and fan. Heat flow from the test plate was measured by an Omega Engineering HFS-4 Thin Film Heat Flux Sensor. The thermocouples, Heat Flux Sensor, Power Supply, and the Humidity Transmitter were all measured by an Agilent 34970A Data Acquisition/Switch Unit with a 34901A Multiplexer.

The frost and defrost process were visually recording by an Edmund Optics USB Camera with a Zoom 7000 Navitar TV Zoom. The camera has a 0.5 inch CCD monochrome sensor, which is capable of capturing images at a resolution of 1280 x 1024 at frame rates of 25 fps. The 6X zoom lens has a maximum magnification of 1.1X, which equates to resolving frost structures down to 9.4 μm. The frost surface is illuminated with by a fiber optic light ring with the light source from an Edmund Optics MI-150 High-intensity Illuminator. The light source has a 150 W EKE Quartz Halogen lamp

Table B-1 Experimental summary.

Experiment		1	2	3	4	5	6
Build	Supply Volts	14	14	14	14	14	14
	Time	7 hours	7 hours	7 hours	7 hours	7 hours	7 hours
	Scan Rate (per min)	1	1	1	1	1	1
	Relative Humidity	Variable	Variable	Variable	Variable	Variable	variable
Melt	Supply Volts	14	11	8	5	2	0
	Time	Variable	Variable	Variable	Variable	Variable	Variable
	Scan Rate (per min)	72-73	72-73	72-73	72-73	72-73	72-73
	Relative Humidity	Variable	Variable	Variable	Variable	Variable	Variable

with a variable light control that ranges from 0 to 100%. The camera is connected to a computer via the USB port and the camera is controlled and recorded by the supplied uc480 viewer.

B.3 Results and discussion

Table B-1 summarizes the first set of experiments. For the frost formation stage, the supply voltage and time were kept constant. When there was about 15 minutes left in the build phase of the experiment, the frost thickness was recorded and some video footage of the front of the frost layer was taken. The thickness of the frost was measured by taking a dry erase marker and drawing a line as close as possible to the frost layer edge and test surface edge and measuring between these lines with a ruler.

During the frost formation stage, the average test surface temperature was -7.4 °C and the average test chamber temperature was 19.5 °C. The average base plate temperature was slightly lower than the test surface temperature at -8.2 °C. The relative humidity was not controlled; however, it generally stayed between 30% and 60% with an average of 45.53%. Throughout the majority of each experiment the relative humidity

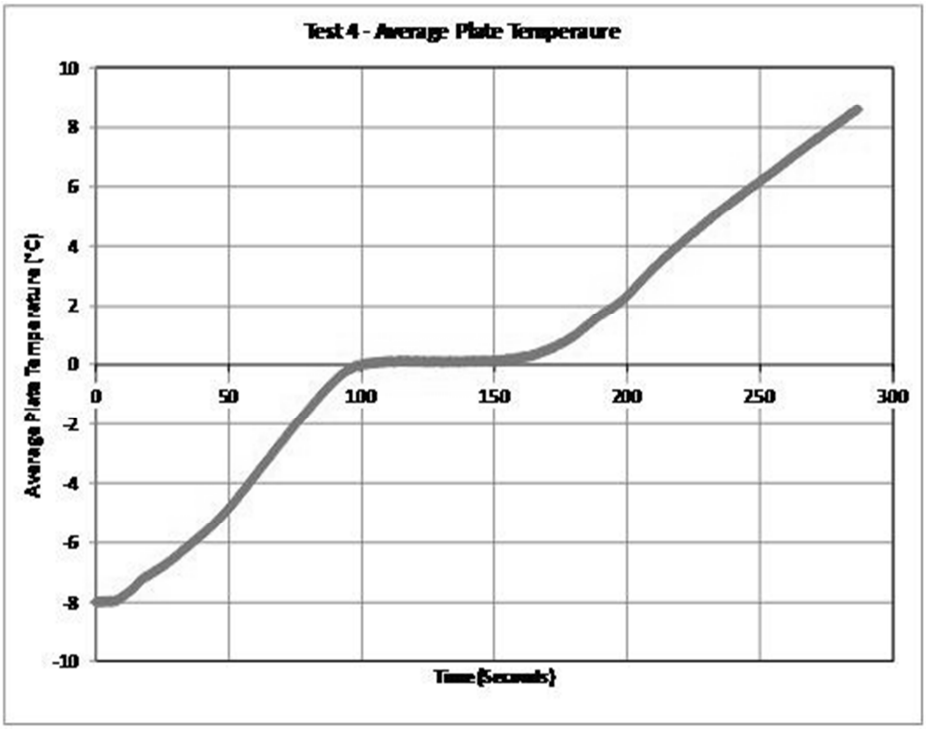

Figure B-3 Average plate temperature during defrost cycle.

generally varied by about 10%. The heat flux would usually start out high before leveling off to about 720 W/m^2.

As expected, the defrost process was found to progress through predictable stages. Figure B-5 show a time trace of defrost for Test 4. The dwell time during Stage II was approximately 75 seconds. The time to defrost was found to vary proportionally with the supply voltage, which was related to the supplied heat flux.

The video footage of the front of the frost layer is for estimating the porosity and eventually the mass of the frost layer. The frost porosity was estimated by use using the visual technique described in section 4.3.3. The contrast of two randomly selected photos was adjusted to provide greater clarity between the frost crystals and voids. A 12 x 12 grid was overlaid on the photo, and the frost occurrence as counted. Squares mostly occupied by frost were counted, while mostly dark squares were not. By dividing the number of white squares by the total number of squares, the porosity was found for each photo. From the porosity, the density and mass of the frost layer could be estimated.

Initially, the average estimated frost porosity was 77%. The computes to an

average frost density was 707.04 kg/m3 and the average frost mass was 15.84 gm. These values seemed to be too high and did not correlate well to a Fossa and Tanda (2002) model. A second set of experiments was conducted where the frost was scraped from the test surface at the conclusion of the build stage and weighed on a scale. The average mass of the secondary experiments was 5.5 gm. When compared against the original experiment, it was found that the originally estimates were off by the same factor of 4.9. The factor was used to adjust mass and density in the primary set of experiments.

The scaling error implied that the original selection criterion through the visualization technique was not inaccurate, but consistent. The original a square with more than 50% coverage was counted in the porosity count. A more selective criterion of 100% coverage was applied to the experiment, the estimated mass match exactly with the measured mass. The grid used was fairly course, leading to a very subjective selection. By using a finer grid, and an automated selection method, the method should produce accurate and repeatable results.

B.4 Conclusion and recommendations

There are a number of improvements that could be made on the test chamber, the optics, and the testing procedure. One improvement that could be made to the test chamber is the addition of some sort of pump or humidifier. This addition would allow for the regulation of humidity within the chamber, so tests can be run to see the effects of different humidity levels on the frost formation and defrost process. Another improvement would be to find a way to weigh the amount of frost built on the test surface. This improvement could be accomplished by collecting the melted frost in some sort of container and weighing it, or finding some way to inject dry air into the test facility and calculate the amount of moisture added to the facility throughout the frost formation phase. If this cannot be done, the test surface should either be extended to the edge of the chamber and/or surrounded by polystyrene strips so the frost does not form on the sides of the surface. This improvement would allow for a clear view of where the test surface ends and the frost layer begins which is needed for measuring the thickness of the frost. The use of another cooling device would decrease the ambient temperature in the test chamber. This decrease in temperature would provide testing conditions closer

to that of the refrigerated trucks that we are trying to improve.

There are some improvements that could be made on the optics as well. One improvement that could be made on the optics is making one side of the apparatus opaque for better contrast. This change would hopefully allow for a better side view of the frost layer. This view of the side would allow the camera to measure the thickness which would hopefully be more accurate than the current method. This measurement could be done by the camera if a picture is taken of a ruler the same distance away from the camera with the same zoom and focus setting as the side view. Then, a conversion could be made of pixels to millimeters. Another improvement that could be made to the optics is the setting up of mirrors in such a way that the test surface could be seen at an angle and straight simultaneously by the camera. Some sort of scale or marking of the test surface that could be seen on the videos would also improve the optics.

Appendix C. Defrost Heat Exchanger Model

C.1 Motivation

While the model described in the proposal has the necessary complexity to model the defrost process at the fin level, its complexity is too cumbersome to be useful in a system simulation. A preferred frosted-defrosted model framework would build upon the structure of existing coil models. For plain fin coils, the most prevalent method of determining coil performance is to calculate the coil effectiveness based upon the fin efficiency of a given fin geometry. Coil effectiveness can simple be viewed as a reduction in the finned area, due to the resistance of heat transfer within the fins. Recall that fin efficiency is defined as the ratio of the actual heat transfer from the fin to the heat that would be transferred by a fin with infinity thermal conductivity (i.e., constant fin temperature). For example, ARI standard 410 (2001), used and developed by coil manufactures, uses coil effectiveness as a means to establish performance ratings for alternate coil design and operation condition. The method described in ARI 410 is suitable for non-frosted fins and can determine the heat transfer of both dry and wet coil. The wet coil performance is determined by the use of a wet-fin correction factor, which is multiplied to the dry coil performance to determine the total performance. There are several published data sets which can be used to validate this model. The proposed model would allow for the optimization of defrost duration and efficiency from a system operation viewpoint.

C.2 Literature review

The potential heat exchanger model builds upon the existing framework for heat exchanger calculation where equivalent fin efficiency will be used to lump the heat and mass transfer effects into a single variable. Zhou et al (2007) noted the inherent inaccuracy of the method described in ARI Standard 410. In Standard 410, the wet fin correction factor is applied to the entire fined area of the coil, when in fact there are distinct wet and dry regions on the coil. In addition, the presence of moisture on the fin surface is a coupled heat and mass transfer problem that will affect the heat transfer from the fin. Zhou's model separates the coil into two regions. The dry portion of the coil is modeled with the existing framework, but the wet portion of the coil is modeled with a

modified framework. In the wet coil region, wet fin efficiency is calculated based upon the combined sensible and latent heat transfer, assuming an analogous heat and mass transfer relationship. Xia and Jacobi (2005) developed a specific fin efficiency relationship for wet and frosted fins. Xia developed fin efficiency relationship for both a logarithmic-mean temperature difference (LMTD) and a logarithmic-mean enthalpy difference (LMED) energy balance. The LMED method was found to be only applicable for a fully wet/frosted fin, while a LMTD formulation was found to be applicable for dry, partially wet/frosted, and fully frosted conditions, which is of a great benefit for modeling.

Frost and defrost (along with dehumidification) is by its very nature a transient problem. A keen interest for the system design engineer is to understand the transient effects of the combined heat and mass transfer problem. Zhou and Braun (2007) demonstrated how to use the wet-fin efficiency to model the transient effects of a dehumidification coil using a lump-parameter model approach. The air-side region of the coil was divided into two regions, dry and wet.

Kier (2006) used the moving-boundary, lumped parameter approach to model the frosting of a heat exchanger. The model is based upon the premise that there are few key dynamic states that can describe the nature of a heat exchanger. The key state variables identified are the evaporation (or condensing pressure), tube wall temperature, mass of the refrigerant flow, tube length of the fluid region, and the average refrigerant void fraction of the flow. The state equations are structure to solve for the time-derivatives of the state variable, which are then integrated to determine the final value. The frost growth ended up becoming an extra thermal capacitance, which tended to delay the dynamic response of the system. Kier used a rather crude empirical correlation to model the frost growth and neglected the heat transfer effects by the frost growth, but overall the technique used showed merit.

Jain (2009) developed lump-parameter heat exchanger models for a transport refrigeration unit operating in both the cool and defrost condition. While operating in a

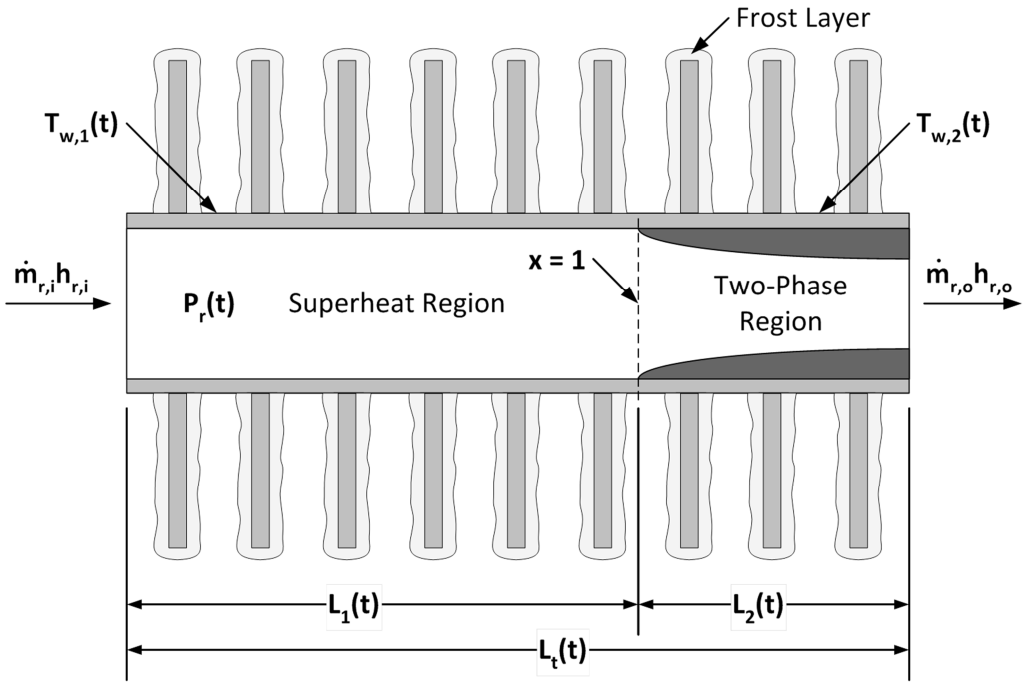

Figure C-1 Moving Boundary Lumped Parameter Heat Exchanger.

defrost mode the evaporator, which now acts as a condenser, has two-phase flow leaving. The mass storage of the evaporator in heat mode is most dependent upon the inlet air condition with a lower entering air temperature resulting in higher refrigerant mass stored. The evaporator model was developed for a dry coil, but there is no reason the framework could not be extended to a frosting-defrosting structure.

C.3 Modeling framework

Figure C-1 shows a representation of lumped parameter heat exchanger model with a moving boundary. The coil geometry is reduced to an equivalent tube of length L_t. Refrigerant enters in as superheated vapor. While passing along the tube, the refrigerant will reject heat to the tube wall, decreasing the enthalpy. Given enough heat loss, the refrigerant will begin to condense at a constant temperature on the tube walls. The lengthof tube for the superheated region, L1, will change with time dependant up the inlet mass flow rate and heat transfer. Furthermore, the heat that is absorbed by the tube will be conducted into the fins and frost layer. As described in the surface model (Chapter 3), the heated frost layer wills loss latent and sensible heat to the surroundings. Once the

tube wall temperature reaches 0 °C, the frost layer will begin to melt.

Key assumptions of the model will be:

- The fin base temperature in a given flow regime is assumed to be constant
- The heat exchanger mass is lumped into a common thermal capacitance
- Assume no refrigerant pressure drop along the length of the tube
- The initial frost layer will be assumed to be evenly dispersed on the finned surface

Appling an energy balance to a single fluid region, one obtains,

$$\left(\left(mc_p\right)_c+\left(mc_p\right)_f\right)\frac{\partial T}{\partial t}=A_r h_r(T_r-T_w)+A_a h_a \eta_e^*(T_a-T_w)+\dot{m}_w c_{p,w}\Delta T. \quad \text{(C.1)}$$

The terms on the left-hand side are the thermal capacitance of the coil and frost layer, respectively. During the Stages I and III of the frost layer, the thermal capacitance of the coil will dominate the dynamics, but during the melting process, the frost becomes the dominate term. The first two terms on the right represent the heat being transferred to from the refrigerant to the tube wall, and then the heat rejection from the tube wall to the ambient space through the fin. The fin efficiency, η_e^*, combines the effect of both the latent and sensible heat transfer. The final term capture the heat leaving through the draining melt water.

Similarly, the mass balances for the refrigerant flow and frost melting are,

$$\frac{\partial m_r}{\partial t}=\dot{m}_{r,i}-\dot{m}_{r,o} \quad \text{(C.2)}$$

$$\frac{\partial m_f}{\partial t}=\dot{m}_v+\dot{m}_w \quad \text{(C.3)}$$

For the final heat exchanger model to be solvable, a few auxiliary models will first need to be generated. At this time there is no set relationship for defrosted fin efficiency. Similar expressions exist for wet and frosted fin efficiency, and one would expect a similar framework to be suitable for this case. The other key unknown is the relative mass flow rates of the water vapor and melt liquid. The model and experimental work described in this proposal will shed light on how to solve this problem.

Appendix D. Water Vapor Measurements

The accuracy heat and mass transfer correlations of the proposed facility are largely dependent on the accuracy of the water vapor concentration measurements in the bulk fluid, along with the prediction of the water vapor concentration near the frost\defrosted surface. This appendix is a general review of psychometric principles, along with any examination of water vapor measurements and methods.

D.1 Fundamental definitions and properties

D.1.1 General terms

Absorption, Retention of water vapor by retention in bulk material

Adsorption, Retention of water vapor in a layer at the material surface

Desiccant, A substance that chemically absorbs water vapor

Desorption, Release of absorbed or adsorbed water vapor

Humidity, The presences of water vapor in a gas.

Hygrometer, An instrument for measuring humidity

D.1.2 Vapor pressure

Vapor pressure, p_v, is the fractional pressure contributed by the water vapor to the total pressure of a gas mixture. The saturated vapor pressure with respect to water, $p_{v,ws}$ can be represented as,

$$p_{v,ws} = (1.007 + 3.46 \times 10^{-6}\, p_t) 6.1121 e^{\left(17.502T / 240.97+T\right)}, \quad \text{(D.1)}$$

where p_t is the total pressure in millibars and T is the gas temperature in °C. The saturation vapor pressure with respect to ice, $p_{v,is}$, can be represented as,

$$p_{v,is} = (1.003 + 4.18 \times 10^{-6}\, p_t) 6.1115 e^{\left(22.452T / 272.55+T\right)} \quad \text{(D.2)}$$

D.1.3 Humidity ratio

Humidity ratio, W, is defined as the ratio of mass of water to the mass of a dry carrier gas for a fixed volume of gas. In terms of vapor pressure, the humidity ratio can be expressed as,

$$W = 0.62198 \frac{p_v}{p_t - p_v}. \quad \text{(D.3)}$$

D.1.4 Relative humidity

Relative humidity, RH, is the ratio of the actual partial vapor pressure, p_v, to the saturation vapor pressure, $p_{v,s,}$,of the gas at the prevailing bulk temperature,

$$RH = \frac{p_v}{p_{v,s}} \tag{D.4}$$

D.1.5 Dew point temperature

The dew point temperature is the temperature that a volume of gas must be cooled such that it becomes saturated with respect to liquid water. It is the solution to equations 10.1 for dew point temperature, T_{dp} where the prevalent vapor pressure, p_v, is substituted for the saturated vapor pressure, $p_{v,ws}$.

D.1.6 Frost point temperature

The frost point temperature is the temperature that a volume of gas must be cooled such that it becomes saturated with respect to ice. It is the solution to equations 10.2 for the frost point temperature, T_f, where the prevalent vapor pressure, p_v, is substituted for the saturated vapor pressure, $p_{v,is}$.

D.1.7 Wet bulb temperature

The wet bulb temperature, T_{wb}, is the equilibrium surface temperature when unsaturated air is passed over a wet surface. As air is passed over a wet surface, water evaporates and causes the surface temperature to drop. As the surface temperature drops, the local vapor pressure at the surface drop, which causes a decrease in the evaporation rate. The relationship between wet bulb temperature T_{wb}, dry bulb temperature T_a, and humidity ratio W is as follows:

$$W = \frac{(2501 - 2.381T_w)W_w - (T_a -)}{2501 + 1.805T_a - 4.186T_w}, \tag{D.5}$$

where W_w is the humidity ratio at T_w calculated by equation D.3.

D.1.8 Pressure effects on dew and frost point temperature

The dew and frost point temperatures are proportional to the partial pressure of the water vapor in the gas mixture. Based upon Dalton's law of partial pressures, if the total pressure of a fix volume of gas is raised, the partial pressures of the constituent

gases must rise by the same ratio. Thus, an increase in the total pressure of moist gas will cause the dew (or frost) point temperature to rise. Conversely, a drop in the total pressure will cause a reduction in the dew (or frost) point temperature.

D.2 Measurement types

D.2.1 Chilled mirror hygrometer

A chilled mirror hygrometer directly measures the dew (or frost) point temperature of a gas sample. The gas sample is passed across a chilled, reflective surface. If the surface temperature is below the saturation temperature of the moist gas, water vapor will condensate on the surface. A light source is reflected off the surface. The condensate on the surface effects amount of reflected light. By measuring the reflected light and using this to control the surface temperature, typically with a thermoelectric cooler, a controlled condensate thickness can be maintained. The controlled surface temperature is the dew (or frost) point temperature of the gas sample and is directly measured by an RTD embedded near the surface. Most chilled meter hydrometers have measurement accuracy of ±0.2 °C over a wide temperature range (-40 to 40 °C), with some specialty devices achieving accuracy of ±0.1 °C.

In general, a chilled mirror hygrometer has excellent accuracy, but there are a few sources of bias errors that must be considered during their application. Contamination of the mirrored surface can cause false reading. This is typically remedied by placing a filter in the sampling system upstream of mirror. Additionally the mirror should be regularly inspected and cleaned. Some devices have automated cleaning and calibration functions that are effective in reducing this source of error. The sampling system should be regularly inspected for leaks, as the sampled air could be contaminated with moisture from the surrounding air. Care should also be taken to avoid an artificial pressure increase (or decrease) near the mirrored surfaces, as this will cause a scaling error of the measurement (see D.1.8 Pressure Effects on Dew and Frost Point Temperatures). Finally, some chilled mirror hygrometers assume that measurements below 0 °C the condensate is deposited as ice on the mirrored surface. In certain situations, such as when the mirror is contaminated with salts, a liquid layer can be formed on the surface for temperatures well below 0 °C. To alleviate this problem, it is important to clean the

mirror and inspect it to make sure an ice layer is being formed at sub-freezing temperature.

D.2.2 Relative humidity hygrometer

Relative humidity hygrometers measure the relative moisture content of a gas mixture. To determine the actual moisture content of the gas mixture, such as humidity ratio or dew point temperature, additional thermodynamic properties need to be known. Generally, measuring the dry bulb temperature and total pressure are sufficient for determine the other humidity properties of the gas mixture.

The most commonly used relative humidity hygrometers are the bulk polymer sensors, which are inexpensive and readily available. Bulk polymers sensor consists of a humidity sensitive polymer sandwich between a miniature cathode and anode. By measuring either the resistance or capacitance between the electrodes, a determination of the relative humidity can be made. A change in the relative humidity at the sensor element causes a corresponding change in the electrical reading. Resistive sensors are generally slower in response rate then capacitive sensors, and also tend to have a smaller operational range. The accuracy of a typical bulk polymer sensor is ±2% RH over a measurement range of 5% to 99% RH. The sensors have a limited temperature operational range, -10 to 80 °C. The accuracy of relative humidity sensor at measuring low frost point temperature is very poor, with the uncertainty of the frost point being greater than ±2 °C.

Relative humidity hygrometers have a few other limitations that must be considered. The output of the sensing element has a tendency to drift as the sensor ages. This can be significant if the sensor is left exposed to an abnormally high or low humidity level. It is recommended calibrate the sensors regularly (at least yearly). The sensors are also susceptible to contamination from air. Regular cleaning and calibration are the best option for keeping this source of error to a minimum.

D.2.3 Other hygrometer types

A number of other humidity measurement types are available, and are briefly discussed. A sling psychrometer is a device to measure the wet bulb temperature of moist air. The sensing element of a thermometer is encased in a moisten cloth. Air is drawn

over the cloth, and the thermometer directly reads the wet bulb temperature. Large errors can occur if the air movement is to slow or if radiation effects are not minimized. Optical absorption hygrometers detect the concentration of water vapor based upon the absorption of radiation in certain wavelengths by water molecules. Optical absorption hygrometers have comparable accuracy to chilled mirror hygrometers, but have limited availability and are more expensive. A saturated salts sensor measures the dew point of a gas. An electrode is coated with an absorptive salt. By passing current through the salt, a heating effect is caused and water to evaporate from the salt. As the water evaporates the resistance of the salt increases, and the heating effect is diminished. The salt will reach equilibrium with the ambient air and the dew point can be measured by an RTD. While measuring dew point directly, saturated salts have worse accuracy and smaller measurement range then a chilled mirror hygrometer.

Appendix E. Facility build

E.1 Test Surface Construction

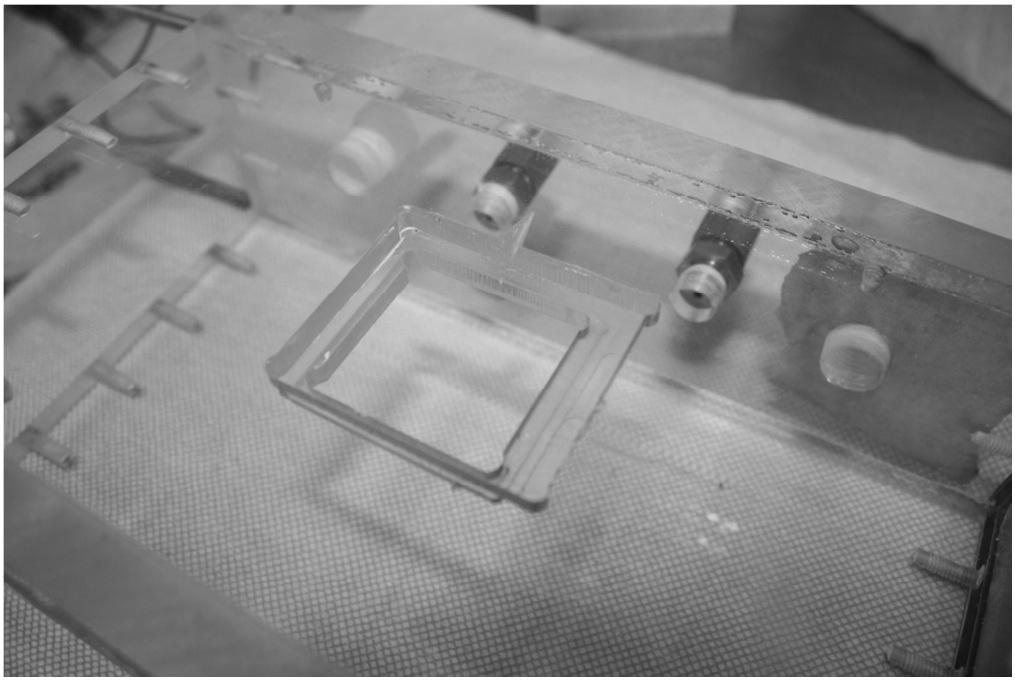

Figure E-1 Close-up of holder for test surface and heat spreader.

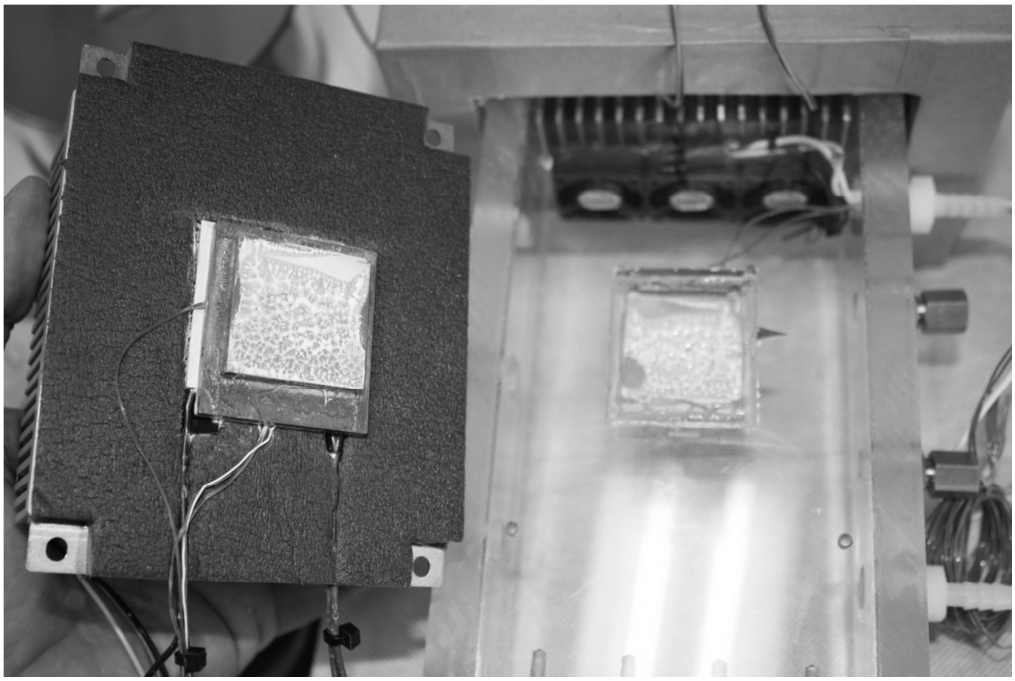

Figure E-2 Assembly of test surface.

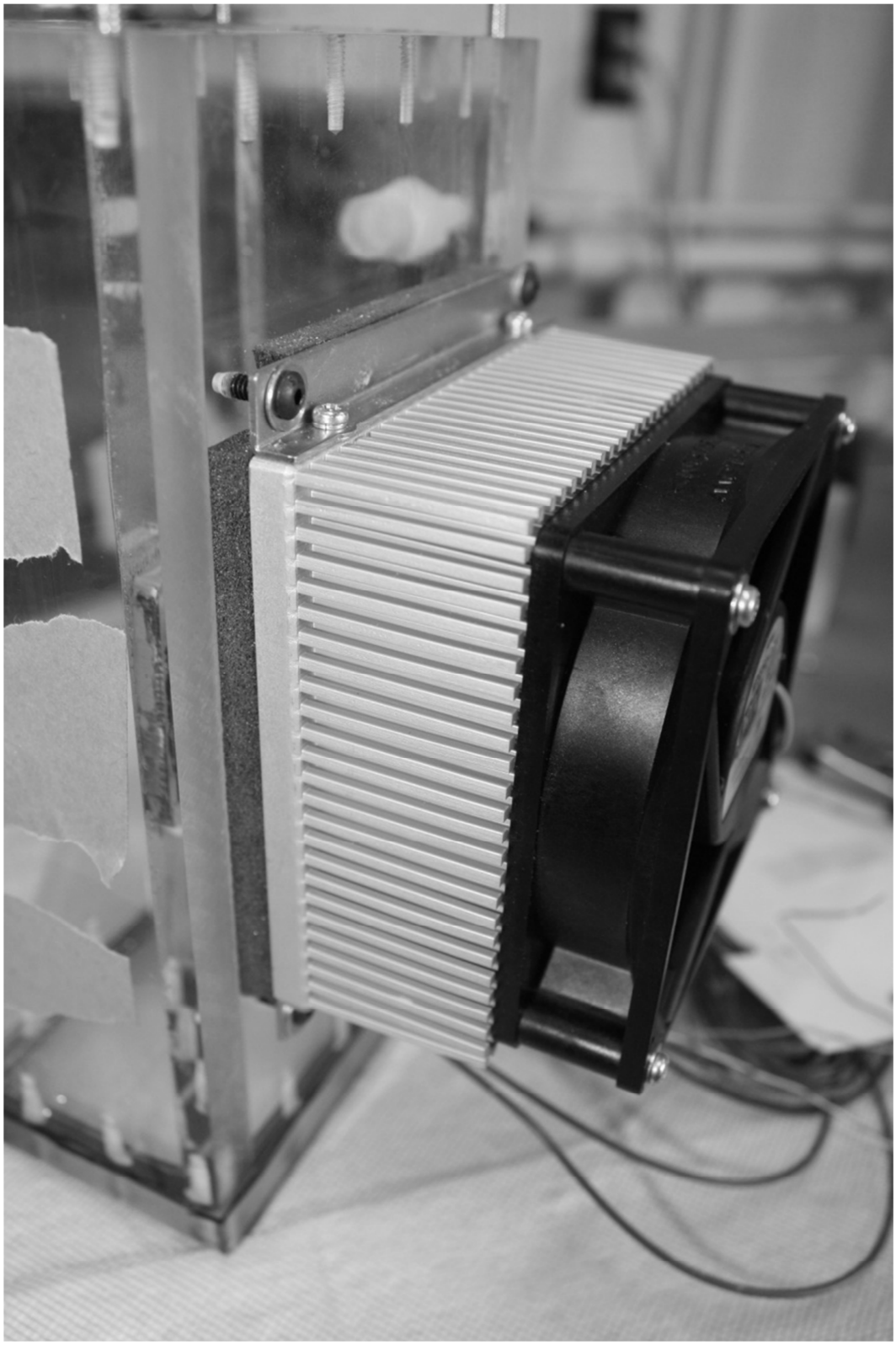

Figure E-3 Completed test surface assembly.

E.2 Chiller Construction

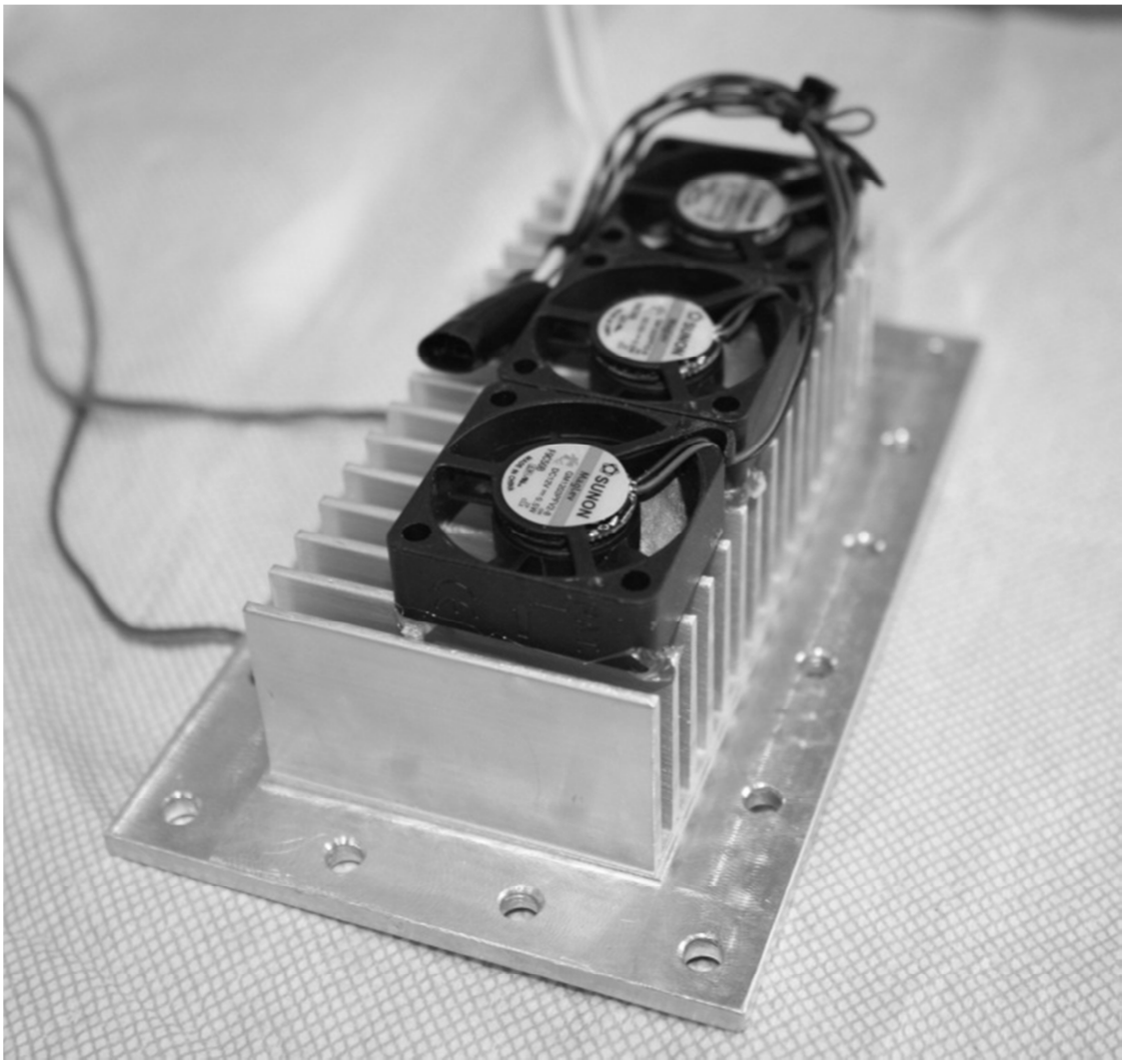

Figure E-4 Chiller heat sink with circulation fans.

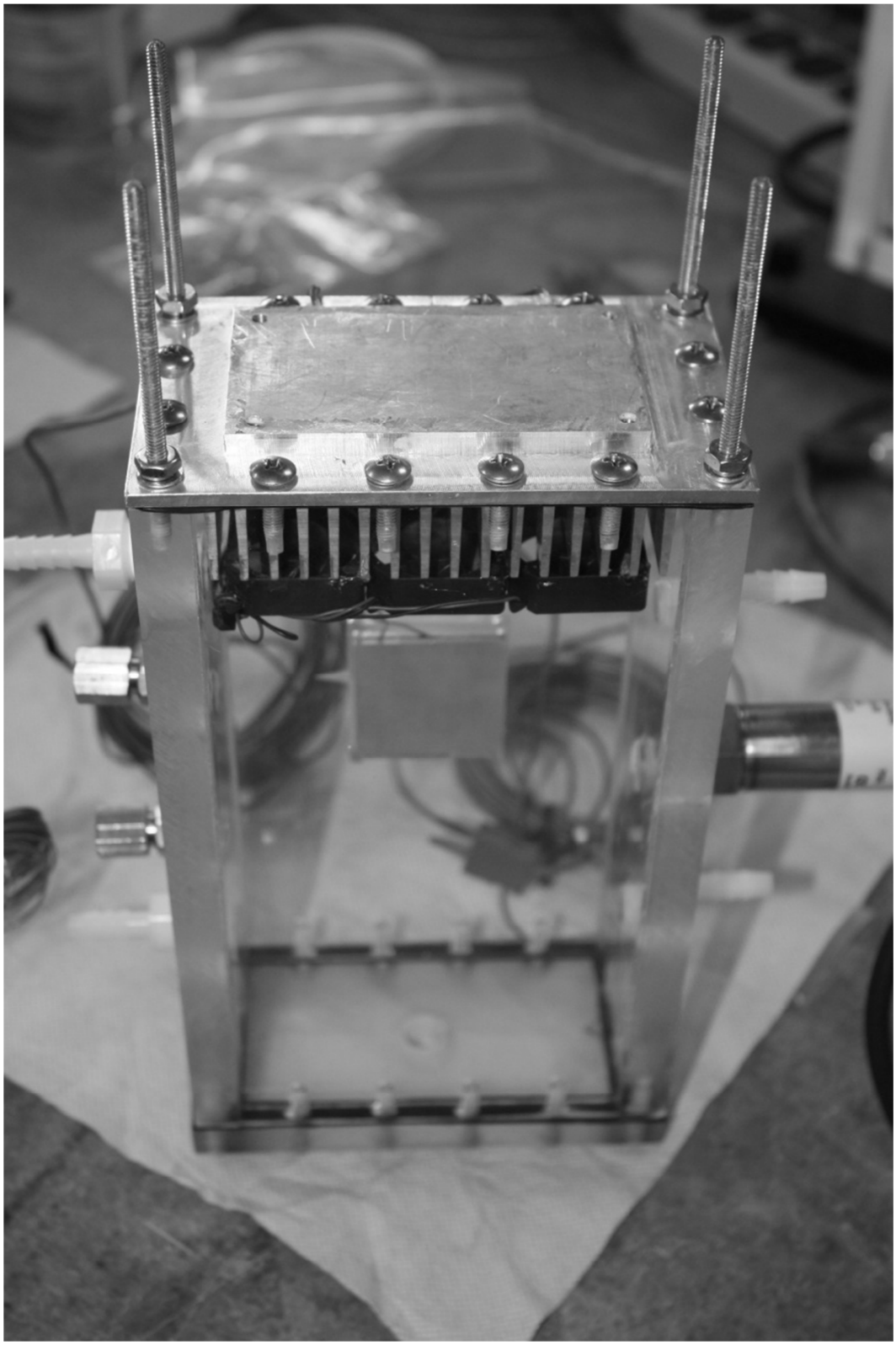

Figure E-5 Chiller heat sink installed on test chamber.

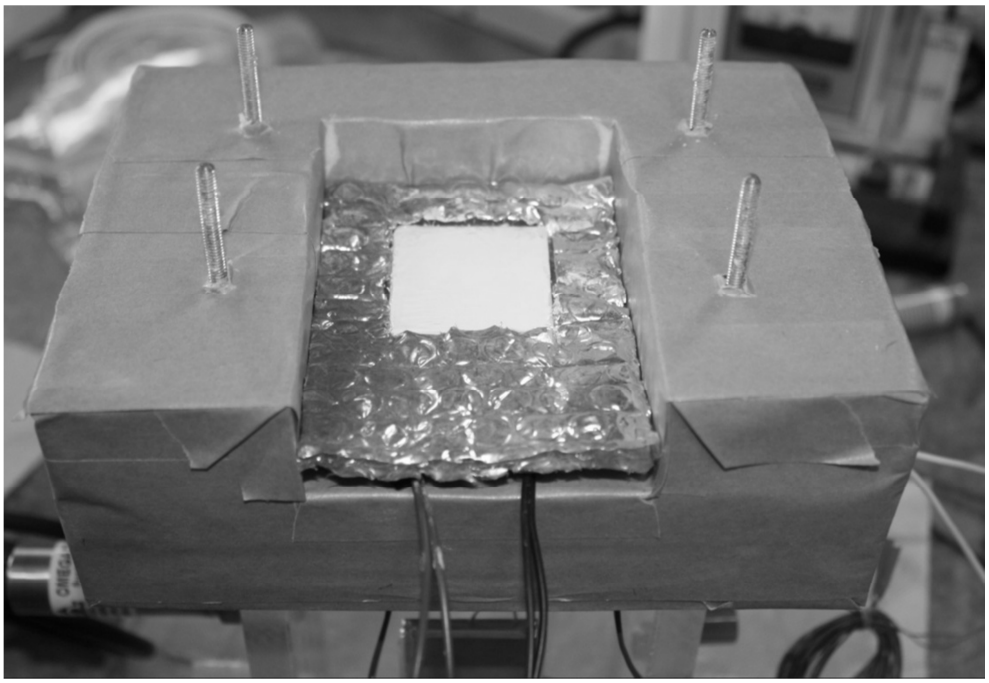

Figure E-6 Chiller thermoelectric module and insullation.

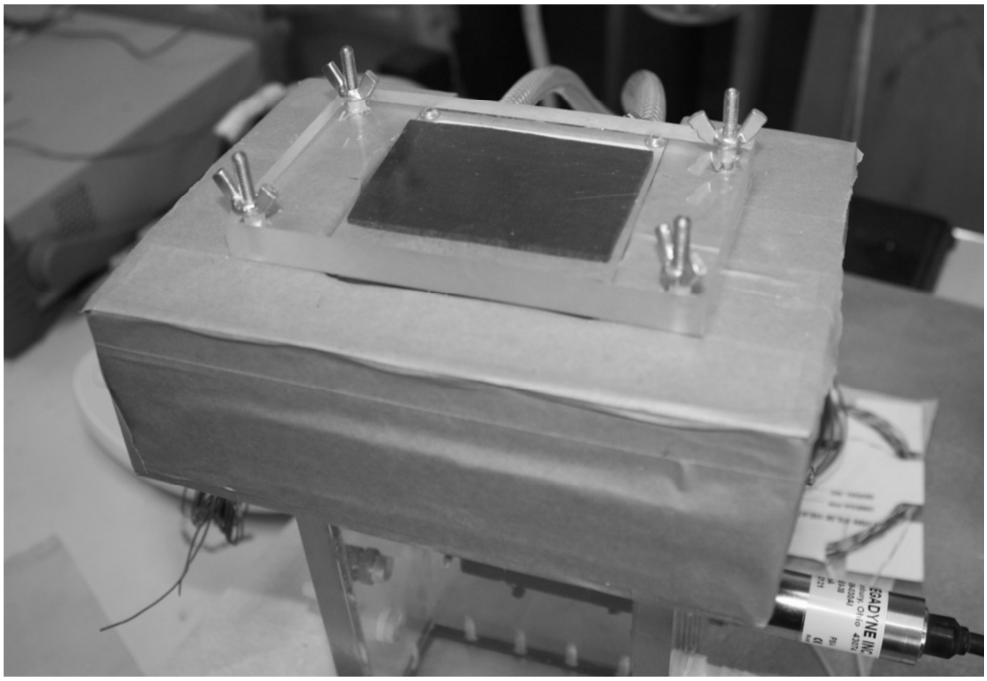

Figure E-7 Completed chiller assembly with water block.

E.3 Test chamber drawings

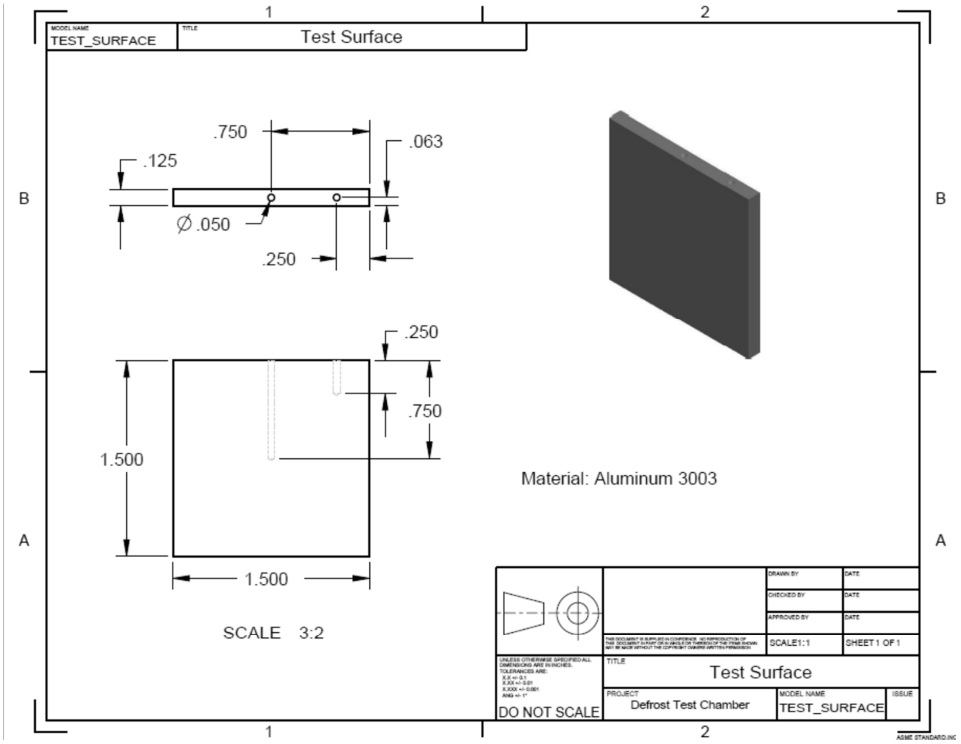

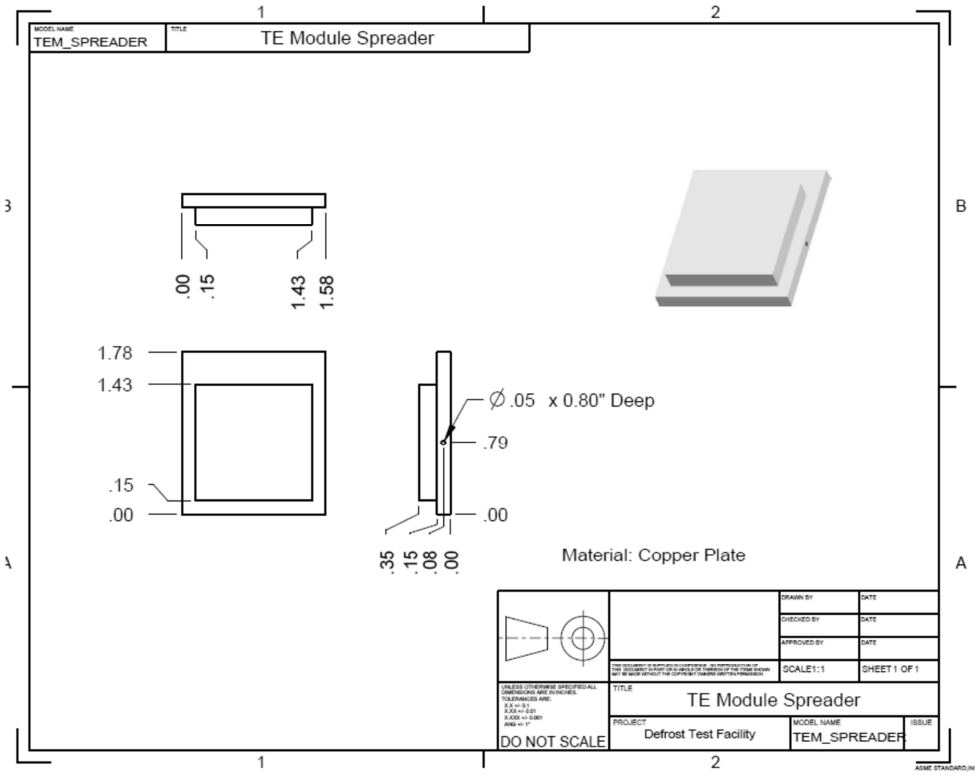

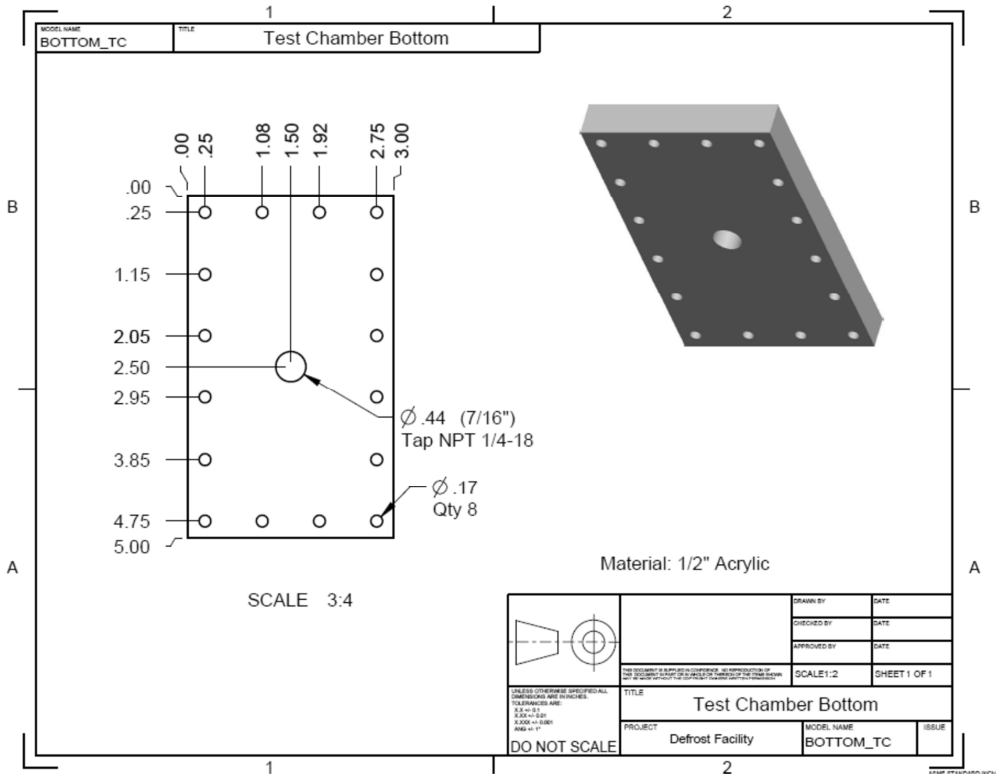
MODEL NAME
BOTTOM_TC
TITLE
Test Chamber Bottom
.00
.25
1.08
1.50
1.92
2.75
3.00
1.15
2.05
2.50
2.95
3.85
4.75
5.00
Ø .44 (7/16")
Tap NPT 1/4-18
Ø .17
Qty 8
SCALE 3:4
Material: 1/2" Acrylic
DRAWN BY
DATE
CHECKED BY
APPROVED BY
SCALE1:2
SHEET 1 OF 1
UNLESS OTHERWISE SPECIFIED ALL DIMENSIONS ARE IN INCHES.
TOLERANCES ARE:
DO NOT SCALE
Test Chamber Bottom
PROJECT
Defrost Facility
MODEL NAME
BOTTOM_TC
ISSUE

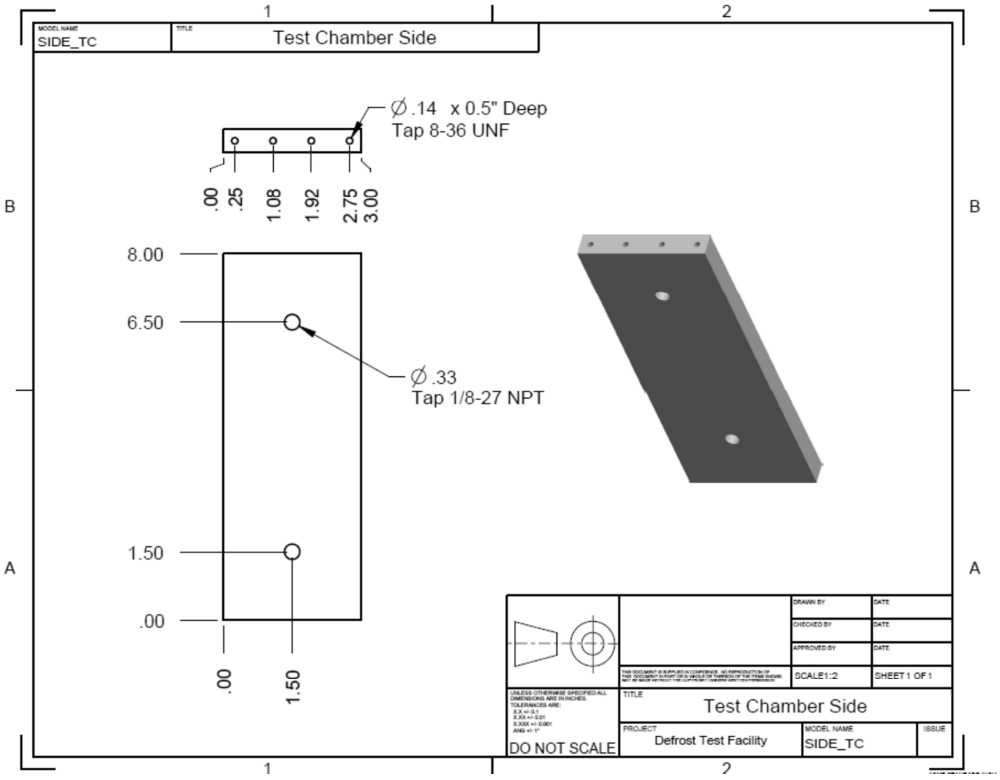
MODEL NAME
SIDE_TC
TITLE
Test Chamber Side
Ø .14 x 0.5" Deep
Tap 8-36 UNF
.00
.25
1.08
1.92
2.75
3.00
8.00
6.50
Ø .33
Tap 1/8-27 NPT
1.50
.00
.00
1.50
DRAWN BY
DATE
CHECKED BY
APPROVED BY
SCALE1:2
SHEET 1 OF 1
UNLESS OTHERWISE SPECIFIED ALL DIMENSIONS ARE IN INCHES.
TOLERANCES ARE:
DO NOT SCALE
Test Chamber Side
PROJECT
Defrost Test Facility
MODEL NAME
SIDE_TC
ISSUE

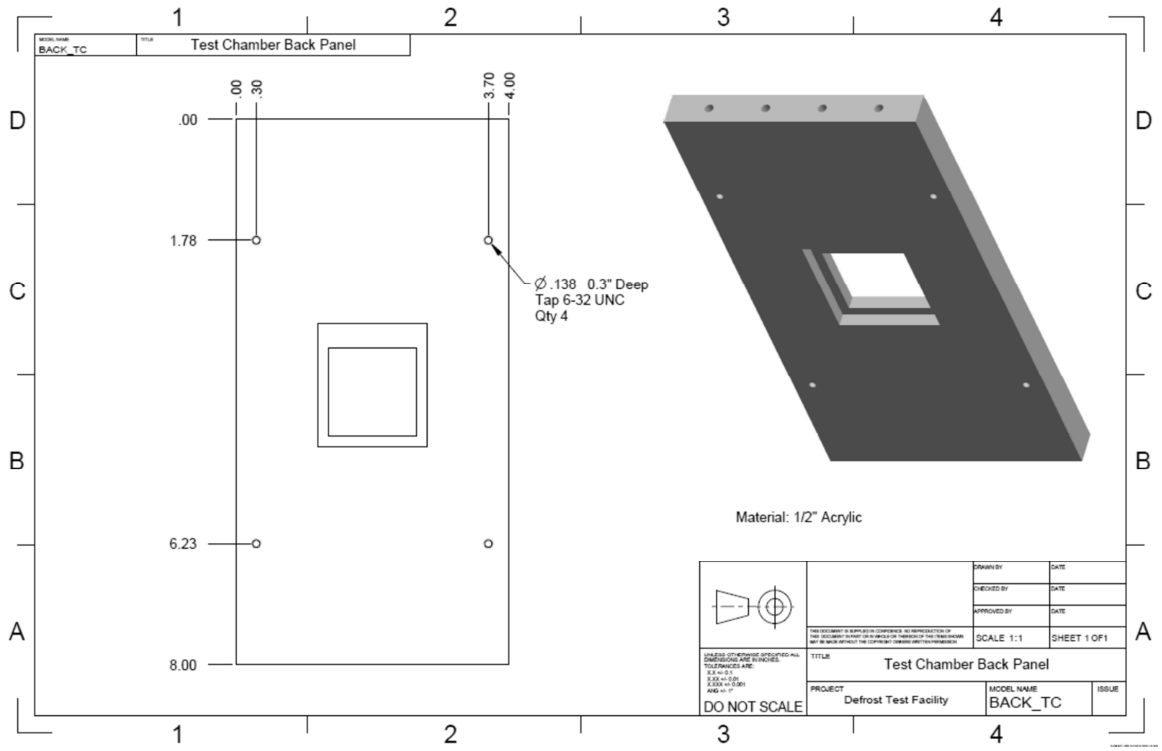
BACK_TC
Test Chamber Back Panel
.00
.30
3.70
4.00
.00
1.78
6.23
8.00
Ø .138 0.3" Deep
Tap 6-32 UNC
Qty 4
Material: 1/2" Acrylic
SCALE 1:1
SHEET 1 OF1
DO NOT SCALE
Test Chamber Back Panel
Defrost Test Facility
BACK_TC

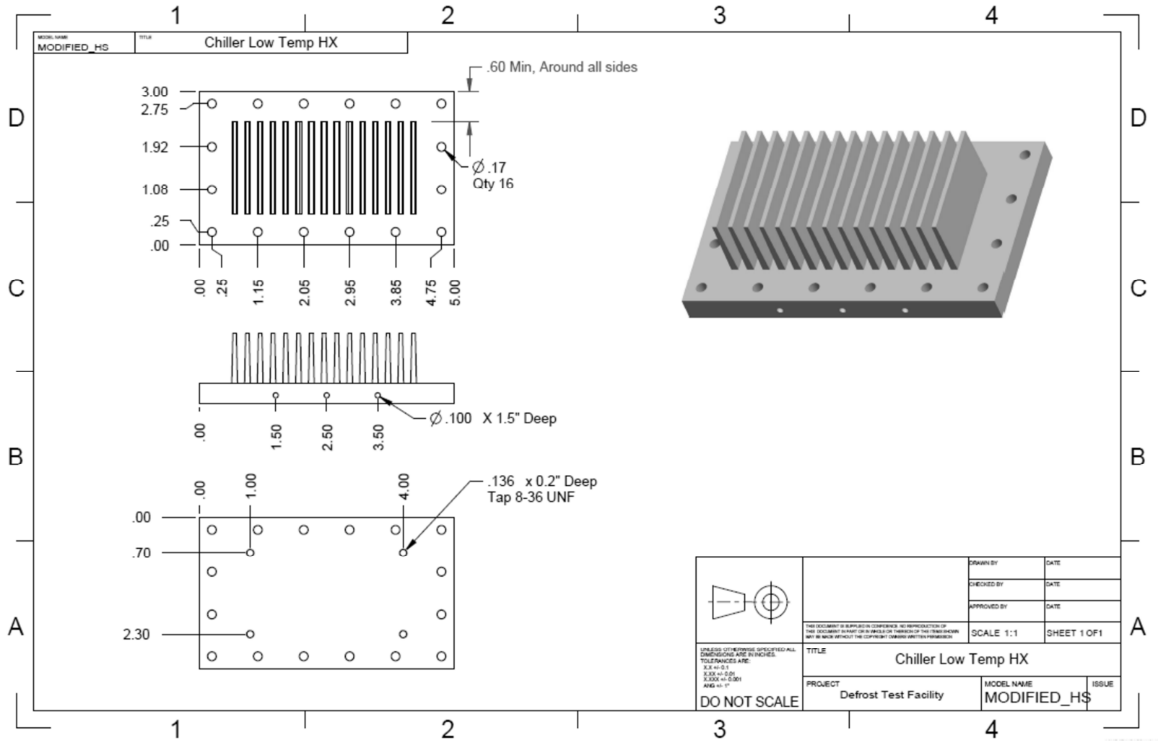
MODIFIED_HS
Chiller Low Temp HX
.60 Min, Around all sides
3.00
2.75
1.92
1.08
.25
.00
Ø .17
Qty 16
.00
.25
1.15
2.05
2.95
3.85
4.75
5.00
Ø .100 X 1.5" Deep
.00
1.50
2.50
3.50
.136 x 0.2" Deep
Tap 8-36 UNF
.00
1.00
4.00
.00
.70
2.30
SCALE 1:1
SHEET 1 OF1
DO NOT SCALE
Chiller Low Temp HX
Defrost Test Facility
MODIFIED_HS

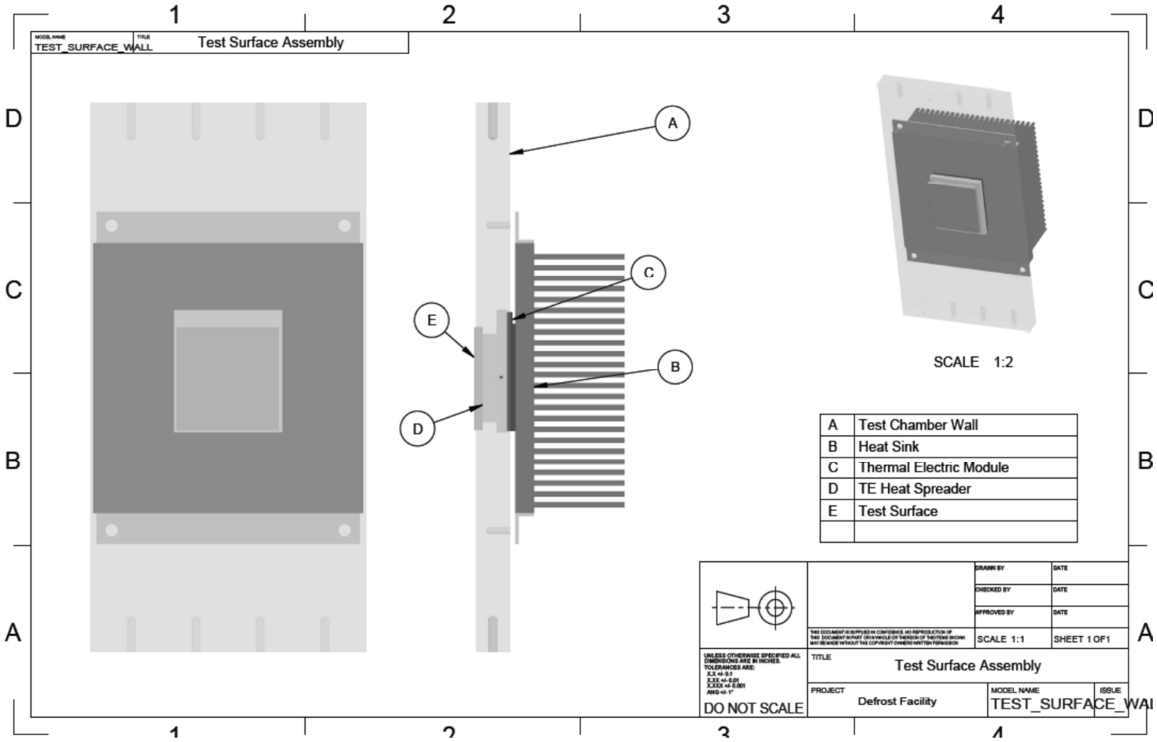
MODEL NAME
TEST_SURFACE_WALL
TITLE
Test Surface Assembly
A
B
C
D
E
SCALE 1:2
A Test Chamber Wall
B Heat Sink
C Thermal Electric Module
D TE Heat Spreader
E Test Surface
DRAWN BY
DATE
CHECKED BY
DATE
APPROVED BY
DATE
SCALE 1:1
SHEET 1 OF1
UNLESS OTHERWISE SPECIFIED ALL DIMENSIONS ARE IN INCHES.
TOLERANCES ARE:
DO NOT SCALE
TITLE
Test Surface Assembly
PROJECT
Defrost Facility
MODEL NAME
TEST_SURFACE_WAL
ISSUE

Appendix F. MATLAB Code

```
% State Space Model for dry heated plate
% Outputs A, B, C, and D matrix for Simulink state-space model
% Bill Mohs, 2011

T_sp_avg = mean(data(:, 4)); % Spreader termperature (C)
T_ts_avg = mean(data(:, 5)); % Test surface temperature (C)
T_e_avg = mean(data(:, 3)); %Mean wall temperature (C)

A_ts = 0.00160; % Test surface area (m^2)

h_a = 20; % Air heat transfer coefficient (W/m^2-K)
R_e = 0.186*T_e_avg+14.377; %Resistance for edge loss (K/W)
R_ts = 0.031*T_sp_avg+1.080; %Contact resistance for K/W

F = 5; %Correction factor for contact resistance
F2 = 3.0; %Correction factor for HTC
F3 = 1.15; %Correction factor for thermal capacitance

%Thermal Capacitance
C_sp = 45.843*F3; % J/K
C_ts = 13.914; % J/K

%Overall heat transfer coefficient
UA_a = h_a*A_ts*F2; %W/K
UA_e = 1/R_e; %W/K
UA_ts = F/R_ts;%W/K

%A and B Matrix
a11 = -1*(UA_ts/C_sp+UA_e/C_sp); % 1/s
a12 = (UA_ts/C_sp); % 1/s
a21 = (UA_ts/C_ts); % 1/s
a22 = -1*(UA_ts/C_ts+UA_a/C_ts); % 1/s
b11 = -1*(1/C_sp); % C/J
b12 = (UA_e/C_sp); % 1/s
b13 = 0;
b21 = 0;
b22 = (0);
b23 = (UA_a/C_ts); % 1/s

%Outputs for state-space model
A = [a11, a12; a21, a22];
B = [b11, b12, b13; b21, b22, b23];
C = eye(2);
D = zeros(2,3);
x0 = [data(1, 4); data(1, 5)];

%end of program
```

```
%Frost porosity analysis
%Routine to calculate frost porosity from frontal images.
%Converts image to black-white binary image, counts the number of
%ice-filled pixels, and divides by the total number of pixels.  Ice
%threshold level set up Matlab 'graythresh' routine.
%Bill Mohs, 2011

close all;
clear;
clc;

%%% Read in frost image %%%
frost = imread('frost_front_12_17_10.jpg');   %Read in
frost = rgb2gray(frost);        %Convert to grayscale
BW = im2bw(frost, graythresh(frost)); %Convert to black and white image

imshow(BW);

%%% Determine image size %%%
s = size(frost);
pix = s(1)*s(2); %Total pixel count

%%% Calculates porosity by summing the number of ice filled pixels
%%% and dividing by the total number of pixels.
porosity = 1- sum(sum(BW))/pix;

%end of program
```

```
%Drop size analysis
%Finds drops, calculates, area, perimeter, and hydraulic diameter.
%Bill Mohs, 2011

close all; clear ; clc;
res = 201;% image resolution (pixels/mm)

ID = imread('2_28_11_drop_0164.png');               % Read in file
ID = rgb2gray(ID);
ID = imadjust(ID);

for loop = 1 : 163;
    if (loop<10);
       imtag = sprintf('%s%1.0f%s','2_28_11_drop_000', loop, '.png');
    elseif (loop>=100)
       imtag = sprintf('%s%1.0f%s','2_28_11_drop_0', loop, '.png');
    else
       imtag = sprintf('%s%1.0f%s','2_28_11_drop_00', loop, '.png');
    end
%%% Read in frost image %%%
I = imread(imtag);               % Read in file
I = rgb2gray(I);

% Adjust images to improve contrast
I = imadjust(I);

%Subtracts base image from drop image
IDiff = imsubtract(ID,I);

%Converts image to black and white, finds transitions and colors
BW = im2bw(IDiff, graythresh(I));
se = strel('disk',80);
BW = imclose(BW,se);

% Determine boundary location
[B,L] = bwboundaries(BW,4,'noholes');     % Locate boundaries

%Sorts vector by curve length
for k = 1:length(B)
    [M(k) N(k)] = size(B{k});
end
[BB IX]= sort(M,'descend');
for k = 1:length(B)
    BNew(k,1) = B(IX(k),1);
end

j = 0;
for k = 1:length(BNew)
    [M N] = size(BNew{k});

    if M >= 200 %Only counts drops with a outside length greater than
200
```

```
        j = 1+j;
        p(loop,j) = 0;
        boundary = BNew{k};
%         plot(boundary(:,2),boundary(:,1), 'w', 'LineWidth', 3)
%       fill(boundary(:,2),boundary(:,1),'k');

%       Loop to determine perimeter of drop
        for i = 1 : M-1
            dx = abs(boundary(i,1)-boundary(i+1,1));
            dy = abs(boundary(i,2)-boundary(i+1,2));
            if ((dx==1)&&(dy==1));
                p(loop,j) = sqrt(dx+dy) + p(loop,j);
            else
                p(loop,j) = dx + dy + p(loop,j);
            end
        end

        area(loop,j) = trapz(boundary(:,1),boundary(:,2)); % calculates
area of each drop
        Dh(loop,j) = 4*area(loop,j)/p(loop,j); % calcuates hydraulic
diameter of drops
    end
end

area(loop,:)=area(loop,:)*(1/res)^2;
p(loop,:) = p(loop,:)/res;
Dh(loop,:) = Dh(loop,:)/res;

area_mean(loop)= mean(area(loop,:));
p_mean(loop) = mean(p(loop,:));
Dh_mean(loop) = mean(Dh(loop,:));
end

area_sort=sort(area,'descend');
p_sort=sort(p,'descend');
Dh_sort=sort(Dh,'descend');

%end of program
```

```
function [x,t,U,tfin,etafin] =
heatCN(nt,nx,gamma,L,tmax,Bi_s,Bi_fs,Uo_fs,U_a)
% heatBTCS Solve 1D heat equation with the Crank-Nicolson scheme
% Bill Mohs, 2012
%
% Synopsis: heatCN
% heatCN(nt)
% heatCN(nt,nx)
% heatCN(nt,nx,gamma)
% heatCN(nt,nx,gamma,L)
% heatCN(nt,nx,gamma,L,tmax)
% heatCN(nt,nx,gamma,L,tmax,Bi_0)
%
% Input:
% nt = number of steps. Default: nt = 10;
% nx = number of mesh points in x direction. Default: nx=20
% gamma = diffusion coefficient. Default: gamma = 0.1
% L = length of the domain. Default: L = 1;
% tmax = maximum time for the simulation. Default: tmax = 0.5
% Bi_s = Biot number at surface, Negative is heat from surface.
%      Default:  Bi_s =  -0.2
% Bi_fs = Biot number at frost-air surface, Negative is heat from
surface.
%      Default:  Bi_fs =  0.1
% Uo_fs = Nondimesional initial temperature at frost-air interface
%      Default:  Uo_fs = 0.1
% U_a = Nondimesional air temperature, Default = 0.75

% Output:
% x = location of finite difference nodes
% t = values of time at which solution is obtained (time nodes)
% U = matrix of solutions: U(:,j) is U(x) at t = t(j)

if nargin<1, nt = 10; end
if nargin<2, nx = 20; end
if nargin<3, gamma = 1.0; end % diffusivity
if nargin<4, L = 1; end
if nargin<5, tmax = 0.5; end
if nargin<6, Bi_s=  -0.2; end % Biot number at surface
if nargin<7, Bi_fs= 0.1; end % Biot number at frost-air surface
if nargin<8, Uo_fs= 0.1; end % Initial temp at frost-air surface
if nargin<9, U_a = .75; end %Air temperature

% --- Compute mesh spacing and time step
dx = L/(nx-1); dt = tmax/(nt-1);
% --- Create arrays to save data for export
x = linspace(0,L,nx)'; t(1) = 0; U = zeros(nx,1);
% --- Set IC and BC
% U(:,1) = sin(pi*x/L); % implies u0 = 0; uL = 0;
U(:,1) = linspace(0,Uo_fs,nx);

E_s = 0;
E_fs = 0;
```

```
% --- Coefficients of the tridiagonal system
a = (-gamma/2/dx^2)*ones(nx,1); % subdiagonal a: coefficients of phi(i-
1)
c = a; % superdiagonal c: coefficients of phi(i+1)
b = (1/dt)*ones(nx,1) - (a+c); % diagonal b: coefficients of phi(i)
b(1) = 1; c(1) = 0; % Fix coefficients of boundary nodes
b(end) = 1; a(end) = 0;
[e,f] = tridiagLU(a,b,c); % Get LU factorization of coefficient matrix
% --- Loop over time steps
for m=2:nt
% Right hand side includes time derivative and CN terms
d = U(:,m-1)/dt - [0; a(2:end-1).*U(1:end-2,m-1); 0] ...
+ [0; (a(2:end-1)+c(2:end-1)).*U(2:end-1,m-1); 0] ...
- [0; c(2:end-1).*U(3:end,m-1); 0];
d(1) = U(1,m-1)+2*gamma^2*dt/dx*(U(2,m-1)-U(1,m-1)-2*dx*Bi_s);
d(end) = U(end,m-1)-2*gamma^2*dt/dx*(U(end,m-1)-U(end-1,m-1)-
2*dx*(Bi_fs*(U_a-U(end,m-1))));
% d(end) = uL; % overwrite BC values
U(:,m) = tridiagLUSolve(d,a,e,f,U(:,m-1)); % solve the system
t(m) = t(m-1)+ dt;
E_s = - Bi_s + E_s;
E_fs =  Bi_fs*(U_a-U(end,m))+E_fs;
eta(m)= 1- E_fs/E_s;
if (U(1,m)>=1),  break, end %Termination when T_surf = T_melt = 0C
end

etafin = eta(m);
tfin = t(m);
% --- Compare with exact solution at end of simulation

%end of program
```

```
function [e,f] = tridiagLU(a,b,c)
% tridiagLU Obtain the LU factorization of a tridiagonal matrix
% Bill Mohs, 2012
%
% Synopsis: [e,f] = tridiag(a,b,c)
%
% Input: a,b,c = vectors defining the tridiagonal matrix. a is the
% subdiagonal, b is the main diagonal, and c is the superdiagonal
%
% Output: e,f = vectors defining the L and U factors of the tridiagonal
matrix
n = length(a);
e = zeros(n,1); f = e;
e(1) = b(1);
f(1) = c(1)/b(1);
for i=2:n
e(i) = b(i) - a(i)*f(i-1);
f(i) = c(i)/e(i);
end

% end of program
```

```
function v = tridiagLUSolve(d,a,e,f,v)
% tridiagLUsolve Solve (LU)*v = d where L and U are LU factors of a
tridiagonal
% matrix
%
% Bill Mohs, 2012
%
% Synopsis: v = tridiagLUsolve(d,e,f)
% v = tridiagLUsolve(d,e,f,v)
%
% Input: d = right hand side vector of the system of equatoins
% e,f = vectors defining the L and U factors of the tridiagonal matrix.
% e and f are obtained with the tridiagLU function
% v = solution vector. If v is supplied, the elements of v are over-
% written (thereby saving the memory allocation step). If v is not
% supplied, it is created. v is used as a scratch vector in the
% forward solve.
%
% Output: v = solution vector
n = length(d);
if nargin<5, v = zeros(n,1); end
% --- Forward substitution to solve L*w = d
v(1) = d(1)/e(1);
for i=2:n
v(i) = (d(i) - a(i)*v(i-1))/e(i);
end
% --- Backward substitution to solve U*v = w
for i=n-1:-1:1
v(i) = v(i) - f(i)*v(i+1);
end

% end of program
```

```
function showTheat(x,t,T,pflag)
% showTheat Plot and print solutions to the heat equation
%
% Bill Mohs, 2012
%
% Synopsis: showTheat(x,t,T)
% showTheat(x,t,T,pflag)
%
% Input: x = vector of positions at which temperature is known
% t = vector of times at which solution is to be evaluated
% T = matrix of T(x,t) values. T(:,t(j)) is T(x) at time t(j)
% pflag = flag to control printing of results.
% Default: pflag = 0, do not print results
% --- Define string matrix of line styles that can be reused.
% nsymb is the total number of line style strings (plot symbols)
% In plot loop the statement isymb = 1 + rem(j-1,nsymb) is an
% index in the range 1 <= isymb <= nsymb

figure
hold on
box on

num = 10; %sets number of lines

lineSymb = strvcat('k-.','k-o','k-v','k-s','k*-','k-d','k-+',...
   'k-<','k-h','k-p','k-^');
nsymb = size(lineSymb,1);
inv = round(length(t)/(num-1));

% --- Plot T(x,t): each time is a different curve with different symbol
isymb = 1;
for j=1:num
   %    isymb = 1 + rem(j-1,nsymb); % cyclic index for line styles.
   pn = (j-1)*inv+1;
   if (pn>length(t)), pn = length(t); end
   plot(x(:,pn),T(:,pn),lineSymb(isymb,:));
   % --- Build string matrix for legend. Each row is a legend string.
   s = sprintf('t = %-4.2f',t(pn));
   if j==1
      legstr = s;
   else
      legstr = strvcat(legstr,s);
   end
   isymb = isymb + 1;
   if isymb>nsymb, isymb=1; end
end

% Create xlabel
xlabel('h','FontSize',12,'FontName','GreekC');

% Create ylabel
ylabel('Q(h,t)','FontSize',12,'FontName','GreekC');
ylim([0 1.200001]);
```

```
% Create legend
legend(legstr,2)
set(legend,'Location','EastOutside','FontSize',12,'FontName','GreekC');

hold off

% end of program
```

Appendix G. Test Log and Experimental Results

Table G-1 Summary of test conditions.

Test ID	Test Date	Test Conditions $T_{ch}/T_{dp}/T_{ts}$ [°C]
1	11/19/2010	-8.5/-19.0/-20.2
2	12/13/2010	-1.2/-8.5/-10.0
3	12/16/2010	0.0/-8.3/-19.2/
4	12/17/2010	-7.9/-18.1/-19.4
5	1/24/2011	-0.6/-8.4/-9.6
6	1/25/2011	-7.2/-16.8/-19.5
7	1/27/2011	-5.6/-13.2/-18.9
8	2/4/2011	-5/-12.5/-18.4
9	2/11/2011	-8.6/-16.2/-18.9
10	2/28/2011	-4.7/-13.9/-17.8
11	3/1/2011	-4.6/-12.1/-18.8
12	3/8/2011	-3.4/-10.0/-17.5

G.1 Test 1: -8.5/-19.0/-20.2

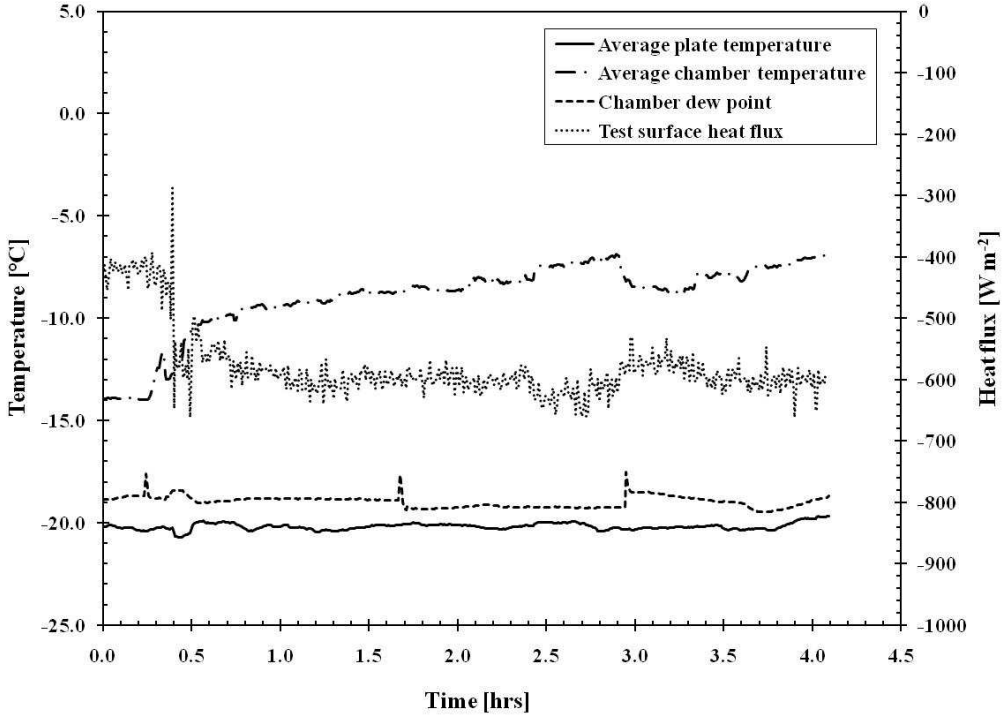

Figure G-1 Temperature and heat flux during frost growth at -8.5/-19.0/-20.2.

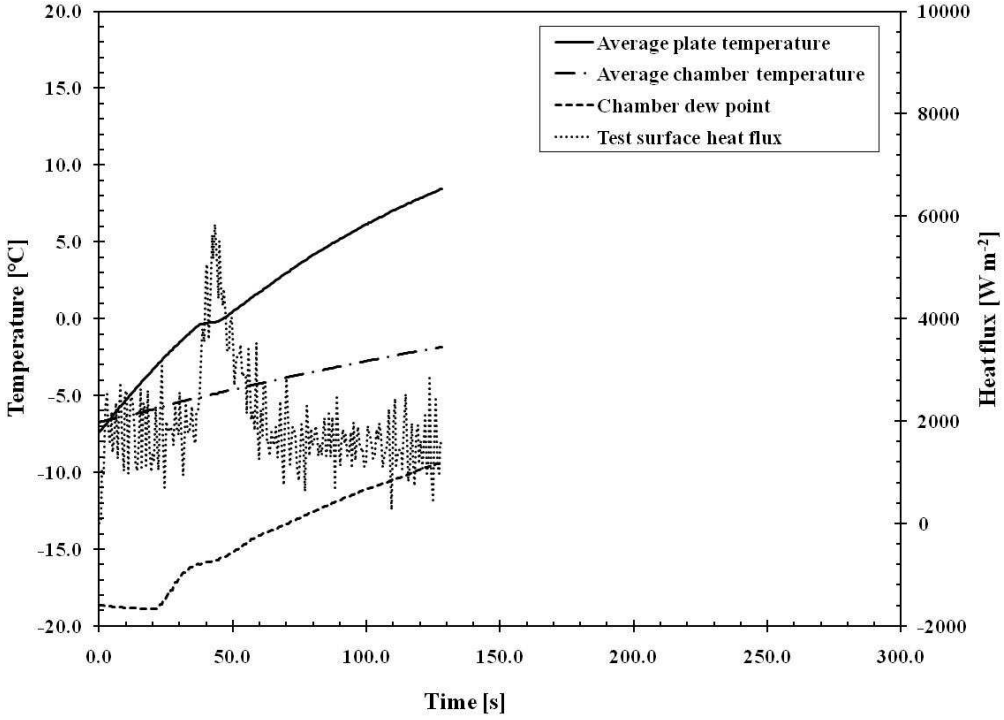

Figure G-2 Temperature and heat flux during defrost at -8.5/-19.0/-20.2.

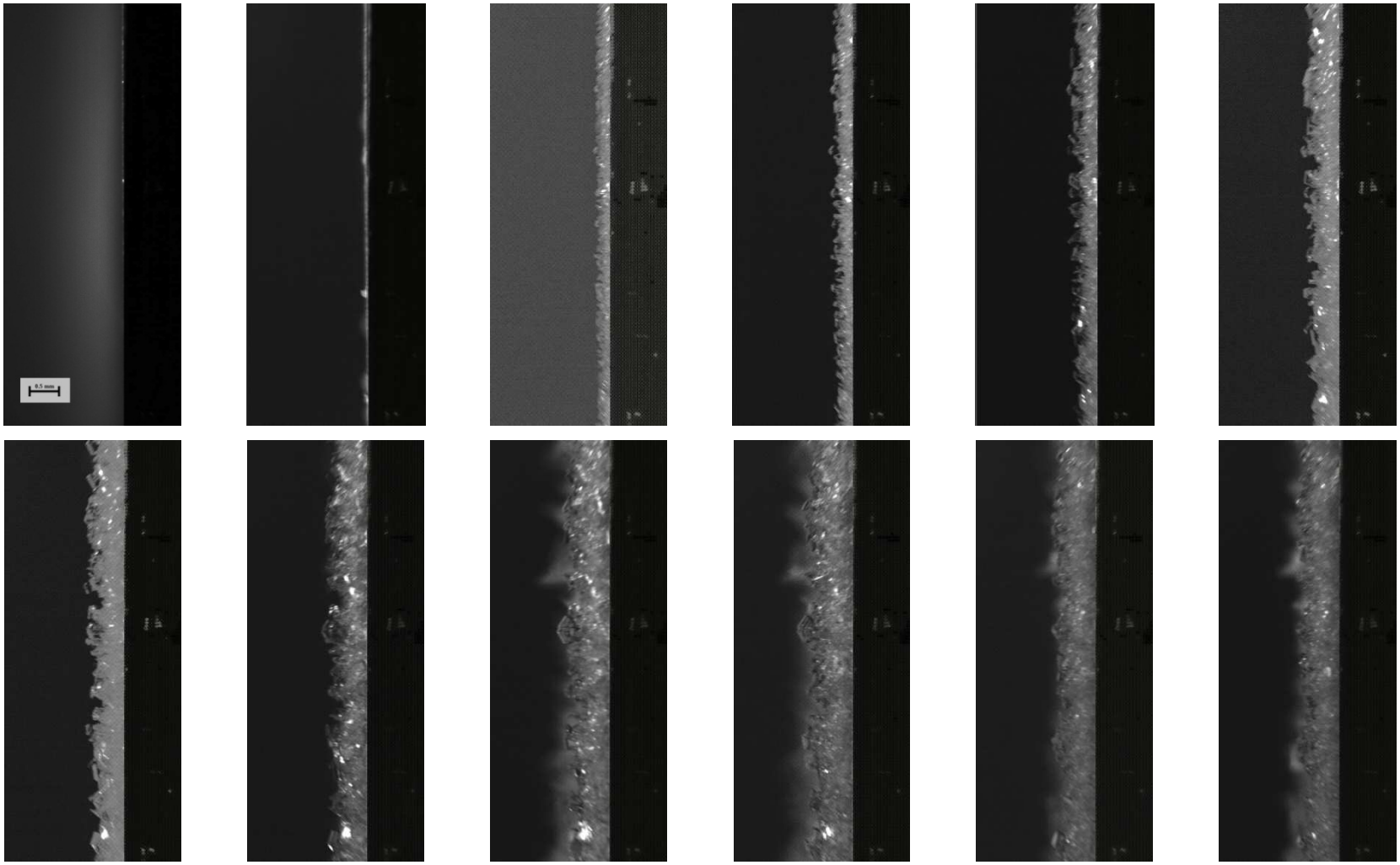

Figure G-3 Side images of frost growth at -8.5/-19.0/-20.2 (20 minute interval).

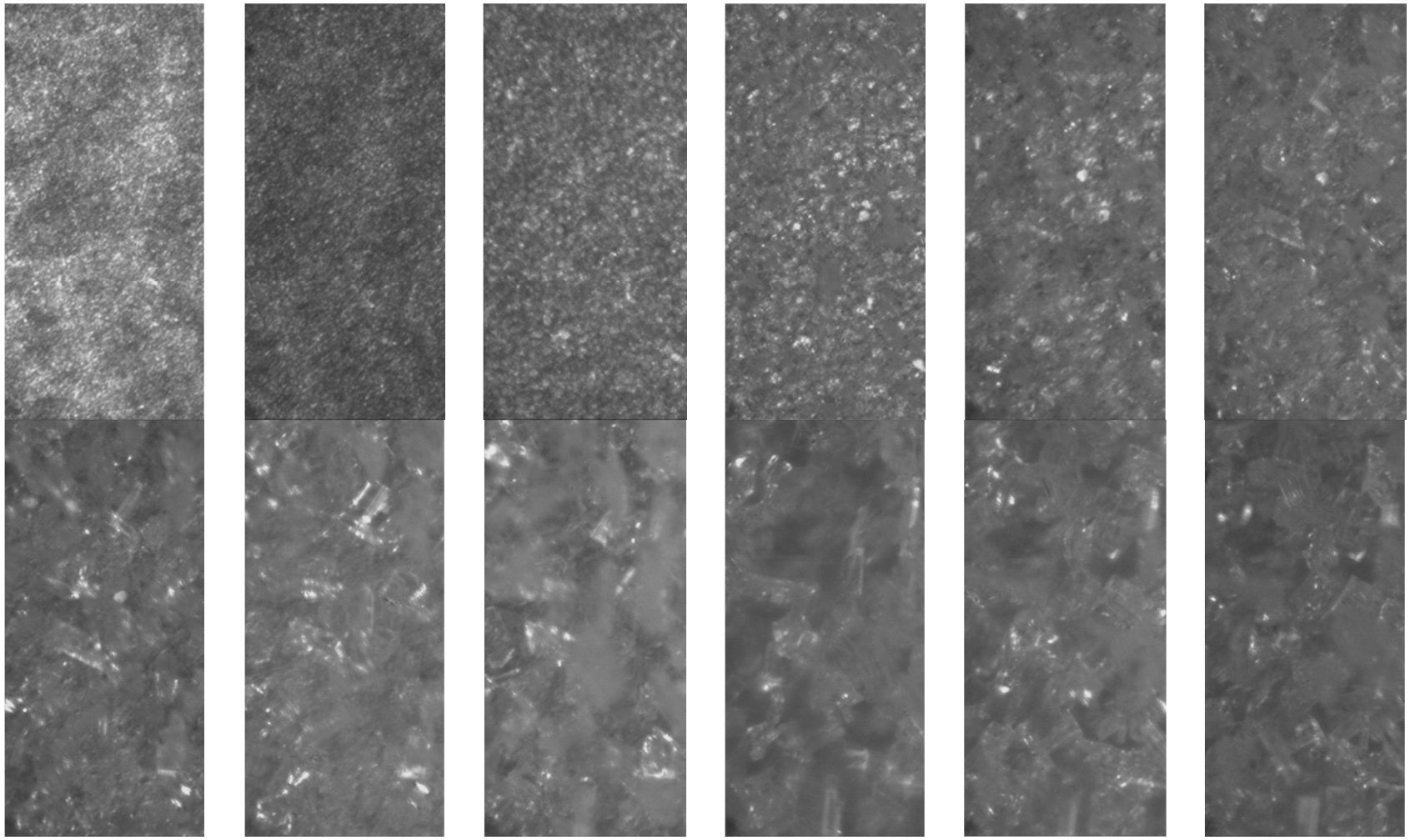

Figure G-4 Frontal images of frost growth at -8.5/-19.0/-20.2 (20 minute interval).

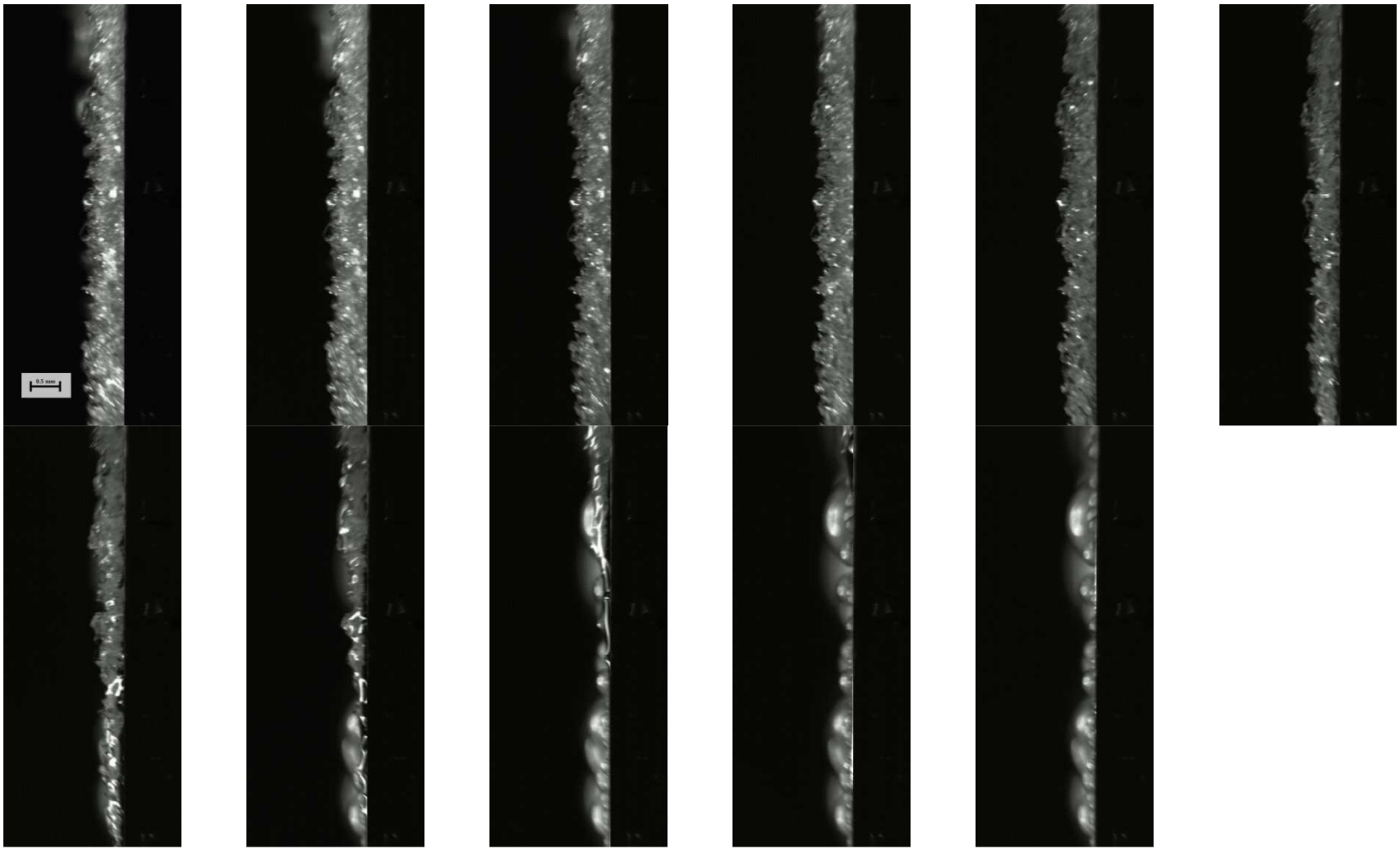

Figure G-5 Side images of defrost at -8.5/-19.0/-20.2 (1.0 second interval).

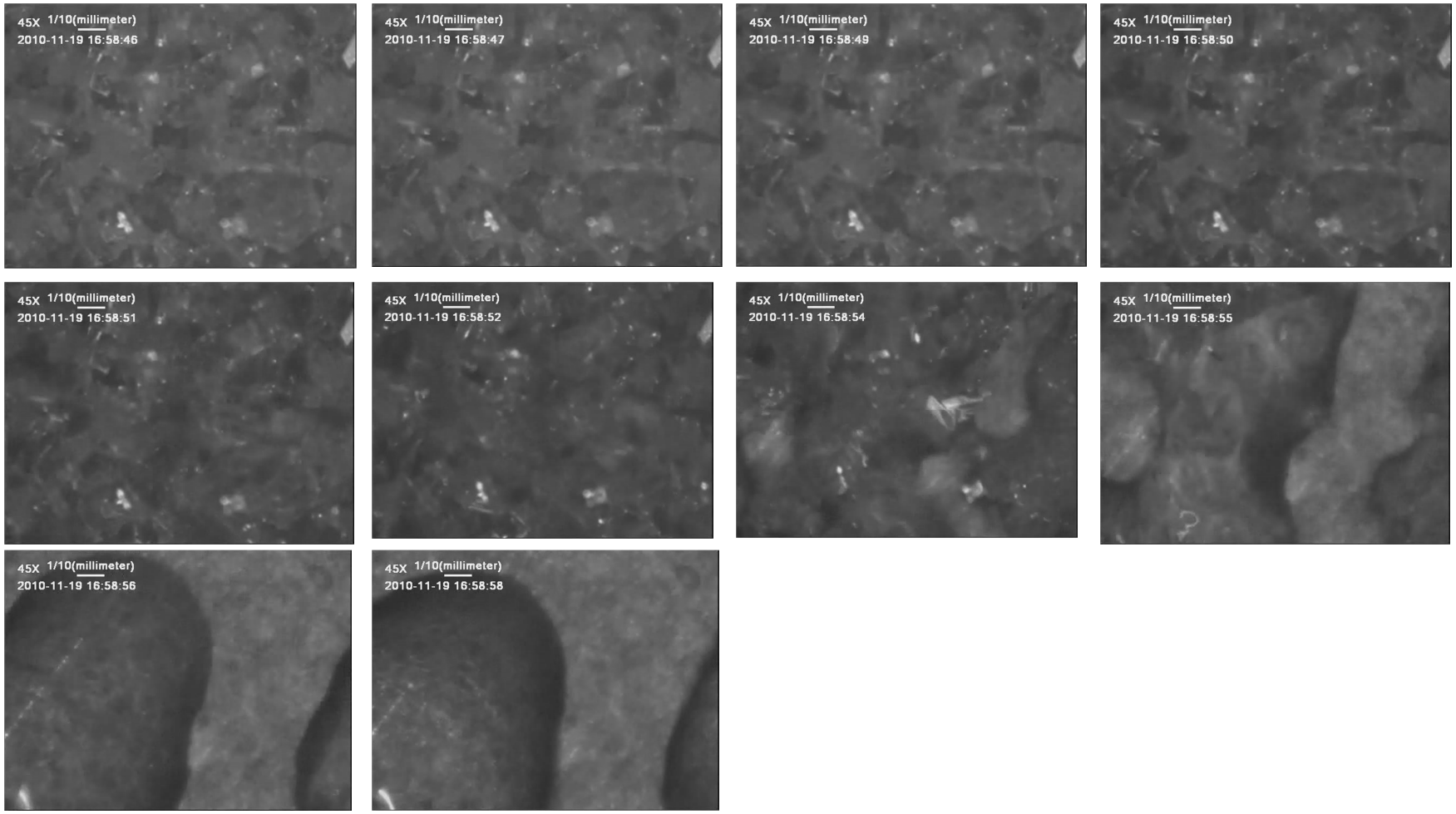

Figure G-6 Frontal images of defrost at -8.5/-19.0/-20.2 (5.0 second interval).

G.2 Test 2: -1.2/-7.8/-10.0

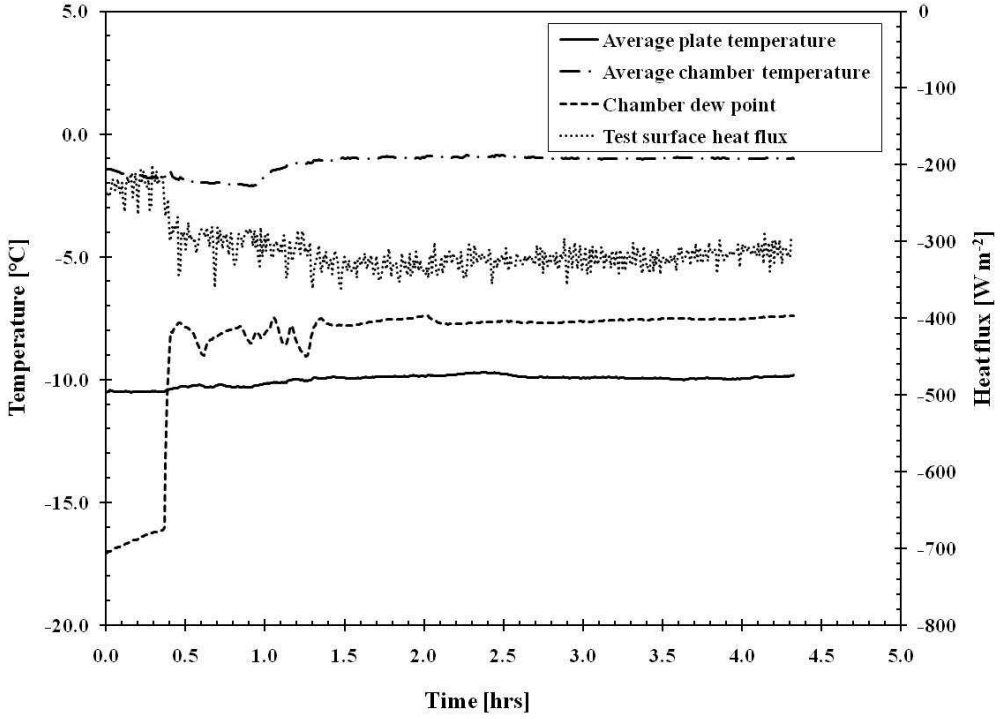

Figure G-7 Temperature and heat flux during frost growth at -1.2/-7.8/-10.0.

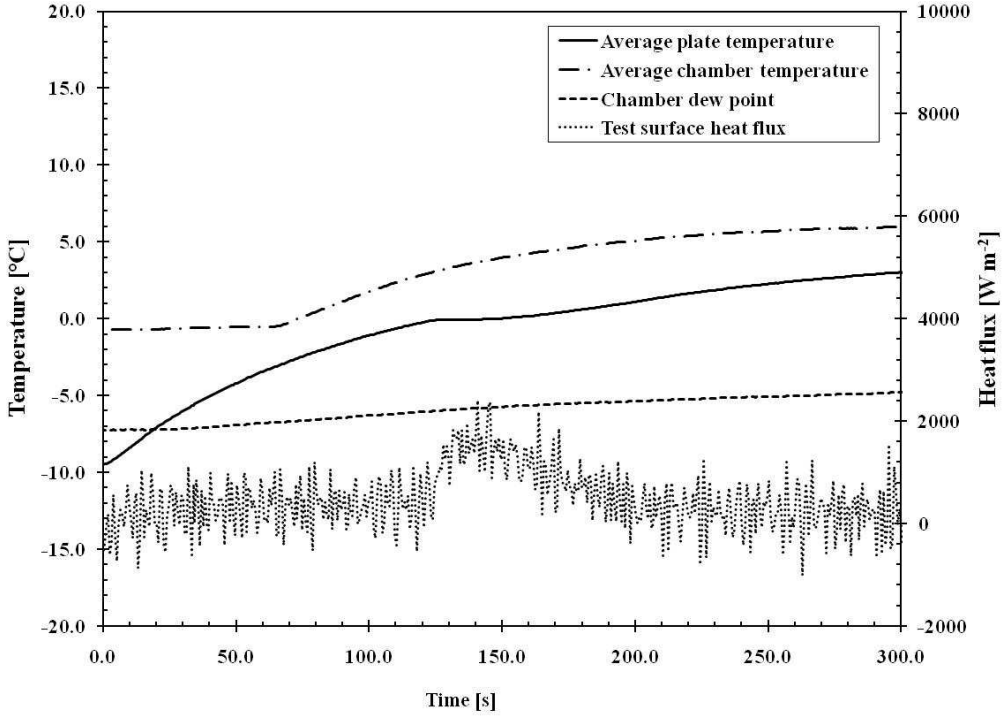

Figure G-8 Temperature and heat flux during defrost at -1.2/-7.8/-10.0.

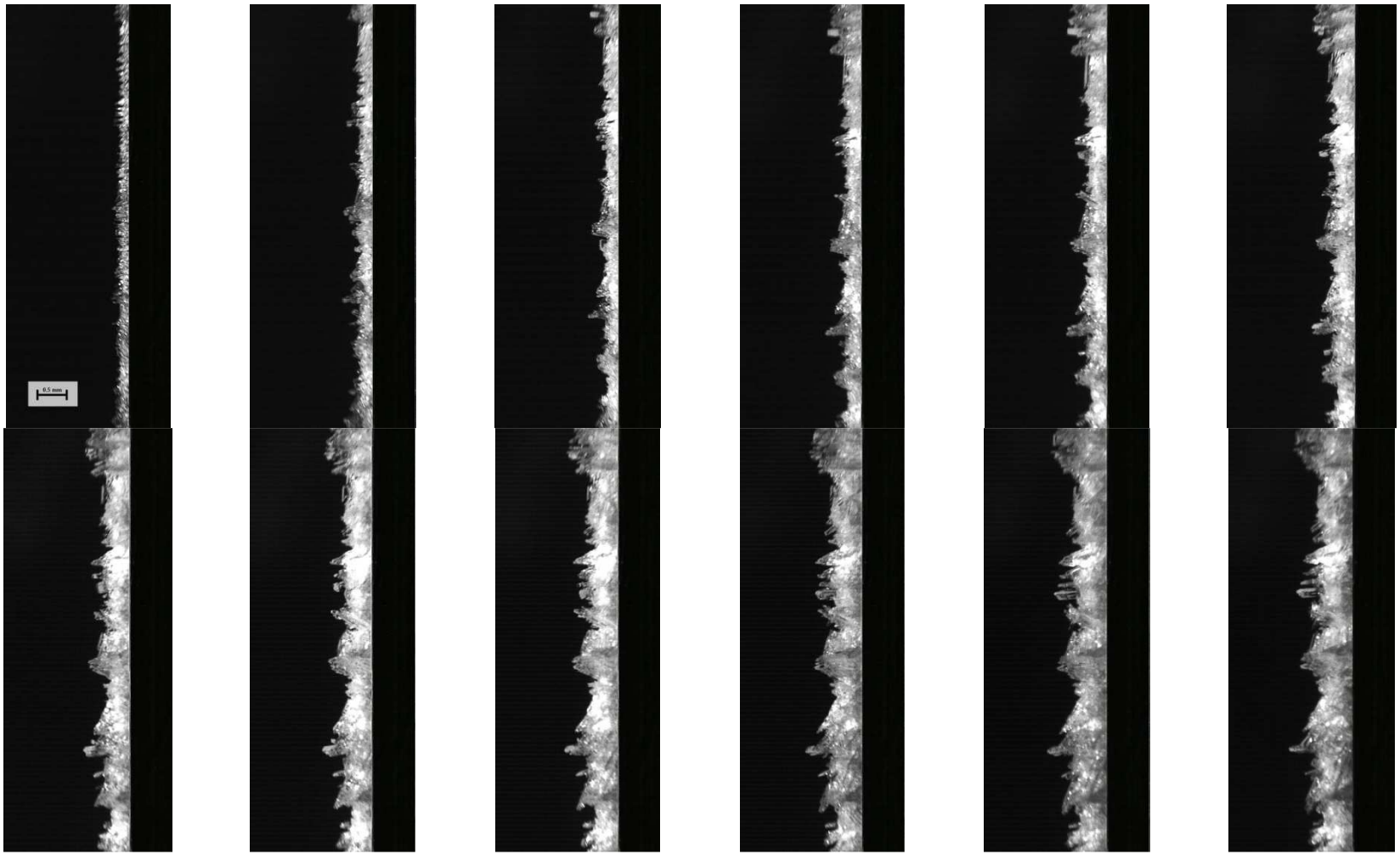

Figure G-9 Side images of frost growth at -1.2/-7.8/-10.0 (20 minute interval).

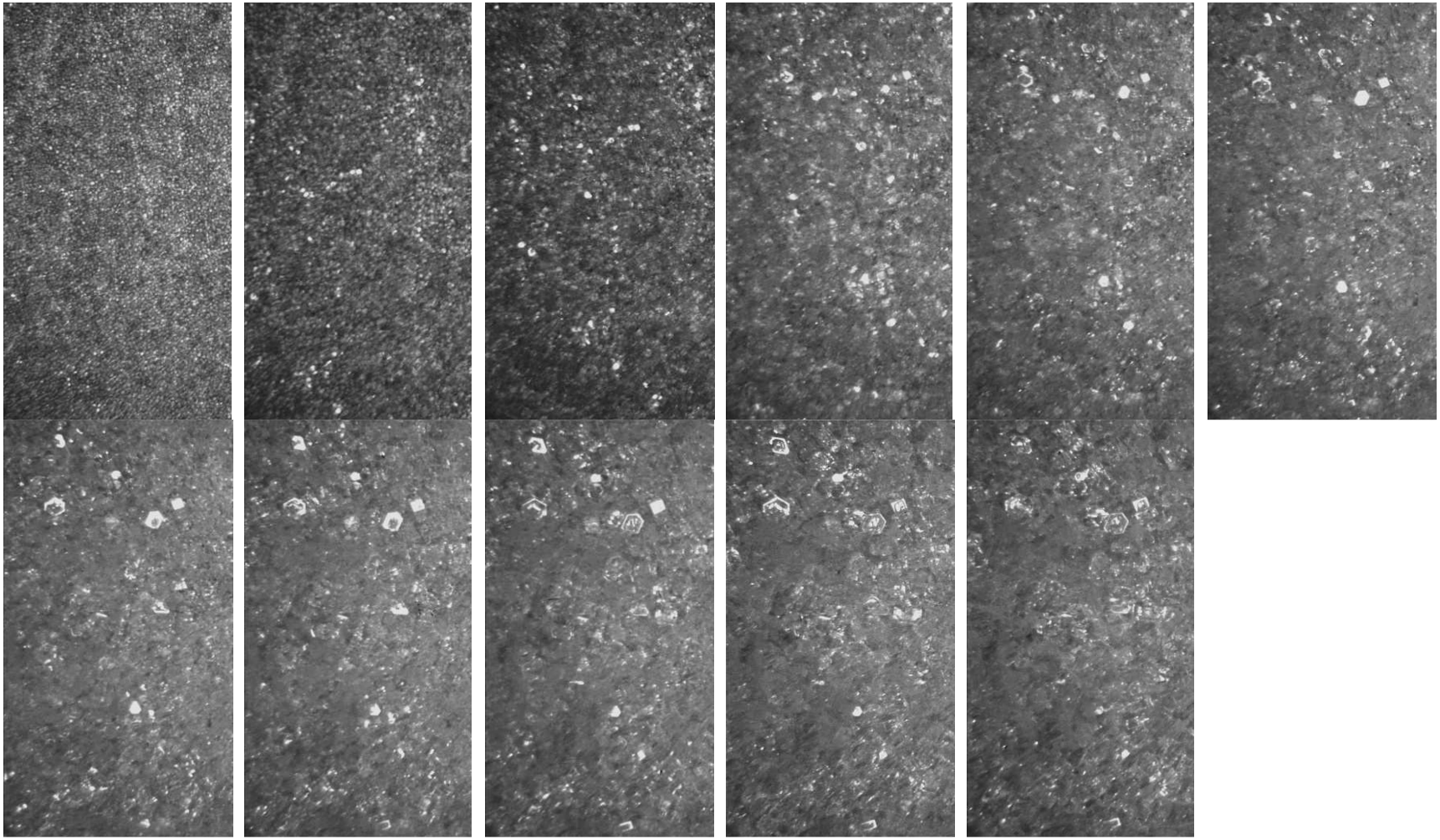

Figure G-10 Frontal images of frost growth at -1.2/-7.8/-10.0 (20 minute interval).

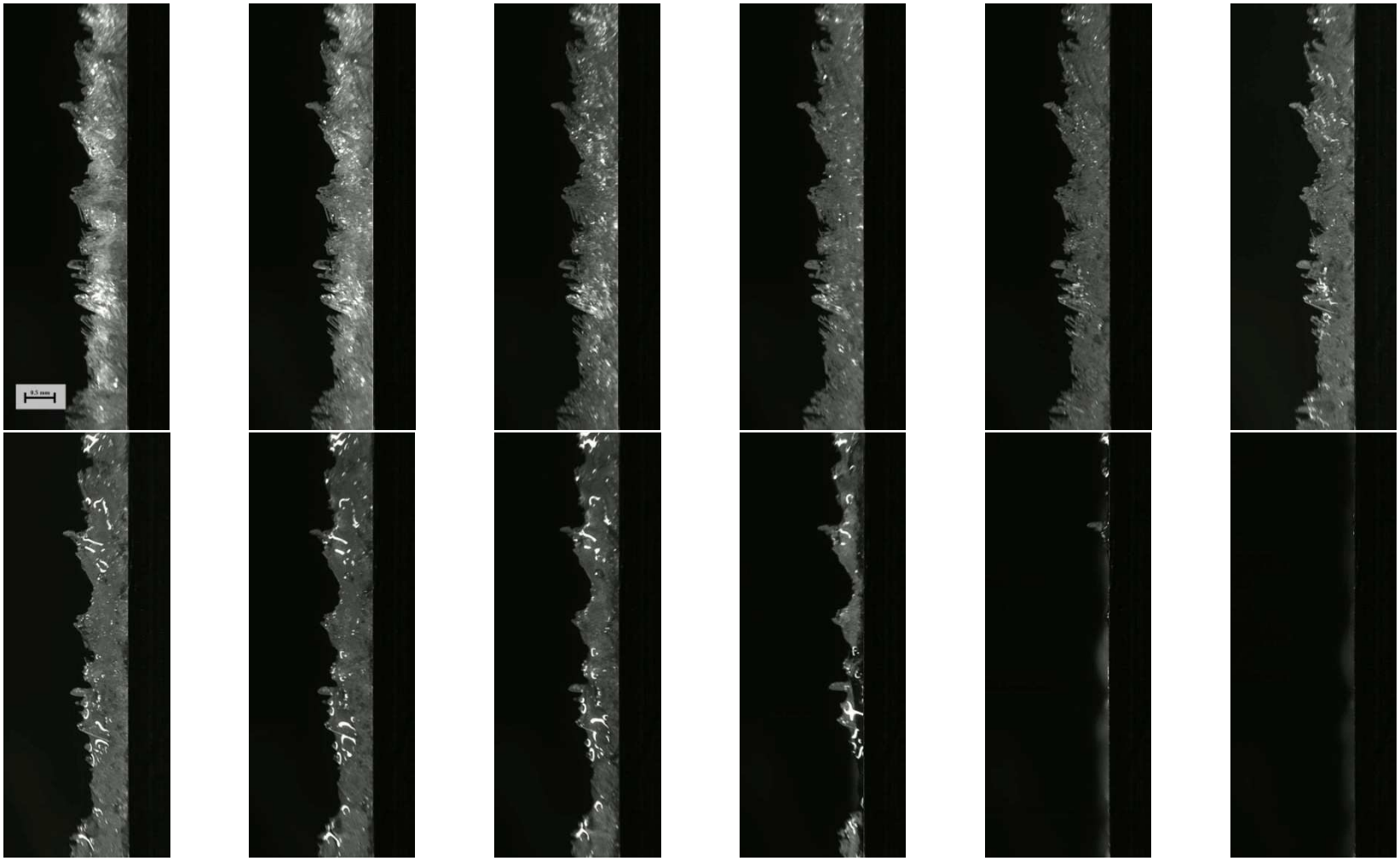

Figure G-11 Side images of defrost at -1.2/-7.8/-10.0 (4.5 second interval).

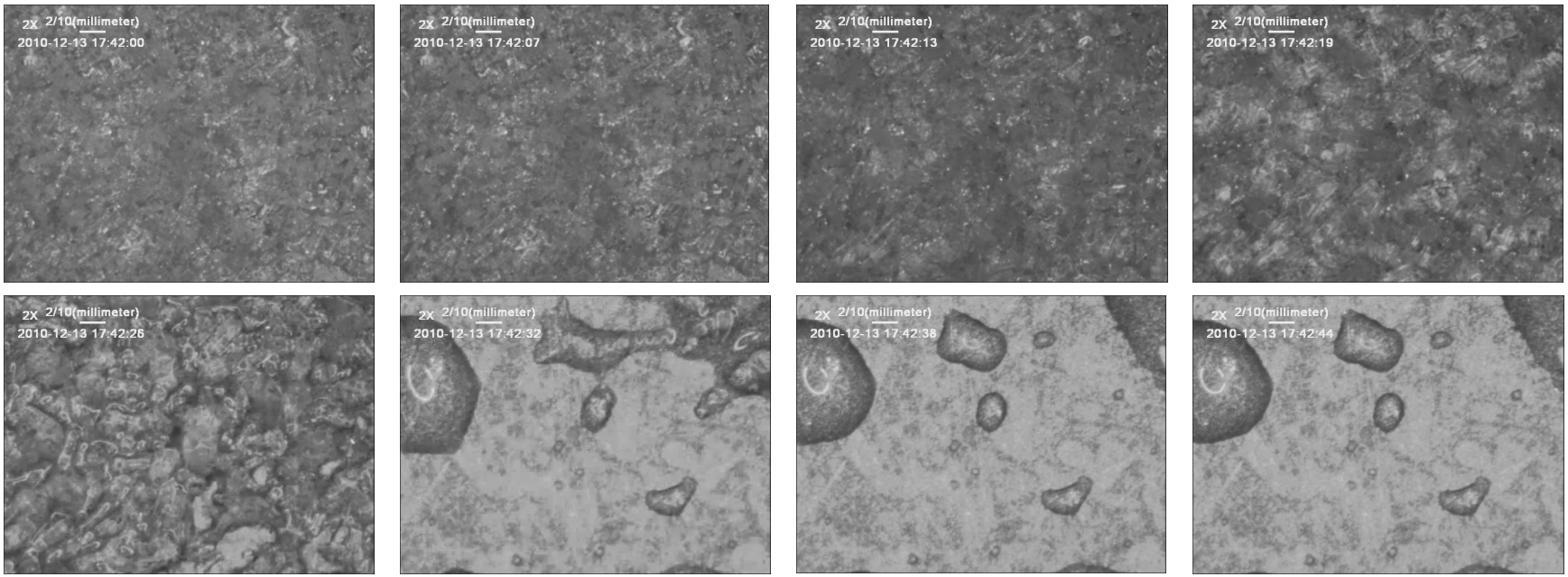

Figure G-12 Frontal images of defrost at -1.2/-7.8/-10.0 (6.0 second interval).

G.3 Test 3: 0.0/-7.7/-19.2

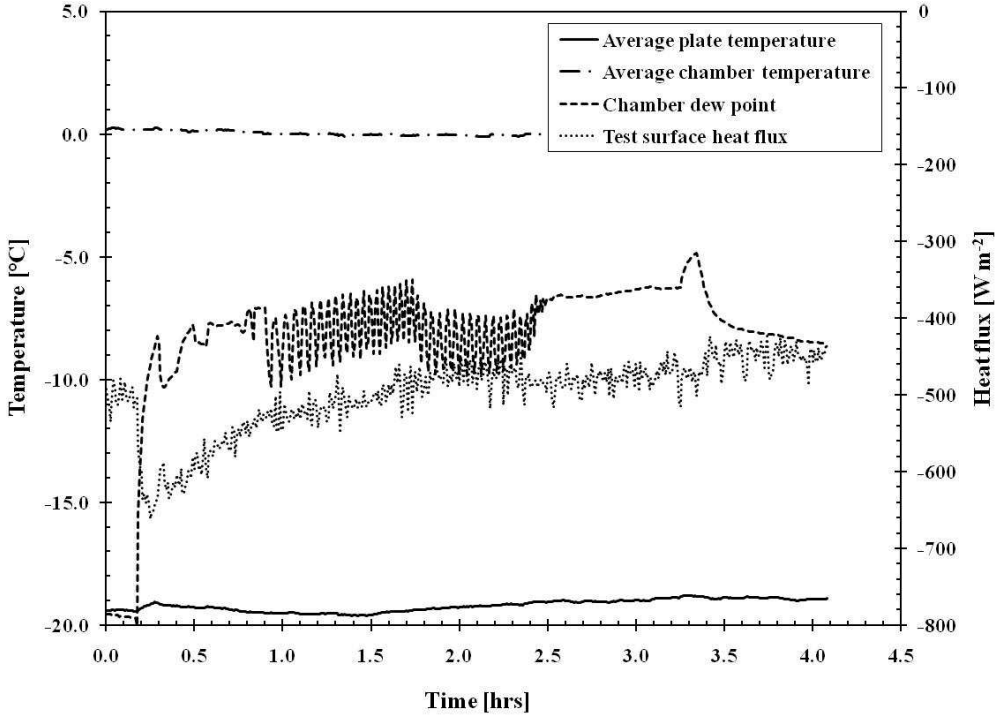

Figure G-13 Temperature and heat flux during frost growth at 0.0/-7.7/-19.2.

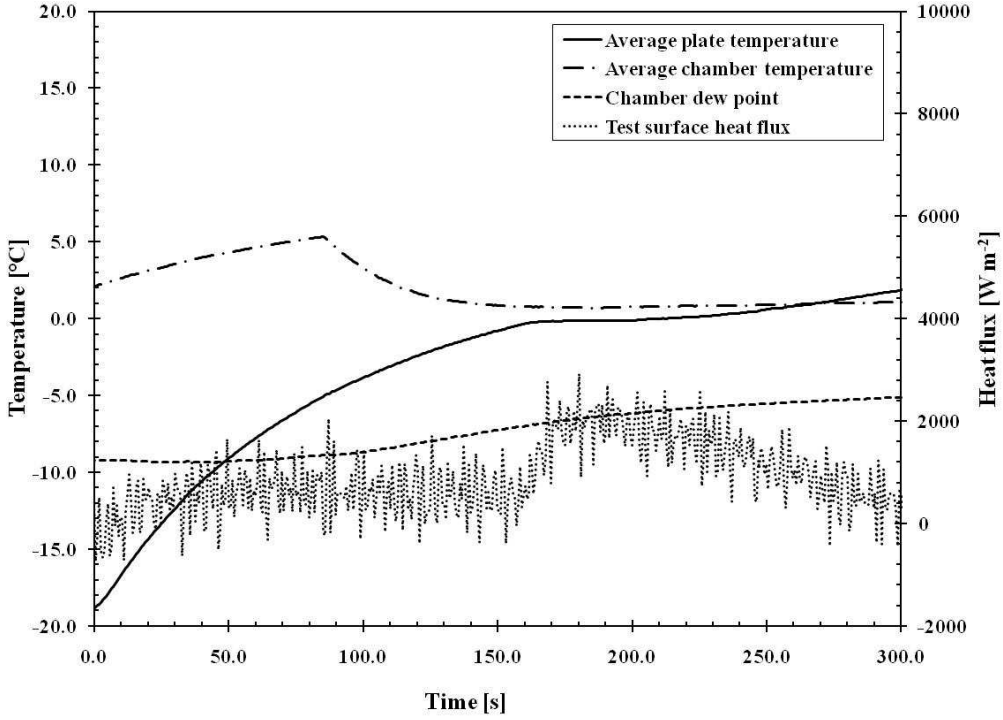

Figure G-14 Temperature and heat flux during defrost at 0.0/-7.7/-19.2.

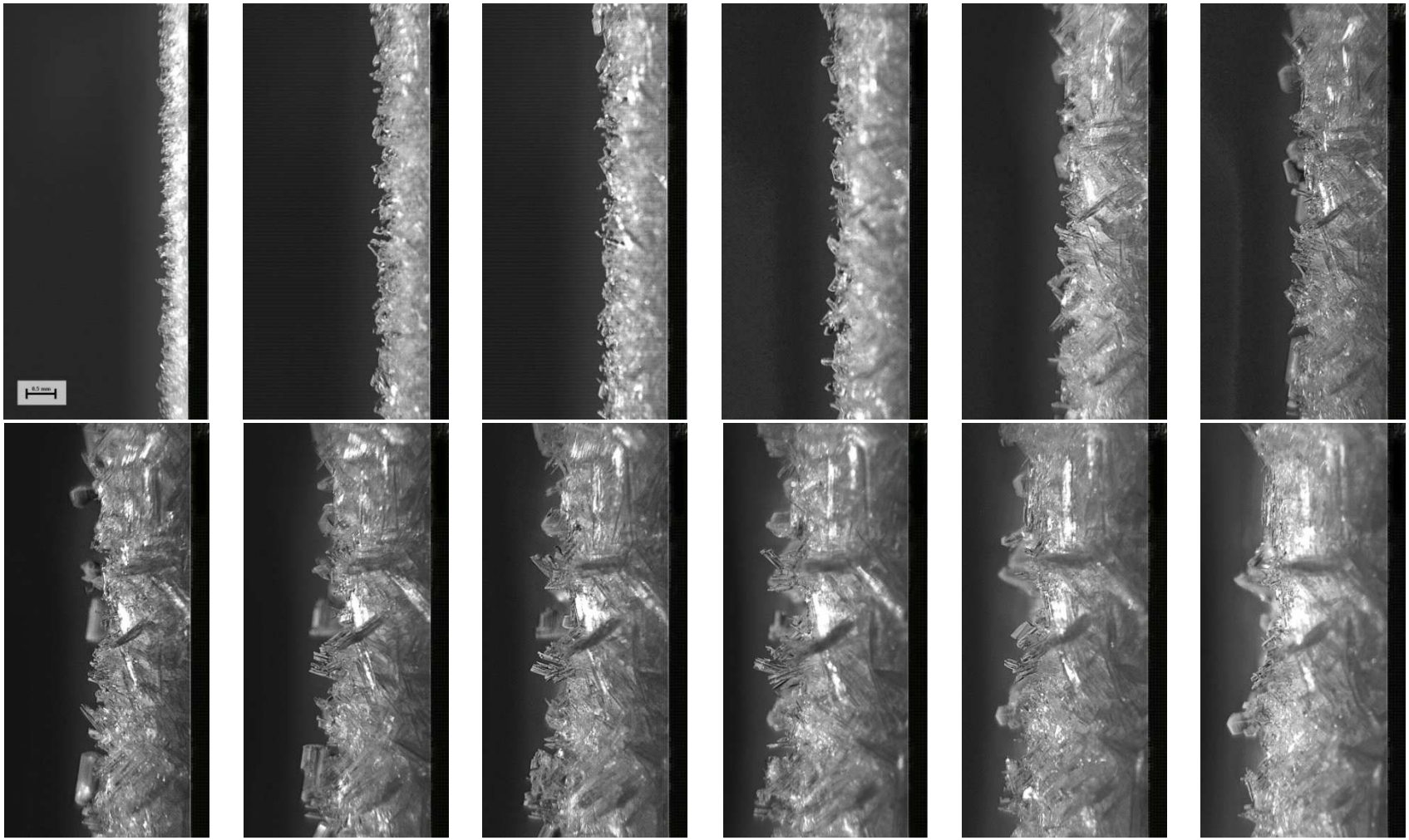

Figure G-15 Side images of frost growth at 0.0/-7.7/-19.2 (20 minute interval).

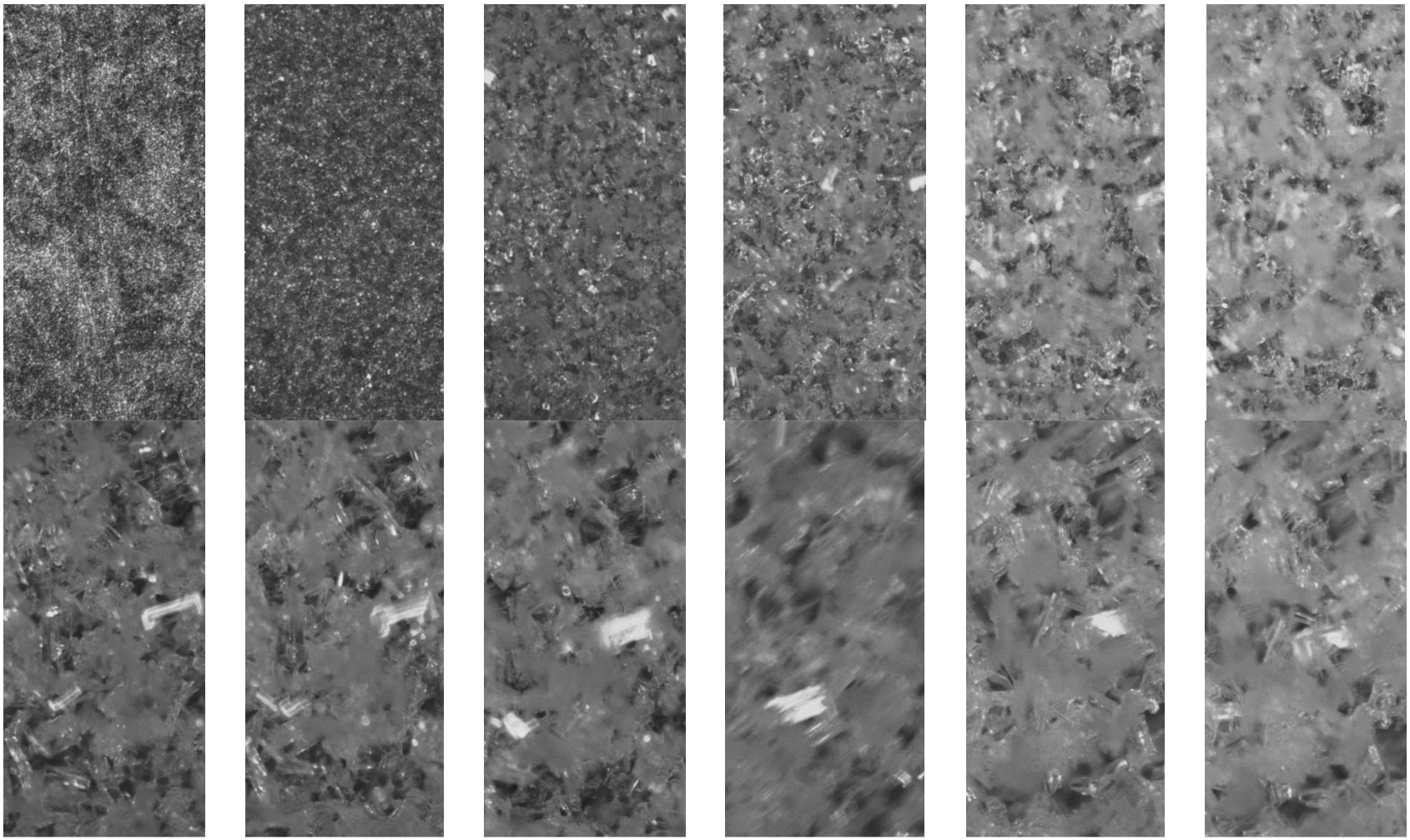

Figure G-16 Frontal images of frost growth at 0.0/-7.7/-19.2 (20 minute interval).

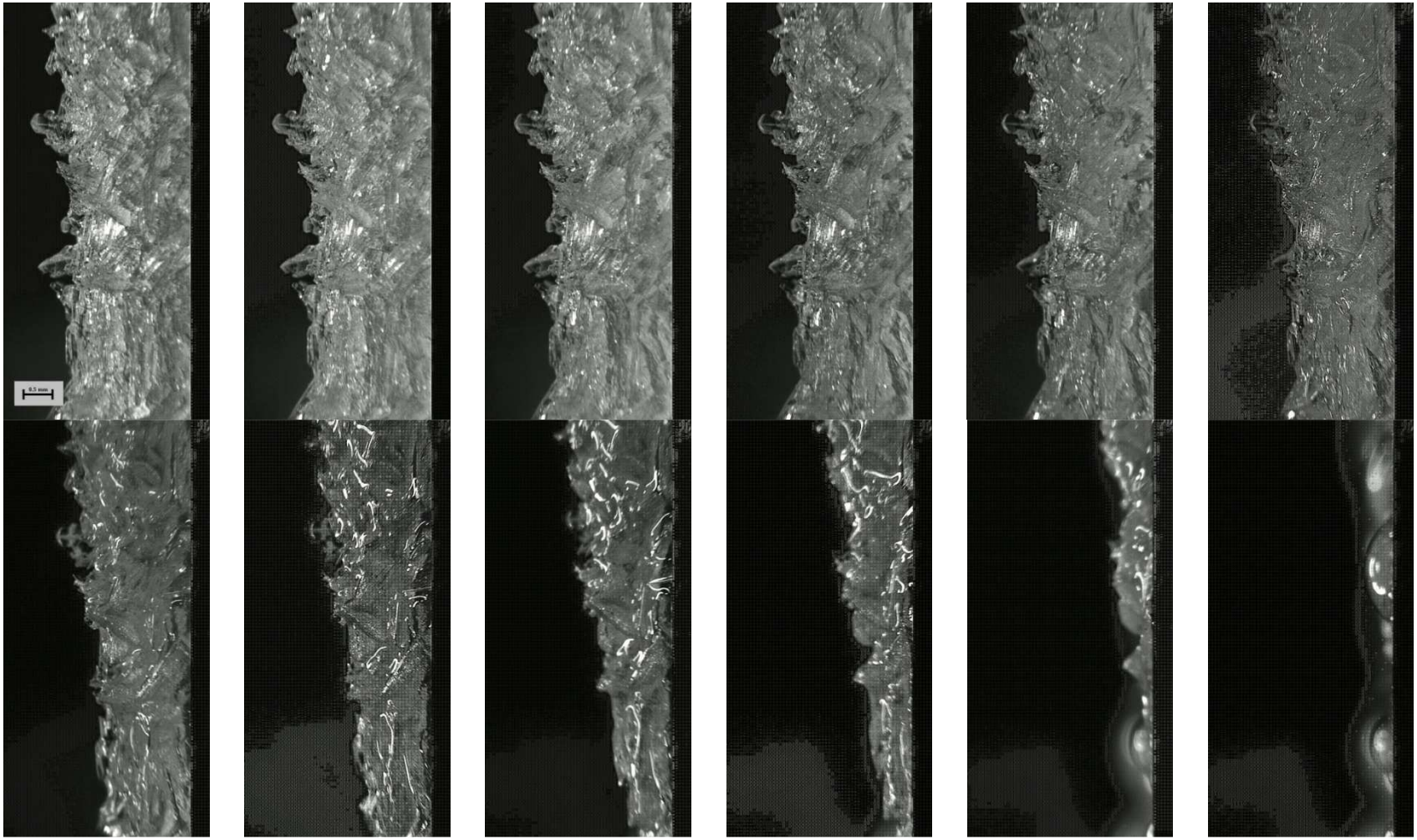

Figure G-17 Side images of defrost at 0.0/-7.7/-19.2 (4.7 second interval).

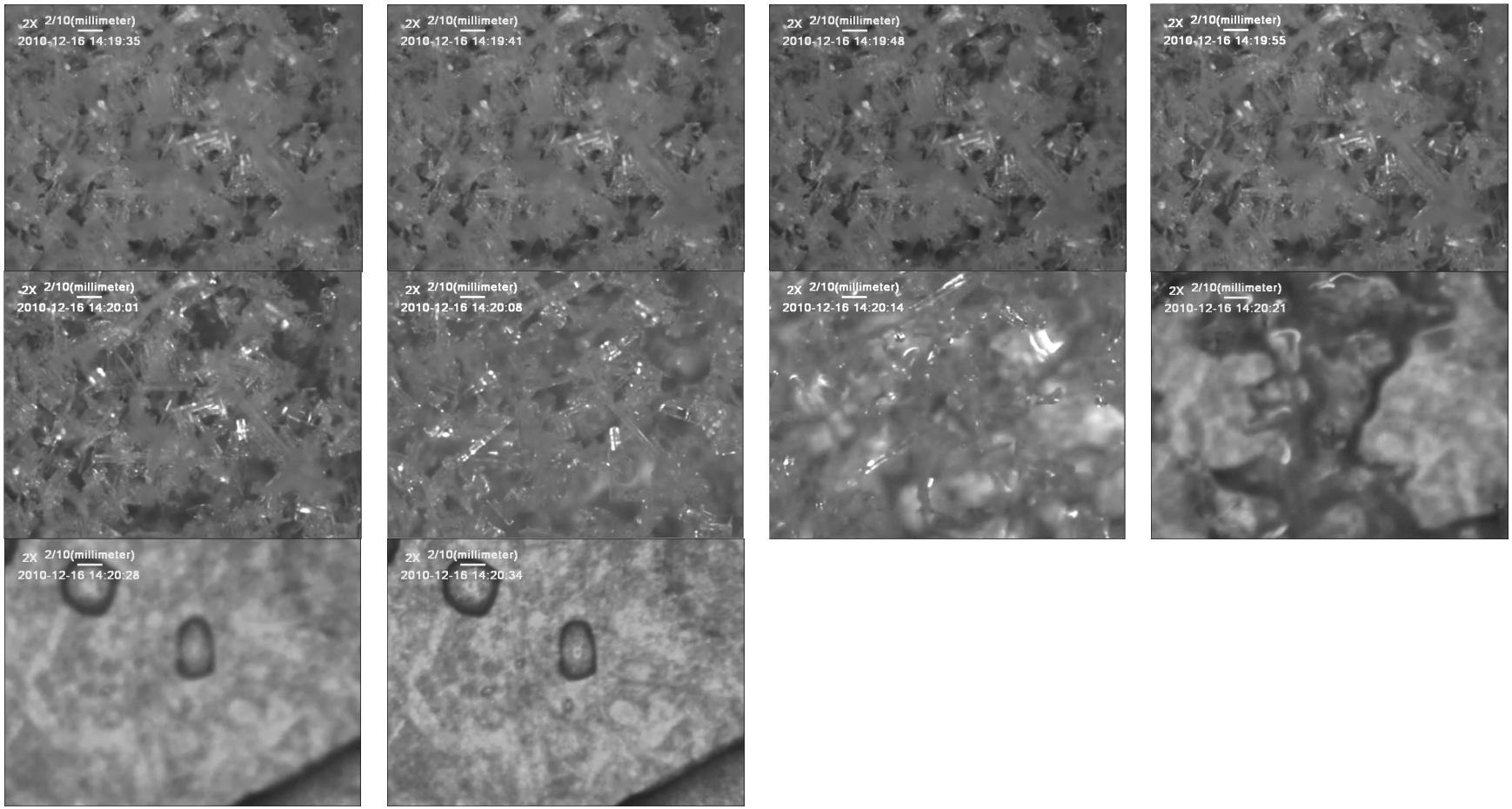

Figure G-18 Frontal images of defrost at 0.0/-7.7/-19.2 (5.0 second interval).

G.4 Test 4: -7.7/-18.3/-19.4

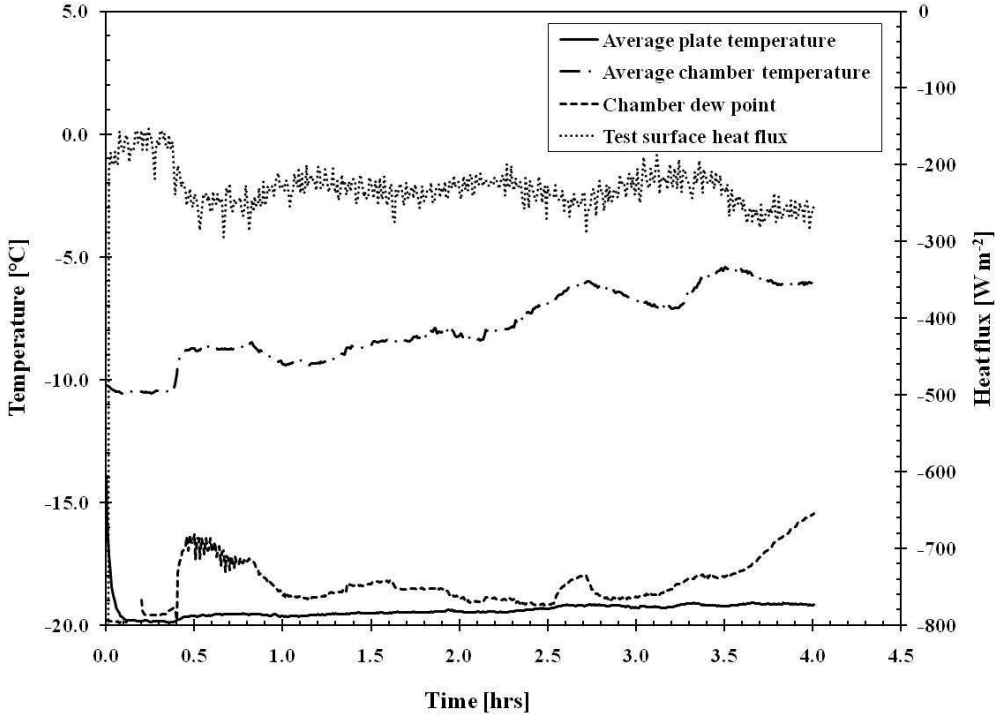

Figure G-19 Temperature and heat flux during frost growth at -7.7/-18.3/-19.4.

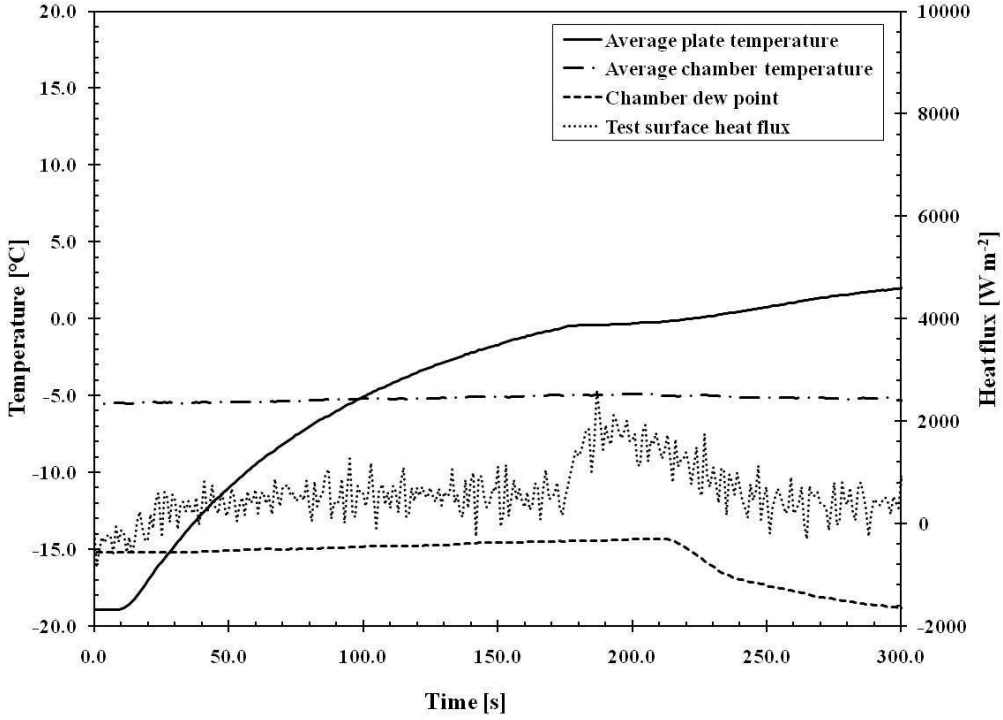

Figure G-20 Temperature and heat flux during defrost at -7.7/-18.3/-19.4.

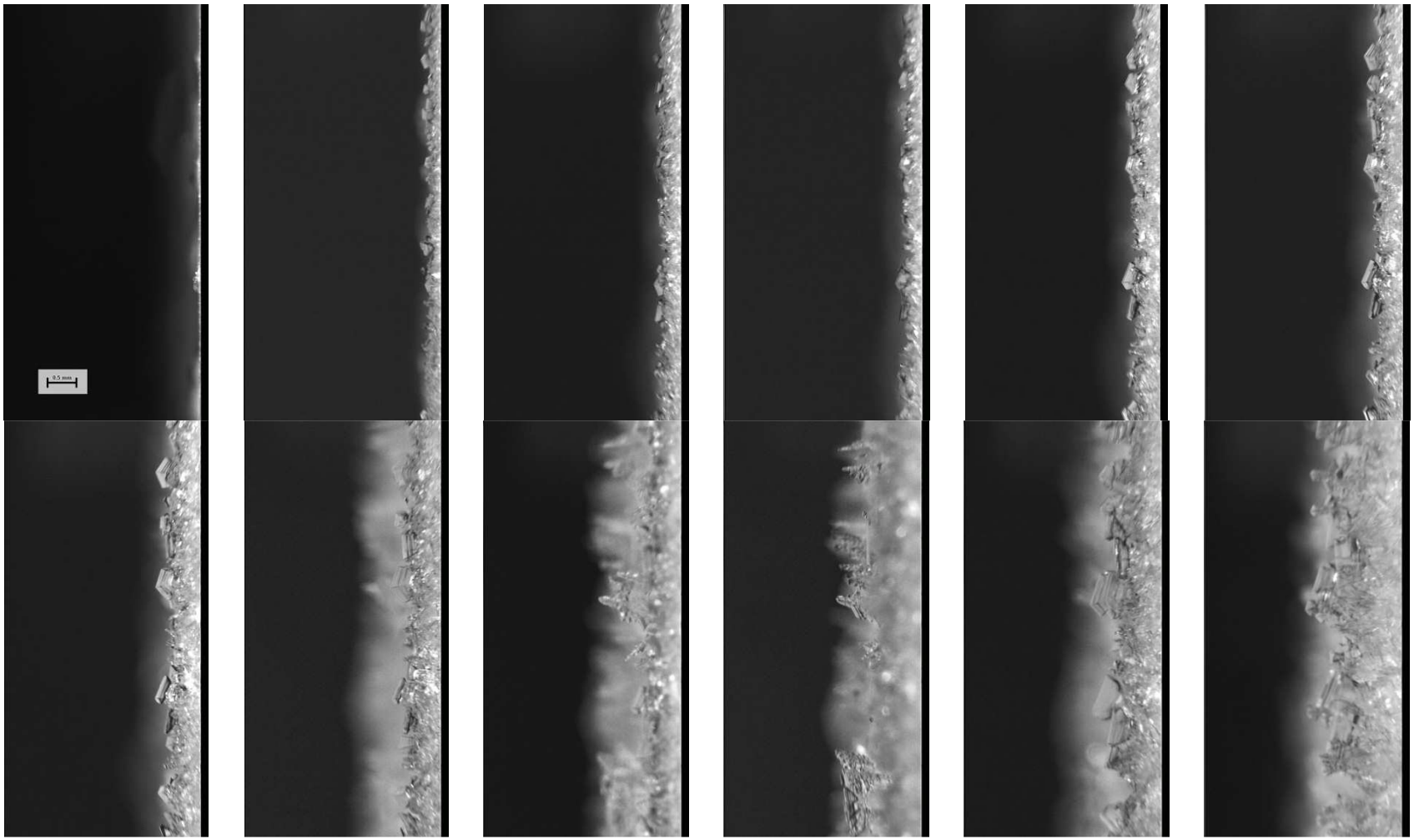

Figure G-21 Side images of frost growth at -7.7/-18.3/-19.4 (20 minute interval).

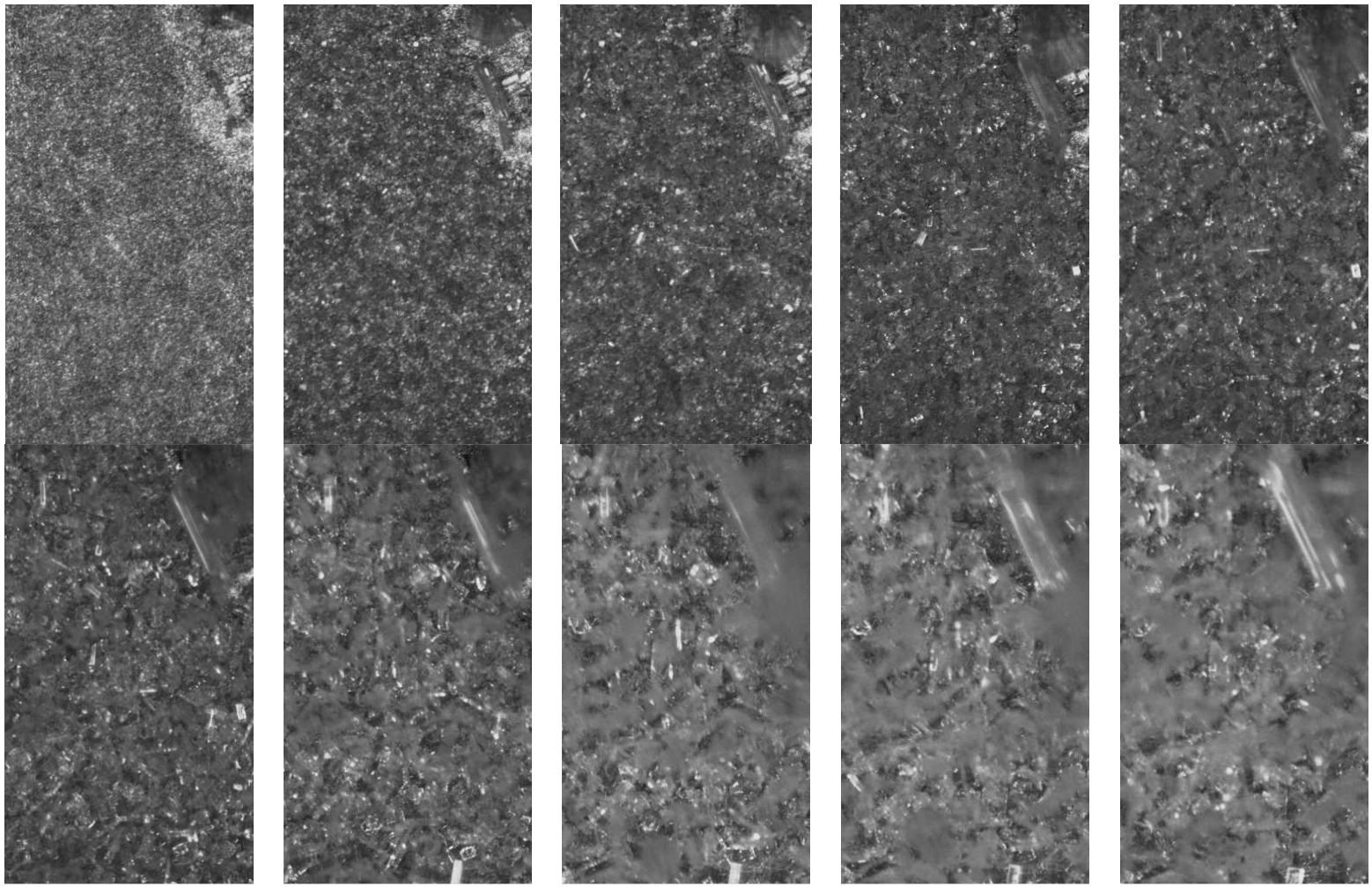

Figure G-22 Frontal images of frost growth at -7.7/-18.3/-19.4 (20 minute interval).

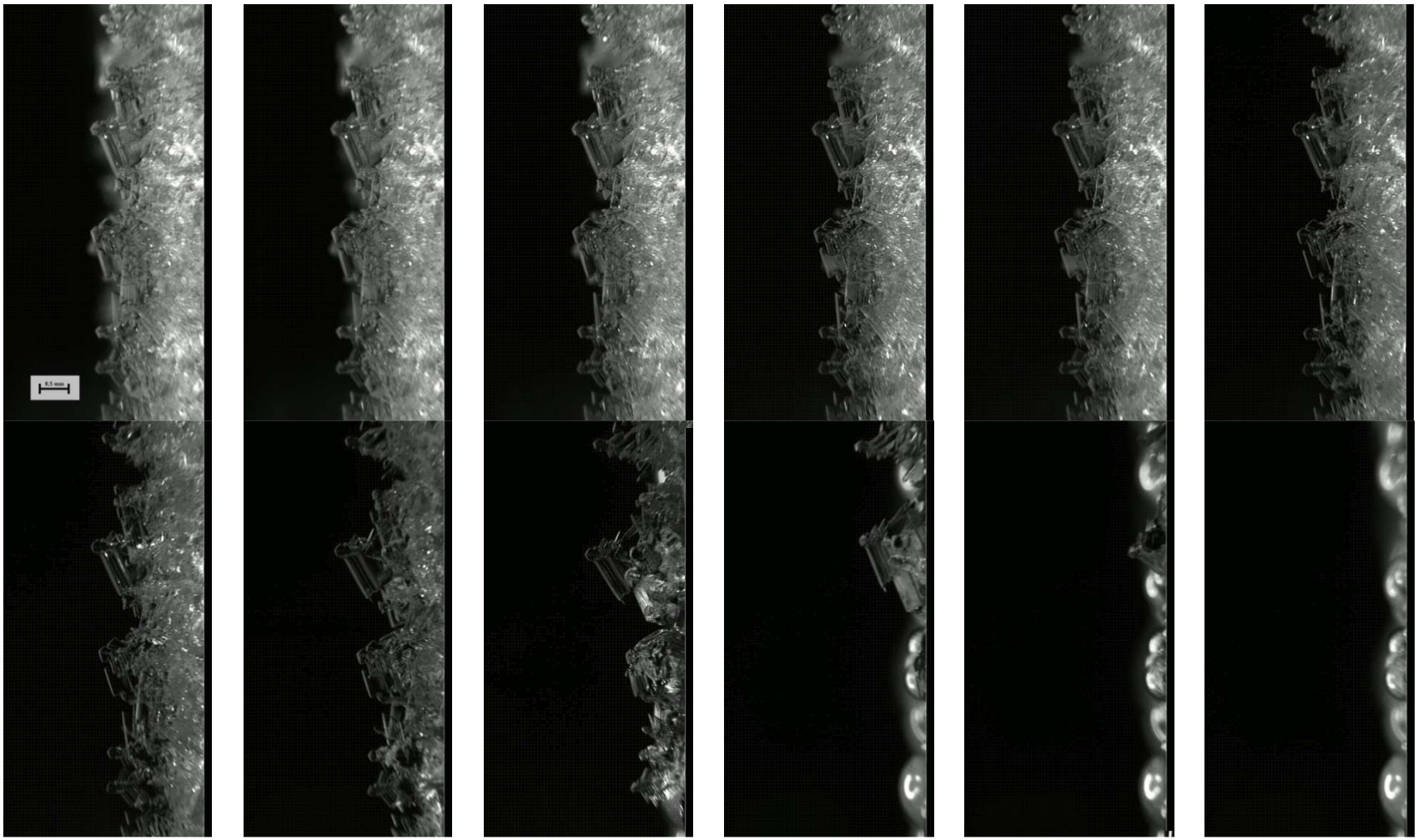

Figure G-23 Side images of defrost at -7.7/-18.3/-19.4 (3.5 second interval).

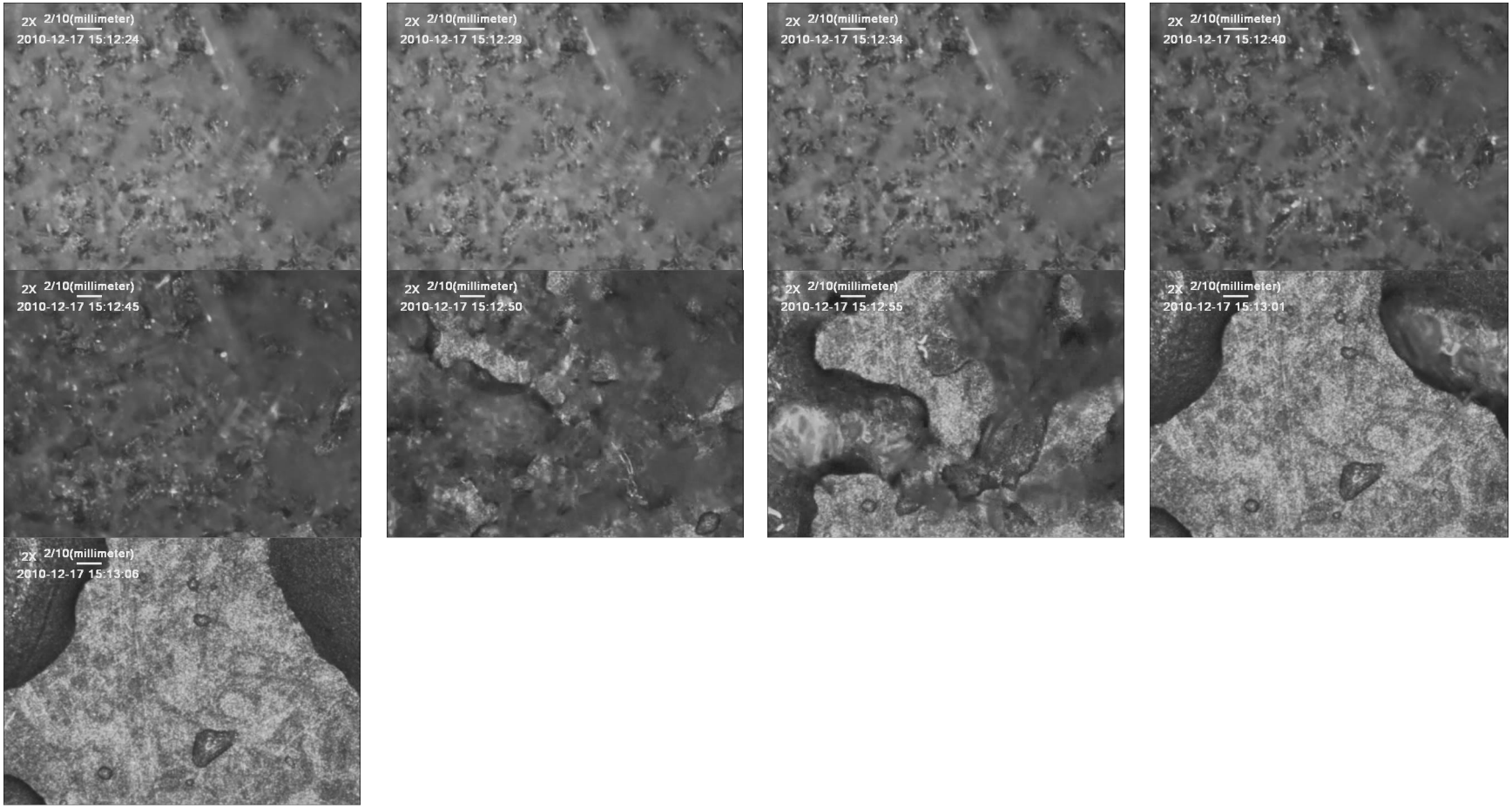

Figure G-24 Frontal images of defrost at -7.7/-18.3/-19.4 (5.0 second interval)

G.5 Test 5: -0.6/-7.8/-9.6

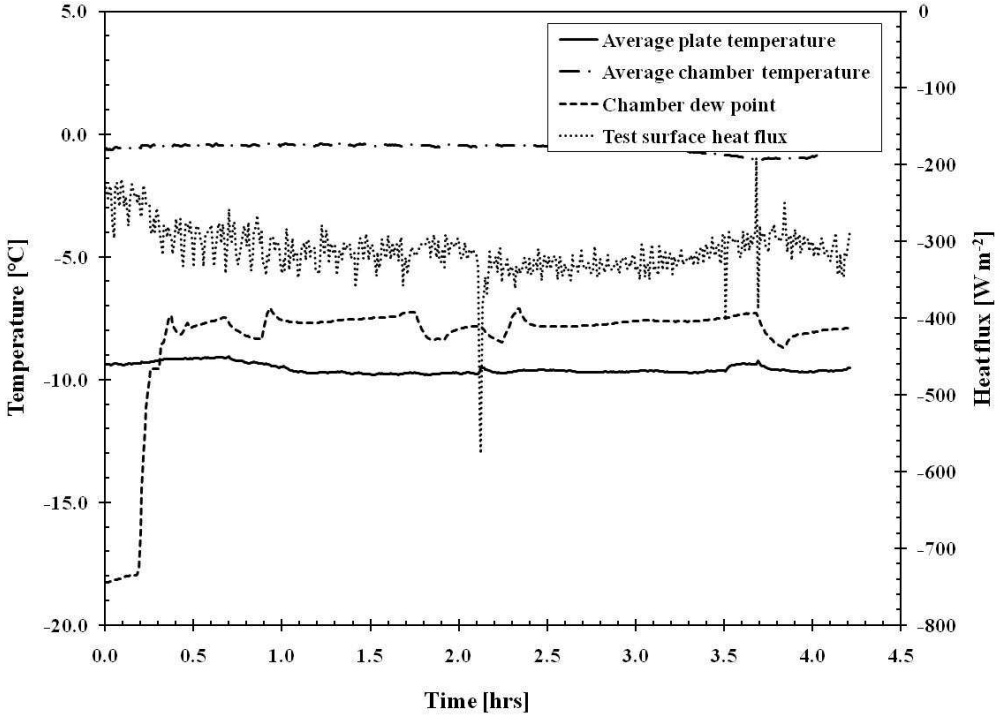

Figure G-25 Temperature and heat flux during frost growth at -0.6/-7.8/-9.6.

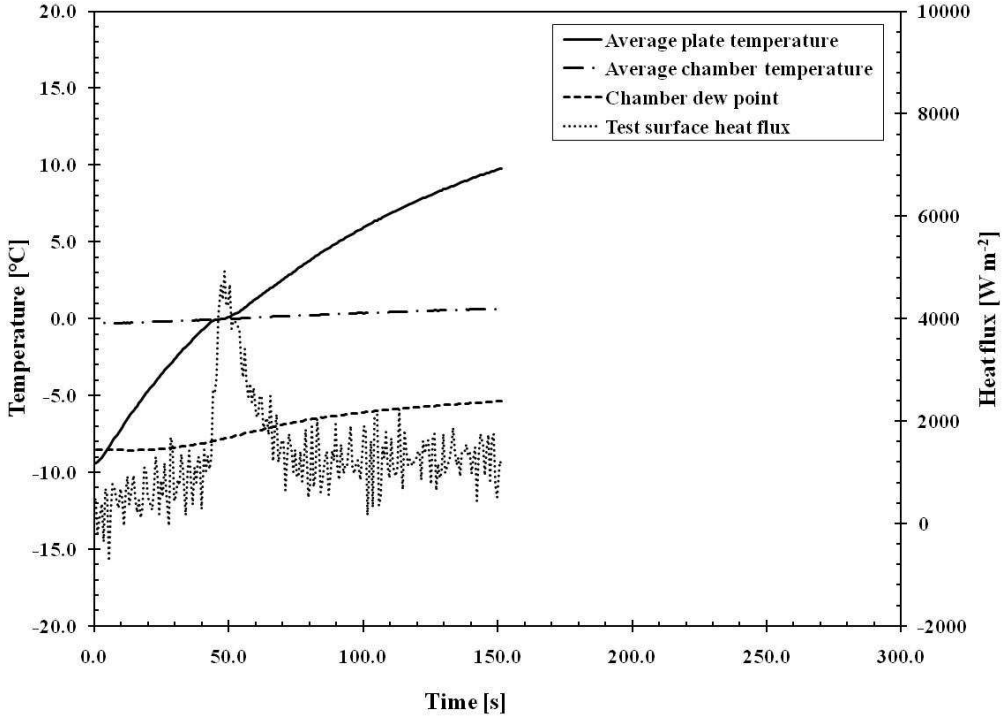

Figure G-26 Temperature and heat flux during defrost at -0.6/-7.8/-9.6.

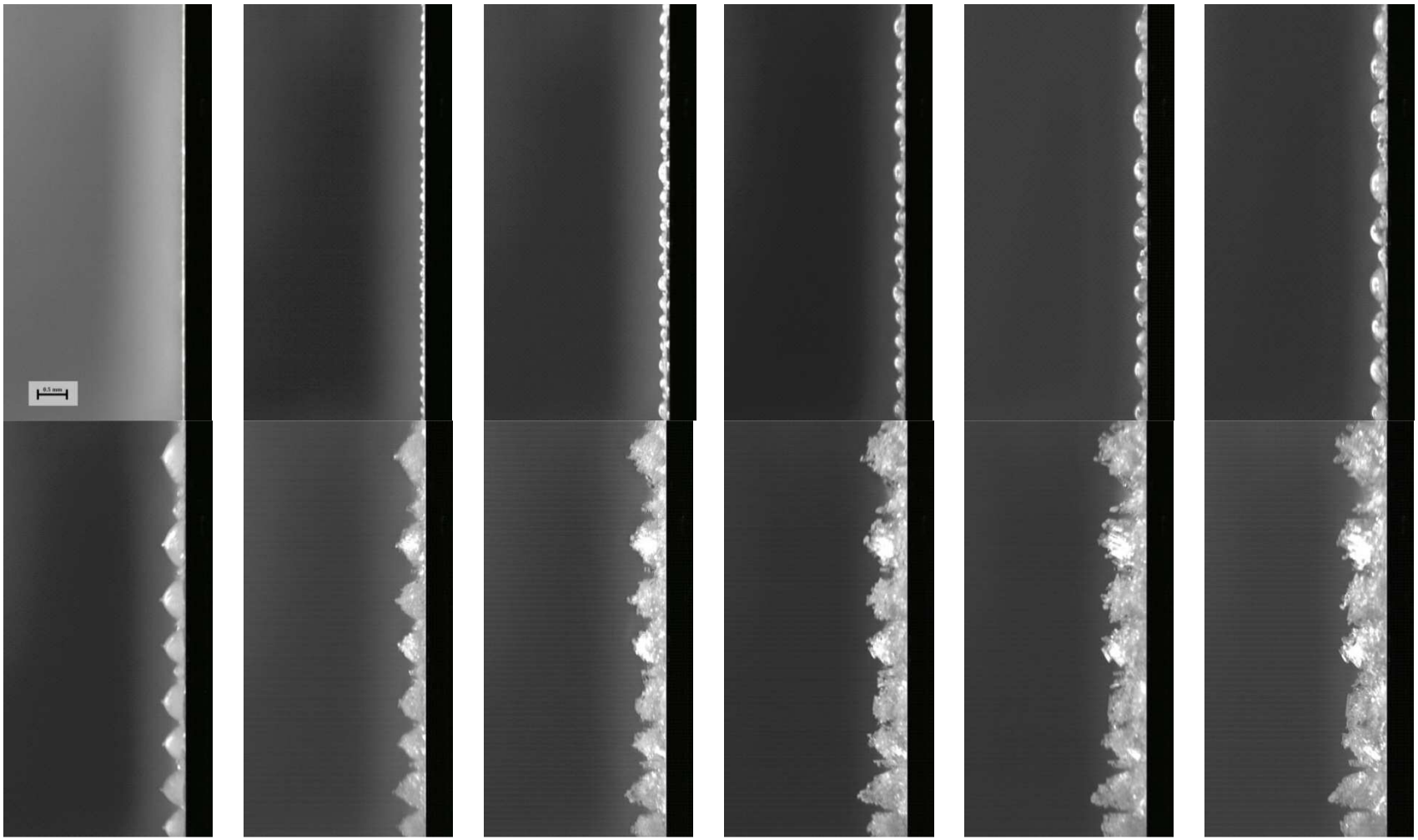

Figure G-27 Side images of frost growth at -0.6/-7.8/-9.6 (20 minute interval).

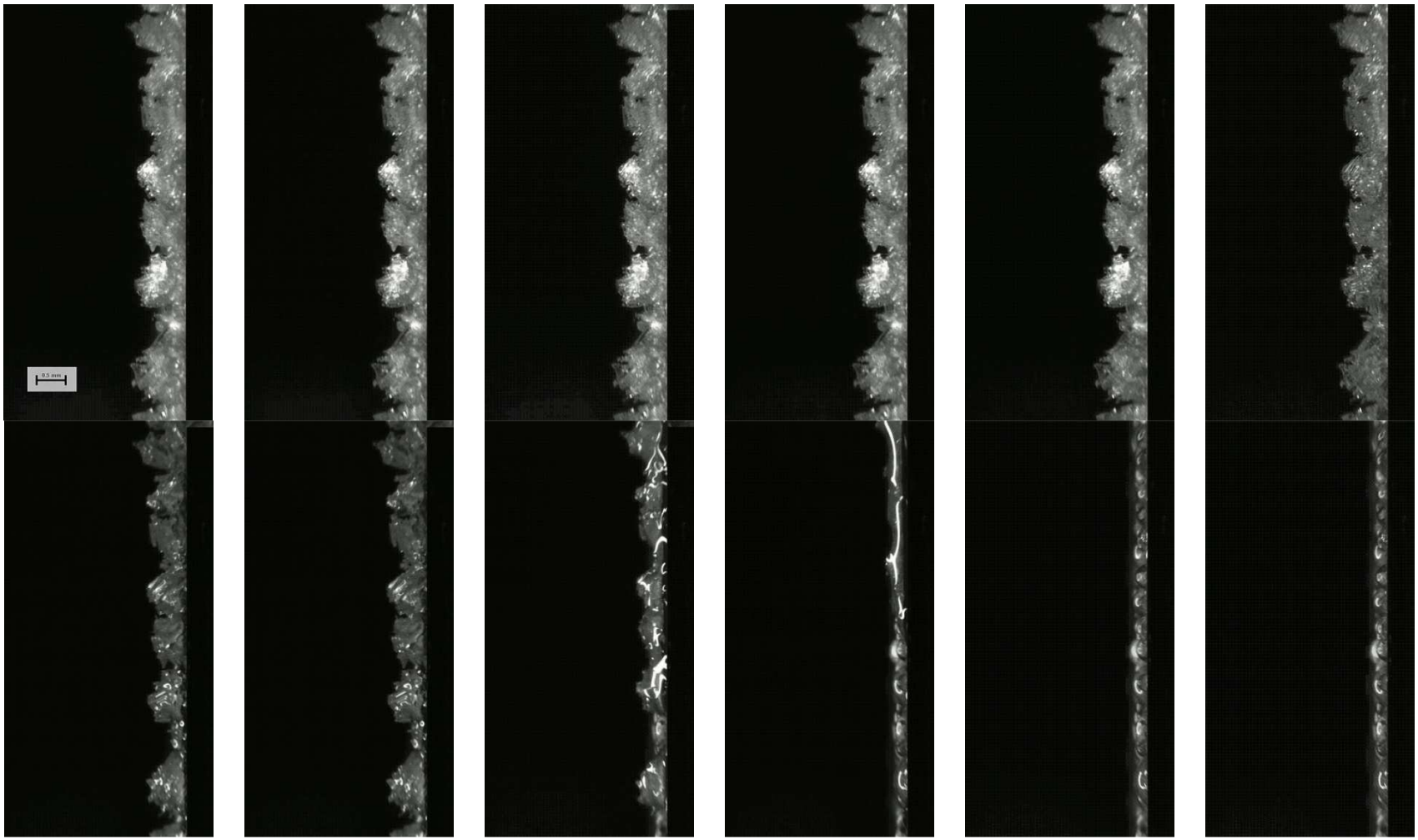

Figure G-28 Side images of defrost at -0.6/-7.8/-9.6 (3.5 second interval).

G.6 Test 6: -6.9/-16.7/-19.5

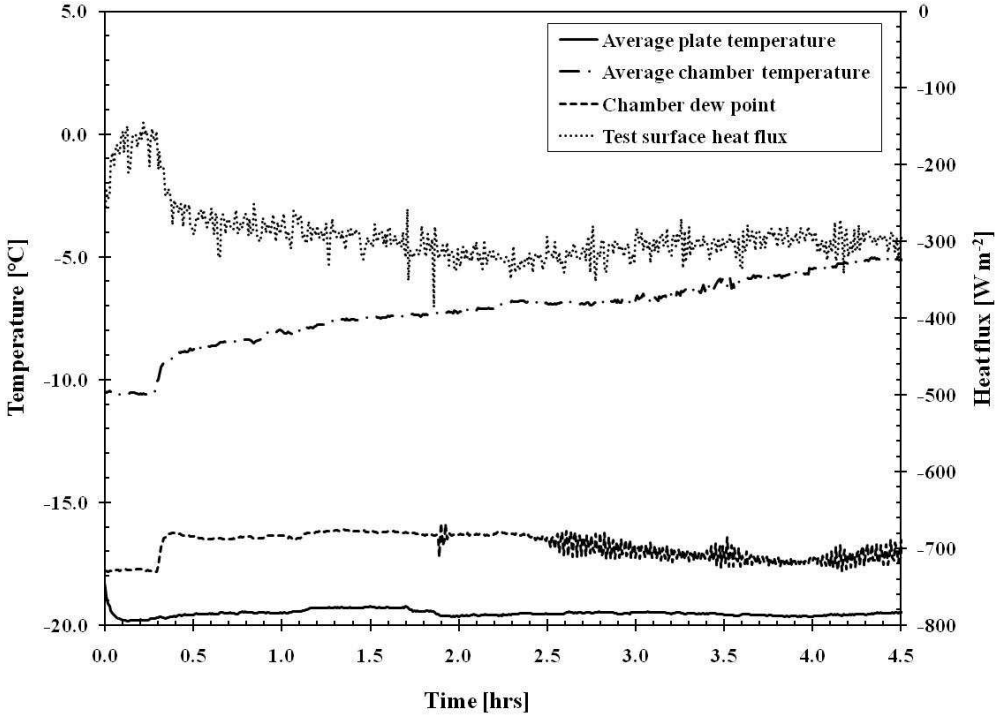

Figure G-29 Temperature and heat flux during frost growth at -6.9/-16.7/-19.5.

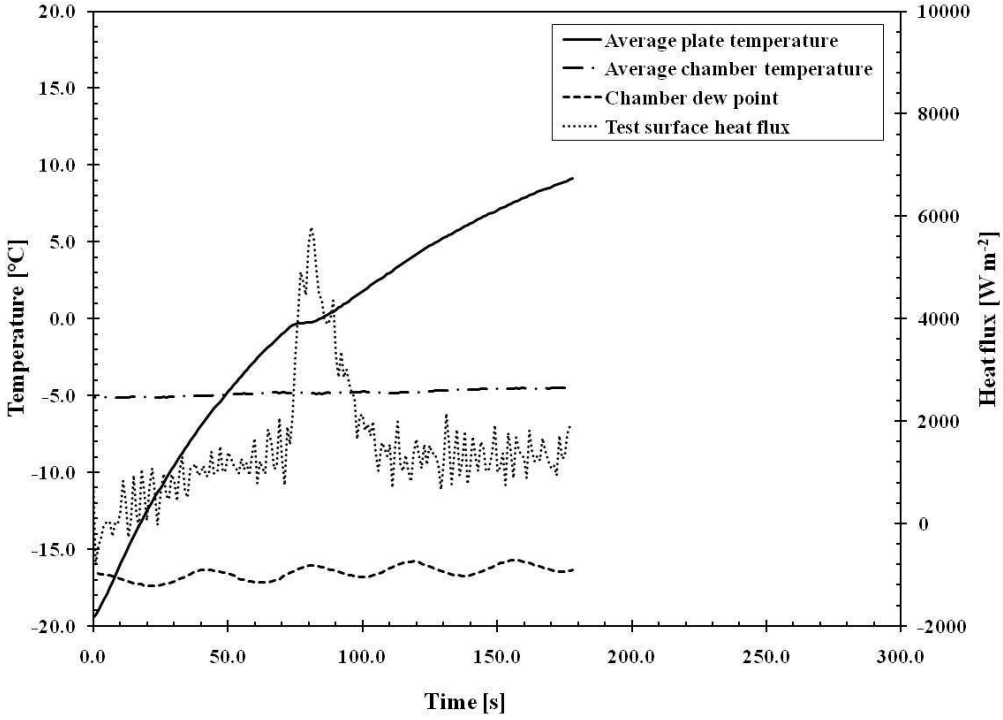

Figure G-30 Temperature and heat flux during defrost at -6.9/-16.7/-19.5.

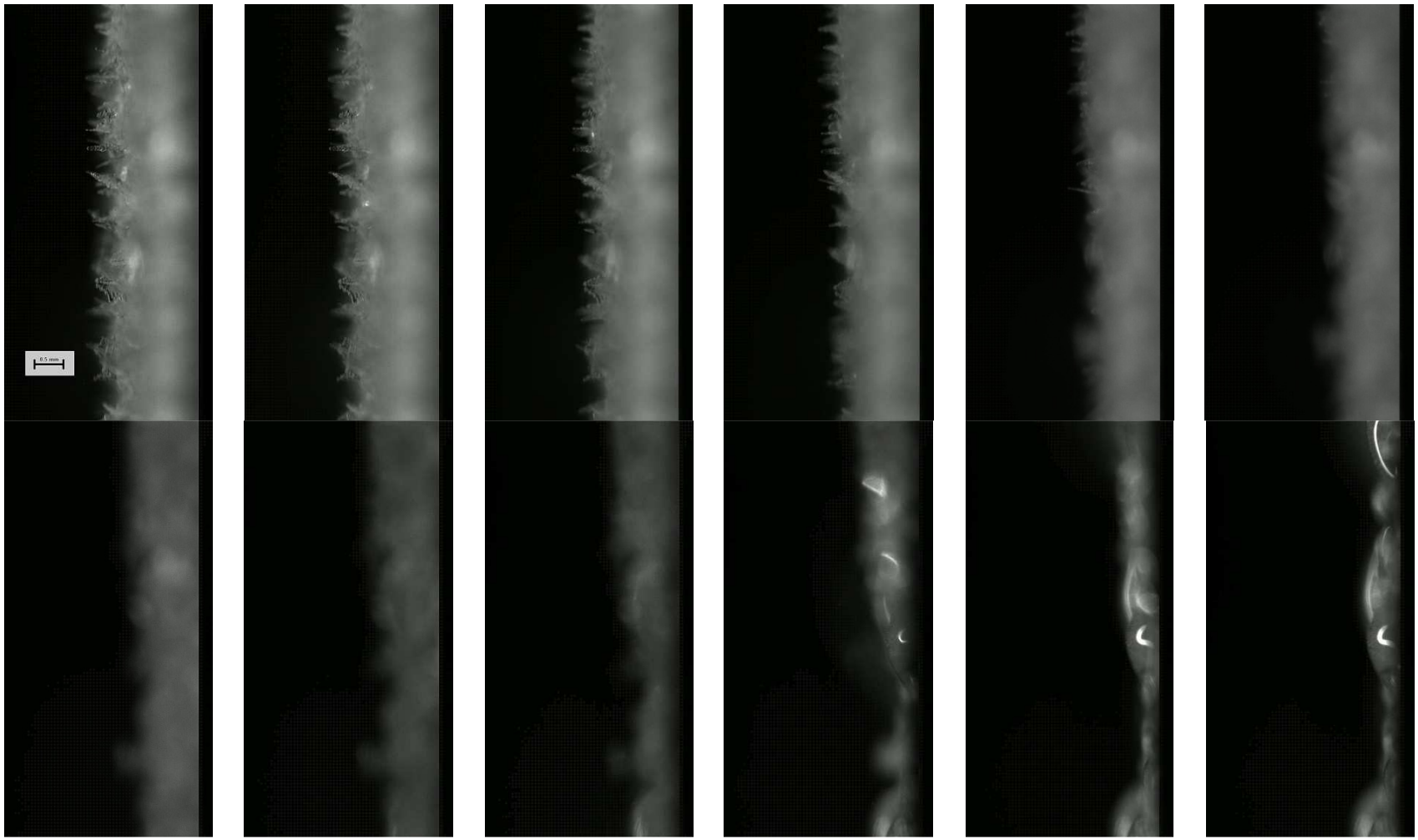

Figure G-31 Side images of defrost at -6.9/-16.7/-19.5. (1.2 second interval).

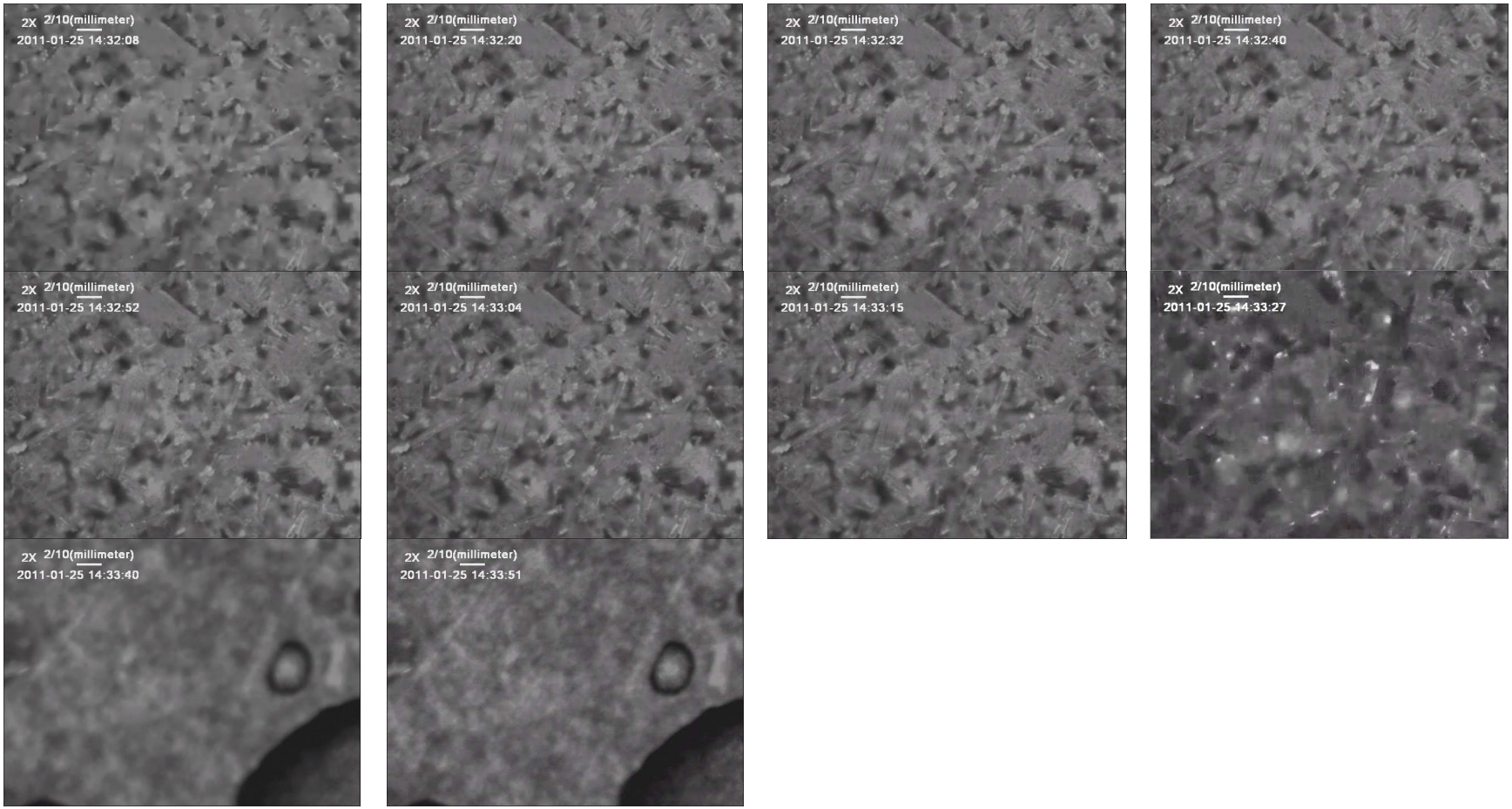

Figure G-32 Frontal images of defrost at -6.9/-16.7/-19.5. (2.0 second interval).

G.7 Test 7: -5.5/-13/-18.9

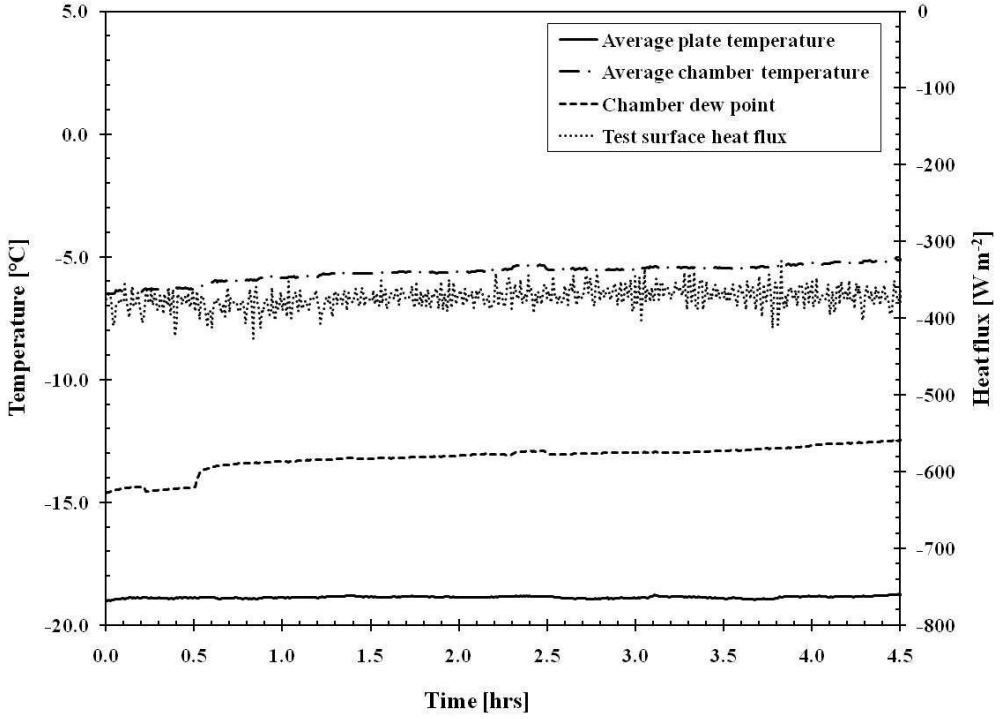

Figure G-33 Temperature and heat flux during frost growth at -5.5/-13/-18.9.

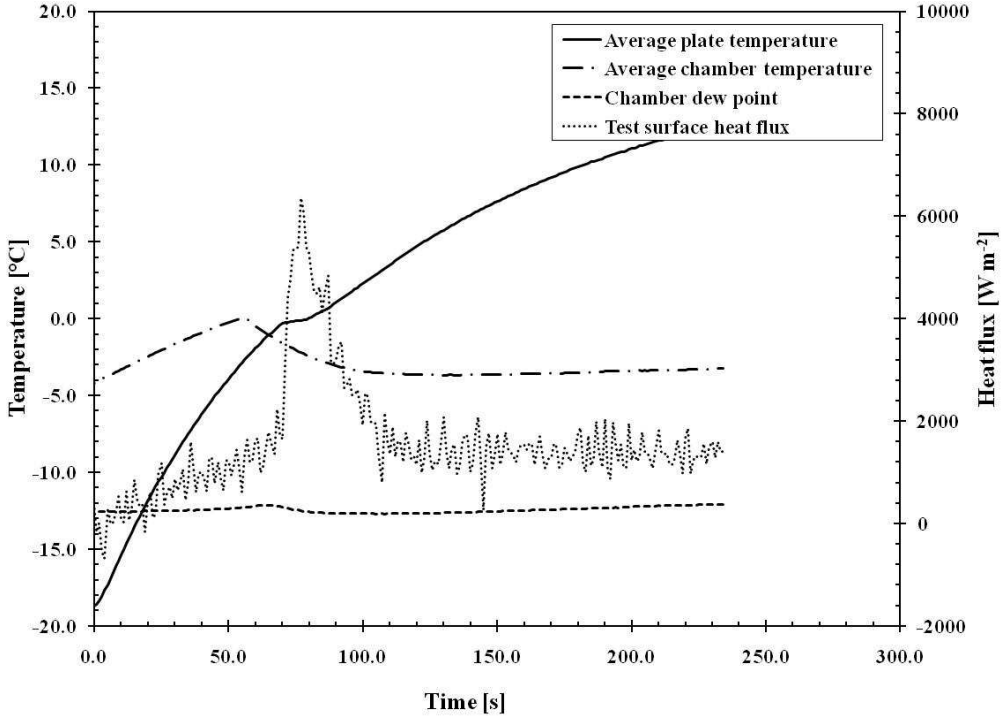

Figure G-34 Temperature and heat flux during defrost at -5.5/-13/-18.9.

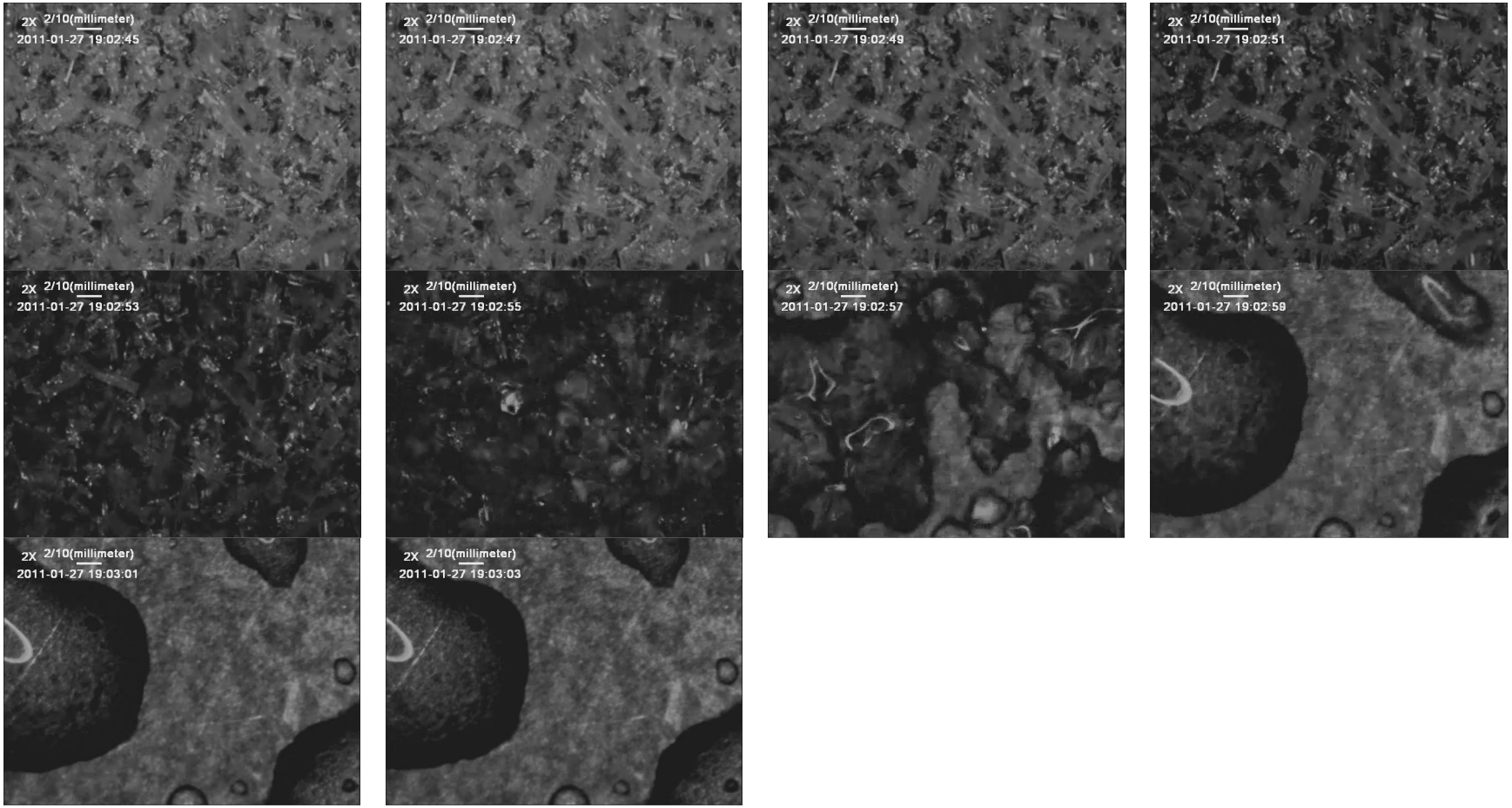

Figure G-35 Frontal images of defrost at -5.5/-13/-18.9. (2.0 second interval).

G.8 Test 8: -5.0/-12.3/-18.3

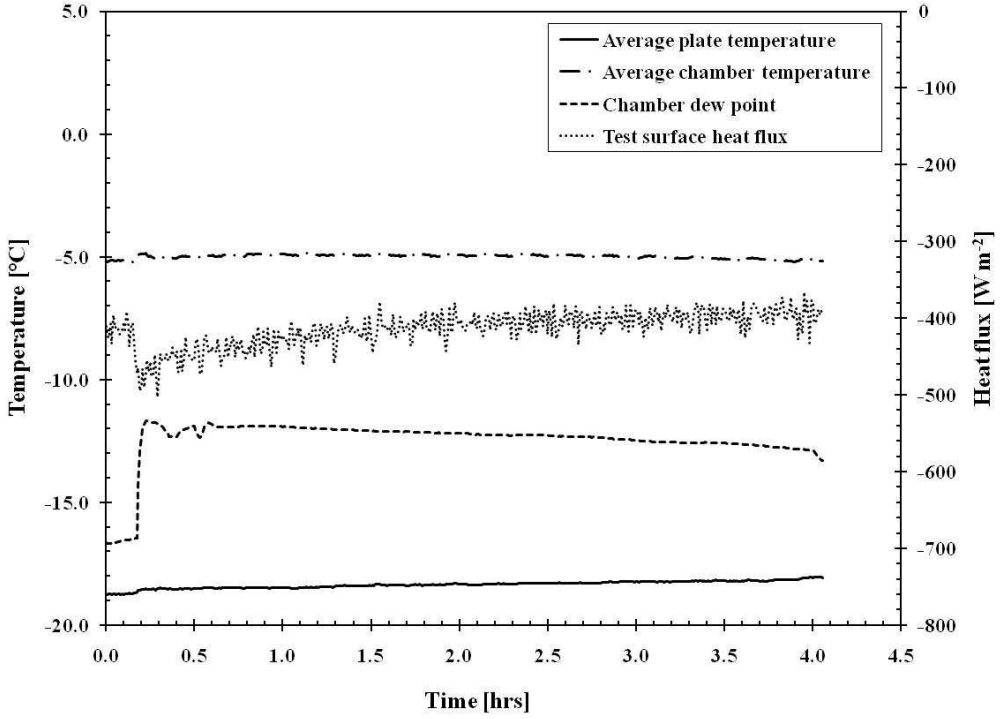

Figure G-36 Temperature and heat flux during frost growth at -5.0/-12.3/-18.3.

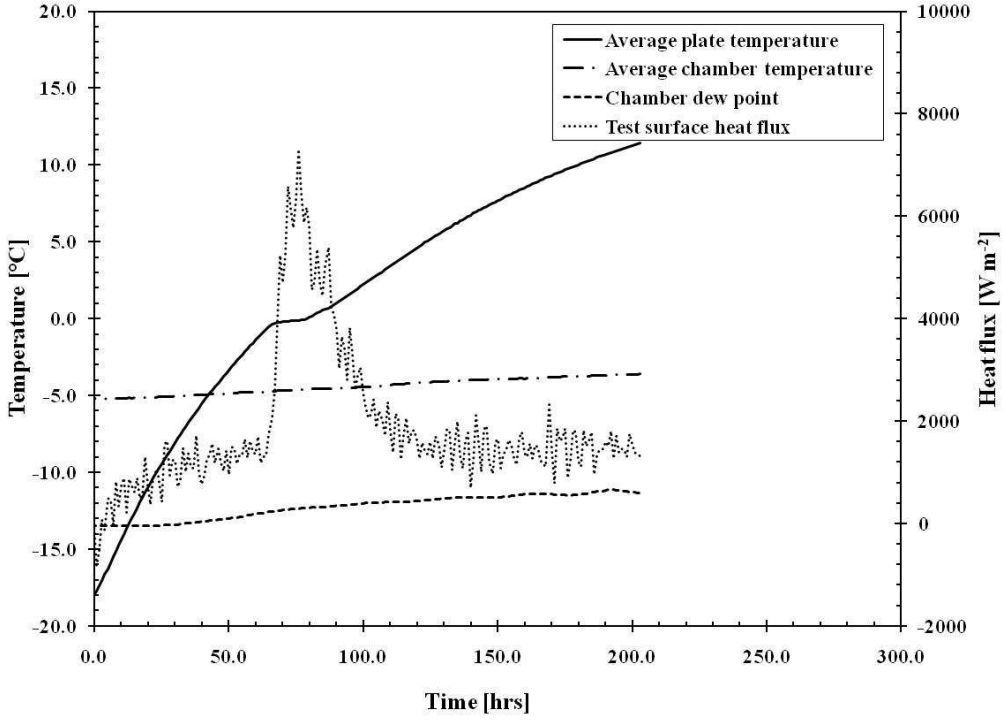

Figure G-37 Temperature and heat flux during defrost at -5.0/-12.3/-18.3.

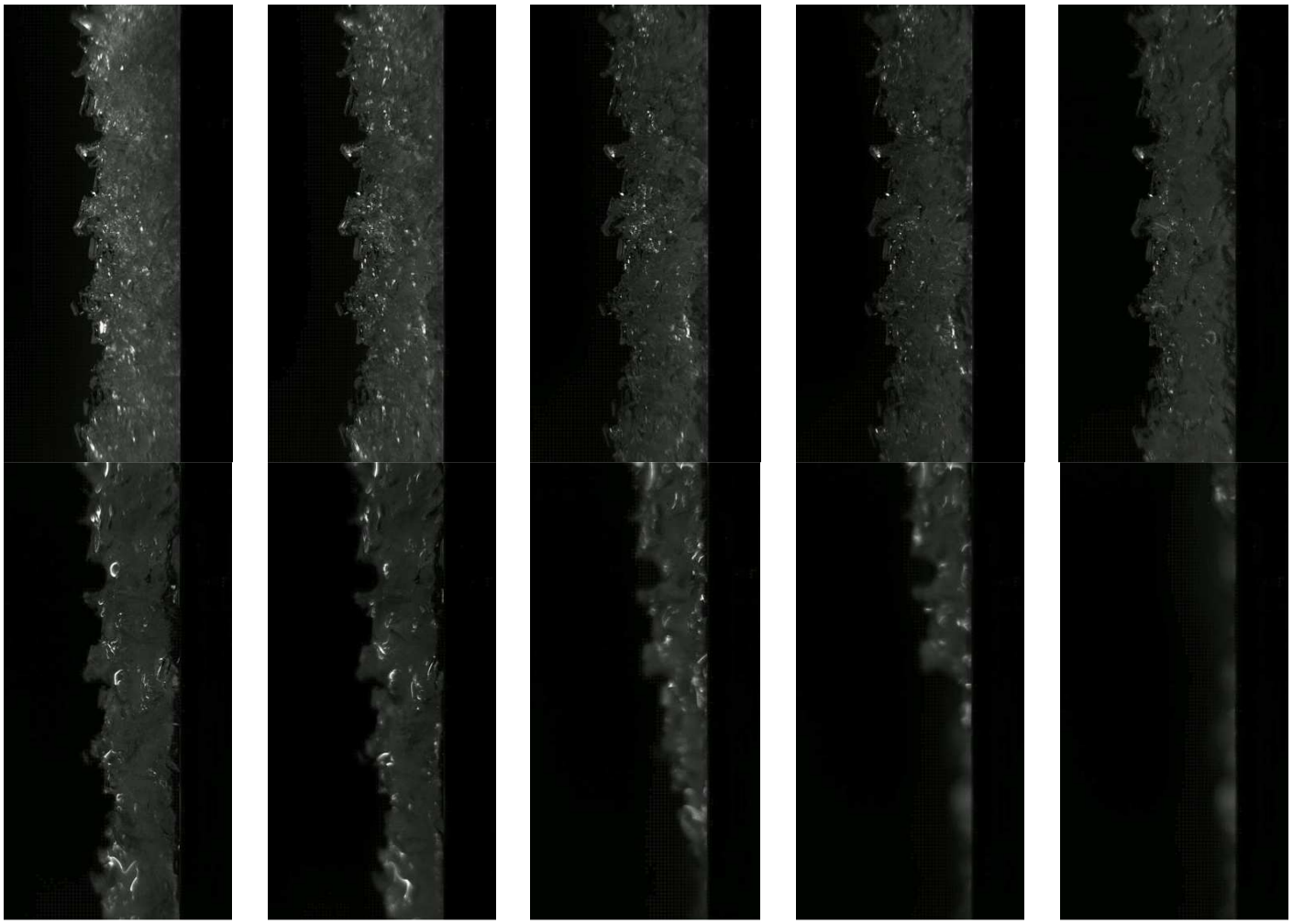

Figure G-38 Side images of defrost at -5.0/-12.3/-18.3. (1.3 second interval).

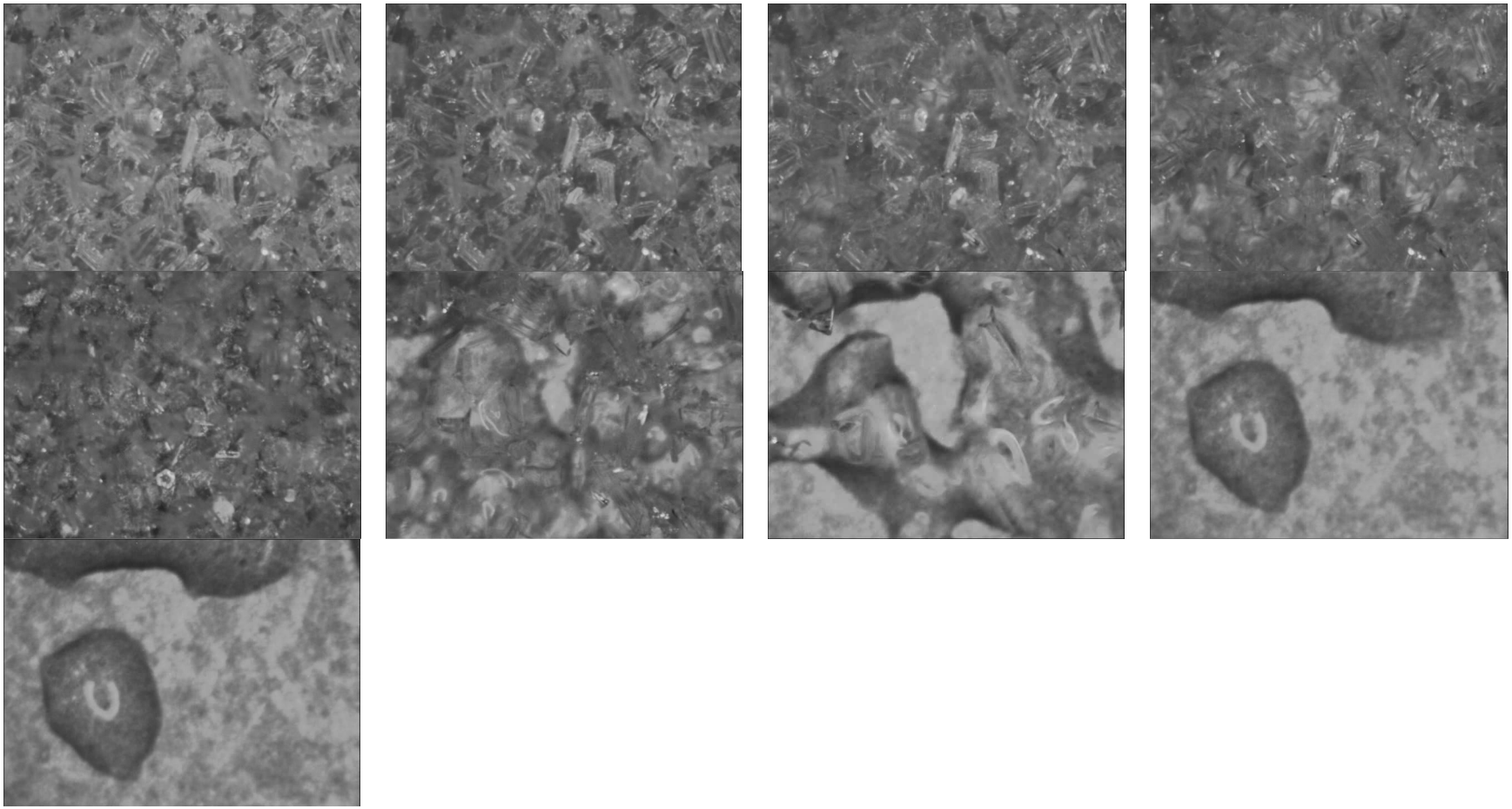

Figure G-39 Frontal images of defrost at -5.0/-12.3/-18.3. (2.0 second interval).

G.9 Test 9: -8.2/-16.1/-18.8

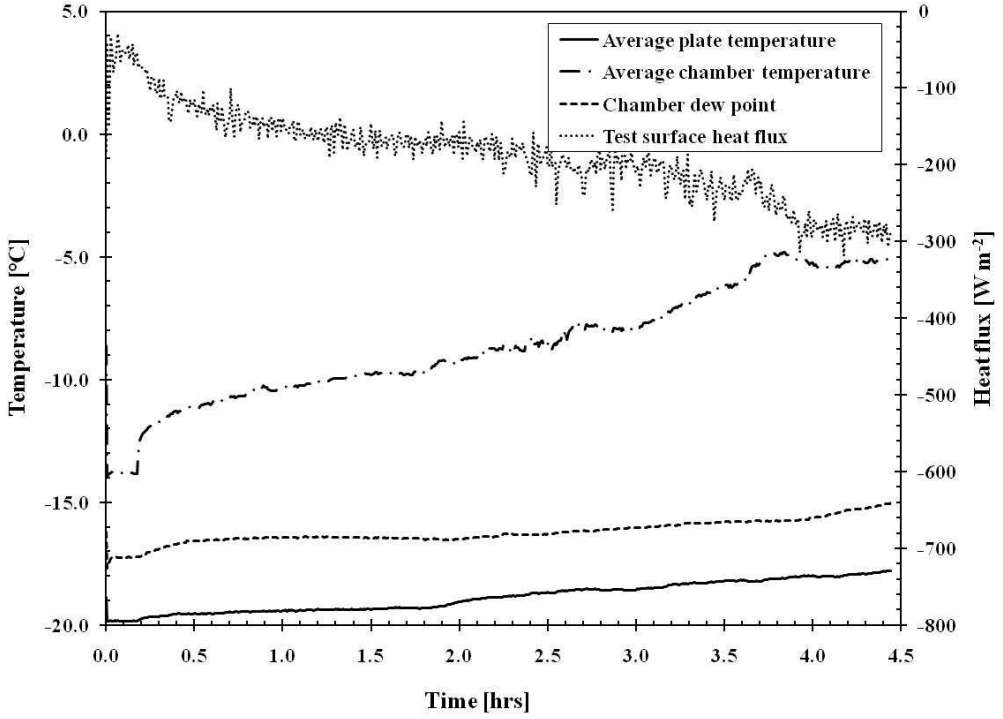

Figure G-40 Temperature and heat flux during frost growth at -8.2/-16.1/-18.8.

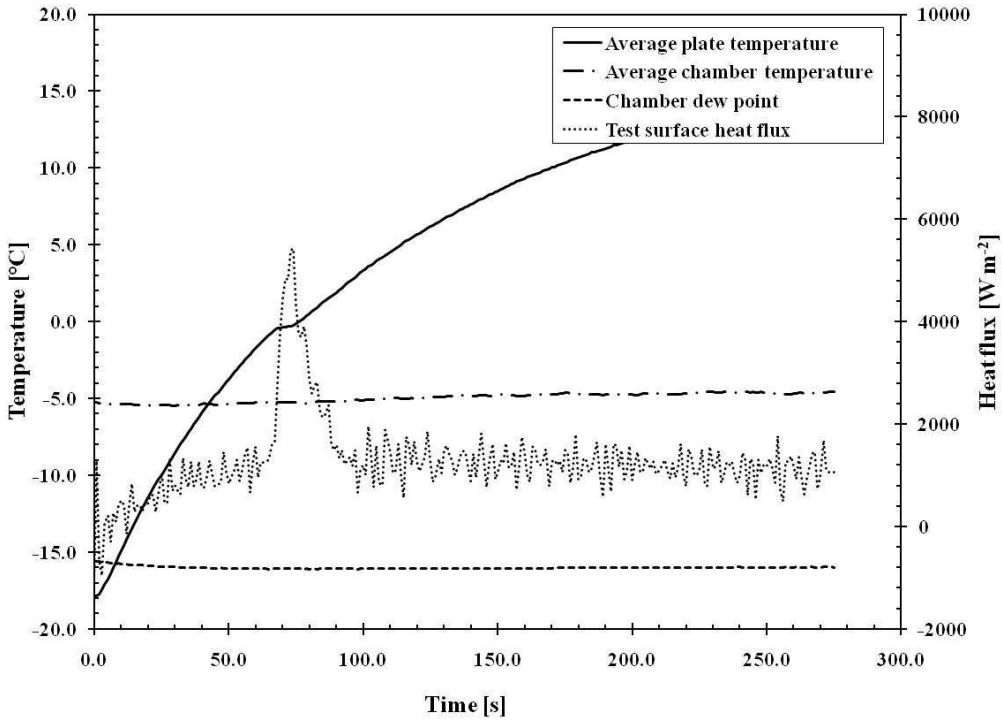

Figure G-41 Temperature and heat flux during defrost at -8.2/-16.1/-18.8.

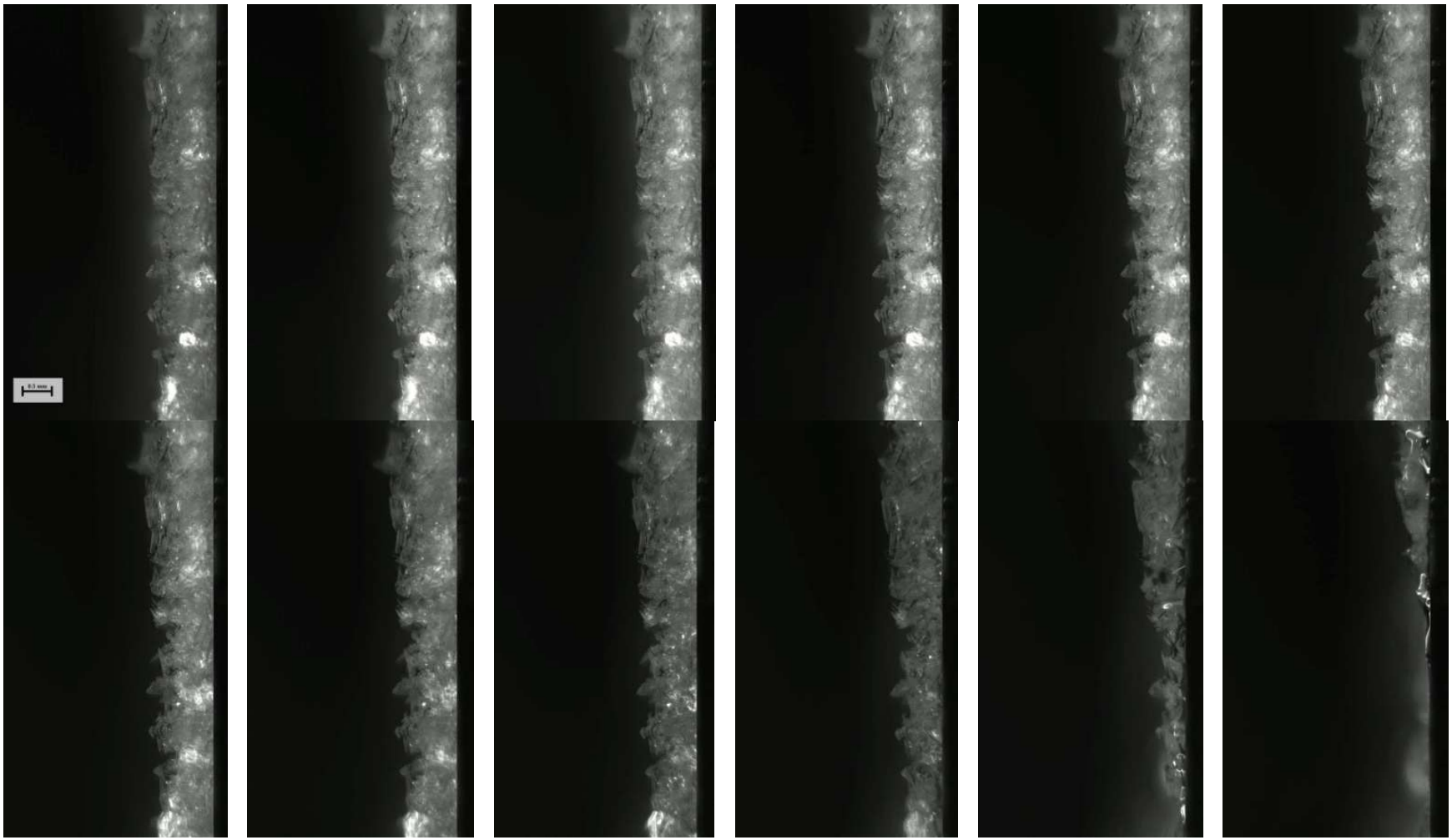

Figure G-42 Side images of defrost at -8.2/-16.1/-18.8. (1.4 second interval).

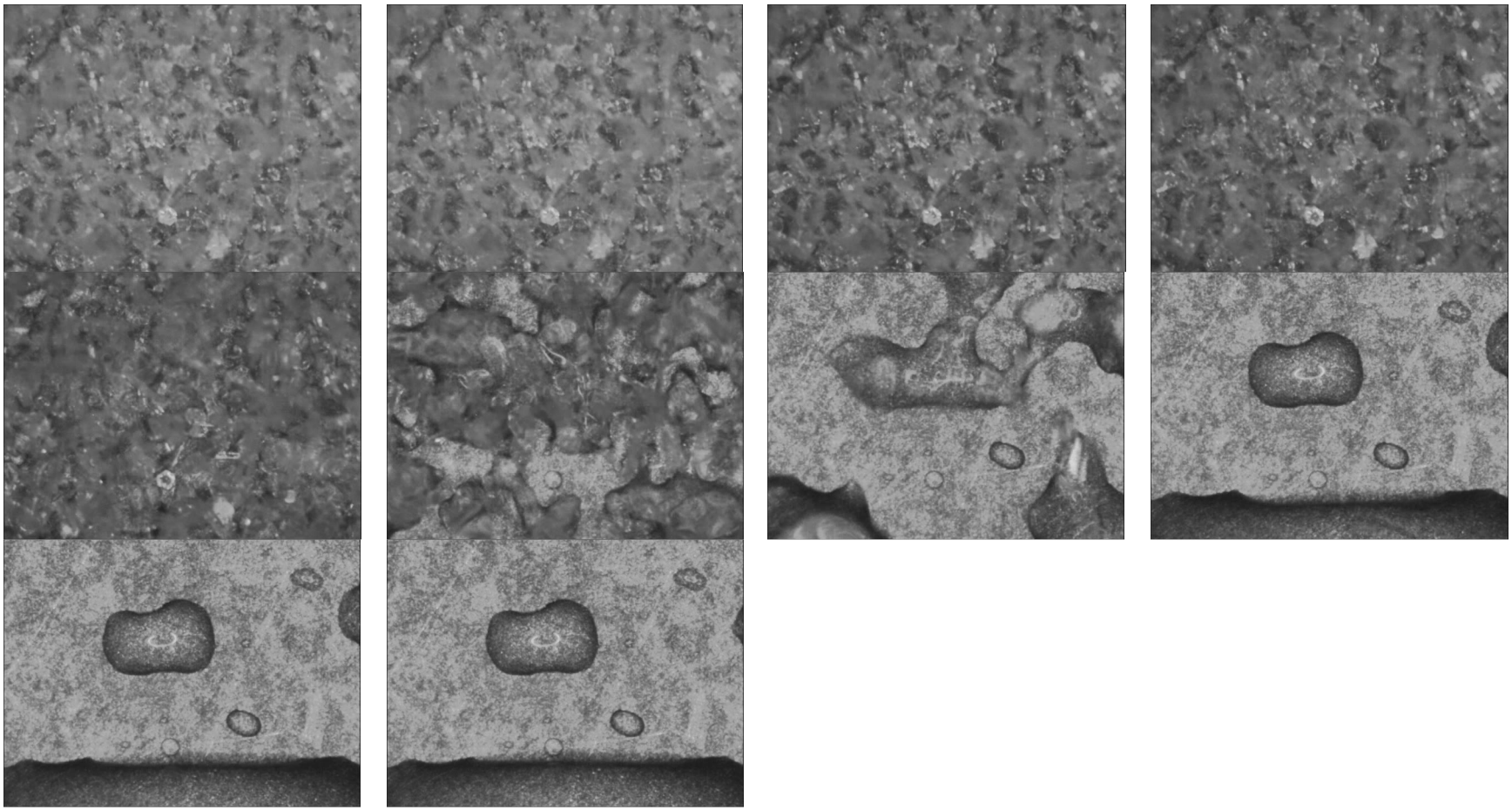

Figure G-43 Frontal images of defrost at -8.2/-16.1/-18.8. (4.0 second interval).

G.10 Test 10: -4.6/-13.6/-17.6

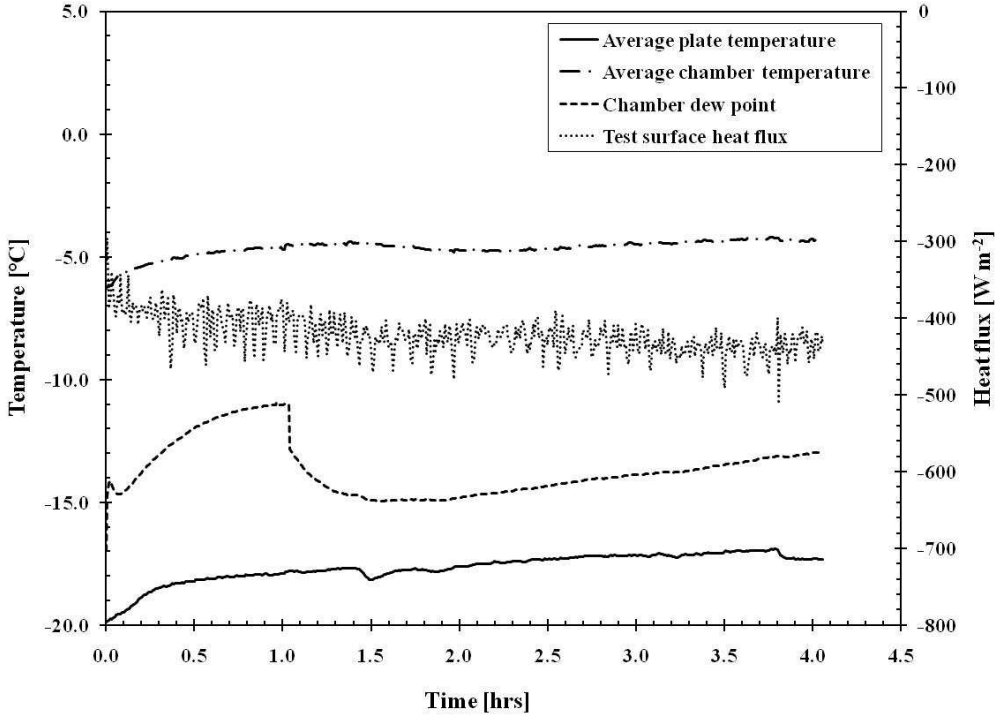

Figure G-44 Temperature and heat flux during frost growth at -4.6/-13.6/-17.6.

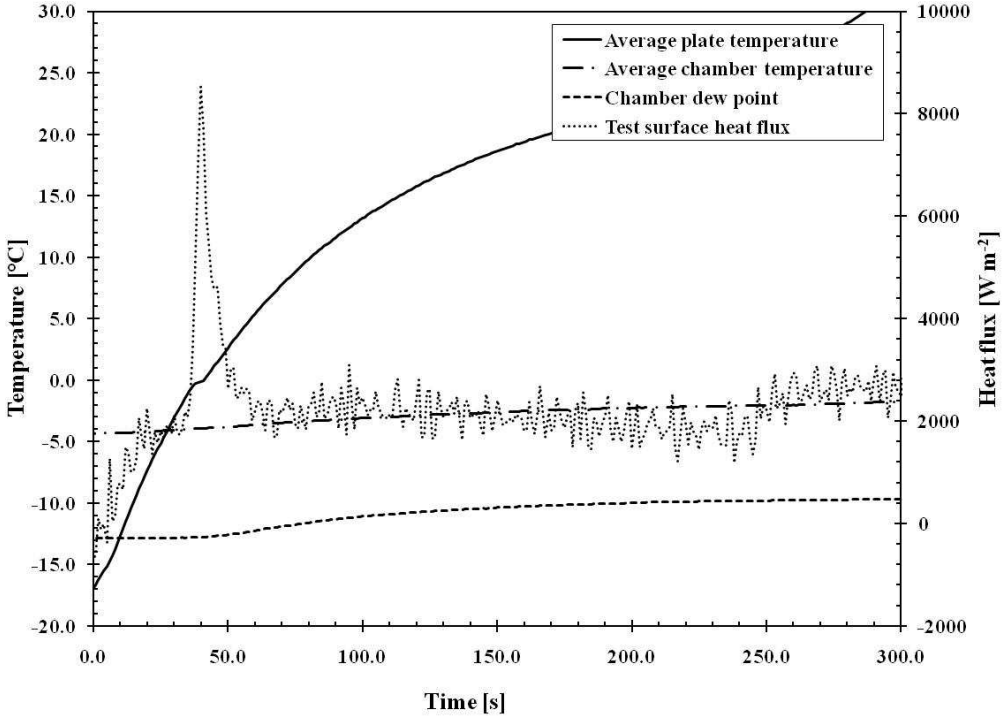

Figure G-45 Temperature and heat flux during defrost at -4.6/-13.6/-17.6.

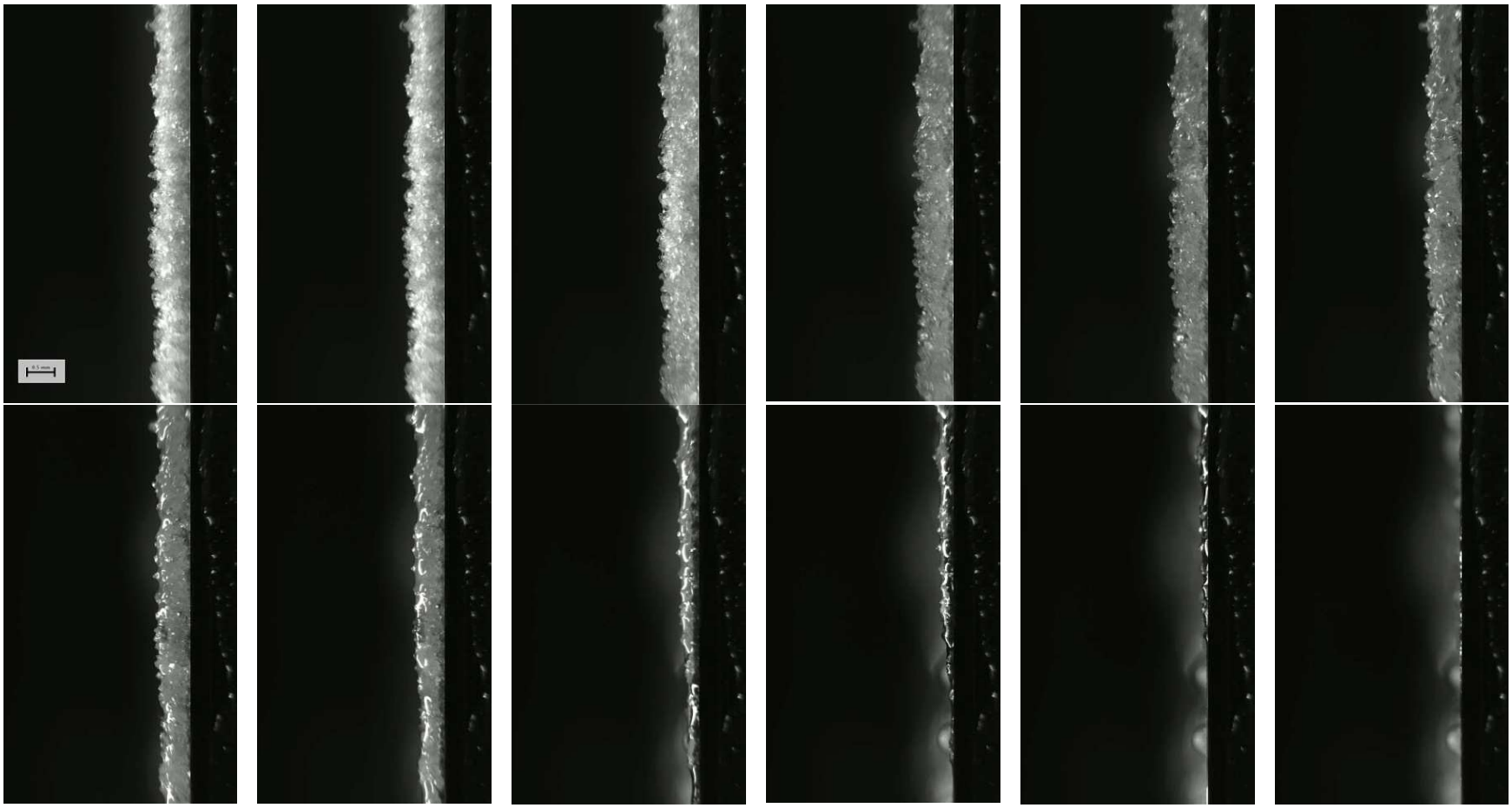

Figure G-46 Side images of defrost at -4.6/-13.6/-17.6. (1.1 second interval).

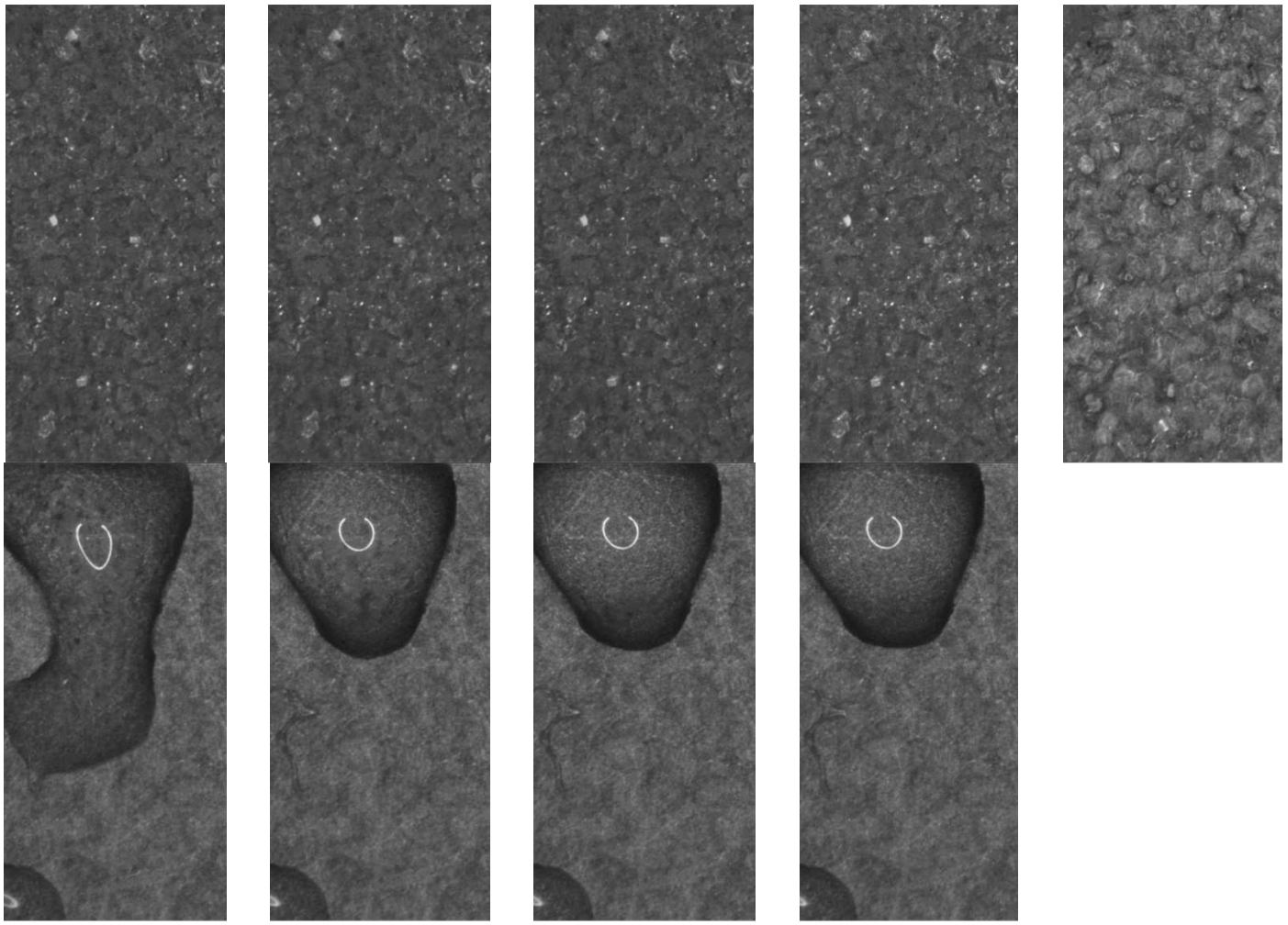

Figure G-47 Frontal images of defrost at -4.6/-13.6/-17.6. (2.0 second interval).

G.11 Test 11: -4.6/-12.0/-18.8

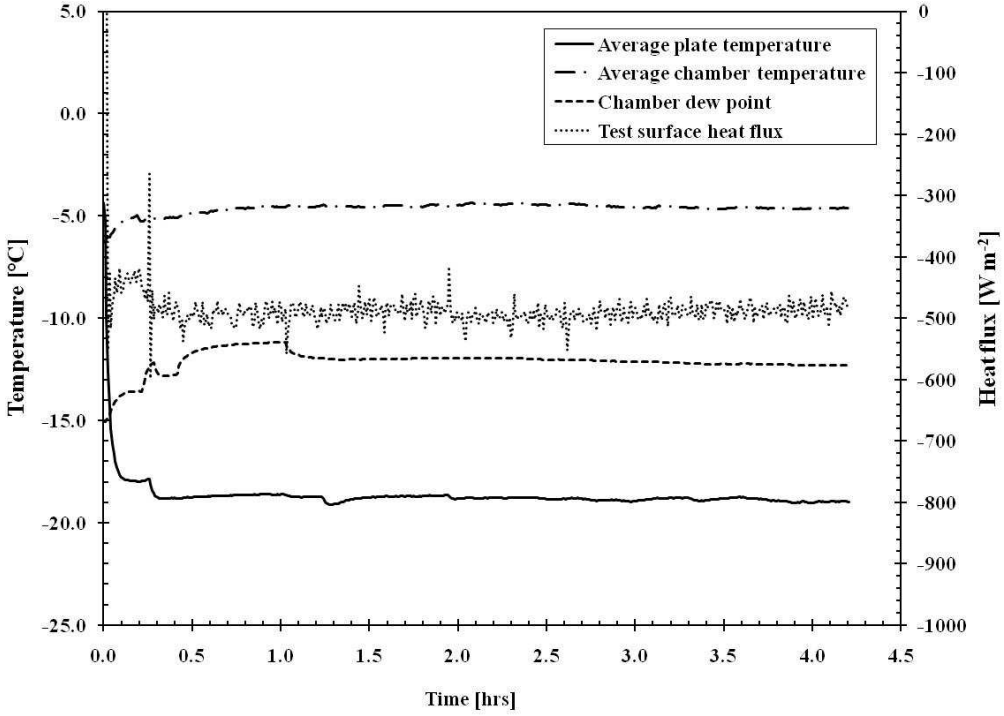

Figure G-48 Temperature and heat flux during frost growth at -4.6/-12.0/-18.8.

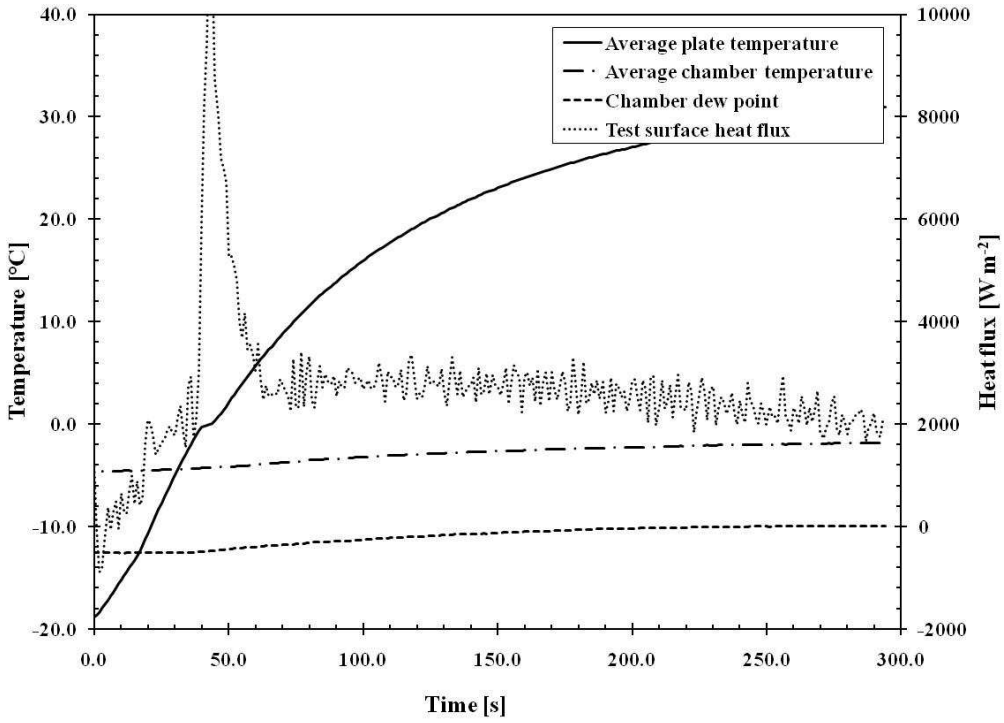

Figure G-49 Temperature and heat flux during defrost at -4.6/-12.0/-18.8.

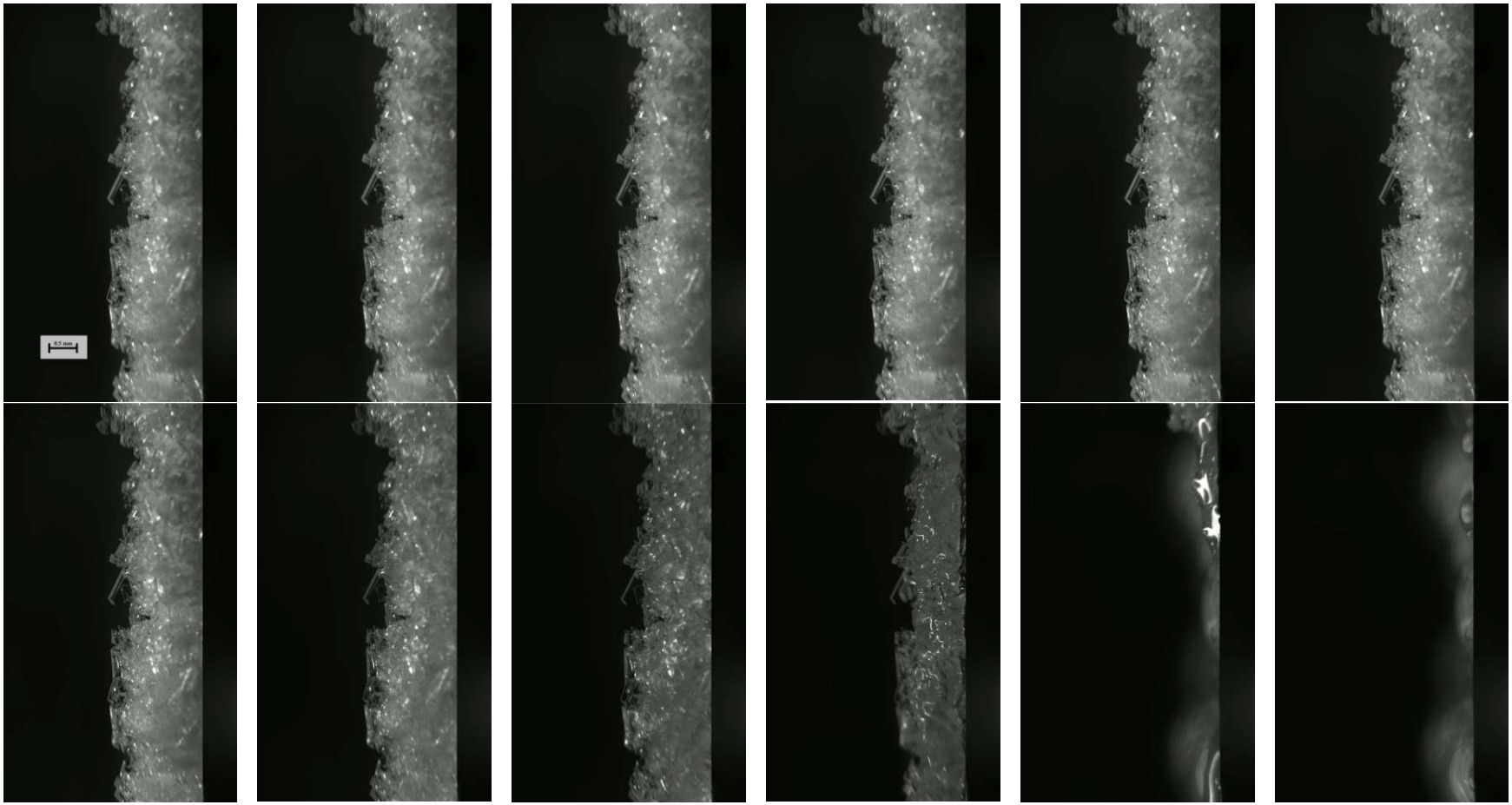

Figure G-50 Side images of defrost at -4.6/-12.0/-18.8. (1.3 second interval).

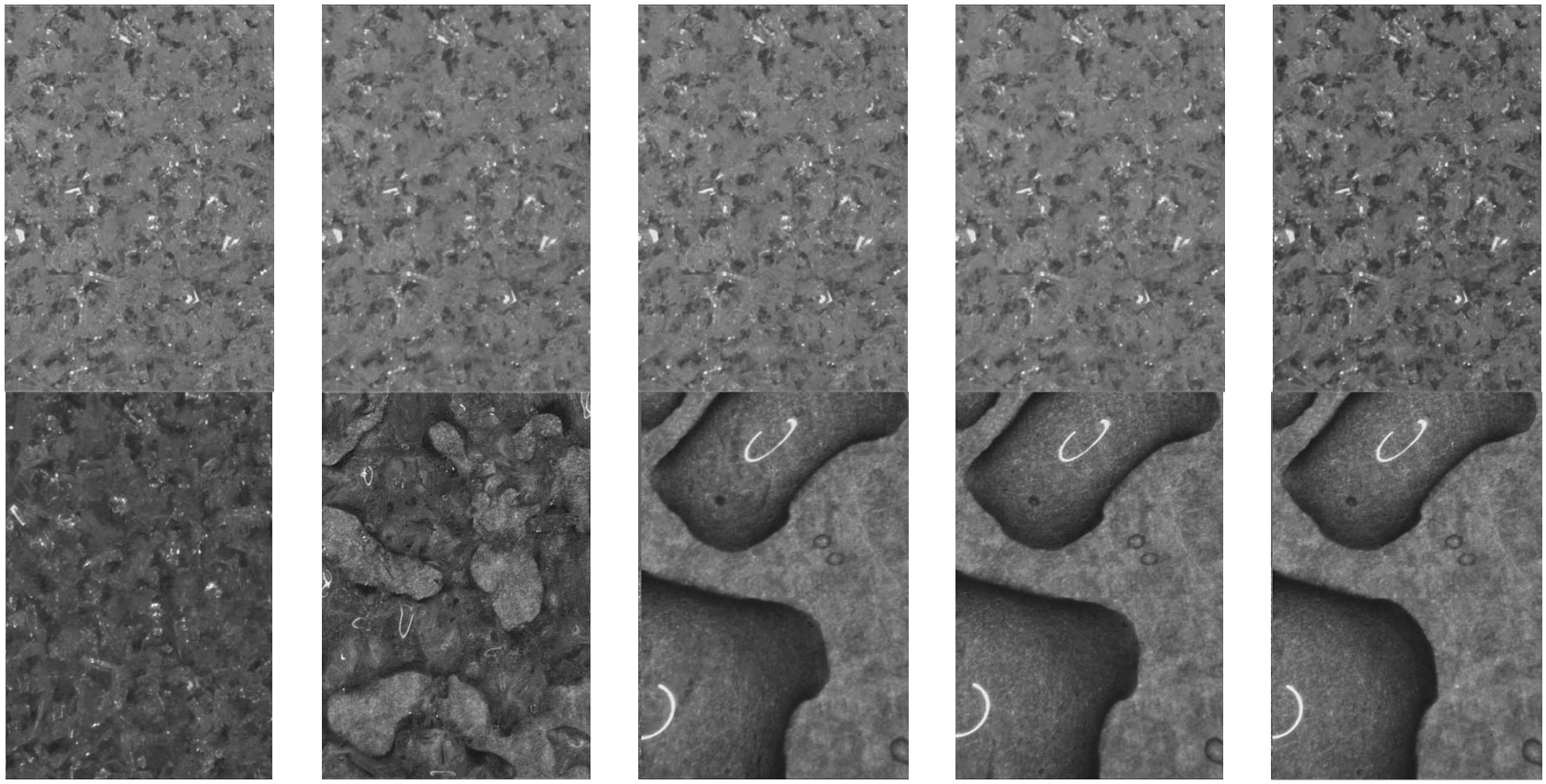

Figure G-51 Frontal images of defrost at -4.6/-12.0/-18.8. (2.0 second interval).

G.12 Test 12: -3.4/-10.0/-17.5

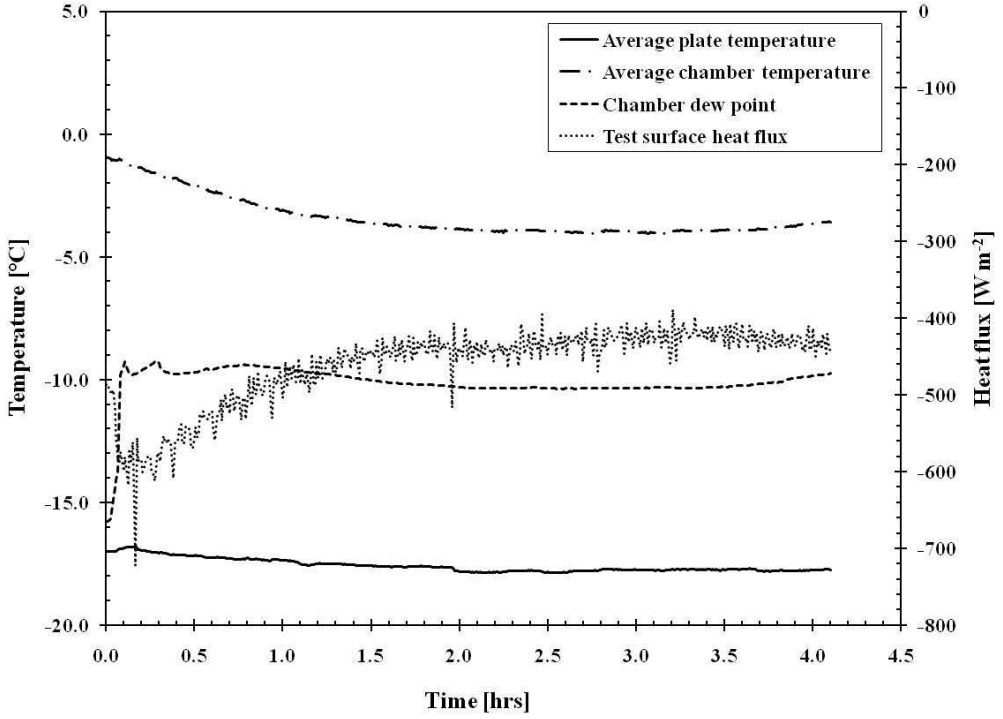

Figure G-52 Temperature and heat flux during frost growth at -3.4/-10/-17.5.

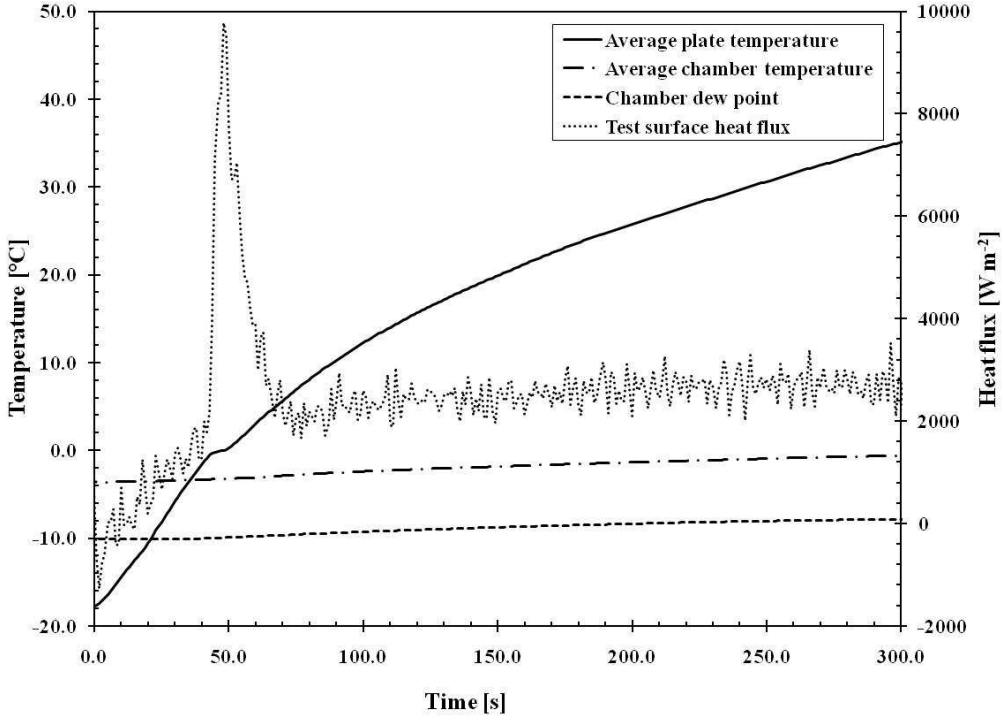

Figure G-53 Temperature and heat flux during defrost at -3.4/-10/-17.5.

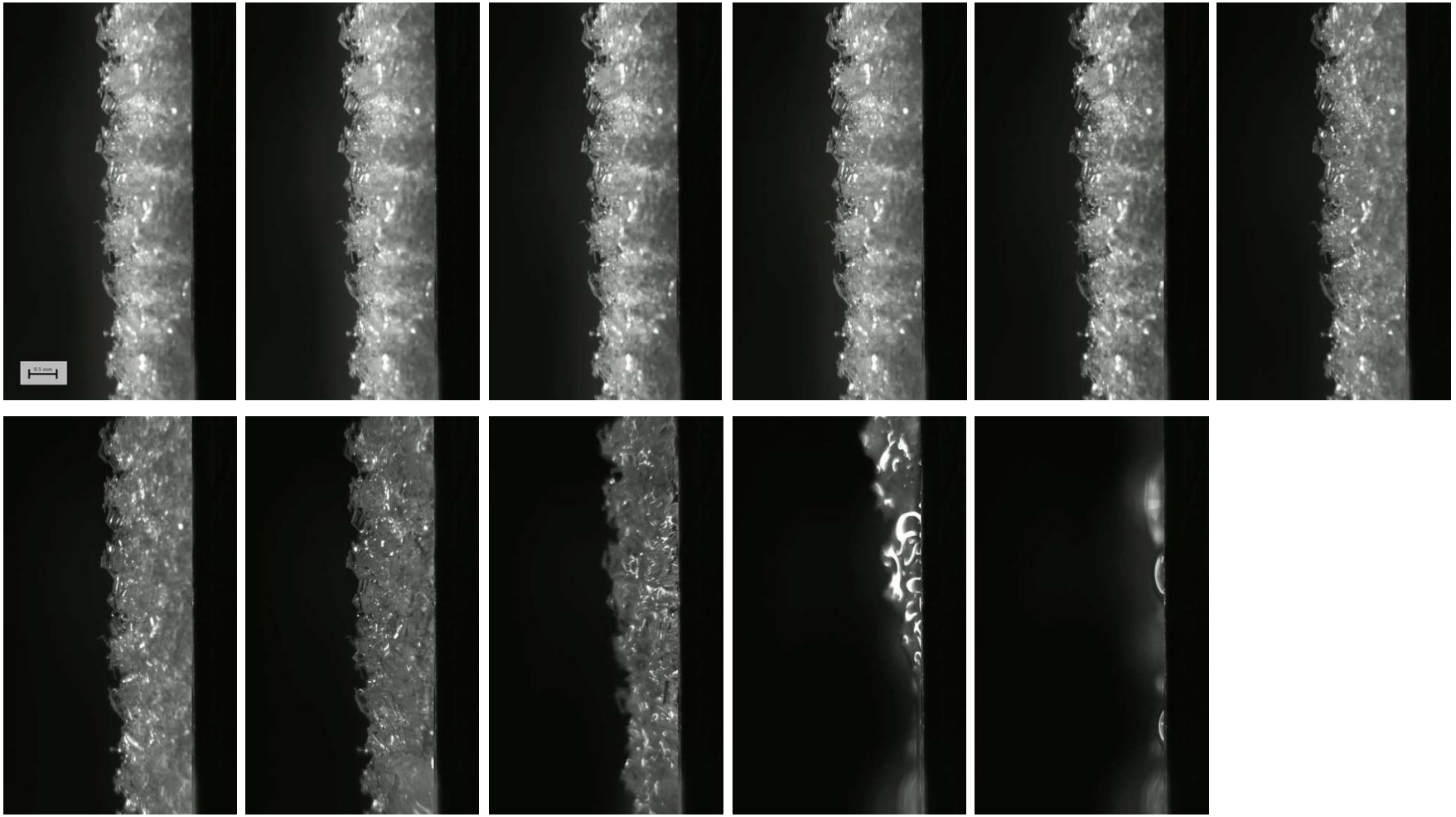

Figure G-54 Side images of defrost at -3.4/-10/-17.5. (2.0 second interval).

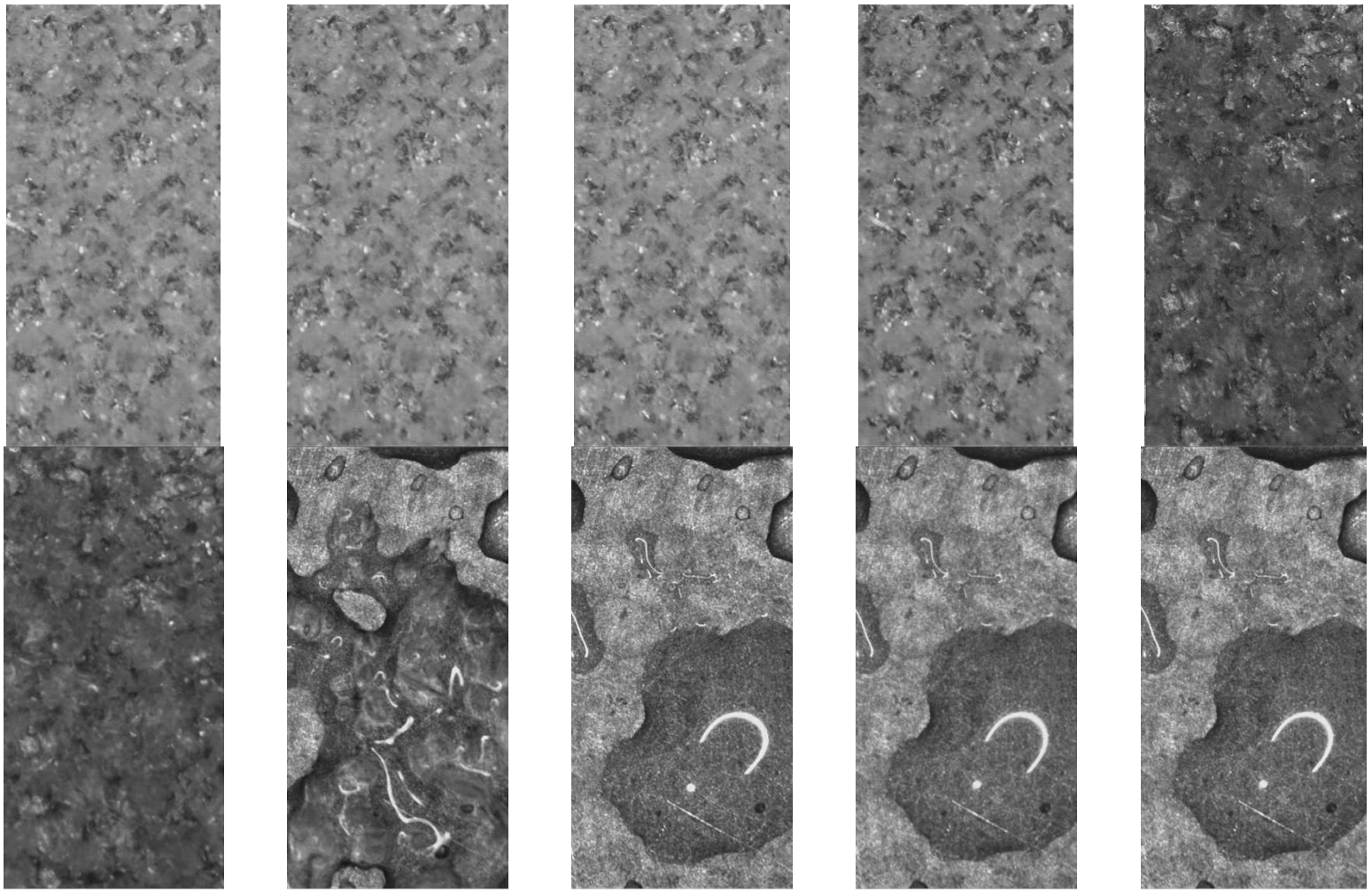

Figure G-55 Frontal images of defrost at -3.4/-10/-17.5. (2.0 second interval).